



NATIONAL TECHNICAL UNIVERSITY OF ATHENS

School of Naval Architecture and Marine Engineering
Division of Ship and Marine Hydrodynamics

Hydrodynamic analysis of ship and marine biomimetic systems in waves using GPGPU programming

PhD Thesis

April 2, 2019

Author:

Evangelos Filippas

Supervisor:

K. A. Belibassakis, Professor NTUA

Committee:

G. A. Athanassoulis, Professor NTUA

G. K. Politis, Professor NTUA

Advisory Committee

- K. A. Belibassakis Professor, National Technical University of Athens, **Supervisor**
G. A. Athanassoulis Professor, National Technical University of Athens
G. K. Politis Professor, National Technical University of Athens

Examination Committee

- K. A. Belibassakis Professor, School of Naval Architecture and Marine Engineering, NTUA
G. A. Athanassoulis Professor, School of Naval Architecture and Marine Engineering, NTUA
G. K. Politis Professor, School of Naval Architecture and Marine Engineering, NTUA
G. S. Triantafyllou Professor, School of Naval Architecture and Marine Engineering, NTUA
K. J. Spyrou Professor, School of Naval Architecture and Marine Engineering, NTUA
S. G. Voutsinas Professor, School of Mechanical Engineering, NTUA
K. C. Giannakoglou Professor, School of Mechanical Engineering, NTUA

*“Those who are inspired by a model other than Nature,
a mistress above all masters,
are laboring in vain.”*

Leonardo Da Vinci

Abstract

Flapping wings located beneath or to the side of the hull of the ship are investigated as unsteady thrusters, augmenting ship propulsion in waves. The main arrangement consists of horizontal wing(s) in vertical oscillatory motion which is induced by ship heave and pitch, while rotation about the wing pivot axis is actively controlled. Moreover, the performance of oscillating foils in the presence of waves and currents is studied for the exploitation of combined renewable marine energy sources in nearshore and coastal regions. The system operates as a semi-activated biomimetic energy device, with imposed pitching motion and induced heaving motion in incident waves and flow. In addition to uniform currents, vertically sheared currents are also considered. In the present thesis, aiming at the detailed investigation of the free-surface effects, a novel method has been developed for the hydrodynamic analysis of 3D foils operating beneath the free surface and undergoing heaving (vertical) and pitching (rotational) oscillations while moving with a constant forward speed.

Mathematical formulation is based on the theory of incompressible, inviscid unsteady potential flow, assuming that the rotational part of the flow is restricted in the trailing vortex sheets emanating from sharp edges; e.g. the trailing edge in the case of a foil. The motion and the geometry of the body are allowed to be general, thus no linearisation has been applied. The fully nonlinear boundary conditions are imposed on the free-surface boundary and an efficient approach is developed for the treatment of oblique nonlinear waves. No smallness assumptions are made, that is, the present approach is a non-perturbative one. The instantaneous angle of attack is influenced by the foil oscillatory motion and by the incident waves. At a first stage of development we consider moderate submergence and relatively low speeds, permitting us to approximately neglect breaking of waves and cavitation. The calculation of generalised forces is obtained by pressure integration, without any further assumption.

The application of Green's formula on the body boundary and the exact free-surface boundary leads to a weakly singular Boundary Integral Equation (BIE) for the unknown boundary fields. For the numerical solution we use a potential based boundary element method (BEM) and a collocation method, obtaining the discretised BIE. The latter after discretisation will be used for the construction of the discretised extended Dirichlet-to-Neumann (DtN) operator that will serve as an algebraic constraint to the equations of the dynamic system, that will be constructed from the free-surface boundary conditions and the Kutta condition. A curvilinear finite difference method (CUFDM), in variable, non Cartesian and non orthogonal coordinate systems, together with the DtN operator, are exploited to express the potential, included in free-surface conditions and the Kutta condition, in terms of the dynamic variables of the problem. The dynamic variables are the free-surface potential and elevation and the potential jump (dipole) intensity at the Kutta strip. The classical time-stepping free-wake analysis in unbounded domain is extended to include the effects of additional boundaries. The evolution of the unknown dynamic variables is obtained by time integration and a novel time-marching scheme is developed for that purpose. Finally, the total solution can be constructed using that information, the DtN operator, the discretised form of the representation theorems and the time history of other known functions.

For the numerical solution of the 3D, unsteady and nonlinear problem an efficient GPU accelerated boundary element method (BEM) is proposed. A computational code is developed, exploiting parallel programming techniques and general purpose programming on graphics processing units (GPGPU), using the CUDA C/C++ application programming interface (API). It is illustrated that the performance of the GPGPU computational code, both in terms of time and space complexity, is substantially higher than the performance of corresponding serial or parallel Central Processing Unit (CPU) codes, implemented by exploiting resources of similar cost.

The present work is structured as follows. We begin in Chapter 1 with a historic review concerning biomimetic wing systems augmenting ship propulsion in waves and oscillating foils operating as a semi-activated biomimetic energy device in incident waves and flow, together with the motivation for the present study and research. Novel contributions of the present thesis are illustrated and an introductory section is dedicated to the GPU implementation.

Subsequently, in Chapter 2, unsteady lifting bodies in an unbounded domain are studied. We assume that the body and the wake boundaries remain in adequately large distance from the other boundaries (free-surface, bottom, lateral walls, shore etc). Moreover, no linearisation is performed in wake dynamics and the evolution of the wake is obtained in the context of a time-stepping method. Numerical results, concerning convergence, stability and efficiency of the proposed method and the developed GPU code are shown and discussed. The interesting problem of efficient thrust production using biomimetic flapping-foil systems is numerically investigated. The present method is applied to obtain numerical estimations of basic hydrodynamic quantities such as lift and thrust coefficient, over a range of motion parameters, including reduced frequency, Strouhal number, maximum angle of attack and aspect ratio. Our analysis indicates that significant efficiency is achieved under optimal operating conditions. The present method and the GPU code could serve as a useful and efficient tool for the assessment, preliminary design and control of the studied efficient marine propulsion system and the reduction of fuel-oil consumption.

Then, in Chapter 3, the method is extended to study the effect of the free-surface boundary and the interaction with the trailing vortex sheet. The modeling includes finite depth effects. We begin with the definition of the unsteady initial boundary value problem (IBVP) problem in a partially bounded domain (Sec.3.2). For simplicity in the description of the present method, and especially concerning the treatment of the free-surface conditions (including the conditions at infinity), we will start our presentation with the boundary integral formulation in the case of non-lifting flow around a body of smooth but arbitrary geometry, undergoing general motion (Sec.3.4). This problem contains, as cases of special interest, the wave-resistance problem due to constant-speed forward motion and the enforced radiation problem due to body oscillations. Then, in Sec.3.5, the whole methodology is extended to model the case of a flapping foil in forward motion beneath the free-surface radiating waves, giving special attention to the treatment of the discretised form of pressure-type Kutta condition and free-surface boundary conditions. The problem of thrust production using biomimetic flapping-foil systems beneath the free-surface including wave-making resistance and finite depth effects is numerically investigated. The importance of free-surface and 3D effects, nonlinearity as well as the superior performance of the developed GPU code, are illustrated.

In the last part of the present work (Chapter 4), the method and the developed GPU code, is extended in cases of lifting flows beneath the free surface and in fully nonlinear waves. That

problem is presented in Sec.4.2. Although, the problem of the system could be treated by the method presented in Chapter 3 using a classical numerical wave tank, a more efficient approach is selected and in that direction a method is developed and presented in Sec.4.3 and in Sec.4.4. The importance of nonlinearity and the performance of the developed GPU code in the case of 3D foils in oblique waves, are also illustrated. The problem of augmentation of the ship's main propulsion in waves is studied in Sec.4.5.3. The present work can be exploited for the design and optimum control of biomimetic systems extracting energy from sea waves for augmenting marine propulsion in rough seas, with simultaneous reduction of ship responses offering dynamic stabilization. Moreover, a semi-activated biomimetic energy device, with imposed pitching motion and induced heaving motion in harmonic incident waves and flow is proposed and a feasibility study is conducted in Sec.4.5.4. The present method can be applied to the design and optimum control of such biomimetic systems operating in the nearshore/coastal region and extracting energy from waves in the presence of ambient currents.

Περίληψη

Βιομηχανικά συστήματα τύπου παλλόμενων πτερυγίων τοποθετημένα στη γάστρα του πλοίου εξετάζονται ως μη μόνιμοι προωστήρες, για τη υποβοήθηση της κύριας πρόωσης του πλοίου σε κυματισμούς. Επιπρόσθετα, εξετάζεται η απόδοση βιομηχανικού συστήματος σε κυματισμούς και ρεύματα για την εκμετάλλευση θαλάσσιας ενέργειας στην παράκτια ζώνη. Στην παρούσα εργασία αναπτύσσεται υπολογιστικό υδροδυναμικό μοντέλο για τη προσομοίωση του ανωτέρω συστήματος σε μη γραμμικούς προσπίπτοντες κυματισμούς, λαμβάνοντας υπόψη τις επιδράσεις της ελεύθερης επιφάνειας.

Η μαθηματική μοντελοποίηση στηρίζεται στη θεωρία ασυμπίεστης, μη συνεκτικής, μη μόνιμης ροής με δυναμικό, με την υπόθεση ότι η στροβιλότητα περιορίζεται στα ακολουθούντα φύλλα στροβιλότητας που παράγονται από αιχμηρές ακμές, όπως η ακμή εκφυγής του πτερυγίου. Η κίνηση και η γεωμετρία του σώματος είναι γενικές και δεν έχει εφαρμοστεί κάποια γραμμικοποίηση. Οι πλήρως μη γραμμικές συνοριακές συνθήκες ικανοποιούνται στο σύνορο της ελεύθερης επιφάνειας και μία αποδοτική μεθοδολογία αναπτύσσεται για την μελέτη σωμάτων σε προσπίπτοντες μη γραμμικούς κυματισμούς. Η γωνία πρόσπτωσης του πτερυγίου επηρεάζεται από τις κινήσεις του σώματος και από τους κυματισμούς. Στην παρούσα μοντελοποίηση δε λαμβάνουμε υπόψη τις επιδράσεις θραύσης του κύματος και της σπηλαίωσης, αφήνοντας τη μελέτη των συστημάτων σε αυτές τις συνθήκες για μελλοντική εργασία. Ο υπολογισμός των γενικευμένων δυνάμεων γίνεται με ολοκλήρωση των πιέσεων στο σύνορο του σώματος χωρίς περαιτέρω παραδοχές.

Εφαρμόζεται το θεώρημα αναπαράστασης του δυναμικού (Green's formula) για την παραγωγή μιας ασθενώς ιδιόμορφης συνοριακής ολοκληρωτικής εξίσωσης. Για την επίλυση χρησιμοποιείται μέθοδος συνοριακών στοιχείων (boundary element method, BEM) βασισμένη στο δυναμικό, σε συνδυασμό με τεχνική ταξίθεσίας (collocation). Προκύπτει έτσι η διακριτοποιημένη εκδοχή της συνοριακής ολοκληρωτικής εξίσωσης, που χρησιμοποιείται για την έκφραση του τελεστή Dirichlet-to-Neumann (DtN), που αποτελεί έναν περιορισμό στις εξελικτικές εξισώσεις του δυναμικού συστήματος. Οι τελευταίες παράγονται από τις συνοριακές συνθήκες στην ελεύθερη επιφάνεια και τη συνθήκη Kutta στην ακμή εκφυγής. Παρουσιάζεται μία μέθοδος πεπερασμένων διαφορών (curvilinear finite difference method, CUFDM) σε καμπυλόγραμμα συστήματα συντεταγμένων. Η μέθοδος αυτή και ο τελεστής DtN, αξιοποιούνται για να εκφραστεί το δυναμικό, που εμφανίζεται στις εξισώσεις της ελεύθερης επιφάνειας και στη συνθήκη Kutta, σαν συνάρτηση των δυναμικών μεταβλητών του προβλήματος, που είναι το δυναμικό στην ελεύθερη επιφάνεια, η ανύψωσή της, καθώς και το άλμα δυναμικού (ένταση διπόλων) στη λωρίδα Kutta. Παρουσιάζεται ένα μοντέλο μη γραμμικού όμορου που λαμβάνει υπόψη τις επιδράσεις των επιπρόσθετων συνόρων και των κυματισμών. Η εξέλιξη των δυναμικών μεταβλητών προκύπτει με αριθμητική ολοκλήρωση του παραπάνω συστήματος ενώ τα λοιπά πεδία μπορούν να υπολογιστούν από τη χρονική ιστορία και τις τιμές των συνοριακών μεγεθών χρησιμοποιώντας το θεώρημα αναπαράστασης και τον τελεστή DtN.

Για την αποδοτική υλοποίηση της αριθμητικής μεθοδολογίας αναπτύσσεται υπολογιστικός κώδικας, αξιοποιώντας τεχνολογίες παράλληλου προγραμματισμού σε κάρτα γραφικών (General-Purpose Computing on Graphics Processing Units - GPGPU), χρησιμοποιώντας τη γλώσσα προγραμματισμού CUDA C/C++. Καταδεικνύεται η ότι απόδοση του GPU κώδικα είναι ουσιαστικά καλύτερη από αυτή που θα είχε αντίστοιχος, σειριακός ή και παράλληλος, CPU κώδικας υπολογιστικής ρευστομηχανικής (computational fluid dynamics, CFD),

χρησιμοποιώντας πόρους αντίστοιχου κόστους με αυτούς που χρησιμοποιήθηκαν στη συγκεκριμένη εργασία.

Η παρούσα εργασία δομείται ως εξής. Στο εισαγωγικό κεφάλαιο ξεκινάμε με μία επισκόπηση της ερευνητικής εργασίας σχετικά με τους προωστές ταλαντούμενων πτερυγίων για την υποβοήθηση της πρόωσης πλοίου σε κυματισμούς και τα ταλαντούμενα πτερύγια για την εκμετάλλευση ενέργειας από κύματα και ρεύματα. Επίσης, παρουσιάζεται ο σκοπός και το κίνητρο καθώς και η συνεισφορά της παρούσας μελέτης και έρευνας. Στη συνέχεια παραθέτουμε βασικές παρατηρήσεις πάνω στην υλοποίηση του παράλληλου GPU κώδικα.

Ακολούθως, στο Κεφάλαιο 2, μελετάται το πρόβλημα μη μόνιμης ροής με άνωση γύρω από σώματα με έμφαση σε τρισδιάστατα παλλόμενα πτερύγια που εξετάζονται ως μη μόνιμοι βιομημητικοί προωστές. Υποθέτουμε ότι το σώμα και το σύνορο του ομόρρου βρίσκονται σε μεγάλη απόσταση από τα υπόλοιπα σύνορα (ελεύθερη επιφάνεια, πυθμένας, παράπλευρα σύνορα). Η μη γραμμική δυναμική του φύλλου στροβιλότητας συμπεριλαμβάνεται στη μοντελοποίηση χωρίς απλοποίηση και η εξέλιξη του φύλλου στροβιλότητας γίνεται στο πεδίο του χρόνου (time-stepping free-wake analysis). Αριθμητικά αποτελέσματα σχετικά με τη σύγκλιση την ευστάθεια και την απόδοση του σχήματος και του παράλληλου GPU κώδικα παρουσιάζονται και σχολιάζονται. Εξετάζεται το πρόβλημα της πρόωσης πλοίου με προωστές ταλαντούμενων πτερυγίων, και παρουσιάζονται αποτελέσματα σχετικά με τους συντελεστές ώσης, άνωσης καθώς και την εξέλιξη της κατανομής της πίεσης πάνω στο σώμα, για ένα εύρος των παραμέτρων κίνησης όπως είναι η reduced frequency, ο αριθμός Strouhal, η γωνία πρόσπτωσης και ο λόγος επιμήκους και συγκρίνονται με άλλες μεθόδους. Η ανάλυσή μας καταδεικνύει πως σημαντική απόδοση μπορεί να επιτευχθεί κάτω από βέλτιστες καταστάσεις λειτουργίας. Η ανάλυσή καταδεικνύει πως μπορεί να επιτευχθεί σημαντική απόδοση κάτω από βέλτιστες καταστάσεις λειτουργίας. Η παρούσα μέθοδος και ο GPU κώδικας μπορεί να χρησιμοποιηθούν σαν χρήσιμα εργαλεία για την μελέτη, την προκαταρκτική σχεδίαση και τον έλεγχο τέτοιων συστημάτων για την αποδοτική πρόωση πλοίων και την εξοικονόμηση ενέργειας.

Στη συνέχεια, στο Κεφάλαιο 3, η μέθοδος επεκτείνεται έτσι ώστε να λαμβάνονται υπόψη οι επιδράσεις της ελεύθερης επιφάνειας με στόχο τη μελέτη των βιομημητικών συστημάτων κοντά στην ελεύθερη επιφάνεια δίνοντας έμφαση στην αλληλεπίδραση της με τον ομόρρο των πτερυγίων. Λαμβάνονται υπόψη και η επιδράσεις του πυθμένα. Ξεκινάμε με τη διατύπωση του μη μόνιμου προβλήματος αρχικών και συνοριακών τιμών γύρω από ανωστικά σώματα στο μερικώς φραγμένο χωρίο (Παράγραφος 3.2). Για απλότητα στην περιγραφή της παρούσας μεθόδου και ιδιαίτερα όσο αφορά τη διαχείριση των συνθηκών ελεύθερης επιφάνειας της θάλασσας (συμπεριλαμβανομένων των συνθηκών στο άπειρο), στην Παράγραφο 3.4, παρουσιάζουμε τη διατύπωση του προβλήματος, στα πλαίσια της θεωρίας ολοκληρωτικών εξισώσεων, για την περίπτωση ροών χωρίς κυκλοφορία γύρω από σώματα ομαλής, αλλά γενικής γεωμετρίας που εκτελούν γενική κίνηση. Το πρόβλημα αυτό σχετίζεται με την κυματογένεση από τις κινήσεις του σώματος και συμπεριλαμβάνει δύο υποπροβλήματα ιδιαίτερου ενδιαφέροντος, το πρόβλημα αντίστασης κυματισμού και το πρόβλημα ακτινοβολίας λόγω των ταλαντωτικών κινήσεων του σώματος. Στη συνέχεια, στην Παράγραφο 3.5, η μεθοδολογία επεκτείνεται στην περίπτωση παλλόμενων πτερυγίων σε πρόσω κίνηση κάτω από την ελεύθερη επιφάνεια, δίνοντας έμφαση στη διαχείριση της συνθήκης Kutta και των συνοριακών συνθηκών στην ελεύθερη επιφάνεια. Εξετάζεται η παραγωγή ώσης από βιομημητικούς προωστές κάτω από την ελεύθερη επιφάνεια, λαμβάνοντας υπόψη την αντίσταση κυματισμού και τις επιδράσεις του πυθμένα. Καταδεικνύεται η σημασία των επιδράσεων ελεύθερης επιφάνειας και τρισδιάστατων φαινομένων, και παρουσιάζεται η απόδοση του GPU κώδικα.

Στο τελευταίο μέρος της παρούσας εργασίας (Κεφάλαιο 4), η μέθοδος και ο GPU κώδικας επεκτείνεται για το πιο περίπλοκο πρόβλημα της ροής γύρω από μη μόνιμα ανωστικά σώματα κοντά στην ελεύθερη επιφάνεια της θάλασσας και σε κυματισμούς. Το πρόβλημα αυτό θα μπορούσε να αντιμετωπιστεί με τη μέθοδο που παρουσιάζεται στο Κεφάλαιο 4, εάν τα παράπλευρα σύνορα μοντελοποιούσαν έναν αριθμητικό κυματιστήρα (numerical wave tank approach). Στην παρούσα εργασία αναπτύσσεται μία αποδοτική μέθοδος που παρουσιάζεται στις Παραγράφους 4.3 και 4.4. και καταδεικνύεται η σημασία των επιδράσεων ελεύθερης επιφάνειας και τρισδιάστατων φαινομένων, καθώς και η απόδοση του GPU κώδικα σε μη γραμμικούς κυματισμούς που προσπίπτουν στο σώμα από διάφορες διευθύνσεις σε σχέση με τη διεύθυνση κίνησης του σώματος.

Στη συνέχεια μελετάται το πρόβλημα της υποβοήθησης της πρόωσης του πλοίου σε κυματισμούς (Σχήμα 1.α) στην Παράγραφο 4.5.3. Η κύρια διάταξη αποτελείται από οριζόντιο πτερυγίο που κινείται με τη σταθερή πρόσω ταχύτητα του πλοίου και παράλληλα εκτελεί κατακόρυφη ταλαντωτική κίνηση λόγω της κατακόρυφης ταλάντωσης και προνευτασμού του πλοίου σε κυματισμούς, ενώ η περιστροφική ταλάντωση του πτερυγίου γύρω από τον άξονά του ελέγχεται ενεργητικά. Πιο συγκεκριμένα, θεωρούμε πως το σύστημα πλοίο - ταλαντούμενο πτερυγίο προωστήρας λειτουργεί σε κυματισμούς που περιγράφονται από φάσμα συχνότητας, που αντιπροσωπεύει συγκεκριμένη κατάσταση θάλασσας, λαμβάνοντας υπόψη τη σύζευξη μεταξύ της δυναμικής της γάστρας και του παλλόμενου πτερυγίου. Η παρούσα μέθοδος μπορεί να χρησιμοποιηθεί για το σχεδιασμό και τον έλεγχο βιομιμητικών συστημάτων για την εκμετάλλευση της ενέργειας των κυματισμών με σκοπό την υποβοήθηση της πρόωσης πλοίων, με ταυτόχρονη ελάττωση των ανεπιθύμητων αποκρίσεων και βελτίωση της δυναμικής ευστάθειας.

Τέλος, εξετάζεται βιομιμητικό σύστημα ταλαντούμενου πτερυγίου για την συνδυασμένη εκμετάλλευση ενέργειας από κύματα και ρεύματα στην παράκτια ζώνη και παρουσιάζονται στοιχεία για την απόδοση του. Η μοντελοποίηση περιλαμβάνει τις επιδράσεις ενός μη μόνιμου ανομοιόμορφου πεδίου υποβάθρου. Πιο συγκεκριμένα, εξετάζονται ημι-ενεργητικά και αυτοδιεγειρούμενα συστήματα ταλαντούμενων πτερυγίων, με εξαναγκασμένη περιστροφική κίνηση και διεγειρόμενη μεταφορική ταλάντωση σε προσπίπτοντες κυματισμούς και ροή κάτω από την ελεύθερη επιφάνεια της θάλασσας και σε γενική βαθυμετρία. Η παρούσα μέθοδος μπορεί να χρησιμοποιηθεί για το σχεδιασμό και τον έλεγχο βιομιμητικών συστημάτων για την εκμετάλλευση των παραπάνω ανανεώσιμων πηγών ενέργειας.

Η εργασία ολοκληρώνεται με τη διατύπωση συμπερασμάτων και προτάσεων για μελλοντική έρευνα πάνω στα θέματα που εξετάστηκαν.

Acknowledgements

I am standing still ticking away the moments. Sharing with Them Your fellowship.
You, our ancient comrade.

"Plans that either come to naught or half a page of scribbled lines".

On the 17th of February, 2019.

In that room, enduring as a long distance runner with his mind traveling in space & time.

Be carried away to Syracuse by the M-use's dance, the bittersweet melody reminding me she's making what I abandoned, her moves whispering it...

acknowledge Those who encouraged the second voyage to begin,

may the odds be a few times in your favor,

little explorer.

The present PhD Thesis is completing an almost six-year period of postgraduate studies at the School of Naval Architecture and Marine Engineering of National Technical University of Athens. Thus, I grab the chance to express my sincere gratitude to a number of people whose contribution was valuable for the accomplishment of this work and of my studies.

First of all, I would like to thank my supervisor and mentor professor Belibassakis for his guidance and support during the preparation of this thesis. His deep and wide knowledge in the field of marine hydrodynamics provided me with the required background to overcome the difficulties encountered during this study. Furthermore, he gave me inspiration and encouragement during that educational, as well as preceptive journey. Sometimes I read a specific *mantinada* when I warm my bones beside the fire or survive through life in that apartment.

Another special thank would be to professor Politis for supporting me and introducing me to application of BEM on the problem of unsteady foils in unbounded domain and answering always on the phone sharing invaluable advice. I would also like to thank professor Politis for encouraging my introduction to GPGPU programming.

I would like to thank professor Athanassoulis for kindly sharing with words and acts the foundation of his philosophy leaving in young students' minds undying quotes. Thank you Professor for transfusing to me your love for mathematics. Many thanks and greetings to professor's students.

I would like to express my sincere gratitude and appreciation to professor Voutsinas, for supporting and mentoring a lot of researchers and for providing me with valuable advice. I would also like to thank his team, especially Dr Manolas, Kostas Diakakis and Theologos Andronikos, as well as assistant professor Papadakis and Senior Lecturer Manolesos.

Moreover, I would like to thank professor Giannakoglou his team for the useful instructions concerning GPGPU computing included in the PhD thesis of Dr Trompoukis.

I would also like to thank professor Triantafyllou for his lectures in ship and marine hydrodynamics that motivated my research in the specific topic.

I would like to express my sincere thankfulness to professor Spyrou for the useful knowledge I earned during his course in nonlinear dynamics also special thanks go to his team, especially PhD students Anastopoulos and Kontolefas. I am particularly grateful for a specific conversation that inspired me to work with undergraduate students.

Thank you Andreas Priovolos, Dimitra Anevlavi and Panagiotis Koutsogiannakis for that invaluable experience. Panagiotis thank you for the useful advice you provided through the development of the GPU code and the preparation of the manuscript in LaTeX.

Moreover, of utmost importance was the inspiration of the aforementioned researchers, as well as assistant professor Papathanasiou, associate professor Gerostathis and professor Tzabiras during my studies.

Another special thank would be to researcher Giannis Georgiou and to Dr Tsarsitalidis, Dr Tsantili and Dr Papoutselis and PhD Candidates Angeliki Karperaki, Flora Karathanasi, Aris Kapelonis and Konstantinos Mamis, for the support and their very useful advice.

I am also grateful to Alexander S. Onassis Public Benefit Foundation for their financial support through the G ZJ 062/2013-2014 scholarship grant. Moreover, I am sincerely grateful to a former grand recipient of the foundation Manolesos.

Last but not least, I would like to thank my family, my friends (Angelina you also belong here), inside and outside the institution and specific truly important people as without their help, support and understanding it would be very difficult to finish my studies.

Contents

Abstract	vii
Acknowledgements	xiii
List of Notation	xxiii
1 Introduction	1
1.1 Augmenting ship propulsion in waves using biomimetic flapping-foil systems	1
1.2 Energy extraction from waves and currents nearshore	10
1.3 Main original contributions	13
1.3.1 Innovations in the numerical method	13
1.3.2 Innovations in the computational code and its performance	15
1.3.3 Innovations in the applications	15
1.3.3.1 The flapping foil as an efficient main propulsion system and the concept of the wave-augmented biomimetic propulsor	16
1.3.3.2 The wavefoil for the augmentation of ship main propulsion in waves	16
1.3.3.3 Biomimetic flapping-foils as combined marine energy extraction devices nearshore	16
1.4 Implementation of the GPGPU computational code	17
2 Unsteady lifting bodies in unbounded domain	21
2.1 Summary	21
2.2 Definition of the unsteady lifting problem	22
2.3 Boundary Integral Formulation	27
2.4 Spatial discretisation - DtN construction	31
2.5 Velocity calculation	36
2.5.1 Calculation of potential gradient with the representation theorem for the velocities	37
2.5.1.1 Velocity representation theorem on body boundary	40
2.5.1.2 Velocity representation theorem in the fluid domain	41
2.5.1.3 Velocity representation theorem on the wake - Discretised form	42
2.5.2 Efficient calculation of the potential surface gradient with curvilinear finite differences	45
2.5.2.1 Differentiation on the boundary	45
2.5.2.2 Curvilinear finite differences on a non-uniform grid	47
2.6 Free-wake analysis	51
2.7 Pressure calculation	56
2.8 Pressure-type Kutta condition	59

2.8.1	Analytical form	59
2.8.2	Discretised form - The dynamical system	62
2.9	Time integration of the system	65
2.10	Numerical results and discussion	66
2.10.1	Stability and convergence	66
2.10.2	Validation and GPU performance	67
2.10.3	Biomimetic flapping-foil thruster	69
2.11	Remarks and conclusions	76
3	Hydrodynamic analysis of bodies beneath the free surface	77
3.1	Summary	77
3.2	Mathematical formulation of lifting bodies beneath the free surface	78
3.3	Pressure calculation and Kutta condition	82
3.4	Boundary integral formulation of non-lifting bodies beneath the free surface . .	85
3.4.1	Discretisation the DtN map	88
3.4.2	Discretised free-surface boundary conditions and the dynamical system	90
3.4.3	Numerical time integration of the system	92
3.4.4	Conditions at infinity - Implementation of PML model	92
3.4.5	Numerical results and discussion	94
3.4.5.1	2D calculations	94
3.4.5.2	3D calculations and GPU performance	96
3.5	Boundary integral formulation and BEM for lifting bodies beneath the free sur- face	97
3.5.1	Discretisation and the extended DtN map	100
3.5.2	Discretised free-surface and Kutta conditions and the dynamical system	102
3.5.3	Numerical results and discussion	108
3.5.3.1	Steady foil beneath the free surface	108
3.5.3.2	Free surface and finite depth effects on flapping-foil thrusters . .	110
3.5.3.3	Nonlinear wake effects	112
3.5.3.4	3D effects nonlinearity and GPU performance	113
3.6	Non-linear numerical wave tank	114
3.7	Remarks and conclusions	114
4	Hydrodynamic analysis of bodies in waves	117
4.1	Summary	117
4.2	Mathematical formulation of lifting bodies in nonlinear waves	119
4.3	The representation of the total fields	121
4.4	Boundary integral formulation and BEM for lifting bodies in waves	125
4.4.1	Representation theorem and BIE for the corrector potential	125
4.4.2	Discretisation and the extended DtN map	127
4.4.3	Pressure calculation and implementation of the pressure-type Kutta con- dition	129
4.4.4	Discretised free-surface and Kutta conditions and the dynamical system	133
4.4.5	Numerical time integration of the system	141
4.5	Numerical results and discussion	142
4.5.1	DtN calculation in the case of propagation of a solitary wave over gen- eral bathymetry	142

4.5.2	Free-surface effects on wave-augmented propulsion using flapping-foil biomimetic systems	145
4.5.3	Augmenting ship propulsion in waves by actively controlled flapping foils	148
4.5.4	Semi-activated oscillating hydrofoil as a nearshore biomimetic energy system in waves and currents	158
4.5.4.1	Numerical simulation of the biomimetic energy system in waves and currents	160
4.5.4.2	Investigation of the operational parameters	164
4.5.4.3	Investigation of the environmental parameters	167
4.6	Remarks and conclusions	172
Conclusions and suggestions for future research		175
References		179

List of Figures

1.1	Ship hull equipped with flapping wing(s) located at a forward station. Detailed view of the flapping wing, which oscillates vertically (shown by a solid arrow) and around its pivot axis (shown by a dashed arrow), is included in the subplot.	2
1.2	Jakobsen equipped fishing research vessel Kystfangst, owned by the Institute of Fishery Technology Research, with a bulbous bow and two foils on each side of the bow.	3
1.3	Fishing vessel equipped with flapping foil to improve propulsion in waves (Terao and Isshiki 1991).	3
1.4	Russian research fishing vessel equipped with flapping foil (Nikolaev et al. 1995).	4
1.5	The Suntory Mermaid II which sailed from Hawaii to Japan in 2008 (Geoghegan 2008).	5
1.6	Terao and Sakagami (2013) equipped an small autonomous boat, for ocean measurements, with a wave devouring propulsion system (WDPS).	5
1.7	Bøckmann (2015) performed experiments with a model equipped with a foil below the hull for motion reduction and thrust production in waves.	6
1.8	Photo of the experimental platforms exploited in the work of Bowker (2018) for the (a) towing tank and the (b) free-running experiments of flapping-foil wave powered vessels.	6
1.9	The case vessel with wavefoils deployed from work Bøckmann et al. (2018) were fuel savings from the wave-foils were estimated.	7

1.10	(a) Ship hull equipped with a flapping wing located below the keel, $T = 2.8$ m at a forward station. (b) Same hull with a vertical flapping wing located below the keel, at the midship section. Geometrical details of the flapping wings are included in the upper subplots. The main flow direction relative to the flapping wings is indicated using a blue arrow. Black arrows indicate linear oscillatory motion and red ones the actively controlled (pitching) motion of the wing about its pivot axis, for which only a quite small amount of energy is provided (Belibassakis and Politis 2013).	8
1.11	The bioSTREAM biomimetic system for exploitation of current flow energy, proposed by BioPower.	11
1.12	A laboratory-scale model of a semi-activated flow-energy harvesting device Huxham et al. (2012).	12
2.1	Comparison of different wake models: (a) 3D free wake model (b) 2D frozen and free wake models.	25
2.2	Potential field induced by constant-strength doublet distribution (double layer potential) on a straight-line panel.	28
2.3	Potential field induced by constant-strength source distribution (single layer potential) on a straight-line panel.	28
2.4	Introduction of a branch cut that permits the existence of circulation around lifting bodies without breaking irrotationality of the flow.	29
2.5	Spatial discretisation via approximation of the boundary with boundary elements and of the trace functions with piecewise constant distributions as well as approximate satisfaction of the BIE by applying a collocation scheme in (a) 2D and in (b) 3D.	31
2.6	Definition of Kutta strip ∂D_K as a transitional region between the bound surface (body boundary) and the free surface (trailing vortex sheet). Discretisation of Kutta strip and representation by N_K boundary elements.	33
2.7	Decomposition of velocity $\nabla_0 \Phi$ to its normal to the boundary $\partial_{n_0} \Phi \cdot \mathbf{n}$ and its tangential to the boundary $\partial_{s_0} \Phi \times \mathbf{n}$ components.	39
2.8	Convergence of thrust coefficient C_T as a function of the number of body panels N_B and the time-step $\Delta t/T(\%)$, for a NACA0012 hydrofoil in flapping motion. The error of thrust coefficient (%) is shown using colorscale. Contour lines indicate the ratio $\Delta s_W/\Delta s_B$ of the length of panels in the vicinity of the trailing edge.	66
2.9	Double precision execution time profile for the calculation of the potential on an ellipsoid with semi-axis ratio selected to be 0.5:2.5:0.06, to have similar shape with a foil.	68
2.10	Mixed precision execution time profile for the calculation of the potential on the ellipsoid of figure 2.9.	68
2.11	Benchmarking between a single threaded CPU core (Intel i5-2300 3.4GHz) and an GTX1080 GPU with 2560 NVIDIA CUDA Cores for the problem of Fig.2.9.	68
2.12	Validation against analytical solution and demonstration of the performance using mixed-precision arithmetics for the example of Fig.2.9.	69
2.13	Amplitude of lift coefficient of NACA0012 hydrofoil, in low-amplitude flapping motion $h_0/c = 0.1, \theta_0 = 10^\circ, \psi = -90^\circ, X_R/c = 0.5$ in infinite domain. Present method results against linearized theory predictions with and without the contribution of added mass effects.	70

2.14	Thrust coefficient for NACA0012 hydrofoil, in flapping motion with $h_0/c = 1, \psi = -90^\circ, X_R/c = 0.33$. Present method compared against experimental data from Read et al. (2003).	71
2.15	Simulation of biomimetic flapping-foil thruster in unbounded domain: (a) Time history of lift and thrust coefficients, comparison of the fully nonlinear 3D calculations with $AR = 6$ & $AR = 40$ against experimental results, 3D calculations with a prescribed wake model and 2D calculations. (b) Potential and velocities on the body and potential jump on the wake (fully nonlinear calculations). For a constant-chord foil with NACA0012 sections and $St = 0.3, h_0/c = 0.75, \theta_0 = 23.3^\circ$, pivot point $X_R/c = 0.33$ and phase lag $\psi = -90^\circ$	72
2.16	Systematic results of averaged thrust coefficient for a 2D NACA0012 hydrofoil, in flapping motion with parameters as in Fig.2.14. Frozen wake model (linearized wake dynamics) compared against free wake formulation in unbounded domain.	73
2.17	(a) Trailing vortex sheet development in 2D for the case of Fig.2.15. (b) Trailing vortex sheet visualization from experiments by Schouveiler et al. (2005).	74
2.18	Systematic results of averaged thrust coefficient for a 2D NACA0012 hydrofoil, in flapping motion with parameters as in Fig.2.14. Pressure-type Kutta condition compared against Morino-type condition.	74
2.19	Pressure coefficient distribution for a 2D NACA0012 hydrofoil, in flapping motion with $h_0/c = 1$ and $\psi = -90^\circ$ at the upper subplots, $St = 0.35, \theta_0 = 35^\circ$ at the lower subplots, in infinite domain for five periods starting from rest. Morino-type Kutta condition (left) compared against Pressure-type condition (right).	75
3.1	Definition of the studied problem (Zhu et al. 2006) in the case of a foil (of mid-chord c_0) moving under the free surface (at mean submergence d). The free surface is initially still and the waves are generated from the motion of moving boundaries.	79
3.2	Definition of the studied problem in the case of a smooth nonlifting body, moving under the free surface (at mean submergence d). The free surface is initially still and the waves are generated from the motion of moving boundaries.	86
3.3	Free-surface elevation generated by moderate-amplitude oscillations of an elliptically shaped, fully immersed body at $\omega^2 H/g = 1.63$. (a) Snapshot where The upper and lower limits of heaving motion are shown using dashed lines. (b) Time history of the free-surface elevation.	93
3.4	Free-surface elevation generated by an elliptically shaped, fully immersed body traveling with constant forward speed at $Fn = U/\sqrt{g\bar{a}} = 0.71$. (a) Snapshot. (b) Time history of the free-surface elevation.	93
3.5	Effect of σ_0 -parameter on the efficiency of the PML, for the example of Fig.3.3. The position of PML is indicated by bold dashed lines. The parameter σ_0 controls the magnitude of the $\sigma(\mathbf{x}_F)$ distribution.	95
3.6	Effect of p -parameter on the efficiency of the PML, for the example of Fig.3.3. The position of PML is indicated by bold dashed lines. p is positive parameter that controls the rate of absorption in the PML	95
3.7	Effect of PML thickness λ on the efficiency of the PML, for the example of Fig.3.3. The position of PML is indicated by bold dashed lines. λ adjusts the support of $\sigma(\mathbf{x}_F)$ and is comparable to the characteristic wave length of the generated wave	95

3.8	Wave resistance study of a prolate spheroid. a) Pressure and velocity fields on the body boundary and free-surface potential and free-surface elevation. b) Total potential field on the free-surface. c) Wave resistance coefficient and comparison against calculations from Belibassakis et al. (2013a).	96
3.9	Enforced radiation study of a prolate spheroid. a) Pressure and velocity fields on the body boundary and free-surface potential and free-surface elevation. b) Total potential field on the free-surface. c) Added mass coefficient and comparison against calculations from Chatjigeorgiou and Miloh (2015). In the case 1 $N_F = 5400$, in the case 2 $N_F = 10000$	96
3.10	NACA4412 hydrofoil, at 5° angle of attack beneath the free surface: (a) Free surface elevation for $Fn = 0.9$ and submergence $d/c = 1$ (with respect to the leading edge of the foil). (b) Pressure coefficient at $Fn = 1.03$ and submergence $d/c = 0.6$ (with respect to the midchord of the foil). (c) Lift coefficient for submergence $d/c = 1$ (with respect to the leading edge of the foil), against Froude number. (d) Lift and wave resistance coefficients at $Fn = 1$, against submergence (with respect to the midchord of the foil).	109
3.11	(a) Thrust coefficient $C_T = -F_x/\rho gh_0^2$ against non dimensional frequency $\Omega = \omega^2 c/2g$, for NACA0006 hydrofoil at $d/c = 0.5$, in heaving and flapping low-amplitude motions. Feathering parameter $\epsilon = 0.6$, pivot point $X_R/c = 0.5$, and heave-pitch phase lag $ \psi = 90^\circ$. (b) Free surface and bottom effects on C_T for NACA0012 hydrofoil for cases of different submergence ratio $d/c = 2.5, 1.5$. The Froude number is $Fn = 1.5$ and the water depth $H/c = 5$. (c) An example of full scale application of flapping foil propulsion is coming from the inland shipping industry. (d) Free surface and bottom effects on C_T for NACA0012 hydrofoil for cases of different water depth conditions. The Froude number is $Fn = 1.5$ and the submergence is $d/c = 1.5$	111
3.12	Free surface and free-wake effects for NACA0012 hydrofoil for submergence ratio $d/c = 2.5$, $h_0/c = 1$, $\psi = -90^\circ$, $X_R/c = 0.33$, $Fn = 1.5$, in deep water condition $H/\lambda \gg 1$. Frozen wake model (linearized wake dynamics) compared against free wake formulation: (a) Systematic calculations of on thrust coefficient (C_T) for $0.2 \leq St \leq 0.45$ and $10^\circ \leq \theta_0 \leq 55^\circ$. (b) Time history of thrust coefficient in the case of $St = 0.45$, and $\theta_0 = 35^\circ$. (c) Time history of lift coefficient in the case of $St = 0.45$, and $\theta_0 = 35^\circ$	112
3.13	Simulation of biomimetic flapping-foil thruster beneath the free-surface. a) Mean value of the thrust coefficient as a function of nondimensional frequency. Comparison of present method for constant-chord foils with NACA0012 sections, $AR = 10$ & $AR = 5$, in heaving motion with $h_0/c = 0.025$ & $h_0/c = 0.1$ and $F = U/\sqrt{gc} = 0.18$, in mean submergence $d/c = 0.5$, against 2D unsteady hydrofoil theory from Grue et al. (1988) and 3D BEM calculations from Zhu et al. (2006). b) Potential and velocities on the body and potential jump on the wake as well as free-surface potential and elevation with the fully non-linear model. For a constant-chord $AR = 6$ foil with NACA0012 sections and $St = 0.3$, $h_0/c = 0.75$, $\theta_0 = 23.3^\circ$, pivot point $X_R/c = 0.33$ and phase lag $\psi = -90^\circ$, Froude number $F = 0.6$, mean submergence $d/c = 0.5$	113
4.1	Definition of the studied problem in the case of a foil (of mid-chord c_0) moving under the free surface (at mean submergence d) and in waves.	120

4.2	Computational domain and boundary element grid for DtN calculation in the case of a solitary wave propagating over a 3D bathymetry with banks and trenches. Four time instances are exploited for the calculations: (a) Case 1. (b) Case 2. (c) Case 3. (d) Case 4.	143
4.3	Normal-derivative field as calculated by the two methods and the difference of the two fields for the four computational domains depicted in Fig.4.2: (a) Case 1. (b) Case 2. (c) Case 3. (d) Case 4.	143
4.4	GPU performance and L^2 error connected with the DtN calculation in the case of a solitary wave propagating over a 3D bathymetry with banks and trenches depicted in Fig.4.2.	144
4.5	Thrust coefficient for NACA0015 at $Fn = 0.87$ and submergence $d/c = 1.28$ and deep water with motion parameters $St = 0.18$, $h_0/c = 0.6$, $\theta_0 = 15.2^\circ$, $X_R/c = 0.3$, $\psi = -105^\circ$, for three cases: (i) without wave, (ii) with an incident wave of amplitude $\eta_0/h_0 = 0.238$, encounter frequency equal to flapping frequency $\omega_0/\omega_h = 1$ and $\phi = -90^\circ$, (iii) the same wave and $\phi = 90^\circ$	146
4.6	Average thrust coefficient for the flapping hydrofoil of Fig.3.11b at $St = 0.4$, $\theta_0 = 35^\circ$ at submergence $d/c = 2.5$, in the presence of an incoming wave of amplitude $\eta_0/h_0 = 0.75$, with flapping frequency equal to encounter frequency $\omega_0/\omega_h = 1$. Comparison between results in deep submergence, beneath the free surface in calm sea, and in head waves.	147
4.7	3D nonlinear simulation of biomimetic flapping-foil thruster beneath the free-surface and in waves with angle of incidence $\beta = 45^\circ$ and wave amplitude $\eta_0/c = 0.2$. For the simulation a constant-chord foils with NACA0012 sections, $AR = 6$, in flapping motion with $St = 0.3$, $h_0/c = 0.75$, $\theta_0 = 23.3^\circ$, pivot point $X_R/c = 0.33$ and phase lag $\psi = -90^\circ$ and $F = U/\sqrt{g\bar{c}} = 0.6$, in mean submergence $d/c = 0.5$. Potential and velocities on the body and potential jump on the wake as well as total free-surface potential and elevation, as calculated with the fully nonlinear model, are presented.	148
4.8	Ship hull, advancing in head waves, equipped with a flapping wing located below the keel, at forward station operating in random wave conditions, gaining its vertical motion from ship heave and pitch responses.	149
4.9	(a) Heave ξ_3/A and pitch response ξ_5/kA of the examined ship hull against non-dimensional wavelength λ/L and ship Froude numbers $Fn = U/\sqrt{gL}$. (b) Comparison of heave and pitch responses for ship speed $U = 5.5$ m/s, with (bold line) and without (dashed line) the operation of the flapping wing thruster.	150
4.10	Sea spectrum ($H_s = 4$ m and $T_m = 10$ sec) with respect to the inertial (S) and the moving (S^U) frame and foil's motion spectrum at station 8 $x_{wing}/L = 0.33$ where the horizontal flapping wing is located, for head seas and ship speed $U = 10.6$ kn ($Fn = 0.25$). The amplitude and phase of the foil's RAO are also plotted using thick lines in the upper and the lower subplots, respectively.	151
4.11	Simulation of the system operating in sea state 5. Results plotted at various instants in one modal period. In the right subplots the distribution of the unsteady pressure coefficient ($c_p = (p - p_{atm})/0.5\rho U^2$) on the flapping foil, located at station $x_{wing} = 0.3L$ (with respect to the midship section), at the same instants is plotted, as calculated by the present method.	153

4.12	Time history of (a) the total free-surface elevation and (b) the disturbance component due to the operation of the foil during the same time interval of one modal period, as in Fig.4.11.	154
4.13	Evolution of motion and integrated hydrodynamic quantities for a NACA0012 flapping hydrofoil in random head waves, corresponding to sea state 5, traveling at $F_{foil} = 1.76$, for time duration of 15 modal periods. Foil mean submergence $d/c = 7$ and control parameter $w = 0.5$	156
4.14	Mean thrust to calm water resistance ratio as (a) function of sea conditions represented by significant wave height, and (b) as function of the mean foil submergence to modal wavelength ratio.	157
4.15	(a) Mean thrust to calm-water resistance as a function of the longitudinal position of the flapping foil for various sea conditions. (b) Mean thrust coefficient (bold line) as a function of pitch control parameter w , for the same as before foil parameters.	157
4.16	(a) Interaction of waves with vertically sheared currents over variable seabed topography around the location where the biomimetic energy converter is installed; see also Belibassakis et al. (2017). (b) Oscillating hydrofoil operating as energy device in waves and sheared currents.	159
4.17	(a) Simulation of the system for $\omega_{\ominus}/\omega = 1$, $k_r = \omega_{\ominus}c/2U = 0.267$ and $\psi = -40^\circ$ during the fifth period. (b,c,d,e) Results at various instances: position of the foil and dipole intensities in the wake are shown in the left subplots, pressure coefficient on the flapping foil in the middle subplots, and calculated free-surface elevation over the shoaling environment in the right subplots.	161
4.18	Time history of (a) enforced pitching angle and output angle of attack, (b) heaving motion, lift and moment coefficients of the hydrofoil, and (c) calculated input and output power coefficients, in the case of $\omega_{\ominus}/\omega = 1$ and $\psi = -40^\circ$	162
4.19	Time history of (a) enforced pitching angle and output angle of attack, (b) heaving motion, lift and moment coefficients of the hydrofoil, and (c) calculated input and output power coefficients, in the case of $\omega_{\ominus}/\omega = 2$ and $\psi = -90^\circ$	163
4.20	Contour plots of a) η_P , b) α_0 and c) Z_0 as functions of pitch frequency ω_{\ominus} and pitch-wave phase difference ψ for specific Strouhal number $St = \omega\sqrt{h_1/g}$, pitch amplitude $\theta_0 = 15^\circ$, oscillator parameters $m^* = 4$, $\zeta = 0.5$, $\omega_0/\omega = 2$ and other parameters as in Fig.4.19.	165
4.21	(a) Average net power extraction η_P , (b) maximum amplitudes of the effective angle of attack α_0 , and (c) heaving amplitude Z_0 , as functions of ψ and θ_0 for $\omega_{\ominus}/\omega = 2$ and other parameters as in Fig.4.19.	166
4.22	Contours of (a) η_P , (b) α_0 and (c) Z_0 for varying wave height H and foil-wave phase difference ψ for $\omega_{\ominus}/\omega = 2$ and other parameters as in Fig.4.19.	168
4.23	Contours of (a) η_P , (b) α_0 and (c) Z_0 for varying wave frequency ω and pitching frequency ω_{\ominus} and other parameters as in Fig.4.19.	169
4.24	Effects of shear S_{max} and foil's mean submergence d on (a) η_P , (b) α_0 and (c) Z_0 for $St = 0.4$, $\omega_{\ominus}/\omega = 2$ and $\psi = -90^\circ$ and $\theta_0 = 15^\circ$ with other parameters as in Fig.4.19.	171

List of Notation

Against each entry is the page at which the notation is introduced.

General:

b	24	The normal to the body boundary derivative of the potential corresponding to the known Neumann data on the body boundary; i.e. $\partial_{n_B}\Phi = \nabla\Phi$. In the case of lifting bodies in waves b is the normal derivative of the corrector potential; see e.g. Eq.4.19.
$Ox_1x_2x_3$	23	Basic earth-fixed Cartesian coordinate system. In unbounded domain it is located at the initial position of the body. When the problem includes free surface it is located at the calm free-surface level.
$Ox_{b1}x_{b2}x_{b3}$	23	Auxiliary boundary-fixed Cartesian coordinate system. In unbounded domain it is located on the moving body boundary. When the problem includes nonlinear free surface there is an additional auxiliary system located on $x_1 = 0, x_2 = 0$ and the x_3 is defined by the specific location of the total free-surface elevation.
$\{\mathbf{e}_1(\zeta, \eta), \mathbf{e}_2(\zeta, \eta)\}$	47	The base of the curvilinear boundary-fixed coordinate system. In general, it is neither Cartesian nor orthogonal, also, it is variable with respect to the parameters (ζ, η) and $\mathbf{e}_1, \mathbf{e}_2$ are not of unit length. In the case of a nonlinear problem with freely deformable wake and free-surface boundaries the base is also variable in time and its construction is part of the solution, introducing an implicit nonlinearity to the problem.

Time derivatives:

$\partial_t(\cdot)$	57	Rate of change with respect to an earth-fixed (inertial) observer (i.e. with regard to an inertial reference frame).
$D_t(\cdot)$	25	Material derivative, based on the mean total velocity $\mathbf{V}_W^m = 0.5(\nabla\Phi_T^u + \nabla\Phi_T^l)$, on the trailing vortex sheet; i.e. $D_t(\cdot) = \partial_t(\cdot) + \mathbf{V}_W^m \cdot \nabla(\cdot)$.

$d_t(\cdot)$	58	Time derivative of functions defined on the body boundary, with respect to a reference frame, moving with the body velocity at the specific point; it holds that $d_t(\cdot) = \partial_t(\cdot) + \mathbf{V}_B \cdot \nabla(\cdot)$. It is essentially similar with the material derivative defined on the wake boundary.
--------------	----	---

Domain and boundaries:

D	23	Domain of definition of the problem.
∂D	22	Boundary of the problem. It is the union of all other boundaries.
∂D_B	23	Body boundary. In general, the boundaries that represent the body, the wake, the Kutta strip, the free surface and the bottom are denoted using the subscripts B, W, K, F and H , respectively.
∂D_K	34	The Kutta strip is part of the wake boundary ∂D_W at the vicinity of the sharp edge of a lifting body. It is used for the numerical implementation of Kutta conditions in the context of a BEM.
$\partial(\partial D)$	39	It is used to denote the integration domain of the Biot-Savart line integral in the calculation of induced velocities from an open surface ∂D or a boundary element. Moreover it denotes the sharp edge where the Kutta condition is applied.
\bar{D}	23	Closure of D ; i.e. $\bar{D} = D \cup \partial D$.
$\mathbf{x}_B, \mathbf{x}_{TE}$	26	Boundary variable denoting points on the body and the trailing edge, respectively. In general, with subscripts B, W, K, F, H we denote points on the body, the wake, the Kutta strip, the free surface and the bottom, respectively.
\mathbf{x}, \mathbf{x}_F	80	In general, the space variable \mathbf{x} refers to a point of the domain \bar{D} and $\mathbf{x} = \{x_1, x_2, x_3\}$. In the case that it refers to a point on the free-surface boundary. In the present nonlinear semi-Lagrangian surface tracking approach the free-surface elevation is a function defined on a horizontal plane. Therefore, for points on the free-surface boundary it holds that $\mathbf{x} = \{\mathbf{x}_F, \eta\}$ and $\mathbf{x}_F = \{x_1, x_2\}$.

Analytical Formulation:

\mathbf{V}_G	23	Unsteady background field velocity in unbounded domain.
\mathbf{V}	23	Unknown disturbance field velocity in unbounded domain.

Φ	23	In unbounded domain it is the unknown disturbance potential field in D . In nonlinear problems beneath the free surface it is the unknown total potential.
$\nabla\Phi$	46	In unbounded domain it is the unknown disturbance velocity field in D ; i.e. $\nabla\Phi = \mathbf{V}_G + \mathbf{V}$. In nonlinear problems beneath the free surface it is the unknown total velocity.
Φ_B	23	Limiting boundary value on ∂D_B . In general, with subscripts B, W, K, F, H we denote boundary values on the body, the wake, the Kutta strip, the free surface and the bottom, respectively.
$\mu_W, \Phi_W^u, \Phi_W^l$	25	μ_W denotes the potential jump (the dipole intensity) on the wake; i.e. $\mu_W = \Phi_W^u - \Phi_W^l$. In general, the superscripts u, l are used to denote wake's upper and lower side respectively.
μ_K	34	μ_W denotes the potential jump (the dipole intensity) on the Kutta strip.
$F^{PK}(\cdot)$	60	Pressure-type Kutta condition operator in unbounded domain.
$F_{fs}^{PK}(\cdot)$	81	Pressure-type Kutta condition operator for lifting flows around bodies in problems that include a free-surface boundary.

Spatial discretisation, the DtN and the dynamical system:

\mathbf{x}_0	30	Collocation points defined on the boundary. The integration points are simply denoted with \mathbf{x} .
$N_F, N_B, N_K, N_W(t)$	101	Number of elements and collocation points of the boundaries of free surface, body, Kutta strip and wake, respectively. The number of panels on the wake increases in time because the length of the wake increases too.
f, s, i, j, k, w	101	Collocation-point and element indices that correspond to specific boundaries and belong to the following subsets of \mathbb{N} : $f, s \in \{0, 1, \dots, N_F - 1\}, i, j \in \{0, 1, \dots, N_B - 1\},$ $k \in \{0, 1, \dots, N_K - 1\}, w \in \{0, 1, \dots, N_W(t) - 1\}$
$S_{ij}^{pot}, D_{ij}^{pot}$	32	Induction factors representing the potential at collocation point i induced by a unit source and a dipole distribution respectively, at element j . That notation is adopted for the problem in unbounded domain.

$\mathcal{D}_B^{pot}, \mathcal{S}_B^{pot}, \mathcal{D}_{B,K}^{pot}, \mathcal{D}_{B,W}^{pot}(t)$	35	Potential induction-factor matrices, with \mathcal{S} denoting source or single-layer integrals, and with \mathcal{D} denoting dipole or double-layer integrals. That notation is adopted for the problem in unbounded domain. To be more precise the induction-factor matrices are 2^{nd} -order systems that contain potential induction factors. For more details on systems see Sec.2.5.1.3. They model body to body (B), Kutta strip to body (B,K) and wake to body (B,W) interactions. $\mathcal{D}_{B,W}^{pot}(t)$ is the only one that must be updated at every timestep.
$\mathcal{A}_{F,B}^{pot}(t), \mathcal{B}_{F,B}^{pot}(t), \mathcal{D}_{F,B,K}^{pot}(t), \mathcal{D}_{F,B,W}^{pot}(t)$	101	Potential induction-factor matrices for lifting flows around bodies beneath the free surface. They model interaction between free-surface and body (F,B), free-surface, body and Kutta strip (F,B,K), free-surface body and wake (F,B,W). For the free-surface and body interactions, the notation \mathcal{A} and \mathcal{B} is adopted, instead of \mathcal{S} and \mathcal{D} , because each system contains both source and dipole induction factors. All of them that must be updated at every timestep.
$\Phi_F, \mathbf{N}_F, \Phi_B, \mathbf{b}, \mu_W$	101	Vectors containing the values of piecewise constant functions defined on the panels, at various parts of the boundary. To be more precise, they are 1^{st} -order systems; for more details see Sec.3.5.2 and Sec.2.5.1.3.
$\mathcal{G}, \mathcal{Z}, \mathcal{P}(t)$	36	2^{nd} -order systems used in the construction of DtN operator in unbounded domain. They model body to body, Kutta strip to body and wake to body interactions, respectively. They are calculated using the induction-factor matrices. For rigid foils in unbounded domain $\mathcal{P}(t)$ is the only one that must be updated at every timestep.

Velocity calculation and curvilinear finite difference method:

$\partial_n(\cdot)$	24	Normal to the boundary derivative of a function defined on the boundary; e.g. for the potential we have $\partial_n \Phi = \nabla \Phi \cdot \mathbf{n}$, where \mathbf{n} is the unit normal vector on the boundary. It is simply called normal derivative. The differentiation is applied with respect to the integration point \mathbf{x} . Sometimes subscripts are used to denote the kind of the boundary; e.g. the expression $\partial_{n_B} \Phi$ is used for the normal to the boundary velocity of the fluid.
$\partial_{n_0}(\cdot)$	38	Normal to the boundary derivative of a function defined on the boundary; e.g. $\partial_n \Phi = \nabla_0 \Phi \cdot \mathbf{n}$, where \mathbf{n} is the unit normal vector on the boundary. The differentiation is applied with respect to the collocation point \mathbf{x}_0 .

$\partial_s(\cdot)$	37	The notation $\partial_s(\cdot) = \mathbf{n} \times \nabla(\cdot)$ is adopted for the differentiation of a scalar field on the surface of a boundary. The surface differentiation is applied with respect to the integration point \mathbf{x} .
$\partial_{s_0}(\cdot)$	37	The notation $\partial_{s_0}(\cdot) = \mathbf{n} \times \nabla_0(\cdot)$ is adopted for the differentiation of a scalar field on the surface of a boundary. The surface differentiation is applied with respect to the collocation point \mathbf{x}_0 .
$\partial_s \Phi \times \mathbf{n}$	46	The tangential velocity on a boundary. That vector has covariant and contravariant components denoted by $(\partial_s \Phi \times \mathbf{n})_i$ and $(\partial_s \Phi \times \mathbf{n})^i$, respectively. Sometimes in the present work the tangential velocity is convenient to be denoted as $\mathbf{V}_t = \partial_s \Phi \times \mathbf{n}$.
$\mathbf{V}_{t1} _1, \mathcal{D}(\mathbf{x}_0 _1), \Phi _1$	49	In the expression $\mathbf{V}_{t1} _1 = \mathcal{D}(\mathbf{x}_0 _1) \cdot \Phi _1$, the curvilinear finite difference operator \mathcal{D} is defined. It is applied on the discretized potential boundary field Φ , for the calculation of the discretised field that represents the ζ -wise component of the tangential velocity ($\mathbf{V}_{t1} _1$). The notation $ _1$ illustrates that the collocation points $\mathbf{x}_0 _1$ and the other data are stored in the GPU memory following ζ -wise numbering; i.e. the data located along the curvilinear direction of \mathbf{e}_1 are stored sequentially.
$\mathbf{V}_{t2} _2, \mathcal{D}(\mathbf{x}_0 _2), \Phi _2$	51	In the expression $\mathbf{V}_{t2} _2 = \mathcal{D}(\mathbf{x}_0 _2) \cdot \Phi _2$, the curvilinear finite difference operator \mathcal{D} is defined. It is applied on the discretised potential boundary field Φ , for the calculation of the discretised field that represents the η -wise component of the tangential velocity ($\mathbf{V}_{t2} _2$). The notation $ _2$ illustrates that the collocation points $\mathbf{x}_0 _2$ and the other data are stored in the GPU memory following η -wise numbering; i.e. the data located along the curvilinear direction of \mathbf{e}_2 are stored sequentially.
$(\mathbf{V}_{t2} _2)^\top$	51	The transpose of the 2^{nd} -order system $\mathbf{V}_{t2} _2$ that represents the η -wise component of the tangential velocity discretised field. The operation $\mathbf{V}_{t2} _1 = (\mathbf{V}_{t2} _2)^\top$ rearranges the velocity data to be stored in the memory following ζ -wise numbering.
$\mathbf{S}_{ij}^{vel}, \mathbf{D}_{ij}^{vel}$	53	Induction factors representing the velocity at collocation point i induced by a unit source and a dipole distribution respectively, at element j .
$\mathcal{S}_B^{vel}, \mathcal{D}_B^{vel}$	53	Velocity induction-factor matrices, with \mathcal{S} denoting source velocity integrals, and with \mathcal{D} denoting dipole integrals. To be more precise they are 2^{nd} -order systems that contain velocity induction factors. For more details on systems see Sec.2.5.1.3.

Notation for the analysis of rigid bodies in waves:

The notation adopted for the specific treatment of the problem in the case of incident fully non-linear waves as described in Chapter 4 is presented in the following list:

Φ	122	The exact solution of the problem of lifting flows around bodies beneath the free-surface and in nonlinear waves.
$\Phi_I, \Phi_{N_{I-1}}$	122	The total wave potential at the specific-time iteration I and at the last specific-time iteration N_{I-1} . At a specific time t , a finite number of N_I iterations are performed, until the total wave potential at the current iteration Φ_I converges to the solution Φ of the fully nonlinear problem, as follows $\Phi(\mathbf{x}; t) \approx \lim_{I \rightarrow N_I} \Phi_I(\mathbf{x}; t) = \Phi_{N_{I-1}}(\mathbf{x}; t)$. The terminology specific-time iterations refers to the iterations performed at a given timestep for the treatment of the implicit nonlinearity of the problem.
Φ_0^0, ϕ_I^{cor}	122	The initial-guess potential and the corrector potential are the terms of the representation of the total wave potential at specific-time iteration I ; i.e. $\Phi_I(\mathbf{x}; t) = \Phi_0^0(\mathbf{x}; t) + \phi_I^{cor}(\mathbf{x}; t)$, $I \in \mathbb{N}$.
$\phi_{N_{I-1}}^{cor}$	122	The corrector potential at the last specific-time iteration N_{I-1} . The representation of the total potential at the last iteration is as follows $\Phi_{N_{I-1}}(\mathbf{x}; t) = \Phi_0^0(\mathbf{x}; t) + \phi_{N_{I-1}}^{cor}$, the initial guess potential remains constant during the specific-time iterative process.
$\partial_{n_B} \phi_{N_{I-1}}^{cor}$	123	The normal to the boundary derivative of the corrector potential at the last specific-time iteration N_{I-1} .
$\eta_{N_{I-1}}^{cor}$	124	The corrector free-surface elevation at the last specific-time iteration N_{I-1} .
$\partial D_{F, N_{I-1}}(t)$	124	The total free-surface boundary at the last specific-time iteration N_{I-1} . In general, with subscript N_{I-1} , are denoted the boundaries, the fields and the operators at the last specific-time iteration N_{I-1} .
$F_{fs, N_{I-1}}^{PK}(\cdot)$	124	Pressure-type Kutta condition operator for lifting flows around bodies beneath the free-surface and in waves written in terms of the representation presented in Sec.4.3.

$\mathcal{A}_{F,B,N_{I-1}}^{pot}(t),$ $\mathcal{B}_{F,B,N_{I-1}}^{pot}(t),$ $\mathcal{D}_{F,B,K,N_{I-1}}^{pot}(t),$ $\mathcal{D}_{F,B,W,N_{I-1}}^{pot}(t)$	128	<p>Potential induction-factor matrices for lifting flows around bodies beneath the free surface and in waves, at the last specific-time iteration N_{I-1}. They model interaction between free-surface and body (F,B), free-surface, body and Kutta strip (F,B,K), free-surface body and wake (F,B,W). For the free-surface and body interactions, the notation \mathcal{A} and \mathcal{B} is adopted, instead of \mathcal{S} and \mathcal{D}, because each system contains both source and dipole induction factors. All of them that must be updated at every timestep. Their specific-time-iteration values (e.g. $\mathcal{A}_{F,B,I}^{pot}$) change also during the specific-time iterations until they take their final values (e.g. $\mathcal{A}_{F,B,N_{I-1}}^{pot}$) at the last specific-time iteration when $I = N_{I-1}$.</p>
$\phi_{F,N_{I-1}}^{cor}, \phi_{B,N_{I-1}}^{cor}$	128	<p>Discretised Dirichlet data on the free-surface boundary and the body boundary, respectively. The values are at the last specific-time iteration N_{I-1}. Concerning their structure, they are 1st-order systems containing the discretised corrector potential field, defined as follows: $\phi_{F,N_{I-1}}^{cor} = \{\phi_{F,N_{I-1},s}^{cor}\}$, $\phi_{B,N_{I-1}}^{cor} = \{\phi_{B,N_{I-1},j}^{cor}\}$.</p>
$\mu_{K,N_{I-1}}^{cor}, \mu_{W,N_{I-1}}^{cor}$	128	<p>Discretised Dirichlet data on the Kutta strip and the wake boundary, respectively. The values are at the last specific-time iteration N_{I-1}. Concerning their structure, they are 1st-order systems containing the discretised field that represents the corrector potential jump (dipole intensity); i.e. $\mu_{K,N_{I-1}}^{cor} = \{\mu_{K,N_{I-1},k}^{cor}\}$ and $\mu_{W,N_{I-1}}^{cor} = \{\mu_{W,N_{I-1},w}^{cor}\}$.</p>
$\mathbf{N}_{F,N_{I-1}}^{cor}, \mathbf{b}$	128	<p>Discretised Neumann data on the free-surface boundary and the body boundary, respectively. The values are at the last specific-time iteration N_{I-1}. Concerning their structure, they are 1st-order systems containing the discretised field that represents the normal to the boundary derivative of the corrector potential; i.e. $\mathbf{N}_{F,N_{I-1}}^{cor} = \{\partial_n \phi_{F,N_{I-1},s}^{cor}\}$ and $\mathbf{b} = \{b_j\}$.</p>
$\mathcal{G}_{N_{I-1}}(t), \mathcal{Z}_{N_{I-1}}(t),$ $\mathcal{P}_{N_{I-1}}(t)$	128	<p>2nd-order systems used in the construction of DtN operator in waves at the last specific-time iteration N_{I-1}. They model body to body, Kutta strip to body and wake to body interactions, respectively. They are calculated using the induction-factor matrices. All of them must be updated at every timestep. Their specific-time-iteration values (e.g. \mathcal{G}_I) change also during the specific-time iterations until they take their final values (e.g. $\mathcal{G}_{N_{I-1}}$) at the last specific time iteration when $I = N_{I-1}$.</p>

Dedicated to my parents and my brother

Chapter 1

Introduction

In the present introductory chapter, we begin with a brief historic review on biomimetic systems, such as flapping-wing propulsors and oscillating wing energy converters, inspired by aquatic and volant organisms, called also aerohydrobionts (Rozhdestvensky and Ryzhov 2003). These systems, as we will demonstrate, are ideally suited for converting directly environmental (sea wave) energy to useful thrust for ships and other marine vehicles. Moreover, flapping-foil systems can be used as novel hybrid energy converters for energy extraction from both tidal currents and waves, nearshore. We will present the basic effort that has been put in this direction, as well as the recent ideas and the contribution of the present thesis in those topics.

1.1 Augmenting ship propulsion in waves using biomimetic flapping-foil systems

Biomimetic propulsors is the subject of extensive investigation, since they are ideally suited for converting directly environmental (sea wave) energy to useful thrust. In addition, in recent years, requirements and inter-governmental regulations related to vehicle technology for reduced pollution and environmental mitigation (e.g. Kyoto treaty and enactment of Energy Efficiency Design Index, EEDI, Energy Efficiency Operational Indicator, EEOI and North American Emission Control Area Regulations, ECA, for ships) have become strict, and immediate response to transportation greening has been recognized to be an important factor concerning global warming and climate change. The contribution of cargo ships in global pollution has been recognized as one of the most important factors (Colvile et al. 2001; Flannery 2005), taking also into account the bad fuel quality of seagoing vessels in relation to other modes of transport. Indeed, images and data available from satellites (MARINTEK et al. 2000) reveal that large areas around the main sea-ocean shipping lines are almost permanently covered by clouds with large concentrations of pollutants from ships' engines. In this direction, current studies examine - among other issues - the optimization of propulsive efficiency of ships operating in realistic sea states, taking into account added resistance effects, see e.g. Belibassakis (2009) and Belibassakis et al. (2013b). We note that in moderate and severe sea conditions, due to waves, wind and other reasons, ship propulsion energy demand is commonly increased well above the corresponding value in calm water for the same speed, especially for bow /quartering seas.

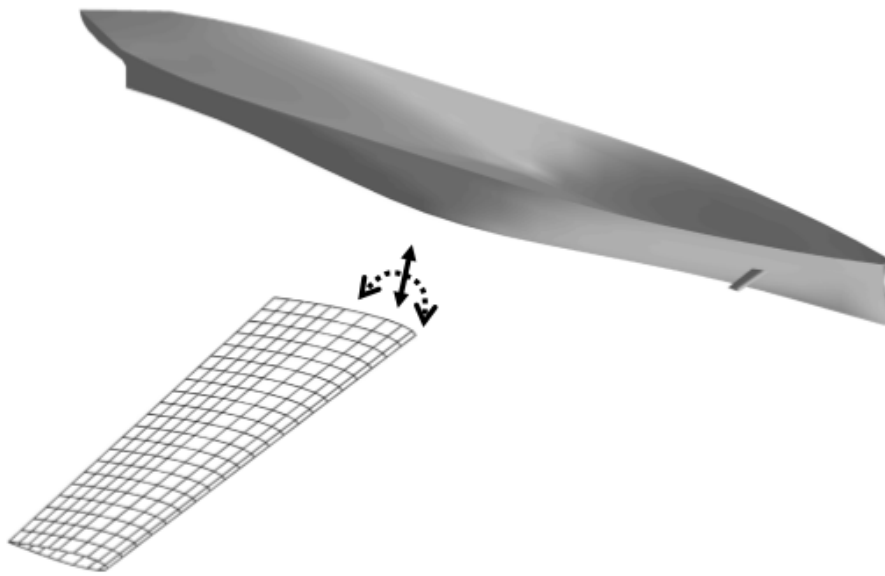


Figure 1.1: Ship hull equipped with flapping wing(s) located at a forward station. Detailed view of the flapping wing, which oscillates vertically (shown by a solid arrow) and around its pivot axis (shown by a dashed arrow), is included in the subplot.

On the other hand, evolution of aerohydrobionts, through millions of years of natural selection/optimization, arrived to the flapping wing as their single propulsion system. The main difference between a biomimetic (flapping wing) propulsor and a conventional propeller is that the former absorbs energy by two independent motions, the heaving and the pitching motion, while for the propeller there is only rotational power feeding. Actually, research and development concerning flapping foils and wings, supported by extensive experimental evidence, theoretical and numerical analysis, has shown that such systems at optimum conditions could achieve high thrust levels; see, e.g. Triantafyllou et al. (2000), Triantafyllou et al. (2004), Von Ellenrieder et al. (2008), Taylor et al. (2010) and Politis and Tsarsitalidis (2014).

In real sea conditions, the ship undergoes moderate or higher-amplitude oscillatory motions, due to waves. In this case the ship motions, especially the vertical to the free surface plane, could be exploited for providing one of the modes of combined/complex oscillatory motion of a biomimetic propulsion system, free of cost; see Fig.1.1. This idea has already been exploited by other scientists. More specifically, the initial attempts focused on using passively flapping wings underneath the ship hull, to transform energy stored in ship motions to useful propulsive thrust with simultaneous reduction of ship motions. In such cases pitching motion is induced by a spring loaded by the unsteady wing pressure distribution. In the following we will present a brief literature review on the subject, while Rozhdestvensky and Ryzhov (2003), Naito and Isshiki (2005) and Bowker (2018) could be good references for a more detailed review.

The first published attempt was in 1895 by Herman Linden who filed a British patent for a wave powered boat (Burnett 1979). Linden's 13 ft long boat named *Autonaut*, moved against the waves with a speed of three to four miles per hour, powered purely by wave-energy. The boat was equipped with two underwater steel plates, one at the bow and one at the stern.



Figure 1.2: Jakobsen equipped fishing research vessel Kystfangst, owned by the Institute of Fishery Technology Research, with a bulbous bow and two foils on each side of the bow.

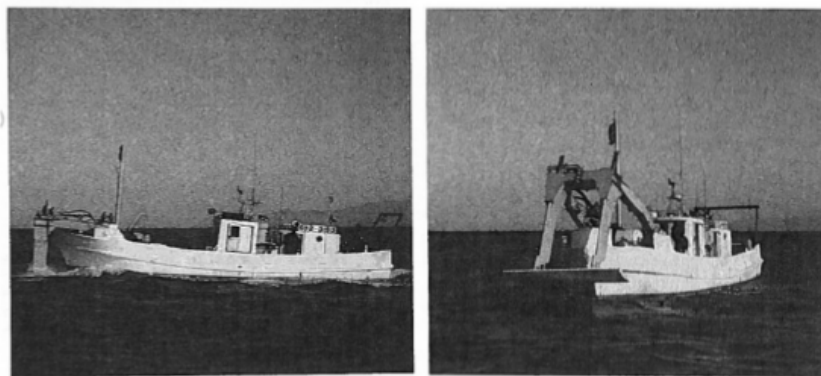


Figure 1.3: Fishing vessel equipped with flapping foil to improve propulsion in waves (Terao and Isshiki 1991).

Latter, Jakobsen (1981) performed experiments in Norwegian Hydrodynamics Laboratories (today MARINTEK) in Trondheim, Norway with a model boat of length 1.02 m, at a speed of 1.15 m/s in harmonic head sea waves of waveheight 0.13 m and wave period 1.2 s. Froude-scaled to full scale, this is equivalent to a 40 m long ship propelling itself forward solely by wave power in head sea waves of height 5.2 m at a speed of 14 kn. The speed in following waves was about 15% lower. The model had spring-regulated wings, one above the bow, and another beneath the stern. Furthermore, Jakobsen and his Wave Control Company used combinations of two and four foils. A maximum speed of six knots was recorded on one occasion. He also, latter, by gaining a funding from Norwegian Government, equipped the fishing research vessel Kystfangst, owned by the Institute of Fishery Technology Research, with two horizontal foils on the bow, see Fig. 1.2. Fuel savings of about 15-20% were obtained in a wave height of 3 m using the foils at speeds of 4-8 knots (Berg 1985). However, the project was terminated due to structural problems.



Figure 1.4: Russian research fishing vessel equipped with flapping foil (Nikolaev et al. 1995).

Similar problem concerning wave energy extracting systems has been studied by Isshiki (1982). In the latter work, a 2D model, treating the problem of an oscillating hydrofoil in water waves was developed, extending Wu (1971) theory by introducing a free surface effect, and applied to the investigation of the possibility of wave devouring propulsion. Terao (1982) also worked on the same direction. Isshiki's work has been further extended both theoretically and experimentally by Isshiki and Murakami (1984) where the basic concept of passive type wave devouring capability of an oscillating hydrofoil was studied. Furthermore, Grue et al. (1988) developed a theory for a two-dimensional flat plate near the free surface using a frequency-domain integral equation approach, where unsteady foil motions and wave devouring capabilities were illustrated. Predictions from the above theoretical model were found to be in good agreement with the experimental measurements by Isshiki and Murakami (1984) for both head and following waves. However, at lower wave numbers there were systematic discrepancies between theory and experimental results attributed to nonlinear and free surface effects which were not fully modeled.

Terao and Isshiki (1991) performed full scale tests on with a 15.7 m long fishing vessel; see Fig.1.3. The projected hydrofoil area was 7.4% of the ship's waterline area. Using the bow foil not only managed to reduce pitching motion and bow slamming, but also a speed increase was achieved in waves.

In 1995, the full-scale tests of a 174 ton Russian research fishing vessel Nikolaev et al. (1995), equipped with a wing device for extracting sea wave energy, showed that such a device could increase the engine power up to 45–87% and reduce ship's motions by a factor of 2–2.5, see Fig.1.4.

More recently, in 2008, the longest known voyage by a wave-powered boat took place. A wave-propulsion mechanism, designed by Terao, was equipped to Suntory Mermaid II catamaran; see Fig.1.5. In this way, Japanese sailor and environmentalist Kenichi Horie, sailed from Honolulu, Hawaii, to the Kii Channel, Japan (Geoghegan 2008) in 110 days with pure wave energy, which was longer than planned, due to unusually good weather and calm seas. In the



Figure 1.5: The Suntory Mermaid II which sailed from Hawaii to Japan in 2008 (Geoghegan 2008).

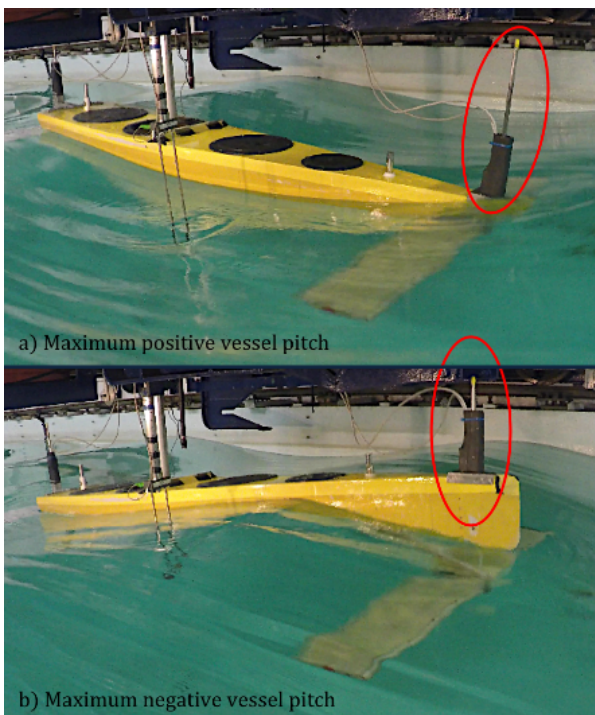


Figure 1.6: Terao and Sakagami (2013) equipped an small autonomous boat, for ocean measurements, with a wave devouring propulsion system (WDPS).

same direction Terao and Sakagami (2013) equipped an autonomous small boat, for ocean measurements, with a wave devouring propulsion system (WDPS), i.e. a dual-fin system at the stern for experimental research and full-scale applications; see Fig.1.6. Furthermore, Bøckmann and Steen (2016) performed experiments with a model equipped with a foil below the hull for motion reduction and thrust production in waves, achieving 60% reduction of the resistance in waves with additional reduction 42% and 45% of vessels' heaving and pitching motions,



Figure 1.7: Bøckmann (2015) performed experiments with a model equipped with a foil below the hull for motion reduction and thrust production in waves.



(a)



(b)

Figure 1.8: Photo of the experimental platforms exploited in the work of Bowker (2018) for the (a) towing tank and the (b) free-running experiments of flapping-foil wave powered vessels.

respectively; see Fig.1.7. Moreover, Huang et al. (2016) proposed an Eco-Ship empowered with active flapping foils exploiting wave propulsion and studied that system experimentally conduction free-running model tests, reporting speed improvement up to 6.24% and significant energy extraction. Recently, Bowker (2018) studied numerically and experimentally the dynamics of a flapping-foil wave powered vessel, focusing on wave propelled unmanned surface vehicles (USVs). They offered design guidance for flapping foil wave powered vessels, and proposed a method to simultaneously control forward speed and recover wave energy and they also conducted free running forward speed experiments. They also reported that an increasing interest in wave-powered vessels after 1980s and an almost twofold increase in that research activity since 2005. Moreover, an extensive literature review on wave-powered USVs can be found in the aforementioned reference. More recently, Bøckmann et al. (2018) estimated the fuel savings for a general cargo ship employing retractable bow foils. They observed that fuel savings were shown to decrease when installed power increases but remain at significant level when the ship advances at full speed. They also demonstrated the importance of accurate thrust calculations in the estimation of fuel savings, illustrating that simulations with the proposed 3D nonlinear method and other high fidelity CFD tools are necessary.

Finally, in the field of computational fluid dynamics (CFD), De Silva and Yamaguchi (2012) examined in detail the possibility of extracting energy from gravity waves for marine propulsion, by numerically studying a two-dimensional oscillating hydrofoil using the commercial software Fluent. The overall results suggest that actively oscillating-foil systems in waves, under suitable conditions, have the possibility to recover the wave energy rendering these systems applicable to marine unsteady thrusters. In the work of Liu et al. (2016), an Unmanned Wave Glide Vehicle (UWGV) which is driven only by wave energy, is proposed. An arrangement of six 2D tandem asynchronous flapping foils was studied via turbulent CFD simulations. More recently, Liu et al. (2018) worked with using the commercial software Fluent and examined the propulsion performance of flexible flapping foils with prescribed deformations in regular waves reporting that flexibility could enhance the propulsive performance increase the wave energy extraction.



Figure 1.9: The case vessel with wavefoils deployed from work Bøckmann et al. (2018) were fuel savings from the wave-foils were estimated.

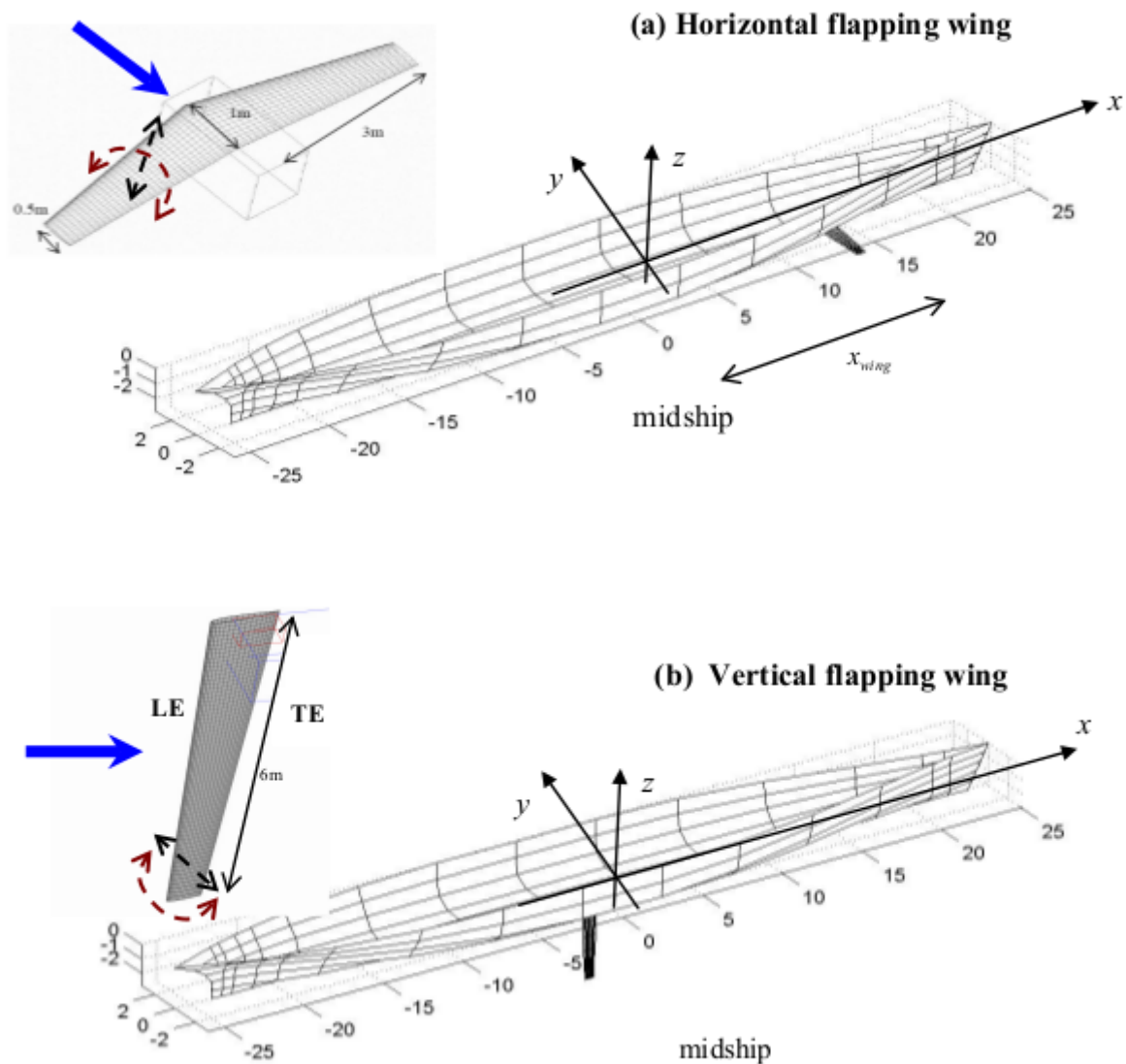


Figure 1.10: (a) Ship hull equipped with a flapping wing located below the keel, $T = 2.8$ m at a forward station. (b) Same hull with a vertical flapping wing located below the keel, at the midship section. Geometrical details of the flapping wings are included in the upper subplots. The main flow direction relative to the flapping wings is indicated using a blue arrow. Black arrows indicate linear oscillatory motion and red ones the actively controlled (pitching) motion of the wing about its pivot axis, for which only a quite small amount of energy is provided (Belibassakis and Politis 2013).

More specifically, ongoing research work of the laboratory of Ship and Marine Hydrodynamics of the School of Naval Architecture and Marine Engineering of National Technical University of Athens implemented in the context of the project BIO-PROPSHIP (<http://www.arion.naval.ntua.gr/biopropship>), is focused on the hydrodynamic analysis of flapping wings located beneath the ship's hull, operating in random motion; see Fig.1.10. The wing(s) undergo a combined transverse and rotational oscillatory motion, while the ship is steadily advancing in the presence of waves, modeled by directional spectrum. The present system is investigated as an unsteady thrust production mechanism, augmenting the overall propulsion system of the ship. In the first arrangement; see Fig.1.10(a), the horizontal wing undergoes a combined

vertical and angular (pitching) oscillatory motion, while traveling at constant forward speed. The vertical motion is induced by the random motion of the ship in waves, essentially due to ship heave and pitch, at the station where the flapping wing is located. Wing pitching motion is controlled as a proper function of wing vertical motion and it is imposed by an external mechanism. A second arrangement of a vertical oscillating wing-keel, located beneath the ship's hull, is also considered; see Fig1.10(b). The transverse motion is induced by ship rolling and swaying motion in waves. The angular motion of the wing about its pivot axis, is again properly controlled based on the ship rolling motion in order to produce thrust, with simultaneous generation of significant antirolling moment for ship stabilization.

Politis and Politis (2014) proposed a simple actively controlled enforced pitch motion, based on the (irregular) history of wing's vertical oscillation. In order to produce thrust, a flapping foil performs a complex motion that can be decomposed to a linear and a rotational oscillation, while it advances with the ship's forward speed. In Belibassakis and Politis (2013), wing's linear oscillation is provided by ship's irregular motion in rough sea, to be more specific by vessel's heaving and pitching, at the exact station that the system is located. On the other hand, foils rotation is actively controlled on the basis of its vertical motion and it is externally enforced with low cost. They introduced a method for the coupling of ship dynamics with unsteady flapping wing hydrodynamics using linear seakeeping analysis in conjunction with unsteady lifting-line theory and non-linear 3D panel methods. First stage numerical calculations reveal that wave energy can be extracted from ship motions by flapping-foil propulsors with concurrently reducing ship's unwanted responses, enhancing in this way its stability and the conditions of traveling.

Focusing in the importance of the effects associated with the interaction of the foil with the sea waves and the free surface boundary, Filippas and Belibassakis (2014) developed a two dimensional time domain boundary element method, in order to study the performance of a hydrofoil that undergoes unsteady motions in the proximity of the free surface and in harmonic waves. The free-surface boundary conditions were linearised. The extension of that method in three dimensions and in the fully nonlinear problem is part of the present work. Validation of the method has been done through comparison of calculations against linear theory, CFD numerical methods and experiments. Moreover, the significance of the effects of the freely moving boundary over the foil is underlined. Finally, it is demonstrated that the system's performance in harmonic-wave conditions is very promising.

Furthermore, in Sec.4.5.3 and in Belibassakis and Filippas (2015), aiming at the investigation of the performance of the system in more realistic irregular waves that corresponds to specific sea states, enriched that time-domain method, so as to be able to handle with random motions in random waves, coupling also the ship hull dynamics with foil hydrodynamics, in the same manner as Belibassakis and Politis (2013) suggested. In this way they studied various parameters of the ship-foil system in realistic sea condition, including the effects of foils finite submergence.

Finally, in the work of the author Filippas (2015), the aforementioned method is applied, so as to examine a pair of roll-stabilization wings, located at the side of the hull, for energy extraction from the waves and thrust production purposes. The fins gain their linear oscillation (heaving) from ship pitching and heaving responses in irregular waves, while the wing's rotation (pitching) is properly controlled with respect to its vertical motion history, producing positive thrust and augmenting ship's overall propulsion.

1.2 Energy extraction from waves and currents nearshore

Interaction of water waves with inhomogeneous currents in variable bathymetry regions is important for a variety of engineering applications, including effects of waves on structures, coastal management and harbor maintenance, as well as design and development of systems for exploitation of marine renewable energy resources. Extensive analysis concerning wave-current interaction in the nearshore and coastal regions have been presented by Peregrine (1976), Jonsson (1990), Soulsby (1990), Thomas and Klopman (1997). Recent information can also be found in the corresponding sections of reviewing articles; Battjes (2006), Cavaleri et al. (2007).

For the prediction of wave-seabed-current interaction, coupled-mode models have been recently developed, with application to the propagation/scattering of water waves over variable bathymetry regions, in the presence of spatially varying currents, extending previous simplified mild-slope/mild shear models that are applicable to cases of slowly varying bathymetry and current; Belibassakis et al. (2011). Also, the problem of transformation of the directional spectrum of an incident wave system over a region of strongly varying three-dimensional bottom topography is further studied in Belibassakis et al. (2014), where also the accuracy and efficiency of the coupled-mode method is tested, comparing numerical predictions against experimental data and calculations by the phase-averaged model SWAN (Booij et al. 1999). In the case of slowly varying environmental currents, where the vertical structure of the boundary layer in the nearshore and coastal region could occupy the entire depth, as in the case of tidal currents, the wave - vorticity interaction, is known to have a significant influence on wave dynamics. In this direction various models for surface waves, interacting with vertically sheared current, have been developed; see, e.g., Kirby (1984), Nwogu (2009), Touboul et al. (2016) and the references cited there. Moreover, multimodal extensions of the mild-slope mild-shear model (Touboul et al., 2016), taking into account the effects of evanescent modes, have been recently presented by Belibassakis et al. (2017). Finally, in the work Belibassakis et al. (2019) extended mild-slope models, able to model opposing shearing currents, are compared and exploited to study Bragg scattering of waves in the presence of currents, over rippled bathymetry.

The mutual existence of waves with currents in nearshore regions offers a motivation for comprehensive investigation of such resources, and the development of hybrid technological devices, based on biomimetic systems (see e.g., <http://www.biopowersystems.com/biostream.html>, and Fig.1.11). The latter could be found useful for the efficient exploitation of this type of combined marine renewables, enhancing the power extraction which is important especially in areas characterized by low wave potential. Recent research and development results, concerning flapping-wing systems, supported also by extensive experimental evidence and theoretical analysis, have shown that such systems, operating under conditions of optimal wake formation, could achieve high levels of efficiency; see e.g. Triantafyllou et al. (2000), Read et al. (2003), Triantafyllou et al. (2004), Schouveiler et al. (2005), Rozhdestvensky and Ryzhov (2003) for extensive review. However, the complexity of kinematics of flapping wings necessitates the development of sophisticated power transmission mechanisms and control devices, as compared to the standard hydrodynamic systems, such as water turbines and marine propellers.

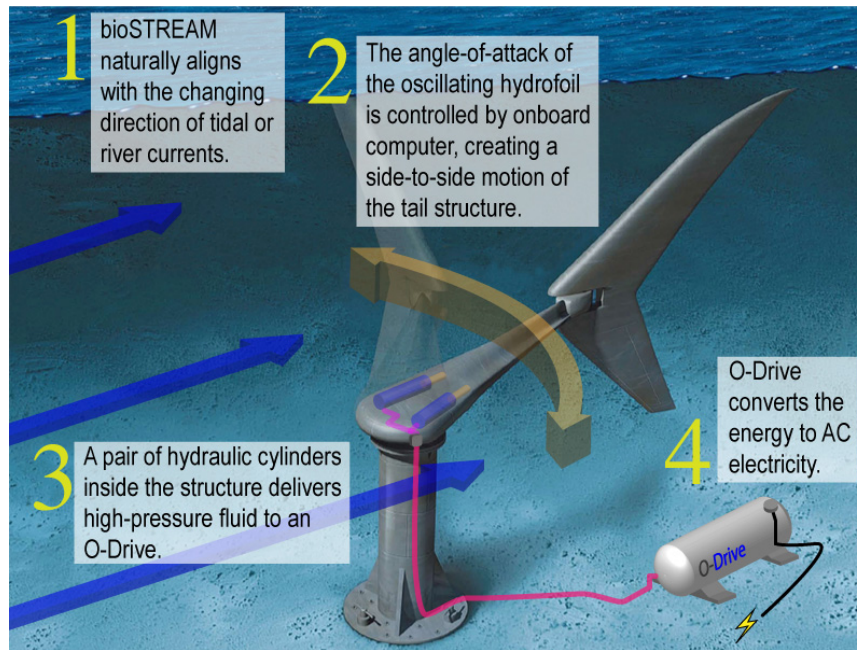


Figure 1.11: The bioSTREAM biomimetic system for exploitation of current flow energy, proposed by BioPower.

Novel biomimetic systems based on oscillating foils could be found useful for the efficient exploitation of combined wave and current marine renewables enhancing the power extraction which is important in areas characterized by lower wave potential coexisting with currents. Alternative biomimetic designs including flapping-foil devices have also been studied (see e.g., http://www.esru.strath.ac.uk/EandE/Web_sites/05-06/marine_renewables/technology/oschydro.htm).

The idea to use a flapping foil to extract energy from currents is not new. McKinney and DeLaurier (1981) have proposed a device to harvest energy by oscillating wings, while first experiments were conducted by DeLaurier and Harris (1982). In the last decade, biomimetic flapping foil devices have been extensively studied as flow energy converters; for a detailed review see Xiao and Zhu (2014). In the majority of these works the foil is considered in an infinite domain and the current flow as the only source of environmental energy, ignoring the effects of free surface and incident waves. Xiao and Zhu (2014) classified those studies into three categories with respect to the activation mechanism of the flapping foil. The first category includes systems with prescribed rotational (pitching) and translatory (heaving) oscillatory motions of the foil, the second category includes semi-activated systems with forced pitching motion and induced heaving oscillations and the last one includes self-sustained systems with induced motions at both degrees of freedom. The majority of the studies belong to the first category, while semi-activated and self-sustained systems have not been explored extensively even though the semi-activated systems seem to be a more feasible approach in practice.

Concerning semi-activated systems, Shimizu et al. (2008) and Peng and Zhu (2009) using Navier-Stokes solvers studied the performance of a flapping foil as a current energy converter. Moreover, the system was studied in the potential-flow framework by Zhu et al. (2009) using 2-D thin-foil theory and 3-D BEM. The study demonstrated that 3-D effects would decrease the absorbed power while ground effect could minimize that loss. Parametric studies supported by numerical models mapped the power extraction performance for different pitching amplitudes

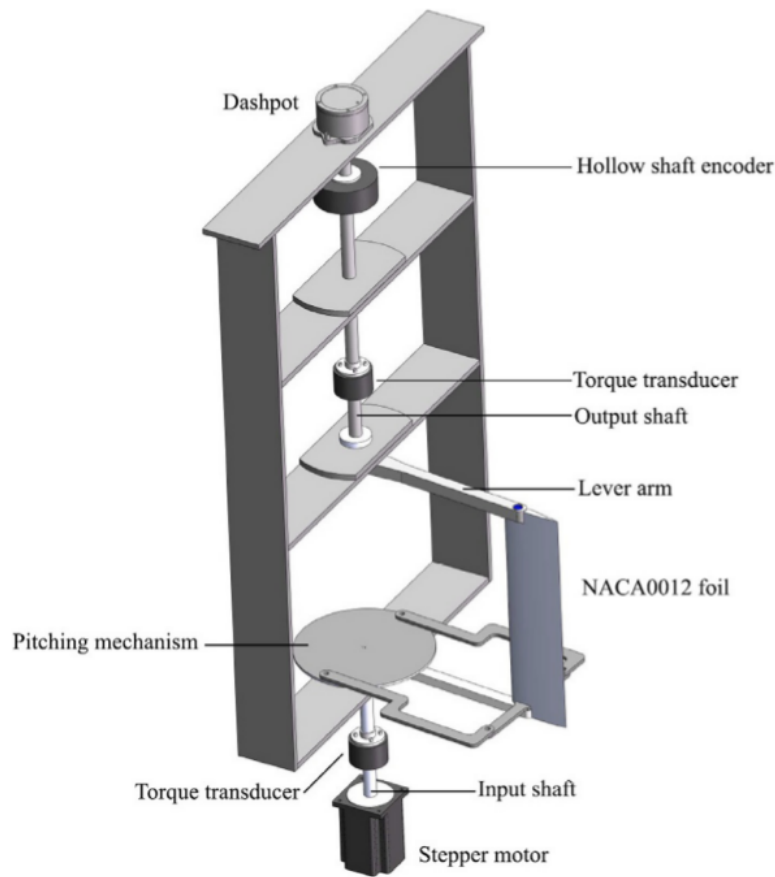


Figure 1.12: A laboratory-scale model of a semi-activated flow-energy harvesting device Huxham et al. (2012).

and oscillation frequencies; see, e.g., Kinsey and Dumas (2008), Zhu (2011). Also, experimental studies were conducted by Huxham et al. (2012) at small scale in a water tunnel with promising results. In a recent work Wu et al. (2015) two auxiliary smaller hydrofoils were employed to enhance the performance of the main oscillating foil energy converter by employing mechanisms of induced vortex interaction. Although, a few works concerning semi-activated systems have been published, there exists an important limitation, the assumption that the incident current flow is uniform and steady, which is an oversimplification, as also reported by Xiao and Zhu (2014), because tidal currents occurs with nonuniform vertical structure and moreover interact with free-surface gravity waves and varying bathymetry.

The effects of incoming waves have been considered in studies of flapping foil propulsion and thrust augmentation. It has been demonstrated that flapping foil thrusters operating in waves, while traveling at constant forward speed, are very efficient, and could be exploited for augmenting the overall ship propulsion in waves by directly converting kinetic energy from ship motions to thrust; see, e.g., Belibassakis and Politis (2013), Politis and Politis (2014), Belibassakis and Filippas (2015), Bøckmann and Steen (2016), Bowker (2018). In previous works potential based panel methods and CFD tools have been developed for the hydrodynamic analysis of these systems, including the effects of the free surface. Predictions are found to be in agreement with other methods and experimental data; Filippas and Belibassakis (2014), De Silva and Yamaguchi (2012). Also, it has been demonstrated that significant energy can be extracted by

the system, and industrial initiatives have appeared for developing the flapping foil system for wave energy extraction and thrust production (see, e.g., <http://www.arion.naval.ntua.gr/biopropship> and <http://www.seaspeed.co.uk/news/wave-foil-developments>). More details on that interesting subject have been presented in Sec.1.1.

Recent results confirmed by experimental evidence illustrate that flapping foils as tidal energy devices could be an attractive alternative to conventional turbines. Many researchers argue that energy harvesters utilizing flapping foils can be more efficient than rotary turbines as they are not prohibited by the Betz limit; see, e.g., Garrett and Cummins (2007), Dabiri (2007), Young et al. (2014). The above limit does not allow the turbines to harness more than 59.3% of the incident power. Kinsey and Dumas (2012) have reported a 59.9% efficiency for two flapping foils in a tandem configuration. Furthermore, in Sec.4.5.4 and in the work Filippas et al. (2018) the flapping foil operating in waves and sheared current in coastal environment is studied, showing that the energy extraction can be significantly increased. In particular, with appropriate control of motion parameters to take advantage of extra power offered by the wave an efficiency of 53.5% is achieved, for a single foil with 25° pitching amplitude.

To be more specific, Sec.4.5.4 is focused on the investigation of oscillating hydrofoils in the presence of waves and sheared currents, examined as biomimetic systems for extraction and exploitation of this kind of marine renewables in nearshore regions, operating as semi-activated wave and flow energy device. The pitching motion of the foil is appropriately tuned in order to develop heaving forces, due to alternating lift, and drive the hydraulic generator. The hydrodynamic analysis is based on the coupled-mode model, presented by Belibassakis et al. (2017), for the propagation of waves in the presence of sheared currents, in conjunction with time domain Boundary Element Methods (BEM) for the disturbance lifting flow developed by the hydrofoil, in variable bathymetry. The effect of the wavy free surface and variable bottom topography are taken into account through the satisfaction of the corresponding boundary conditions. It is indicated that significant energy can be extracted, and that the power gain from the waves increases well above the maximum values predicted for the system in nonuniform flow.

1.3 Main original contributions

In the context of the present PhD thesis a) a time-domain boundary element method (BEM) and b) a high performance computing (HPC) code are developed and c) employed for the study of novel biomimetic systems, with application to ship and marine hydrodynamics exploiting renewable energy resources to enhance the efficiency and the performance of the systems. In the sequel, the main original contributions are presented, categorised to innovations related to a) the numerical method, b) the computational code and c) the application. A short CV containing a list of the most significant publications is included at the end of the thesis.

1.3.1 Innovations in the numerical method

Our effort aims to the hydrodynamic analysis of lifting flows around solid bodies of arbitrary geometry, performing general unsteady motion, in a fluid bounded by the free surface and the

general-shaped bottom, in the presence of periodic (linearised or nonlinear) or more general free-surface gravity waves. The method and the computational code can be 2D or 3D and linearised in various levels or fully nonlinear with respect to a) the geometry of the body b) the motions, the evolution of the c) free surface and d) the trailing vortex sheet and the incident waves. In specific cases, the additional effects of shear currents and general bathymetry are included in the modeling.

In the work of Zhu et al. (2006), implemented in the context of a collaboration between Massachusetts Institute of Technology (MIT) and the University of California, San Diego (UCSD), the effects of the free-surface, in the unsteady motion of a foil without incident waves are presented. To be more specific, the free-surface effects on an underwater three-dimensional foil undergoing constant translation and periodic oscillation using a hybrid computational implicitly coupled method. In this approach, for the fluid motion around the foil potential flow is assumed and a BEM is used for the solution. The shed vorticity is represented as a shear layer originated from the trailing edge, while the linearised free-surface waves are resolved by a spectral algorithm. Moreover, in the recent work Xu et al. (2017), the 2D version of our method, presented in Filippas and Belibassakis (2014), is extended to treat flapping hydrofoils beneath the free-surface including weakly nonlinear 5th-order Stokes incident waves.

Via the present PhD thesis, the research team of the project BIO-PROPSHIP (<http://www.arion.naval.ntua.gr/biopropship>), proceed a few steps forward, by implementing a) a fully non-linear formulation, b) including nonlinear oblique incident waves with c) the coupling between the free-surface and the lifting body-wake dynamics, implemented in a strong explicit manner.

The direct coupling is obtained as follows. The kinematics of the problem are exploited to set up a linear boundary integral constraint and the dynamics of the free-surface, the evolution of the wake and the pressure-type Kutta condition are used to set up the dynamical-system equations. The reformulation of the initial boundary value problem (IBVP) to a boundary integral formulation is performed and the extended¹ Dirichlet-to-Neumann (DtN) operator is obtained in the form of a weakly singular boundary integral equation (BIE). The spatially discretised form of the dynamic system and the extended DtN is obtained by means of BEM, collocation, curvilinear finite difference method (CUFDM), obtaining in this way a system of 1st-order (spatially and temporarily) nonlocal differential equations, with explicit and implicit nonlinearities, with a linear algebraic constraint. A time-stepping method is then implemented, based on the time integration of the nonlinear constrained system of evolution equations. High-order multi-step time-integration schemes, that belong to the family of Runge Kutta methods for 1st-order systems, are exploited for the solution. Explicit high-order methods, with extended stability manifold, are used in general, while implicit schemes, that are theoretically A-stable, are selected when the system is stiff, implemented via a Newton-Raphson general iterative scheme, with the Jacobian calculated numerically with 2nd-order central finite differences. The special treatment of the implicit and the explicit nonlinearities is presented in detail at the corresponding sections and will not be discussed here.

In the studied cases, small differences in calculated integrated quantities were observed between present method and CFD analysis which are attributed to viscosity effects. The present method is able to provide good predictions, at least in the examples that are characterized by

¹The classical DtN operator is extended to lifting flows beneath the free-surface. The extended form include the effect of the trailing vortex sheet and the Kutta strip.

small and moderate angles of attack, where leading edge separation and dynamic-stall effects are not significant. It is worth noting, that the computational cost of the present boundary element method is order(s) of magnitude less, rendering our approach quite competitive and efficient, especially for initial design, optimization and active control development.

1.3.2 Innovations in the computational code and its performance

The software development is implemented using for its backend, general-purpose computing on graphics processing units (GPGPU), exploiting the programming language CUDA² C/C++. The frontend of the software is implemented using programming language MATLAB³. Moreover, the design of a user interface and a reference manual has been initiated, however that task is left as a subject for future work. In the present work, the simulations are performed in a GTX1080 Nvidia GPU, with 2560 single precision cores and 8GB available device random access memory (DRAM), while for the programming of the computational code the version 8 of CUDA is used. The HPC GPU-accelerated computational code that is developed, enables us to study efficiently the spatial and temporal grid independence of the numerical method and to perform systematic investigation of complex, coupled, nonlinear and unsteady phenomena even at the cases when the simulation duration is necessary to extend over many periods. It is worthwhile to mention that the performance of the computational code, both in terms of time and space complexity, is substantially higher than the performance of a corresponding serial or parallel CPU-BEM code (and even higher in the case of a viscous CFD code), implemented by exploiting resources of similar cost. Moreover, due to the the specific numerical treatment of the problem (see also Sec.1.3.1), the truncation of the horizontally infinite domain using a PML, the exploitation of mixed precision arithmetics and the proper handling of induction-factor matrices (see the discussion bellow Eq.2.25), the present GPGPU computational code is very efficient in terms of space complexity. To be more specific, in the present case where free-surface discretisation is required the memory demand from the VRAM is only 0.1GB higher in comparison with the infinite domain case. This is crucial if we consider the limited amount of memory available even in modern GPUs.

1.3.3 Innovations in the applications

The present work features a few original contributions to the field of applied ship and marine hydrodynamics. It is demonstrated that the proposed method can be exploited for the design and optimisation, efficient operation, assessment and control of novel systems, that are inspired by nature and are designed to exploit renewable energy resources enhancing their efficiency or performance. Particularly, a specific lifting body that is thoroughly studied in the present thesis is the flapping foil. Novel applications of flapping-foil biomimetic systems, together with the main original contributions of the present work, are discussed in the following subsections.

²To be more specific, CUDA (compute unified device architecture) is a parallel computing platform and application programming interface (API) model, created by Nvidia.

³To be more specific, MATLAB (matrix laboratory) is a multi-paradigm numerical computing environment and proprietary programming language, developed by MathWorks.

1.3.3.1 The flapping foil as an efficient main propulsion system and the concept of the wave-augmented biomimetic propulsor

That novel biomimetic system, that is inspired by the aquatic locomotion of hydrobionts as it is demonstrated in Chapter 2 and in other references from the literature (Rozhdestvensky and Ryzhov, 2003; Taylor et al., 2010; Triantafyllou et al., 2000, 2004; Tsarsitalidis, 2015; Von Ellenrieder et al., 2008), can be applied for the efficient propulsion of marine vehicles. Moreover, remaining in the context of ship hydrodynamics and performance enhancement, that system is studied as an efficient wave-augmented unsteady main propulsor; for more details see Sec.4.5.2, Filippas and Belibassakis (2014). Our analysis indicates that significant efficiency is achieved under optimal operating conditions and the free surface effects cannot be neglected. In the presence of waves the thrust coefficient is observed to raise well above its value in infinite domain, with maximum gain reaching 20%, for appropriate selection of the parameters. The present method could serve as a useful tool for the assessment, preliminary design and control of the studied system, extracting energy from sea waves for marine propulsion.

1.3.3.2 The wavefoil for the augmentation of ship main propulsion in waves

Our interest is mainly focused to biomimetic flapping foils (wavefoils⁴) operating as innovative auxiliary propulsion systems, augmenting ship main propulsion in waves; see Sec.1.1 and Sec.4.5.3, the state-of-the-art reviews Rozhdestvensky and Ryzhov (2003), Naito and Isshiki (2005) and the original-research articles Belibassakis and Politis (2013), Belibassakis and Filippas (2015), Filippas (2015), Bøckmann and Steen (2016) and Bowker (2018). Numerical results concerning thrust and power coefficients are presented, indicating that significant thrust can be produced under general operating conditions. The present work can be exploited for the design and optimum control of such systems extracting energy from sea waves for augmenting marine propulsion in rough seas, with simultaneous reduction of ship responses offering dynamic stabilization.

1.3.3.3 Biomimetic flapping-foils as combined marine energy extraction devices nearshore

The aforementioned application initially attracted the entirety of our efforts and attention. However, later the set of our scientific interests was enriched by the inclusion another potential application of the oscillating-foil biomimetic systems, i.e. the utilization of combined renewable energy resources, such as tidal currents and waves, nearshore; see e.g. Sec.1.2 and Sec.4.5.4, the state-of-the-art review Xiao and Zhu (2014) and the original-research articles Zhu and Peng (2009), Huxham et al. (2012), Filippas et al. (2018). Results are presented concerning the performance of the system in both waves and nonuniform currents, for a wide range of parameters, including cases where the wave frequency is different from the pitching frequency of the hydrofoil. It is indicated that significant energy can be extracted, and that the power gain from the waves increases well above the maximum values predicted for the system in uniform flow. The present method can be applied to the design and optimum control

⁴The terminology wavefoil is introduced in the recent PhD thesis of Bøckmann (2015), whose main original contribution was the experimental study of the system. Another recent experimental study on the specific subject can be found in Bowker (2018)

of such biomimetic systems operating in the nearshore/coastal region and extracting energy from waves in the presence of ambient currents.

1.4 Implementation of the GPGPU computational code

For the efficient implementation of the numerical algorithm, a computational code is developed, exploiting parallel programming techniques and general purpose programming on graphics processing units (GPGPU), using the CUDA C/C++ application programming interface (API). One of the GPUs exploited in the present work is the Nvidia GTX1080, based on the GP104 Pascal architecture with 2560 single precision cores and 8GB available VRAM. For the development of the code the cuBLAS and cu-SOLVER libraries were used for matrix-vector, matrix-matrix operations and linear system solvers. Moreover the version 8.0 of CUDA is used. In the sequel we briefly present a few aspects of the present GPGPU code and useful guidelines on the GPGPU programming

The present numerical method can be characterised as compute-intensive, due to the computationally demanding calculation of the singular integrals required for the construction of the induction-factor matrices. A mixed precision arithmetic scheme (Trompoukis, 2012) is used to optimise the performance of the algorithm and is implemented in the context of object-oriented programming using templates; see e.g. Horton (2014). The exploitation of mixed precision arithmetic reduces the total number of global memory accesses increasing the parallel efficiency of the GPU code without compromising the accuracy of the solution. Most commercial GPUs have more cores capable of single precision operations than double precision. This leads to a higher total throughput of single precision calculations, meaning that the same problem can be solved faster using single precision floating point arithmetic. For example, the NVidia Pascal architecture SM has 128 FP32 (single-precision) cores but only 4 FP64 (double-precision) cores. Furthermore, storing large matrices in single precision can reduce significantly the memory usage of the software. In this way, larger problems can be solved entirely on the GPU without the need of data transactions between the RAM and the device memory. Of course some calculations need double precision in order to be evaluated correctly. So, a mixed precision arithmetic scheme should be devised to achieve the best performance possible. In case of the Boundary Elements Method, the calculation of the singular integrals, for the diagonal elements of the induction-factor matrices, that appear in the evaluation of the self-induced potential demand double-precision arithmetic. The results are then converted to single-precision and stored together with the induced potential factors calculated with single-precision arithmetic. The solution of the linear system is then performed in single-precision. Extensive use of templates allows for fine control over precision. In this way a precision scheme can be found that balances computation time and solution error. In Sec.2.10.2 the execution times and the error for double precision and mixed precision arithmetic are compared.

Of the utmost importance is the proper design of the GPU grid. This is crucial in the case of data-intensive processes where the proper storage and transfer of the data affects significantly the simulation time. However it is still important in the present case of compute-intensive method when it comes to the development of an elegant, comprehensive code and its performance. To be more specific, the basic processing unit is the thread. The thread can be perceived as a set of instructions to be executed by the assigned core. A GPU, as any other processing unit, can handle a fixed maximum number of threads at a time. This maximum number of parallel

threads is determined by the capabilities of the GPU and is limited by the number of available cores. The threads are organized in groups called blocks. A block cannot contain more than 1024 threads, and the optimal number of threads per block are determined by the demand in registers a thread has, the number of cores available and the nature of the algorithms used. When a kernel is launched the user sets the number of threads in a block and the number of blocks. This structure of blocks and threads is referred to as a grid. The grid and the blocks can be 1D, 2D or 3D, with different number of dimensions having advantages in different cases. For example, for the calculation of induction factor matrices, the GPU-BEM code developer will find it easier and more intuitive to use 2D grids and blocks. In order to facilitate the access to specific data and the execution of specific instructions, the thread is assigned a unique ID within the block. Similarly, the blocks are assigned a unique ID within the grid. Therefore, by combining the two IDs, each thread in the global grid can be identified by a unique number.

The instruction execution model adopted by Nvidia for their GPUs is that of "Single Instruction Multiple Data" (SIMD). The threads of a block are grouped together in "warps" of 32 threads. The threads belonging to a warp must execute the same instruction simultaneously, but the data onto which the threads operate can differ. This model of instruction execution is ideal for massively parallel applications and the simplicity of the hardware implementation allows for greater efficiency and enhanced performance. On the other hand, the SIMD model can have some drawbacks in certain applications. For example, when an "if" statement is introduced in the application and differentiates the execution flow of the threads in the same warp to two blocks, the threads executing the second block will stall until the threads executing the first block have finished, affecting the performance significantly. According to the SIMD same instructions on different data are performed simultaneously and not different instructions on different data. However, as denoted in Sanders and Kandrot (2010): "there is yet another class of parallelism to be exploited on Nvidia graphics processors. This parallelism is similar to the task parallelism that is found in multithreaded CPU applications. Rather than simultaneously computing the same function on lots of data elements as one does with data parallelism, task parallelism involves doing two or more completely different tasks in parallel". Although in the present problem the calculation a) of single and b) double layer induction-factor matrices require essentially different instructions, we have used pointers to functions and a 3D grid to perform simultaneously that two distinct compute-intensive parts of the algorithm. An alternative could be the implementation of the computational code exploiting streams; more details can be found in the aforementioned reference.

Moreover, special attention should be given to the above considering also the number of registers the GPU-kernels require, aiming to the maximization of the achieved occupancy during the execution of the kernel. In order to achieve the maximum computational capacity of the GPU, all the available CUDA cores must be used. There are many parameters that must be determined to accomplish the maximum occupancy of the GPU *Achieved Occupancy*. First of all, the workload of the threads within a block must be balanced. This means that the threads should take the same time to finish the scheduled work. If some threads need more time to execute, at the end of the kernel there will be less active warps, using only a subset of the cores. The same is true about the unbalanced workload of blocks within a grid. In this case, limiting the size of the blocks and distributing the workload to more blocks will increase the efficiency of the algorithm, because new blocks will be launched as the previous ones will finish their execution. Another issue that can have an impact on the occupancy is when too few blocks are launched. If the number of blocks launched is less than the maximum number of blocks that

can run simultaneously across all streaming multiprocessors (SMs) then the occupancy is limited. The maximum number of blocks that can run at once on the GPU is called a "full wave". When a kernel is launched with more blocks than a full wave then the blocks that cannot fit into an SM will be scheduled for after another block has finished. Moreover, each thread of a block will use the registers available to that block. This means that the limited register file must be adequate for all the threads of the block. To achieve this the block size may need to be decreased or the register count per thread may be limited at compilation. Taking into consideration all the above effects, the size of the block and the number of registers allocated to each thread should be determined for the hardware the code is run on. To determine these factors, the NVidia occupancy calculator can be used. For a GTX1080 GPU with compute capability 6.1, to achieve maximum warp occupancy on each SM, the register count for each thread is limited to 63, due to the limited register file.

The other problem that arises during implementation is memory coalescence. In order to maximize the efficiency of the algorithm, the right data-structures should be chosen in order for threads of a warp running in parallel to access data that are spread in an as small as possible memory interval. In this way, we can take advantage of the hardware and use the complete bandwidth of the GPU memory.

For the proper summation and storage of data that are calculated simultaneously atomic operations are exploited. To be more specific, the "atomicAdd" function whose double precision version is supported by the version 8.0 of CUDA, is used. In this way the calculation of the right hand side of the DtN operator and the multiplication of that matrix with the corresponding vector of singularity intensity, as well as the calculation of the free-wake velocities is implemented in an efficient manner both in terms of time and space complexity.

In the case of frequent communication between GPU (device) and CPU (host), the proper selection of method for the storage and transfer of data is important. In the present case the backend of the software is executed in GPU and therefore a minimum amount of data is transferred between the device and the host. For this reason, the conventional memory management functions "cudaMalloc" and "cudaMemcpy" are used for the allocation and transfer of data, respectively. However, in the case of more frequent CPU-GPU communication or in the case of shared memory Multi-GPU systems (Cabezas et al., 2015) the alternative offered by zero-copy techniques and the unified memory should be examined. To be more specific, Nvidia has introduced the unified memory technology to facilitate the development of HPC codes. This technology allows the use of RAM and device memory (even for multiple GPUs) in a unified address space that hides the data migration from and to the RAM. The data transfer is managed by the CUDA API and as a result the programmer does not need to devote time into optimizing this process accelerating development.

The performance of the GPGPU computational code, both in terms of time and space complexity, is substantially higher than the performance of corresponding serial or parallel Central Processing Unit (CPU) codes, implemented by exploiting resources of similar cost. That argument is supported by performance analysis and benchmarking between serial CPU and parallel GPU calculations in Sec.2.10.2, Sec.2.10.3, Sec.3.4.5.2, Sec.3.5.3.4, Sec.4.5.1 and Sec.4.5.2.

Chapter 2

Unsteady lifting bodies in unbounded domain

2.1 Summary

The present chapter is dedicated to the problem of unsteady lifting bodies in unbounded domain. We assume that the body and the wake boundaries remain in adequately large distance from the other boundaries (free-surface, bottom, lateral walls, shore etc) so as to be able to ignore the interaction with them. The effects of an unsteady non-uniform background field, that could model weakly rotational fields lying on the background (ship wake, incident waves, non-uniform current etc), are also included in the formulation. Mathematical formulation is based on the theory of incompressible, inviscid, potential flow, assuming that the rotational part of the flow is restricted in the trailing vortex sheets emanating from sharp edges; e.g. the trailing edge in the case of a foil. The motion and the geometry of the body are general, thus no linearisation has been applied. The body contour is modeled as a surface of potential discontinuity. In the present chapter the body motion is prescribed, however the method has been extended to solve problems that include free motions of finite degrees of freedom; see e.g. the problem of the semi-activated foil in Sec.4.5.4. The studied lifting-flow problem has unsteady character and a vortex sheet, with spatially variable vorticity, is generated from the trailing edge of the hydrofoil, modeled as a surface of potential discontinuity too. The dynamics of the wake are not linearised and the evolution of the wake is obtained in the context of a time-stepping method. To be more specific, we have developed two versions of the wake model, one based on the linearization of the trailing vortex sheet dynamics and another that includes fully nonlinear free-wake analysis. Both models lead to similar results in the region of interest to the problem and therefore the first simplest scheme which demands also lower computational cost is more efficient and suitable for application at the present problem. Also a Pressure-type and a Morino-type Kutta conditions are compared demonstrating that the first gives more accurate results concerning both pressure distribution and integrated loads. The formulation of the problem is based on the potential theory and the boundary integral equations (BIE). For the numerical solution of the 3D, unsteady and nonlinear problem an efficient (in terms of both time and space complexity) GPU-accelerated boundary element method (BEM) is developed, based on a formulation that is direct with respect to the potential. The calculation of generalised forces is obtained without any further assumption by pressure integration. The latter is calculated using an approximate Bernoulli equation, capable to treat weakly nonlinear background flows.

We begin with the definition of the unsteady initial boundary value problem (IBVP) problem in infinite domain. The pressure-type Kutta condition will serve for the construction of the dynamical system equation and the other kinematic boundary conditions will provide appropriate constraints. The application of Green's formula for the representation of the potential from its boundary values will be used to obtain a weakly singular Boundary Integral Equation (BIE), that will serve after discretisation as an algebraic constraint. Derivation of representation theorem and BIE and also the treatment of the singular integrals that appear have been discussed in Filippas (2013), Politis (2011b). In the next, we describe the way we can obtain the aforementioned algebraic constraint that is a DtN operator via discretisation of the BIE. We use a boundary element method (BEM) for the spatial discretisation obtaining a discretised BIE that satisfies an approximate form of the boundary condition on the body's contour through collocation. Then the method for the velocity calculation with the representation theorem and a curvilinear finite difference method (CUFDM), in variable, non Cartesian and non orthogonal coordinate systems is presented. A thorough description of the free-wake model follows, for the treatment of the implicit nonlinearity that is introduced by the wake dynamics. That approach is based on the velocity representation theorem supported with desingularisation techniques and is implemented efficiently in the context of GPGPU programming. Also, an approximate Bernoulli's equation, for the calculation of pressure is derived by integrating Euler's equations for incompressible flows. That theorem is exploited for the derivation of the pressure-type Kutta condition. Exploiting the latter dynamic condition we proceed to the construction of a system of (spatially and temporarily) nonlocal differential equations, with explicit and implicit nonlinearities, with a linear algebraic constraint. Next, a method for time integration is presented.

Concerning numerical results and applications, the interesting problem of efficient thrust production using biomimetic flapping-foil systems is investigated. The predictability of the method and its limitations, concerning the problem of a flapping-foil propulsor, are investigated through comparison with experimental measurements from the literature while the importance of 3D effects and nonlinearity as well as the superior performance of the developed GPU code, are illustrated. The present method is applied to obtain numerical estimations of basic hydrodynamic quantities such as the lift and thrust coefficients, over a range of motion parameters, including reduced frequency, Strouhal number, maximum angle of attack and aspect ratio. Our analysis indicates that significant efficiency is achieved under optimal operating conditions. The present method and the GPU code could serve as a useful and efficient tool for the assessment, preliminary design and control of the studied efficient marine propulsion system.

2.2 Definition of the unsteady lifting problem

Consider a lifting body performing unsteady motion on a non-uniform unsteady background field and in unbounded domain. Practically, the assumption of unbounded domain is adequate when the body remains at large distance from additional boundaries (free-surface, bottom, lateral walls, shore etc). The domain of definition of the problem is an open semi-bounded domain $D(t) \subseteq \mathbb{R}^n$ (where $n = 2, 3$) with boundary $\partial D(t)$ which is supposed to be smooth everywhere except at trailing edge. The problem is time dependent including moving with prescribed motion boundaries or free-boundaries, therefore the domain of definition and most of the boundaries are variable in time. The unsteady foil is represented by a moving boundary

$\partial D_B(t)$, whose motion is prescribed. Another boundary $\partial D_W(t)$, that represents the trailing vortex sheet, is generated from the trailing edge. The basic reference frame is earth-fixed and a corresponding Cartesian coordinate system $Ox_1x_2x_3$ is defined. However, another auxiliary boundary-fixed frame of reference will be exploited in some cases and a corresponding Cartesian coordinate system¹ $Ox_{b1}x_{b2}x_{b3}$ is defined. The total velocity field $\nabla\Phi(\mathbf{x};t)$ (where $\mathbf{x} \in \bar{D}$, $t \in \mathbb{R}_0^+$) consists of the unsteady background velocity² $\mathbf{V}_G(\mathbf{x};t)$ which is assumed to be known and the disturbance velocity $\mathbf{V}(\mathbf{x};t)$ due to the presence of the body and its wake. We assume that the disturbance flow is irrotational and thus a velocity potential $\Phi(\mathbf{x};t)$ can be defined as a twice continuously differentiable function in $D(t)$, with $\nabla\Phi = \mathbf{V}$. Also the limiting boundary value³ of potential, denoted by $\Phi_B(\mathbf{x};t)$, is defined on the boundary.

To proceed, let $\partial D(t)$ denote the boundary and A a point on it. Let also (ζ, η) denote variable, non Cartesian and non orthogonal curvilinear coordinates⁴ on ∂D . Then, in the case of moving boundary, we can describe boundary surface ∂D as

$$\mathbf{r}_A(\zeta, \eta; t) = \mathbf{r}_A[\mathbf{x}(\zeta, \eta; t)]. \quad (2.1)$$

The limiting boundary value of Φ on ∂D is denoted by the function Φ_B , defined by:

$$\Phi_B(\zeta, \eta; t) \doteq \lim_{\delta \rightarrow 0} \Phi[\mathbf{r}_A(\zeta, \eta; t) + \mathbf{n}_A(\zeta, \eta; t)\delta; t], \quad (2.2)$$

where δ is a small parameter and \mathbf{n}_A a unit vector which is not tangent to ∂D at A (Politis, 2011b). Thus function Φ_B has a domain of definition the surface ∂D and equals the limiting value of $\Phi(\mathbf{x};t)$ as $\mathbf{r} \rightarrow A \in \partial D$. In the most general case, as we have mentioned, the function $\Phi(\mathbf{x};t)$ can be discontinuous through the boundary.

In order to evaluate the total velocity field we need to solve the problem for the unknown disturbance potential field $\Phi(\mathbf{x};t)$, thus in the following we will present the mathematical formulation for the disturbance field.

¹In the present case the boundary-fixed Cartesian coordinate system is located on the moving body boundary. When the problem includes nonlinear free surface another boundary-fixed system is defined. The latter is located on $x_1 = 0, x_2 = 0$ and the x_3 is defined from the calculated total free-surface elevation, introducing to the problem an implicit nonlinearity.

²The background field could model the ship wake where the propeller, rudder of flapping foil propulsor operates, for example at the design of wake adapted propulsors; the wake of a bluff body, when arrays of devices are considered. It could also be a first approximation of the unsteady free surface wave field, when devices interacting with waves are studied in the context of an unbounded domain formulation, assuming that the distance from the free surface is adequate enough and emphasising to the effect of the velocity field and not to the interaction with the free surface.

³The limiting boundary values or simply boundary values are defined with a specific limiting process. In this way, each Φ is made by definition to be continuous in the \bar{D} (i.e. in closure of D), even if it is discontinuous through the boundary, like in the case of the trailing vortex sheet, where Φ_B has different values as we approach the boundary from the upper or the lower side. In the present work, the subscripts B, W, K, F, H denote boundary values on the body, the wake, the Kutta strip, the free surface and the bottom, respectively.

⁴In the case of lifting bodies with foils (e.g. foils, rudders, propeller foils), not necessarily of trapezoidal planform, ζ defines the chordwise curvilinear direction and η the spanwise direction. In the case of trailing vortex sheets emanating from trailing edges, the curvilinear directions of ζ and η are defined in order to smoothly extend the bound curvilinear coordinate system beyond the trailing edge.

The governing equation is the Laplace equation

$$\Delta\Phi(\mathbf{x};t) = 0, \quad \mathbf{x} \in D, \quad (2.3)$$

which represents the conservation of mass for incompressible and irrotational fluid.

Also, the boundary condition on the body

$$\partial_{n_B}\Phi(\mathbf{x};t) = [\mathbf{V}_B(\mathbf{x};t) - \mathbf{V}_G(\mathbf{x};t)] \cdot \mathbf{n}_B(\mathbf{x};t) \doteq b(\mathbf{x};t), \quad \mathbf{x} \in \partial D_B, \quad (2.4)$$

where the directional derivative is denoted as

$$\partial_n\Phi(\mathbf{x};t) = \nabla\Phi(\mathbf{x};t) \cdot \mathbf{n}. \quad (2.5)$$

The boundary condition in Eq.(2.4), is the Neumann type, no entrance condition, which ensures that the fluid particles follows the body surface and not penetrate into it. The second term in Eq.(2.4) is the background-field velocity on the body contour.

We treat the above as an initial value problem and we assume that the potential and its derivatives vanish at large distance from the body

$$\lim_{r(\mathbf{x}|\mathbf{x}_{B0}) \rightarrow \infty} \Phi(\mathbf{x}|\mathbf{x}_{B0};t) = 0, \quad \lim_{r(\mathbf{x}|\mathbf{x}_{B0}) \rightarrow \infty} \nabla\Phi(\mathbf{x}|\mathbf{x}_{B0};t) = 0, \quad r(\mathbf{x}|\mathbf{x}_{B0}) = \|\mathbf{x} - \mathbf{x}_{B0}\|_2. \quad (2.6)$$

In the above equations, \mathbf{V}_B denotes the velocity on body boundary at the point $\mathbf{x}_B \in \partial D$, \mathbf{n} is the unit normal to the boundary vector pointing in D and $\|\cdot\|_2$ is the Euclidean norm while \mathbf{x}_{B0} is a characteristic point on the body boundary, e.g. the origin of the body-fixed coordinate system.

Furthermore, dynamic and kinematic boundary conditions should be satisfied on the wake ∂D_W . The dynamic boundary condition

$$p_W^u(\mathbf{x};t) = p_W^l(\mathbf{x};t), \quad \mathbf{x} \in \partial D_W, \quad (2.7)$$

mandates that a free shear layer cannot carry loading and thus the pressure at the both sides of it should be the same.

The kinematic boundary condition

$$\partial_{n_W}\Phi_W^u(\mathbf{x};t) = \partial_{n_W}\Phi_W^l(\mathbf{x};t), \quad \mathbf{x} \in \partial D_W, \quad (2.8)$$

demands that the upper and the lower side of the shear layer cannot be separated to two distinct surfaces, thus the normal to the surface velocity is continuous through ∂D_W . The superscripts u, l are used to denote the wake's upper and lower side respectively, while the indices B, W are used to denote values of the potential field and its derivative at the body surface and the wake of the foil, respectively.

Using Eq.(2.7) and Eq.(2.8) in conjunction with the following approximate form of Bernoulli's equation (whose derivation is presented in Sec. 2.7)

$$\frac{p(\mathbf{x};t)}{\rho} + \partial_t\Phi(\mathbf{x};t) + \frac{1}{2}[\nabla\Phi(\mathbf{x};t)]^2 + \mathbf{V}_G(\mathbf{x};t)\nabla\Phi(\mathbf{x};t) = 0, \quad \mathbf{x} \in D, \quad (2.9)$$

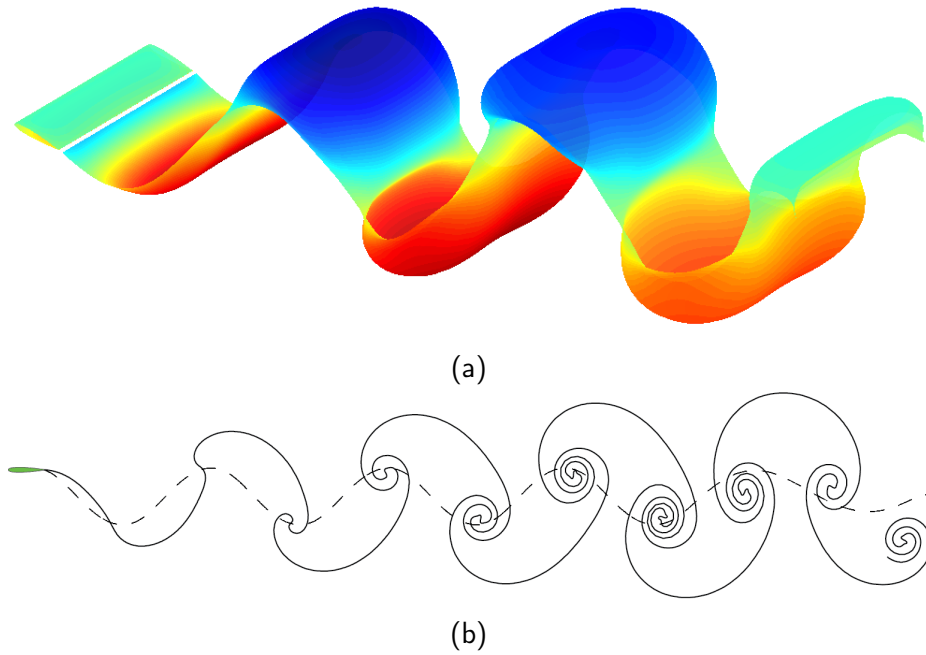


Figure 2.1: Comparison of different wake models: (a) 3D free wake model (b) 2D frozen and free wake models.

we obtain

$$D_t \mu_W(\mathbf{x}; t) = 0, \quad \mathbf{x} \in \partial D_W, \quad (2.10)$$

where $\mu_W = \Phi_W^u - \Phi_W^l$ denotes the potential jump (the dipole intensity) on the wake and $D_t(\cdot) = \partial_t(\cdot) + \mathbf{V}_W^m \cdot \nabla(\cdot)$ is the material derivative, based on the mean total velocity $\mathbf{V}_W^m = 0.5(\nabla\Phi_T^u + \nabla\Phi_T^l)$, on the trailing vortex sheet. The above relation states that ∂D_W evolves in time, as a material curve (when mean velocity is considered⁵) and its exact motion is a part of the solution, introducing an implicit nonlinearity and increasing the complexity of the problem and the computational effort for the solution; see Fig.2.1a. In the present work the later difficulty is tackled by means of general-purpose computing on graphics processing units (GPGPU). Another possibility is the application of a simplified wake model, based on the assumption that the generated vortex sheet emanates parallel to the bisector of the trailing edge and has the shape of trailing edge's path; see the dashed line in Fig.2.1b. In this way, the free wake dynamics are linearized, simplifying the problem and providing satisfactory predictions

⁵In the present work in order to obtain a tool to predict the vortex sheet dynamics we follow the approach presented in Politis (2004). In the latter work, the author states that Eq.(2.10) is "an equivalent form of the Helmholtz dynamic equations for the case of free vortex sheets" in terms of μ . However, the argument that the vortex sheet and dipole intensity evolves in time with the mean velocity, is quite heuristic and a more rigorous discussion of the vortex sheet equation can be found in the work of Marchioro and Pulvirenti (2012). In the aforementioned work, authors state clearly that a complete rigorous argument is not trivial and they provide a relevant discussion in Sec.6.3. Moreover, in Saffman (1992) authors state that the argument "vortex sheets move with the fluid and are composed of the same fluid particles" is "inadequate", because "it assumes that the proof of the Helmholtz laws commutes with the limiting process which gives the vortex sheet. Also, the proof of Kelvin's circulation theorem, which provides an alternative approach to the Helmholtz laws, depends upon the velocity being continuous and is incomplete in the presence of vortex sheets".

in the case of low and moderate unsteadiness; more details can be found in Filippas and Be-libassakis (2014). A similar wake model, assuming that the generated components of the wake remain where shed, has also been described and used by La Mantia and Dabnichki (2009, 2011, 2012, 2013). Detailed analysis of different wake modes has been done by Politis (2016), demonstrating their range of applicability as well as their limitations, concluding that "in the range of the Strouhal numbers where natural flyers and swimmers operate, the frozen wake model can be an attractive alternative for preliminary force predictions". Both models have been included in the computational code we develop and are compared in Sec.2.10.

In the lifting case, enforcement of the Kutta condition is required in order to fix the circulation at each time instant. A possible choice is a Morino-type version of the Kutta condition (Morino and Kuo, 1974), which permits direct calculation of vorticity transport to the wake, expressed in terms of the potential jump at the trailing edge.

$$\lim_{\xi \rightarrow \xi_{TE}} (\Phi_B^u[\mathbf{x}_B(\xi, \eta); t] - \Phi_B^l[\mathbf{x}_B(\xi, \eta); t]) = \lim_{\xi \rightarrow \xi_{TE}} \mu_W[\mathbf{x}_W(\xi, \eta); t],$$

$$\mathbf{x}_B \in \partial D_B, \quad \mathbf{x}_W \in \partial D_W \quad \text{and} \quad \mathbf{x}_{TE} \in \partial D_B \cup \partial D_W, \quad (2.11)$$

Morino condition at the steady case is compatible with Kutta–Joukowski hypothesis that no vortex filament exists at the trailing edge, see also Mohammadi-Amin et al. (2012) and Morino and Gennaretti (1993). Morino-type Kutta condition can be derived from pressure-type Kutta, under the assumption of linearized quasi-steady flow; see e.g. Politis (2011b) or Filippas (2013). However, this approximation would lead to an overestimation of the thrust at high Strouhal numbers, while a significant pressure jump is calculated as the trailing edge is approached; similar findings have also been reported by other authors; see, e.g., Bose (1992). On the other hand, application of the pressure-type Kutta condition has been recently criticized by La Mantia and Dabnichki (2009), stating that there is no experimental evidence supporting the notion that the pressure difference at the trailing edge, especially for unsteady motion of high frequency and large amplitude, ought to be equal to zero; see the detailed discussion and justification of this approach in the aforementioned reference and in La Mantia and Dabnichki (2011). Moreover, in Politis (2011a) a mixed-type Kutta condition is proposed. That idea is inspired by the observation that at higher loadings, imposition of a pressure-type condition at blade tips occasionally leads to a destruction of the shear layer geometry at those regions. According to this approach a Morino condition is applied near the tips of the foil and a pressure-type condition at the remaining trailing edge region. Leaving this interesting subject to be investigated in detail in future research, in the present work, apart from the simple Morino condition that is also included at the computational code as an alternative, a non-linear (quadratic), pressure-type Kutta condition, requiring zero pressure difference at the trailing edge, is imposed as follows

$$\lim_{\xi \rightarrow \xi_{TE}} F^{PK}[\mathbf{x}_B(\xi, \eta); t] = 0, \quad \mathbf{x}_B \in \partial D_B \quad \text{and} \quad \mathbf{x}_{TE} \in \partial D_B \cup \partial D_W, \quad (2.12)$$

where the operator $F^{PK}(\cdot)$ is defined as follows

$$F^{PK}[\mathbf{x}_B(\xi, \eta); t] = \left\{ \partial_t(\Phi^u - \Phi^l) + \left[0.5(\nabla\Phi^u + \nabla\Phi^l) + 0.5(\mathbf{V}_G^u + \mathbf{V}_G^l) \right] \cdot (\nabla\Phi^u - \nabla\Phi^l + \mathbf{V}_G^u - \mathbf{V}_G^l) - 0.5 \left[(\mathbf{V}_G^u)^2 - (\mathbf{V}_G^l)^2 \right] \right\}. \quad (2.13)$$

The above form of pressure-type Kutta condition, that is appropriate for the treatment of lifting flows in a weakly rotational background field, can be derived using the approximate Bernoulli's theorem on the body at upper and lower sides of trailing edge. To be more specific see Secs. 2.7 and 2.8 and the derivation of Eqs.(2.116 & 2.117).

2.3 Boundary Integral Formulation

Applying Green's theorem to the infinite domain lifting problem (Filippas 2013; Kress et al. 1989; Politis 2011a) we obtain an integral representation for the potential in \bar{D} in terms of the potential Φ (dipole intensity⁶) and its normal derivative $\partial_n\Phi$ ⁷ (source intensity) on the boundary.

$$\begin{aligned} \Phi_B(\mathbf{x}_0; t) &= \Phi_J(\mathbf{x}_0; t) + \int_{\partial D_B(t)} \partial_n\Phi_B(\mathbf{x}; t)G(\mathbf{x}_0|\mathbf{x}) - \Phi_B(\mathbf{x}; t)\partial_nG(\mathbf{x}_0|\mathbf{x}) ds(\mathbf{x}) \\ &+ \int_{\partial D_W^u(t)} \partial_n\Phi_W^u(\mathbf{x}; t)G(\mathbf{x}_0|\mathbf{x}) - \Phi_W^u(\mathbf{x}; t)\partial_nG(\mathbf{x}_0|\mathbf{x}) ds(\mathbf{x}) \\ &+ \int_{\partial D_W^l(t)} \partial_n\Phi_W^l(\mathbf{x}; t)G(\mathbf{x}_0|\mathbf{x}) - \Phi_W^l(\mathbf{x}; t)\partial_nG(\mathbf{x}_0|\mathbf{x}) ds(\mathbf{x}), \end{aligned} \quad (2.14)$$

where

$$\Phi_J(\mathbf{x}_0; t) = \begin{cases} 0, & \mathbf{x}_0 \in D. \\ \frac{\text{sign}(\mathbf{r}\cdot\mathbf{n})}{2}\Phi_B(\mathbf{x}_0; t), & \mathbf{x}_0 \in \partial D_B. \end{cases} \quad (2.15)$$

The second branch of Eq.(2.15) is known as jump relation for the potential induced by a dipole distribution (Kress et al., 1989) and reveals the nature of potential field that is defined in \bar{D}

⁶In general on ∂D it holds that $\mu = \Phi^+ - \Phi^-$, where "+" corresponds to the one side of the boundary and "-" to the other. In the case of boundaries like the wake that model potential discontinuities no special explanation is needed, because the limiting boundary value of the potential is defined on both sides. Contrarily, in the case of body boundary, bottom and free surface the limiting boundary value of the potential is defined only at the side of D . In those cases a "virtual flow" is considered in $\mathbb{R}^n \setminus \bar{D}$. That flow in the simplest case is chosen to have zero velocity everywhere and therefore the potential is constant and can be chosen to be zero; i.e. $\mu = \Phi^+$. For more details on that topic see e.g. Politis (2011b).

⁷In the above relations the gradient $\nabla(\cdot)$ is applied with respect to the integration point \mathbf{x} and $\partial_n(\cdot) = \mathbf{n} \cdot \nabla(\cdot)$. Moreover, the notation $\partial_{n_0}(\cdot) = \mathbf{n} \cdot \nabla_0(\cdot)$ will be used when the gradient is applied with respect to the control point \mathbf{x}_0 ; see e.g. the representation theorem of the velocities Sec.2.5.1.

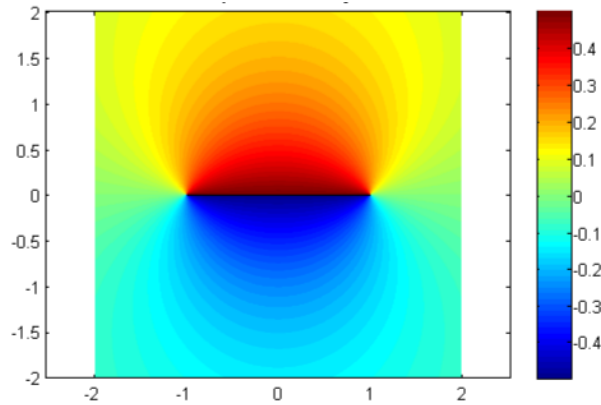


Figure 2.2: Potential field induced by constant-strength doublet distribution (double layer potential) on a straight-line panel.

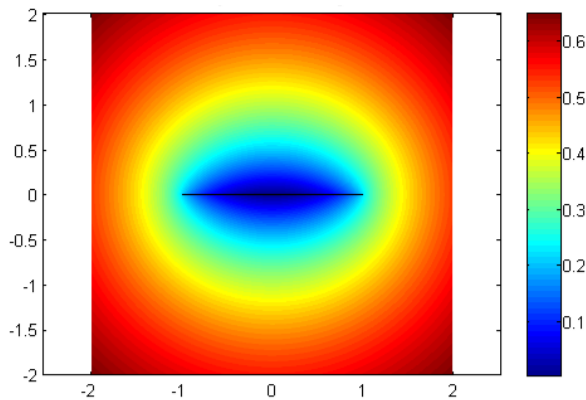


Figure 2.3: Potential field induced by constant-strength source distribution (single layer potential) on a straight-line panel.

with the introduction of its limiting boundary value on ∂D via Eq.(2.2). In general, a field defined in this way is continuous up to the boundary, but can be discontinuous through it. This is the case of the potential induced by a distribution of dipoles located on a part of ∂D . To be more specific, when approaching the boundary from the side where the normal to the boundary unit vector points the trace of the potential can be calculated by Eq.(2.15) with sign "+", while approaching from the other side is leading to sign "-", introducing a jump at the potential through the boundary, that equals the dipole intensity distributed at the specific point. This is the meaning of notation $sign(\mathbf{r} \cdot \mathbf{n})$. The above discussion explains the reason why the potential induced by a dipole distribution is termed double layer potential, see Fig.2.2. On the contrary the potential induced by a source distribution is continuous through the boundary and is termed single layer potential, see Fig.2.3.

Moreover ∂D_W^u and ∂D_W^l are the upper and the lower sides of the shear layer respectively defined using a branch cut (Fig.2.4). Introduction of the wake surface of potential discontinuity and the use of branch cut, permit the existence of finite circulation Γ around the lifting body, body, that is required for lift generation according Kutta-Joukowski theorem, see e.g. Moran (2003), Batchelor (2000) or Kundu et al. (2008).

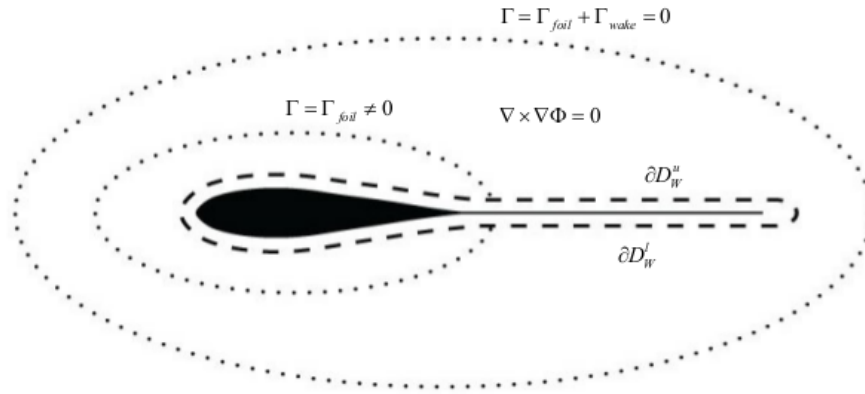


Figure 2.4: Introduction of a branch cut that permits the existence of circulation around lifting bodies without breaking irrotationality of the flow.

In the above relation we have used Green's function, consisted of the fundamental solution of 2D/3D Laplace equation and its normal to the boundary derivative

$$G(\mathbf{x}_0|\mathbf{x}) = \begin{cases} \frac{1}{2\pi} \ln r(\mathbf{x}_0|\mathbf{x}), & D \subseteq \mathbb{R}^2, \\ -\frac{1}{4\pi} \frac{1}{r(\mathbf{x}_0|\mathbf{x})}, & D \subseteq \mathbb{R}^3, \end{cases} \quad (2.16)$$

$$\partial_n G(\mathbf{x}_0|\mathbf{x}; t) = \begin{cases} -\frac{1}{2\pi} \frac{\mathbf{r}(\mathbf{x}_0|\mathbf{x}) \cdot \mathbf{n}(\mathbf{x}; t)}{[r(\mathbf{x}_0|\mathbf{x})]^2}, & D \subseteq \mathbb{R}^2, \\ -\frac{1}{4\pi} \frac{\mathbf{r}(\mathbf{x}_0|\mathbf{x}) \cdot \mathbf{n}(\mathbf{x}; t)}{[r(\mathbf{x}_0|\mathbf{x})]^3}, & D \subseteq \mathbb{R}^3, \end{cases} \quad (2.17)$$

with

$$\mathbf{r}(\mathbf{x}_0|\mathbf{x}) = \mathbf{x}_0 - \mathbf{x}, \quad r(\mathbf{x}_0|\mathbf{x}) = \|\mathbf{x}_0 - \mathbf{x}\|_2. \quad (2.18)$$

The above functions represent source and dipole singularities respectively. The first term in the integral is the potential induced at \mathbf{x}_0 from a source with intensity $\partial_n \Phi(\mathbf{x})$ located on the boundary at \mathbf{x} , while the second term represents similarly the effect of normal to the boundary dipole with intensity $\Phi(\mathbf{x})$. In this way the whole information for the potential in the domain D is stored on the boundary ∂D whose dimension is of one order lower. Therefore, if the boundary value of the potential and the derivative on the boundary are known, using Green's formula Eqs.(2.14, 2.15) we can evaluate potential everywhere in D .

Replacing body boundary condition Eq.(2.4) and wake kinematic condition Eq.(2.8) into the representation theorem on the boundary Eqs.(2.14, 2.15), we obtain the following Fredholm 2nd kind, weakly singular integral equation

$$\begin{aligned} \frac{1}{2} \Phi_B(\mathbf{x}_0; t) + \int_{\partial D_B(t)} \Phi_B(\mathbf{x}; t) \partial_n G(\mathbf{x}_0|\mathbf{x}) ds(\mathbf{x}) \\ = \int_{\partial D_B(t)} b(\mathbf{x}; t) G(\mathbf{x}_0|\mathbf{x}) ds(\mathbf{x}) - \int_{\partial D_W(t)} \mu_W(\mathbf{x}; t) \partial_n G(\mathbf{x}_0|\mathbf{x}) ds(\mathbf{x}), \quad \mathbf{x}_0 \in \partial D_B(t), \end{aligned} \quad (2.19)$$

where $\mu_W = \Phi_W^u - \Phi_W^l$ denotes the potential jump or the dipole intensity on the wake. Referring to a specific chordwise section (not necessarily flat), the potential jump at the trailing edge equals the instantaneous value of circulation around the hydrofoil section. This is demonstrated as follows

$$\Gamma_B(t) = \int_{\partial D_{B,section}(t)} \nabla \Phi_B(\mathbf{x}; t) G(\mathbf{x}_0 | \mathbf{x}) ds(\mathbf{x}) = \Phi_B^u(\mathbf{x}_{TE}; t) - \Phi_B^l(\mathbf{x}_{TE}; t) = \mu_B(\mathbf{x}_{TE}; t). \quad (2.20)$$

On the one hand, according to Kelvin's theorem, at every time instant the change of Γ_B around the body must be balanced by the change of Γ_W around the wake; see also Fig.(2.4). On the other hand, Kutta condition Eq.(2.11) or Eqs.(2.12, 2.13) introduces a connection between the wake potential jump and the body potential jump at the vicinity of trailing edge. In unsteady problems both Γ_B and μ_B vary in time leading to the production of alternating forces on the body. Considering the above arguments and the fact that the wake ∂D_W is a material curve that travels with the flow and that the same thing happens with μ_W that is initially generated at the trailing edge in the sense of Eq.(2.10), we conclude that dipole intensity μ_W is not constant along ∂D_W , contrary to the steady case (Moran, 2003). Therefore in unsteady lifting flows the dipole intensity varies along the wake and represents the history of circulation on the body. In general, information concerning the flow motion is stored in values of μ_W on ∂D_W and the presence of the wake introducing a memory effect which is represented by the last integral at Eq.(2.19).

Before we continue, it is important to take a closer look to the integrals appeared in the BIE (Eq.2.19). Since $\mathbf{x}_0 \in \partial D$ there is a point at the domain of integration where $\mathbf{x}_0 = \mathbf{x}$ and therefore $r = 0$. At this point the right hand side integrals become infinite and bear no meaning in the usual Riemann sense. Those integrals are called singular and can be determined as the limit of a well defined regular integral. The integrals appeared in Eq.(2.19) are weakly singular; i.e. informally speaking, the rate of blow up equals the rate that differential surface/arc ds tends to zero. The definition of weakly singular or Cauchy principal value⁸ integrals as the limit of a well defined integral have been presented in Politis (2011b) and in Filippas (2013). More extended and rigorous studies in singular integrals can be found in the literature; see e.g. Muskhelishvili (1953), Mikhlin (2014), Polyanin and Manzhirov (2008).

The weakly singular boundary integral equation Eq.(2.19), together with Morino-type Kutta condition Eq.(2.11) or pressure-type Kutta conditions Eqs.(2.12, 2.13), provide us with a system of equations for the unknown boundary fields Φ_B on the body and μ_W at the vicinity of trailing edge. The above system of equations can be solved numerically after the appropriate discretisation, implemented with a boundary element method (BEM) and collocation; for more details see e.g. Politis (2004) and Filippas (2013). Furthermore, in the most interesting case of pressure-type Kutta condition, that includes a partial time derivative of the unknown potential, numerical solution of the system can be achieved following

⁸Cauchy principal value integrals appear in the representation theorem of the velocity, which is necessary for the calculation of the velocity field and the implementation of the free wake model (Sec.2.6)

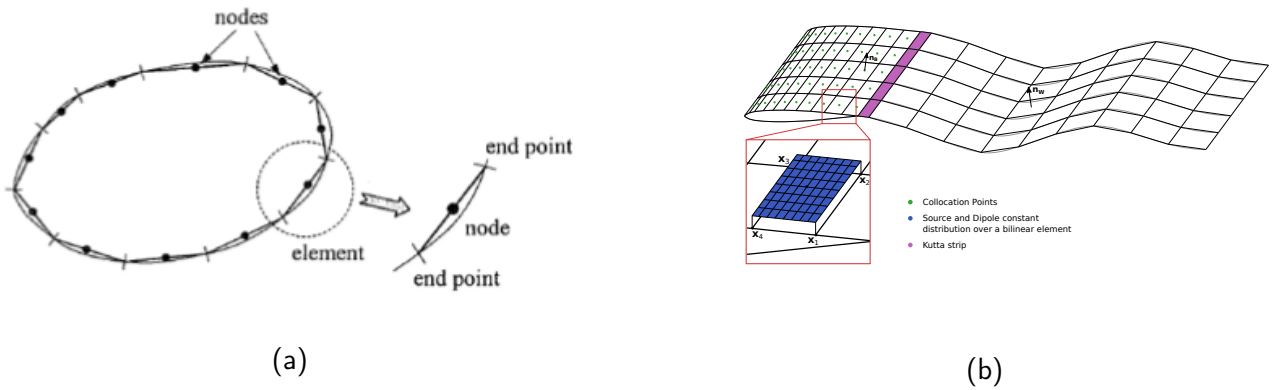


Figure 2.5: Spatial discretisation via approximation of the boundary with boundary elements and of the trace functions with piecewise constant distributions as well as approximate satisfaction of the BIE by applying a collocation scheme in (a) 2D and in (b) 3D.

two different paths. Either by time integration, where Kutta condition is treated as a dynamic system and BIE as an algebraic constraint (Sec.2.8.2) or using a finite difference method (FDM) for the temporal discretisation of Kutta condition. In the later case, BIE and Kutta condition are treated similarly forming a non-linear algebraic system. In the case of Morino condition, that is simply a linear algebraic equation, a linear system of equations is just formed and solved and no temporal discretisation on the Kutta condition is necessary (Filippas 2013; Politis 2011a). A detailed discussion of the different approaches is presented in Anevlavi (2019).

2.4 Spatial discretisation - DtN construction

The spacial discretisation mainly⁹ consists of the following approximations¹⁰ of the analytical model (see also Fig.2.5):

- Concerning the geometry, a C^0 representation of the boundary is used as follows:
 - in 2D formulation, following a low-order panel method, the body contour is replaced by a closed polygonal line, and N_B denotes the number of panels. The trailing vortex sheet is also approximated by an open polygonal line composed of $N_W(t)$ panels, whose number increases in time.
 - in 3D formulation, the boundary is approximated using bilinear-quadrilateral elements.

⁹Another approximation, that will not be mentioned here, can be applied to the surface gradient operator on the body contour in order to calculate efficiently tangential velocities; see Sec.(2.5.2) and Sec.(2.8).

¹⁰The method described in the present manuscript and the developed computational code, make use of bilinear-quadrilateral elements, piecewise constant distributions and collocation. However, the generalisation to a higher order approach is straightforward, due to the efficient (of arbitrary order and GPU-accelerated) numerical calculation of the factors. Therefore, it is left as a very interesting subject for future work to extend our method and code to higher (arbitrary n^{th}) order, or even to a meshless spline-based (probably isogeometric) approach (Cottrell et al., 2009; Ginnis et al., 2014; Takahashi and Matsumoto, 2012).

- Concerning the representation of the functions on the boundary, the potential, its normal derivative and the potential jump at each time step, are approximated by piecewise constant distributions, as follows:

$$\begin{aligned}\Phi_B(\mathbf{x}; t) &= \Phi_{B_i}(t), \text{ at body element } i, \quad i = 0, 1, \dots, N_B - 1, \\ \partial_n \Phi_B(\mathbf{x}; t) &= \partial_n \Phi_{B_i}(t) = b_i(t), \text{ at body element } i, \quad i = 0, 1, \dots, N_B - 1, \\ \mu_W(\mathbf{x}; t) &= \mu_{W_w}(t), \text{ at wake element } w, \quad w = 0, 1, \dots, N_W(t) - 1.\end{aligned}\quad (2.21)$$

As demonstrated in the end of Sec.2.3 the dipole intensity varies along the wake and represents the history of the time dependent circulation on the body. Therefore in the unsteady case, in the context of a low order approximation, a piecewise constant dipole distribution is required, contrary to the steady case where a constant distribution is used.

- Finally, following a collocation scheme, the BIE (Eq.2.19) is satisfied in a finite number of points (or control points) and in order to avoid singularities the centroids¹¹ of the panels have been chosen as collocation points. In the present case, that we deal with a Neumann problem, the BIE must be satisfied in N_B collocation points so as to balance the N_B unknown values of Φ_{B_i} that are required in order to represent the unknown trace of the potential on the body boundary in the context of our approximation.

In the present manuscript the numbering begins with zero to be in compliance with the developed CUDA C/C++ code. A fundamental element of programming in C/C++ is the usage of pointers that store the memory address of the object they pointing to. Arrays are implemented using pointers and pointer incrementation. To be more specific, an array of objects is constructed by allocating a specific amount of space in RAM (or VRAM) and the address of the first element of the array is stored in a pointer p . In order to obtain/store¹² data from/at the address that corresponds to the first element of the array (with index 0) we must dereference $*(p + 0)$, for the second element (with index 1) we must dereference $*(p + 1)$, for the $(i + 1)^{th}$ element (with index i) we must dereference $*(p + i)$; where " $*$ " in C/C++ is the dereference operator.

To proceed, the discretised form of Eq.(2.19) is as follows

$$\sum_{j=0}^{N_B-1} \left(\frac{\delta_{ij}}{2} + D_{ij}^{pot} \right) \Phi_{B_j}(t) = \sum_{j=0}^{N_B-1} S_{ij}^{pot} b_j(t) - \sum_{w=0}^{N_W(t)-1} D_{iw}^{pot}(t) \mu_{W_{iw}}, \quad i = 0, \dots, N_B - 1 \quad (2.22)$$

where δ_{ij} is Kronecker's delta and the quantities S_{ij}^{pot} and D_{ij}^{pot} are induction factors and represent the potential¹³ at collocation point i induced by a unit source and a dipole distribution¹⁴,

¹¹In 3D formulation, bilinear-quadrilateral elements are not flat surfaces and the centroid is calculated in the curvilinear space.

¹²When obtaining data with $*p$ at the right hand side of an assignment operation (a statement that contains the $op=$ assignment operator), that expression is a r-value; i.e. refers to the data value that is stored at the address in memory that p points to. When storing data to the address that p points to, the expression $*p$ is at the left hand side of the assignment operation and is l-value, i.e. refers to the memory location which identifies an object. For more details on pointers, r-values and l-values; see e.g. Horton (2007, 2014).

¹³The upper index pot indicates that the present integrals are potential induction-factors. Using a unified notation in Sec.2.5.1.3 we will introduce the velocity induction-factor integrals using the upper index vel .

¹⁴Potential induced by a source distribution located on a boundary is continuous through the boundary, contrary to the potential induced by a dipole distribution. For this reason the first is well known as single layer

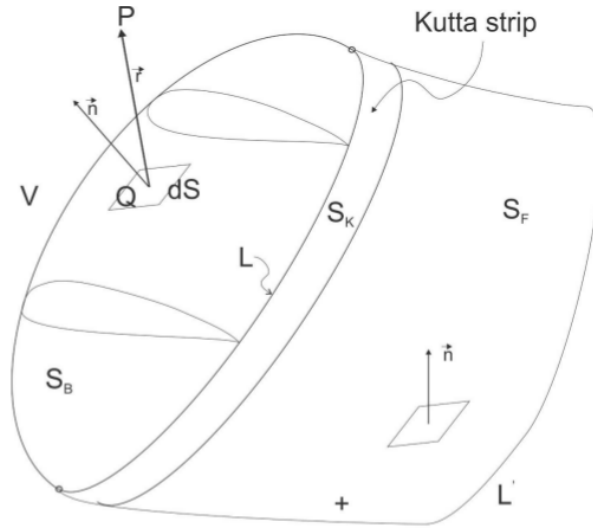


Figure 2.6: Definition of Kutta strip ∂D_K as a transitional region between the bound surface (body boundary) and the free surface (trailing vortex sheet). Discretisation of Kutta strip and representation by N_K boundary elements.

respectively, at element j , defined as follows

$$S_{ij}^{pot} = \int_{\text{element } j} G(\mathbf{x}_i|\mathbf{x}) ds(\mathbf{x}), \quad (2.23)$$

$$D_{ij}^{pot} = \int_{\text{element } j} \partial_n G(\mathbf{x}_i|\mathbf{x}) ds(\mathbf{x}). \quad (2.24)$$

In general, the above integrals could be evaluated numerically. In the present work, in 2D case, where a low order BEM is applied, analytical evaluation is possible. In 3D case, a combination of semi-analytical, numerical, and analytical calculations, depending to the strength of singularity, is applied.

Following Politis (2011a,b, 2016), we proceed to the introduction of Kutta strip in order to treat Kutta condition and the transition from the bound surface (i.e. the body boundary) to the free¹⁵ shear layer; see also Fig.(2.6) and Politis (2011b). Until this point, the boundary of D consists of the body boundary and the trailing vortex sheet i.e. $\partial D = \partial D_B \cup \partial D_W$. In ∂D_W at the vicinity of trailing edge there is a transitional region where the trailing vortex sheet transform from a free surface to a bound surface. In the sequel that region will be termed Kutta strip and will be denoted by ∂D_K and with ∂D_W we will denote the remaining free boundary. Moreover, in

potential and the second as double layer potential, for more details see the discussion bellow Eq.(2.15), Politis (2011b) or Kress et al. (1989).

¹⁵The terminology free and bound surfaces demonstrate the fact that, on the one hand the motion of body boundary (or even deformation) is governed by a non-hydrodynamic law (for example absence of motion, prescribed motion, finite/infinite degrees of freedom equation of motion of a rigid/deformable body), on the other hand shear layer motion is free, in the sense that it is a material surface moving and deforming with the fluid velocity. Another example of bound surface, from the field of coastal engineering and the modeling of water waves, is the rigid or even deformable bottom. Examples of free surfaces are the interface of the sea and air (called simply free surface in the modeling of water waves), or interface surfaces of non-mixing fluids and the vapor-liquid interface in gravitating flows.

the discretised model, in 2D case, Kutta arc will be approximated by a single panel, in 3D case, Kutta strip is approximated by N_K boundary elements distributed in the direction of span (i.e. curvilinear direction of η). Therefore, the discretised form of Eq.(2.19) becomes

$$\sum_{j=0}^{N_B-1} \left(\frac{\delta_{ij}}{2} + D_{ij}^{pot} \right) \Phi_{Bj}(t) = \sum_{j=0}^{N_B-1} S_{ij}^{pot} b_j(t) - \sum_{k=0}^{N_K-1} D_{ik}^{pot} \mu_{Kik}(t) - \sum_{w=0}^{N_W(t)-1} D_{iw}^{pot}(t) \mu_{Wiw}, \quad i = 0, \dots, N_B - 1. \quad (2.25)$$

Concerning the time dependence of the various quantities in Eq.(2.25), the Dirichlet $\Phi(t)$ and Neumann $b(t)$ data on the body boundary are time dependent, due to the arbitrary motion of the body and to the action of the unsteady background field. Concerning now the potential jump on the wake, from the Eulerian point of view¹⁶ it is variable in time, however, from the Lagrangian point of view, with respect to a reference frame moving with fluid particles at the wake, it is not variable in time. The notation used in the present paragraph is essential for the derivation of the solution algorithm and the implementation of the computational code that includes a Lagrangian-based algorithm for the assessment of the wake. To be more specific, at an arbitrary timestep, Kutta strip ∂D_K obtains dipole intensity μ_K , that is stored in specific address in memory. At the next timestep, Kutta strip location and dipole intensity data are copied to the end of the dynamic array that is allocated in the heap to store ∂D_W -data. Implementing in this way, an efficient Lagrangian based algorithm for the vorticity transportation on the wake, in the sense of Eq.(2.10). In this way, during the time marching process, the size of the device¹⁷ memory allocated for the ∂D_W -data increases¹⁸, nevertheless the content of the addresses that are allocated to store dipole intensity on the wake remains constant. For this reason μ in Eq.(2.25) is presented as time invariant corresponding to a constant quantity at the code during the time-marching process. In contrast $\mu_K(t)$ ¹⁹ at the Kutta strip is time dependent and its integral corresponds to the change in circulation around the foil. Moreover, the time

¹⁶In the whole manuscript, when writing analytically (non-discretised) boundary integral forms, we will refer to the inertial reference frame and therefore the domain of definition of the integrals for moving objects will be time dependent. That applies even to non-deformable body boundaries. However, when we write the discretised form that its purpose is to be directly programmable, the Lagrangian reference frame will be used, illuminating that some matrices has to be calculated only at specific timesteps; e.g. a non-deformable body induction factor matrix is not time dependent even if the body moves in a highly unsteady way and it could be calculated only during the first timestep.

¹⁷In GPGPU programming the processes can be either executed in CPU kernels or in GPU kernels, moreover data are stored either in classical random access memory (RAM) or in video random access memory (VRAM). The terminology host and device will be adopted to distinguish when referencing to CPU or GPU, respectively

¹⁸Of course compromisation between memory management and computational speed is crucial. Therefore, to minimise the overhead of memory allocation on the heap, the reallocation process is applied repeatedly after a specific number of timesteps and not at every single one. For more details on efficient memory management and for a pedagogical introduction to programming see e.g. Horton (2007) for procedural programming in C, or Horton (2014) for object oriented programming in C++.

¹⁹In Eqs.(2.19, 2.21) the potential jump at the wake μ_W is presented as time dependent because at that point of the manuscript the wake induced the transitional region (Kutta strip) where μ is time dependent.

dependence of the induction factors is of the utmost importance, especially concerning computational complexity²⁰ (space and time complexity) of the algorithm²¹. In the present case of a rigid body, induction factors from the body panels to the body control points are constant in time. Furthermore, the Kutta strip is selected to be always at the plane of the bisector of the corner that forms the neighboring to the trailing edge body panels²² (those geometrical objects, i.e. bisector and corner, are generalisations from the plane to the 3D curvilinear space). Therefore, the relative location of Kutta and body panels remains constant and the corresponding double layer induction factors are not time dependent. Finally, the relative position of the wake and the body changes both due to the motion of the body and the evolution of the free wake, rendering wake induction factors variable in time.

The discretised BIE Eq.(2.25) can be written in a more compact matrix form

$$\mathcal{D}_B^{pot} \cdot \Phi_B(t) = \mathcal{S}_B^{pot} \cdot \mathbf{b}(t) + \mathcal{D}_{B,K}^{pot} \cdot \boldsymbol{\mu}_K(t) + \mathcal{D}_{B,W}^{pot}(t) \cdot \boldsymbol{\mu}_W, \quad (2.26)$$

where \mathcal{D}_B^{pot} , \mathcal{S}_B^{pot} , $\mathcal{D}_{B,K}^{pot}$, $\mathcal{D}_{B,W}^{pot}(t)$ are potential²³ induction-factor matrices, with \mathcal{S} denoting source or single-layer integrals, and with \mathcal{D} denoting dipole or double-layer integrals. To be more specific \mathcal{D}_B^{pot} and \mathcal{S}_B^{pot} model body-body interactions and exist even at a non-lifting problem, while the additional terms involving the matrices $\mathcal{D}_{B,K}^{pot}$ and $\mathcal{D}_{B,W}^{pot}$ model wake-body interactions and are associated with the second and the last term in the right hand side of Eq.(2.25). The above matrices are defined as follows

$$\mathcal{D}_B^{pot} = \{0.5\delta_{ij} + D_{ij}^{pot}\}, \quad \mathcal{S}_B^{pot} = \{S_{ij}^{pot}\}, \quad \mathcal{D}_{B,K}^{pot} = \{-D_{ik}^{pot}\}, \quad \mathcal{D}_{B,W}^{pot}(t) = \{-D_{iw}^{pot}(t)\}, \quad (2.27)$$

and the indices belong to the following subsets of \mathbb{N}

$$i, j \in \{0, 1, \dots, N_B - 1\}, \quad k \in \{0, 1, \dots, N_K - 1\}, \quad w \in \{0, 1, \dots, N_W(t) - 1\}. \quad (2.28)$$

In Eq.(2.26) $\Phi_B = \{\Phi_{Bj}\}$, $\mathbf{b} = \{b_j\}$, $\boldsymbol{\mu}_K = \{\mu_{Kk}\}$, $\boldsymbol{\mu}_W = \{\mu_{Ww}\}$. In the sequel, we will denote with bold, vectors containing the values of piecewise constant trace functions on the panels, representing the boundaries boundary.

²⁰In computer science, the computational complexity, of an algorithm (or of a program that is the implementation of an algorithm via a computational code), is the amount of resources (execution time or memory) required for running it. Time complexity is the computational complexity that describes the amount of time it takes to run an algorithm, i.e. execution time. Space complexity represents the total amount of memory space required to solve a given computational problem with a given algorithm.

²¹On the one hand, numerical solution with BEM is more a compute-intensive rather than a data-intensive task and the calculation of N^2 singular integrals to fill the induce factor matrices is the core of the problem. Therefore if a part of the matrix remains constant during time marching, this should be exploited to the design of the algorithm possibly by storing the matrix to the device memory during the first timestep. On the other hand, although the memory size of GPUs increases rapidly, still VRAMs available are much more smaller than RAMs, therefore in GPGPU developers must be cautious concerning space complexity of their algorithms, in the specific case, when allocating naively large amounts of device memory for the induction factors. To be more specific, taking also into account the computational power that modern GPUs with thousands of cores provide, it is sometimes more preferable to recalculate parts of the induction factors than to store them.

²²That selection of the position of Kutta strip is computationally efficient, but is not panacea, for more details see Filippas and Belibassakis (2014) and Politis (2011b).

²³The upper index *pot* indicates that the present objects are potential induction-factor matrices. Using a unified notation in Sec.2.5.1.3 we will introduce the velocity induction-factor matrices using the upper index *vel*.

The above form of discretised BIE together with the discretised form of the selected Kutta condition could provide us with a system of nonlinear algebraic equations that could be solved using a general iterative method; e.g. the Newton-Raphson method. More details on that approach are presented in Anevlavi (2019).

However, in the present work the pressure-type Kutta condition is used to construct the evolution equations of the dynamical system, solved by time integration, as will be demonstrated in Sec.2.8. In that case we multiply Eq.(2.26) with \mathcal{D}^{-1} and we obtain

$$\Phi_B(t) = \mathcal{G} \cdot \mathbf{b}(t) + \mathcal{Z} \cdot \boldsymbol{\mu}_K(t) + \mathcal{P}(t) \cdot \boldsymbol{\mu}_W, \quad (2.29)$$

where

$$\mathcal{G} = (\mathcal{D}_B^{pot})^{-1} \cdot S_B^{pot}, \quad \mathcal{Z} = (\mathcal{D}_B^{pot})^{-1} \cdot \mathcal{D}_{B,K}^{pot}, \quad \mathcal{P}(t) = (\mathcal{D}_B^{pot})^{-1} \cdot \mathcal{D}_{B,W}^{pot}(t). \quad (2.30)$$

The above mapping is a discrete Dirichlet-to-Neumann (DtN) operator²⁴ that connects the potential (Dirichlet data) with its normal derivative (Neumann data) on body boundary ∂D_B , but also involves the unknown values of the dipole intensity $\boldsymbol{\mu}_K$ (Dirichlet data) on the Kutta strip ∂D_K , as well as the (known from the past) potential jump $\boldsymbol{\mu}_W$ (Dirichlet data) on the wake ∂D_W . We observe in the above equation that the influence of the wake, that introduces memory effects, is taken into account through $\mathcal{P}(t) \cdot \boldsymbol{\mu}_W$. Also, the effect of the body velocity and of the unsteady background field is considered through the components \mathbf{V}_B and \mathbf{V}_G , included in \mathbf{b} , as described by the body boundary condition Eq.(2.4). In Sec.2.8 using the appropriate part of the DtN map, Eq.(2.29), in the discrete form the pressure-type Kutta condition, we will obtain a system of (spatially and temporarily) nonlocal differential equations, with explicit and implicit nonlinearities, that approximately describe the dynamics of the system.

2.5 Velocity calculation

Under the assumption of incompressibility, an unsteady disturbance, divergent-free²⁵, vector field $\mathbf{V}(\mathbf{x}; t)$ can be defined in open²⁶ D , representing the fluid velocity, in the context of the mathematical modeling of the physical fluid. Moreover, assuming irrotationality, a purely mathematical object is allowed to be defined as an unsteady scalar field, i.e. the velocity potential $\Phi(\mathbf{x}; t) = \nabla \mathbf{V}(\mathbf{x}; t)$. The aforementioned relation between those two fields reveals their connection and moreover is directly associated with an technique for the approximate computation of the velocity, when numerical data for the potential are available in the whole D , i.e. by a stencil of finite differences in 3D/2D space. However, potential theory is fundamentally connected with the theory of BIE, and the representation theorems provide us with an

²⁴The terminology DtN operator is common in the modeling of inviscid water waves. Here we derive a DtN operator for lifting-flow problems in infinite domain. In Sec.3.4.1 the DtN for the problem of free surface - non lifting body will be presented. Finally, in Sec.3.5.1 the extended form of the DtN operator, that is suitable for lifting flows beneath the free surface, will be constructed.

²⁵The conservation of mass law in incompressible fluids reduces to $\nabla \mathbf{V} = 0$. That equation has kinematic content and characterises the velocity field as divergent-free.

²⁶Moreover velocity $\mathbf{V}(\mathbf{x}; t)$ can be defined in \bar{D} by a continuous expansion on the boundary ∂D , by the appropriate definition of its limiting boundary value. This is done in a similar manner with the definition of the limiting boundary value of the potential, see Eq.(2.2) and the relevant discussion or Politis (2011b).

alternative and more elegant way for the calculation of both potential and velocity, when only the Dirichlet and Neumann data on the boundary are known. In the present section we will provide the representation theorem for the velocities whose discretised form can be applied for calculations in the \bar{D}^{27} (Sec.2.5.1). That representation theorem will also be applied for the calculation of the velocity on ∂D_W and the implementation of the free wake model (Sec.2.6). Contrarily, it is efficient and usual, when a direct formulation is followed, the surface gradient of the velocities on the boundary to be calculated with curvilinear finite differences (Sec.2.5.2). That approach will also be adopted for the imposition of a) non-linear free-surface boundary conditions in Chapters 3 and 4, as well as b) linearised free-surface conditions in the presence of a current in Sec.4.5.4.

2.5.1 Calculation of potential gradient with the representation theorem for the velocities

In order to produce a representation theorem for the velocities, it is necessary to calculate the derivative of the representation formula of the potential Eq.(2.14). In the case of points in the domain, i.e. $\mathbf{x}_0 \in D$, the integrals at the right hand side are regular and thus, in order to produce a representation theorem for the gradient of potential $\nabla_0 \Phi(\mathbf{x}; t)$ we can simply interchange the limit processes of integration and differentiation. However, that process cannot be applied directly on the boundary ($\mathbf{x}_0 \in \partial D$), because in that case the integrals at the right hand side of Eq.(2.14) become singular. The special treatment of that technical issue have been presented, in detail, in Politis (2011b) and Filippas (2013).

Before we proceed, we introduce the following notation $\partial_s(\cdot) = \mathbf{n} \times \nabla(\cdot)$ for the differentiation of a scalar field on the surface of a boundary. When that operation applies to a scalar field X , the result is a vector in the direction of the tangent to the surface unit vector \mathbf{s} . Of course, the direction of \mathbf{s} depends (it is coplanar and normal) to the direction of the surface gradient of the limiting boundary value of quantity to whom the differential operator is applied. Then applying the operator $\partial_s(X) \times \mathbf{n}$ we obtain a vector that equals the surface gradient of the limiting boundary value of X , which is denoted by ∇X^* and the following decomposition holds $\nabla X = \partial_n X \cdot \mathbf{n} + \partial_s X \times \mathbf{n} = \partial_n X \cdot \mathbf{n} + \nabla X^*$; for more details see the Section 11: "A useful vector decomposition formula" of Politis (2011b). Moreover, the notation $\partial_{s_0}(\cdot) = \mathbf{n} \times \nabla_0(\cdot)$ will be used when the gradient is applied with respect to the collocation point \mathbf{x}_0 . In the present case the velocity is decomposed to its normal to the boundary and its tangential to the boundary components (see also Fig.2.7) as follows

$$\begin{aligned} \nabla_0 \Phi(\mathbf{x}_0) &= \partial_{n_0} \Phi(\mathbf{x}_0) \cdot \mathbf{n}(\mathbf{x}_0) + \partial_{s_0} \Phi(\mathbf{x}_0) \times \mathbf{n}(\mathbf{x}_0) \\ &= \partial_{n_0} \Phi(\mathbf{x}_0) \cdot \mathbf{n}(\mathbf{x}_0) + \nabla_0 \Phi_B(\mathbf{x}_0). \end{aligned} \quad (2.31)$$

²⁷The representation theorem for the velocities in ∂D is exploited in Belibasakis and Politis (1995, 1998) following an approach that provides us with a velocity/vorticity-based formulation which is direct with respect to the tangential to the boundary velocity. That formulation is termed direct because it leads to the direct calculation of the surface vorticity. Another classical but indirect formulation is the one developed by Hess (1972). That formulation is based on the linearity of Laplace equation and the linear superposition of distributed singularity elements (Green functions) on the boundaries, with unknown intensities. The indirectness of that method stems from direct calculation of singularity intensities instead of the velocity or the potential. The later can be calculated indirectly from the superposition of singularity-induced velocities and integration. The formulation followed in the present manuscript is potential-based and a direct one with respect to the potential.

To proceed, the representation theorem for the velocities in terms of the boundary values of the normal to the boundary derivative of the potential $\partial_n \Phi$ (source intensity) and its tangential to the boundary derivative of the potential $\partial_s \Phi$ (surface vorticity intensity) is as follows

$$\nabla_0 \Phi(\mathbf{x}_0; t) = \mathbf{V}_J(\mathbf{x}_0; t) + \mathbf{V}_s(\mathbf{x}_0 | \partial D; t) + \mathbf{V}_d(\mathbf{x}_0 | \partial D; t), \quad \mathbf{x}_0 \in \bar{D} \quad (2.32)$$

where the jump-relation component is

$$\mathbf{V}_J = \begin{cases} 0, & \mathbf{x}_0 \in D, \\ \frac{\text{sign}(\mathbf{r} \cdot \mathbf{n})}{2} [\partial_{n_0} \Phi(\mathbf{x}_0; t) \cdot \mathbf{n}(\mathbf{x}_0) + \partial_{s_0} \Phi(\mathbf{x}_0; t) \times \mathbf{n}(\mathbf{x}_0)], & \mathbf{x}_0 \in \partial D, \end{cases} \quad (2.33)$$

the source-induced velocity is

$$\mathbf{V}_s(\mathbf{x}_0 | \partial D; t) = \int_{\partial D(t)} \partial_n \Phi(\mathbf{x}; t) \nabla_0 G(\mathbf{x}_0 | \mathbf{x}) ds(\mathbf{x}), \quad (2.34)$$

and the dipole-induced velocity is

$$\begin{aligned} \mathbf{V}_d(\mathbf{x}_0 | \partial D; t) &= - \int_{\partial D(t)} \Phi(\mathbf{x}; t) \nabla_0 [\partial_n G(\mathbf{x}_0 | \mathbf{x})] ds(\mathbf{x}) \\ &= + \int_{\partial D(t)} \Phi(\mathbf{x}; t) (\mathbf{n} \nabla) [\nabla G(\mathbf{x}_0 | \mathbf{x})] ds(\mathbf{x}) \\ &= - \int_{\partial D(t)} \partial_s \Phi(\mathbf{x}; t) \times \nabla G(\mathbf{x}_0 | \mathbf{x}) ds(\mathbf{x}) + \mathbf{V}_{BS}(\mathbf{x}_0; \partial D_W(t); t), \end{aligned} \quad (2.35)$$

with

$$\mathbf{V}_{BS}(\mathbf{x}_0 | \partial D; t) = \begin{cases} 0, & \partial(\partial D) = \emptyset. \\ \left\{ \begin{array}{l} +\Phi(\mathbf{x}_2; t) \cdot \nabla_2 G_v(\mathbf{x}_0 | \mathbf{x}_2; \mathbf{x}; t) \\ -\Phi(\mathbf{x}_1; t) \cdot \nabla_1 G_v(\mathbf{x}_0 | \mathbf{x}_1; \mathbf{x}; t), \quad D \subseteq \mathbb{R}^2 \\ \frac{1}{4\pi} \int_{\partial(\partial D)(t)} \Phi(\mathbf{x}; t) \frac{d\mathbf{l}(\mathbf{x}) \times \mathbf{r}(\mathbf{x}_0 | \mathbf{x})}{|\mathbf{r}(\mathbf{x}_0 | \mathbf{x})|^3}, \quad D \subseteq \mathbb{R}^3 \end{array} \right\}, & \partial(\partial D) \neq \emptyset. \end{cases} \quad (2.36)$$

The second branch of Eq.(2.33) is the jump relation for the velocities induced by a source distribution (first component) and a dipole/surface vorticity distribution (second component); see also the discussion below Eq.(2.15) and Kress et al. (1989). To be more specific, the normal to the boundary component of the velocity induced by a source distribution presents a discontinuity, while the tangential to the boundary component of the velocity induced by a dipole/surface vorticity distribution is also discontinuous through the boundary.

Lets proceed to a physical interpretation of the components of the velocity representation theorem. The first integral term in Eq.(2.32) represents the velocity at \mathbf{x}_0 , induced by a distribution of sources, of intensity $\partial_n \Phi$, located on ∂D . The second part of the integral, together with the

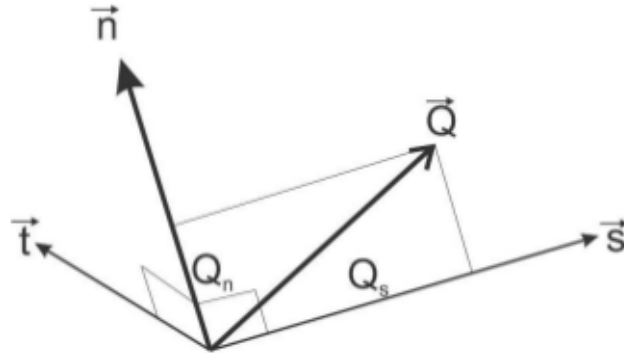


Figure 2.7: Decomposition of velocity $\nabla_0\Phi$ to its normal to the boundary $\partial_{n_0}\Phi \cdot \mathbf{n}$ and its tangential to the boundary $\partial_{s_0}\Phi \times \mathbf{n}$ components.

integral \mathbf{V}_{BS}^{2829} , is the velocity at \mathbf{x}_0 , induced by a distribution of dipoles on ∂D , directed normal to it, with intensity Φ ; or equivalently³⁰, the velocity induced by surface vortices on ∂D that are directed perpendicularly to it, with intensity $\partial_s\Phi$. To be more specific, it holds that the velocity, induced from a dipole distribution with intensity $\Phi(\mathbf{x})$ on a closed surface³¹, equals the velocity induced from a surface vorticity distribution on the same surface with intensity $\partial_s\Phi(\mathbf{x})$. Moreover, when the surface ∂D has a boundary denoted by $\partial(\partial D)$, one must include the Biot-Savart integral (Eq.2.36) to the calculation. That line integral³² represents the velocity induced from a vortex filament located along the boundary of the boundary; i.e. on $\partial(\partial D)$.

In the above relations we have used the derivative of Green's function as well as the derivative of the normal to the boundary derivative of Green's function and the derivative of vortex

²⁸That component of the velocity is termed Biot-Savart integral. The origin of that characterization comes from the field of electromagnetism, more precisely, from a similar formula that connects the magnetic-flow field with the current flow in a wire. To be more specific, it is named after Jean Baptiste Biot and his colleague Félix Savart honoring them for their work in 1820; see Biot and Savart (1820). Moreover, James Clerk Maxwell in 1861 in his work "On Physical Lines of Force" (Maxwell, 1861), related magnetic permeability with the intensity of a vortex formed in a fluid. Finally, the first application of the Biot-Savart law in practical fluid dynamics appeared in the lifting-line theory developed by Frederick Lanchester (Lanchester, 1907) and Ludwig Prandtl (Prandtl, 1918) in early 90's.

²⁹The notation $\mathbf{V}_{BS}(\mathbf{x}_0|\partial D;t)$ reveals that the Biot-Savart integral is a non-local operator that depends on both the shape of the boundary ∂D and the boundary values of the potential.

³⁰A rigorous proof of that equivalence, that holds for general-shaped boundaries (not only flat or piecewise-flat) and generally distributed dipoles/surface vortices (not only constant or piecewise constant distributions) can be found in the works of Hess (1972) and Politis (2004, 2011b) and Batista (2016). In Politis (2004, 2011b) an elegant proof of the generalised equivalence theorem is given using tensor calculus and the Lemma is called reformulations of Stoke's theorem. In Batista (2016) a proof using vector calculus is provided and result is named Politi's Lemma.

³¹A closed boundary surface is also a boundary whose boundary equals the empty set; i.e. $\partial(\partial D) = \emptyset$.

³²In 2D case the vortex filament reduces to point vortices at the termination ends of the curve ∂D , those points are denoted here with \mathbf{x}_1 and \mathbf{x}_2 .

singularity denoted with ∇G_v . Those singularities are given by the following formulas

$$\nabla_0 G(\mathbf{x}_0|\mathbf{x}) = -\nabla G(\mathbf{x}_0|\mathbf{x}) = \begin{cases} \frac{1}{2\pi} \frac{\mathbf{r}(\mathbf{x}_0|\mathbf{x})}{[r(\mathbf{x}_0|\mathbf{x})]^2}, & D \subseteq \mathbb{R}^2, \\ \frac{1}{4\pi} \frac{\mathbf{r}(\mathbf{x}_0|\mathbf{x})}{[r(\mathbf{x}_0|\mathbf{x})]^3}, & D \subseteq \mathbb{R}^3, \end{cases} \quad (2.37)$$

$$\nabla_0[\partial_n G(\mathbf{x}_0|\mathbf{x};t)] = (\mathbf{n}\nabla)[\nabla G(\mathbf{x}_0|\mathbf{x};t)] = \begin{cases} \frac{1}{2\pi} \frac{2\mathbf{r}(\mathbf{x}_0|\mathbf{x})[\mathbf{n}(\mathbf{x};t)\cdot\mathbf{r}(\mathbf{x}_0|\mathbf{x})]}{[r(\mathbf{x}_0|\mathbf{x})]^4} - \frac{\mathbf{n}(\mathbf{x};t)}{[r(\mathbf{x}_0|\mathbf{x})]^2}, & D \subseteq \mathbb{R}^2, \\ \frac{1}{4\pi} \frac{3\mathbf{r}(\mathbf{x}_0|\mathbf{x})[\mathbf{n}(\mathbf{x};t)\cdot\mathbf{r}(\mathbf{x}_0|\mathbf{x})]}{[r(\mathbf{x}_0|\mathbf{x})]^5} - \frac{\mathbf{n}(\mathbf{x};t)}{[r(\mathbf{x}_0|\mathbf{x})]^3}, & D \subseteq \mathbb{R}^3, \end{cases} \quad (2.38)$$

$$\nabla G_v(\mathbf{x}_0|\mathbf{x}_i;\mathbf{x};t) = \frac{1}{2\pi} \frac{\mathbf{e}_3(\mathbf{x};t) \times \mathbf{r}(\mathbf{x}_0|\mathbf{x}_i)}{[r(\mathbf{x}_0|\mathbf{x}_i)]^2}, \quad i = 1, 2, \quad D \subseteq \mathbb{R}^2, \quad (2.39)$$

with

$$\mathbf{r}(\mathbf{x}_0|\mathbf{x}) = \mathbf{x}_0 - \mathbf{x}, \quad r(\mathbf{x}_0|\mathbf{x}) = \|\mathbf{x}_0 - \mathbf{x}\|_2, \quad (2.40)$$

and \mathbf{e}_3 , in the 2D case, denoting the unit normal to the 2D domain ($D \subseteq \mathbb{R}^2$) vector, defined by $\mathbf{e}_3 = \mathbf{e}_1 \times \mathbf{e}_2$. Where $\mathbf{e}_1, \mathbf{e}_2$ are the tangential to the boundary and the normal to the boundary unit vectors, respectively.

In the sequel the velocity representation theorem will be applied to the boundary value problem (BVP) presented in Sec.2.2, distinguishing three cases with respect to the location of the control point. The first case concerns points on the body boundary ($\mathbf{x}_0 \in \partial D_B$) where the calculation of the velocity and pressure (by applying Bernoulli's theorem) is crucial both for the solution (calculation of tangential to the boundary velocity and implementation of pressure-type Kutta condition) and the calculation of the generalised forces acting on the body (via the integration of boundary pressure). The second case refers to points in the interior of the domain ($\mathbf{x}_0 \in D$) and the formula that will be obtained is useful for the calculation of the velocity and the pressure fields around the body; for visualisation purposes and for gaining insight to the physics of the problem, in the context of our inviscid approximation. The third case is about points on the wake ($\mathbf{x}_0 \in \partial D_W$) where the calculation of the velocity is necessary for the implementation of the free wake model.

2.5.1.1 Velocity representation theorem on body boundary

To proceed, for points on body boundary ($\mathbf{x}_0 \in \partial D_B$) it holds

$$\begin{aligned} \frac{1}{2} \nabla_0 \Phi_B(\mathbf{x}_0;t) &= \frac{1}{2} [b(\mathbf{x}_0;t) \cdot \mathbf{n}_B(\mathbf{x}_0;t) + \partial_{s_0} \Phi_B(\mathbf{x}_0;t) \times \mathbf{n}_B(\mathbf{x}_0;t)] \\ &= \int_{\partial D_B(t)} b(\mathbf{x};t) \nabla_0 G(\mathbf{x}_0|\mathbf{x}) - \partial_s \Phi_B(\mathbf{x};t) \times \nabla G(\mathbf{x}_0|\mathbf{x}) ds(\mathbf{x}) + \mathbf{V}_{BS}(\mathbf{x}_0|\partial D_B;t) \\ &\quad - \int_{\partial D_W(t)} \gamma_W(\mathbf{x};t) \times \nabla G(\mathbf{x}_0|\mathbf{x}) ds(\mathbf{x}) + \mathbf{V}_{BS}(\mathbf{x}_0|\partial D_W;t), \quad \mathbf{x}_0 \in \partial D_B(t), \end{aligned} \quad (2.41)$$

where $\gamma_W = \mathbf{n}_W \times \nabla \mu_W = \partial_s \Phi_W^u - \partial_s \Phi_W^l$ denotes the tangential velocity jump (the surface gradient of the dipole intensity or the free vorticity intensity) on the wake. We denote that in

a specific time t the boundary vector field γ_W is known from the past, everywhere with the exception of the Kutta strip. Moreover, the Biot-Savart term is zero on the body boundary of a smooth non-lifting body, because it is a closed surface. Also, that term on the wake can be calculated in terms of the potential jump/dipole intensity on the wake surface that is a two-sided open surface, as follows

$$\mathbf{V}_{BS}(\mathbf{x}_0|\partial D;t) = \begin{cases} 0, & \partial(\partial D) = \emptyset. \\ \left\{ \begin{array}{l} +\mu(\mathbf{x}_2;t) \cdot \nabla_2 G_v(\mathbf{x}_0|\mathbf{x}_2;\mathbf{x};t) \\ -\mu(\mathbf{x}_1;t) \cdot \nabla_1 G_v(\mathbf{x}_0|\mathbf{x}_1;\mathbf{x};t), \quad D \subseteq \mathbb{R}^2 \\ \frac{1}{4\pi} \int_{\partial(\partial D_W)(t)} \mu(\mathbf{x};t) \frac{d\mathbf{l}(\mathbf{x}) \times \mathbf{r}(\mathbf{x}_0|\mathbf{x})}{[\mathbf{r}(\mathbf{x}_0|\mathbf{x})]^3}, \quad D \subseteq \mathbb{R}^3 \end{array} \right\}, & \partial(\partial D) \neq \emptyset. \end{cases} \quad (2.42)$$

The above relation is a singular BIE with unknown the tangential component of the boundary velocity on the body $\partial_{s_0}\Phi_B$. Moreover the potential jump on the Kutta strip is unknown. That equation together with the potential-based BIE Eq.(2.19) and the pressure-type Kutta condition Eqs.(2.12, 2.13) could be used in order to obtain a system of equations for the unknown values of both the potential and the tangential velocity on the body inducing also the unknown potential jump on the Kutta strip. However, that approach in its practical application, is quite computational demanding due to a couple of reasons; see also Politis (2011a). On the one hand, the integrals that are required to be evaluated include more singular (Cauchy principal value and not weakly singular, see Politis (2011b) and Filippas (2013).) kernels than the integrals in the potential-based BIE. Therefore, more intensive computations are required for their calculation. On the other hand, by including to the unknowns the boundary values of the tangential velocity, the degrees of freedom become almost twice, increasing in this way the computational complexity of the algorithm, both in terms of space and time complexity. For those reasons, in the present work, the discretisation of pressure-type Kutta condition and the calculation of the tangential velocities is implemented by applying a curvilinear finite difference scheme, as will be described, in detail, in Sec.2.5.2 and in Sec.2.8.

2.5.1.2 Velocity representation theorem in the fluid domain

In the interior of the domain ($\mathbf{x}_0 \in D$) there are no discontinuities and the boundary integrals, inducing the velocity field, are regular; therefore, no velocity jump exists, i.e. $\mathbf{V}_J = 0$. Also, the velocity can be decomposed in the sense of Eq.(2.31), into two components, as discussed above the aforementioned relation. To be more specific, we consider a plane that passes from \mathbf{x}_0 and we select a normal to the plane vector $\mathbf{n}(\mathbf{x}_0)$. The velocity $\nabla_0\Phi(\mathbf{x}_0;t)$ at the point \mathbf{x}_0 can be decomposed to a normal to the plane component $\partial_{n_0}\Phi \cdot \mathbf{n}$ and a tangential to the plane component $\partial_{s_0}\Phi \times \mathbf{n}$. Finally, the velocity representation theorem is as follows

$$\begin{aligned} \nabla_0\Phi(\mathbf{x}_0;t) &= [\partial_{n_0}\Phi(\mathbf{x}_0;t) \cdot \mathbf{n}(\mathbf{x}_0;t) + \partial_{s_0}\Phi(\mathbf{x}_0;t) \times \mathbf{n}(\mathbf{x}_0;t)] \\ &= \int_{\partial D_B(t)} b(\mathbf{x};t) \nabla_0 G(\mathbf{x}_0|\mathbf{x}) - \partial_s\Phi_B(\mathbf{x};t) \times \nabla G(\mathbf{x}_0|\mathbf{x}) ds(\mathbf{x}) + \mathbf{V}_{BS}(\mathbf{x}_0|\partial D_B;t) \\ &\quad - \int_{\partial D_W(t)} \gamma_W(\mathbf{x};t) \times \nabla G(\mathbf{x}_0|\mathbf{x}) ds(\mathbf{x}) + \mathbf{V}_{BS}(\mathbf{x}_0|\partial D_W;t), \quad \mathbf{x}_0 \in \partial D_W(t), \end{aligned} \quad (2.43)$$

where

$$\mathbf{V}_{BS}(\mathbf{x}_0|\partial D;t) = \left\{ \begin{array}{l} 0, \quad \partial(\partial D) = \emptyset. \\ \left\{ \begin{array}{l} +\mu(\mathbf{x}_2;t) \cdot \nabla_2 G_v(\mathbf{x}_0|\mathbf{x}_2;\mathbf{x};t) \\ -\mu(\mathbf{x}_1;t) \cdot \nabla_1 G_v(\mathbf{x}_0|\mathbf{x}_1;\mathbf{x};t), \quad D \subseteq \mathbb{R}^2 \\ \frac{1}{4\pi} \int_{\partial(\partial D_W)(t)} \mu(\mathbf{x};t) \frac{d\mathbf{l}(\mathbf{x}) \times \mathbf{r}(\mathbf{x}_0|\mathbf{x})}{[\mathbf{r}(\mathbf{x}_0|\mathbf{x})]^3}, \quad D \subseteq \mathbb{R}^3 \end{array} \right\}, \quad \partial(\partial D) \neq \emptyset. \end{array} \right. \quad (2.44)$$

2.5.1.3 Velocity representation theorem on the wake - Discretised form

The proper implementation of the non-linear free wake model is quite important for the accurate estimation of the forces acting on a lifting body in strongly unsteady flows (Politis, 2016) and crucial for the modeling of the flow of the surrounding fluid (in the context of the present inviscid approximation), especially when the interaction of multiple bodies and free boundaries is studied³³. As illuminated in Sec.2.2 by Eq.(2.10) and the discussion bellow, the trailing vortex sheet is a surface/curve of discontinuity of the tangential velocity and a material surface/curve, evolving freely with the mean total velocity of the flow $\mathbf{V}_W^m = 0.5(\nabla\Phi_T^u + \nabla\Phi_T^l)$. The mean disturbance velocity on the wake ($\mathbf{x}_0 \in \partial D_W$) can be obtained by the following form of the representation theorem

$$\begin{aligned} \mathbf{V}_W^m(\mathbf{x}_0;t) &= \int_{\partial D_B(t)} b(\mathbf{x};t) \nabla_0 G(\mathbf{x}_0|\mathbf{x}) - \partial_s \Phi_B(\mathbf{x};t) \times \nabla G(\mathbf{x}_0|\mathbf{x}) ds(\mathbf{x}) + \mathbf{V}_{BS}(\mathbf{x}_0|\partial D_B;t) \\ &- \int_{\partial D_W(t)} \gamma_W(\mathbf{x};t) \times \nabla G(\mathbf{x}_0|\mathbf{x}) ds(\mathbf{x}) + \mathbf{V}_{BS}(\mathbf{x}_0|\partial D_W;t), \quad \mathbf{x}_0 \in \partial D_W(t), \end{aligned} \quad (2.45)$$

where

$$\mathbf{V}_{BS}(\mathbf{x}_0|\partial D;t) = \left\{ \begin{array}{l} 0, \quad \partial(\partial D) = \emptyset, \\ \left\{ \begin{array}{l} +\mu(\mathbf{x}_2;t) \cdot \nabla_2 G_v(\mathbf{x}_0|\mathbf{x}_2;\mathbf{x};t) \\ -\mu(\mathbf{x}_1;t) \cdot \nabla_1 G_v(\mathbf{x}_0|\mathbf{x}_1;\mathbf{x};t), \quad D \subseteq \mathbb{R}^2 \\ \frac{1}{4\pi} \int_{\partial(\partial D_W)(t)} \mu(\mathbf{x};t) \frac{d\mathbf{l}(\mathbf{x}) \times \mathbf{r}(\mathbf{x}_0|\mathbf{x})}{[\mathbf{r}(\mathbf{x}_0|\mathbf{x})]^3}, \quad D \subseteq \mathbb{R}^3 \end{array} \right\}, \quad \partial(\partial D) \neq \emptyset, \end{array} \right. \quad (2.46)$$

where the mean value of the jump-relation terms $0.5(\mathbf{V}_J^u + \mathbf{V}_J^l)$ is zero due to the unique definition of the unit normal vector; see also Fig.2.4.

In the sequel, we apply the discretisation process described in Sec.2.4, excluding collocation³⁴.

³³In the present work the interaction of free surface and the trailing vortex sheet of a lifting body is studied, see Sec. 3.2.

³⁴The implementation of collocation or Galerkin methods aim to the approximate satisfaction of a system of equations. Therefore it is irrelevant to the calculation of velocities via the discretised form of a representation theorem.

For the implementation of the free wake model, the velocity must be calculated on the nodes of the wake panels; for more details see Sec.2.6.

In order to use a unified notation (that is also directly connected with the concept object oriented programming and the polymorphism) for representation theorems of both scalar and vector (and in general tensor) discrete fields, we will use ordered systems (lists)³⁵. The components of a system are in general systems and in the present case 1st-order systems, i.e. vectors of \mathbb{R}^3 , or 0th-order systems, i.e. scalars of \mathbb{R} . We define the system $\mathbf{x} = \{\mathbf{x}_i\}$ where $\mathbf{x}_i \in \mathbb{R}^3$ and $i = 1, \dots, N$. There exists a relation between the 1st-order system \mathbf{x} and a vector that belongs to finite dimensional linear (or vector) space which is a subspace of \mathbb{R}^{3N} . Moreover, a 2nd-order system can be defined as $\mathcal{A} = \{\mathbf{a}_{ij}\}$ where $\mathbf{a}_{ij} \in \mathbb{R}^3$ and $i, j \in \{0, 1, \dots, N-1\}$, $N \in \mathbb{N}$. Again, there exists a relation between the 2nd-order system \mathcal{A} and a usual non-square matrix that belongs to a space of matrices with dimensions $3N \times N$. Finally, given the fact that we stay in the context of finite dimensional spaces ($N \in \mathbb{N}$) and that dot and cross product between vectors of \mathbb{R}^3 are well defined, we may "overload the operators of dot and cross product" (define dot and cross product between systems that contain vectors). We introduce two linear operators one for the dot product and another for the cross product, denoted with $\mathcal{A}_{dot}(\cdot)$ and $\mathcal{A}_{cross}(\cdot)$, respectively. Both of them map systems to systems³⁶, therefore, have as domain of definition and as range, spaces of systems³⁷ and the proof of their linearity is obvious. To be more specific, consider the aforementioned system of order one \mathbf{x} and the system of order two \mathcal{A} that both contain systems of order one. Using system \mathcal{A} we can define the operator $\mathcal{A}_{dot}(\cdot)$ that maps \mathbf{x} to another system \mathbf{y} with contents systems of order zero. The overload process of the binary operator of dot product can be done as follows $\mathcal{A} \cdot \mathbf{x} \doteq \mathcal{A}_{dot}(\mathbf{x})$ and finally, concerning the result and the calculation, it holds that

$$\mathbf{y} = \mathcal{A} \cdot \mathbf{x} = \{y_i\} = \left\{ \sum_{j=1}^N \mathbf{a}_{ij} \cdot \mathbf{x}_j \right\}, \quad i \in \{0, 1, \dots, N-1\}. \quad (2.47)$$

Moreover, using system \mathcal{A} we can define the operator $\mathcal{A}_{cross}(\cdot)$ that maps \mathbf{x} to another system \mathbf{z} that contains vectors. The overload process of the binary operator of cross product can be done

³⁵A N -dimensional matrix (or a tensor of N^{th} order, if it is a tensor) is a N^{th} -order system, a vector is a 1st-order system and a scalar is a 0th-order system; see e.g. Borisenko and Tarapov (1979). and McConnell (2014).

³⁶In the present paragraph we try to apply the process of "overloading of binary operators" in a quite rigorous way. This is straightforward for the 3D case. However, in 2D the result of cross (exterior) product is a vector that does not belong to the same vector space (from the point of view of an exterior 3D observer it does not belong to the same plane) that the initial vectors belong; i.e. cross (exterior) product is an exterior operation. When working with the classical algebraic quantity, i.e. the vector, the argument "map systems (of vectors) to systems (of vectors)" in 2D, requires special justification to be rigorous. We denote also that the dot (interior) product, both in 2D and in 3D, results to a lower-dimension quantity i.e. a scalar. Contrarily, there are not such inconveniences encountered, when the modern (but more complex) concept of a blade, instead of a vector, is applied. For more details on that interesting topic see any reference of geometric algebra; e.g. Flanders (1963) and Macdonald (2017). Moreover, for an application of Clifford algebra to the well-posedness of the 3D non-linear water-wave problem; see Wu (1999). Leaving that interesting task as a subject of future work, in the present manuscript, even when we refer to 2D case, we will informally speak as an exterior 3D observer and the vectors in that case will be 3D vectors. To be more specific, when applying cross product, the initial systems are two collections of vectors that belong to the 2D space that is a plane in 3D space. Also, the resulting system is a collection of vectors that belong in 3D space. The resulting vectors are vertical to the 2D plane.

³⁷A system that contains vector quantities is a system with components systems of order 1. Also, a system that contains scalar quantities is also a system with components systems of order 0. Therefore the result of dot product is also a system.

as follows $\mathcal{A} \times \mathbf{x} \doteq \mathcal{A}_{cross}(\mathbf{x})$ and finally, concerning the result and the calculation, it holds that

$$\mathbf{z} = \mathcal{A} \times \mathbf{x} = \{\mathbf{z}_i\} = \left\{ \sum_{j=1}^N \mathbf{a}_{ij} \times \mathbf{x}_j \right\}, \quad i \in \{0, 1, \dots, N-1\}. \quad (2.48)$$

To proceed, the following approximate form of the velocity representation theorem on the wake nodes is obtained

$$\mathbf{V}_W^m(t) = \mathcal{S}_B^{vel}(t) \cdot \mathbf{b}(t) + \begin{cases} \mathcal{D}_B^{vel}(t) \cdot \boldsymbol{\mu}(t) + \mathcal{D}_K^{vel}(t) \cdot \boldsymbol{\mu}_K(t) + \mathcal{D}_W^{vel}(t) \cdot \boldsymbol{\mu}_W, & D \subseteq \mathbb{R}^2. \\ \mathcal{D}_B^{vel}(t) \times \boldsymbol{\mu}(t) + \mathcal{D}_K^{vel}(t) \times \boldsymbol{\mu}_K(t) + \mathcal{D}_W^{vel}(t) \times \boldsymbol{\mu}_W, & D \subseteq \mathbb{R}^3. \end{cases} \quad (2.49)$$

The above 2^{nd} -order systems are defined in terms of velocity induction factors as follows

$$\mathcal{S}_B^{vel} = \{\mathbf{S}_{ij}^{vel}\}, \quad \mathcal{D}_B^{vel} = \{0.5\delta_{ij} + \mathbf{D}_{ij}^{vel}\}, \quad \mathcal{D}_K^{vel} = \{\mathbf{D}_{ik}^{vel}\}, \quad \mathcal{D}_W^{vel}(t) = \{\mathbf{D}_{iw}^{vel}(t)\}, \quad (2.50)$$

where the indices belong to the following subsets of \mathbb{N}

$$v \in \{0, \dots, N_{Wnodes} - 1\}, \quad j \in \{0, \dots, N_B - 1\}, \quad k \in \{0, \dots, N_K - 1\}, \quad w \in \{0, \dots, N_W(t) - 1\}, \quad (2.51)$$

and the velocity induction factors are defined as follows

$$\begin{aligned} \mathbf{S}_{ij}^{vel} &= - \int_{\text{element } j} \nabla G(\mathbf{x}_i | \mathbf{x}) ds(\mathbf{x}), & (2.52) \\ \mathbf{D}_{ij}^{vel} &= \int_{\text{element } j} (\mathbf{n} \nabla) [\nabla G(\mathbf{x}_i | \mathbf{x})] ds(\mathbf{x}) \\ &= \begin{cases} \nabla_2 G_v(\mathbf{x}_i | \mathbf{x}_2; \mathbf{x}) - \nabla_1 G_v(\mathbf{x}_i | \mathbf{x}_1; \mathbf{x}), & D \subseteq \mathbb{R}^2. \\ -\frac{1}{4\pi} \int_{\partial(\text{element } j)} \frac{d\mathbf{l}(\mathbf{x}) \times \mathbf{r}(\mathbf{x}_i | \mathbf{x})}{[\mathbf{r}(\mathbf{x}_i | \mathbf{x})]^3}, & D \subseteq \mathbb{R}^3. \end{cases} & (2.53) \end{aligned}$$

It is clear that $\mathcal{S}_B^{vel}, \mathcal{D}_B^{vel}, \mathcal{D}_K^{vel}, \mathcal{D}_W^{vel}(t)$ are velocity induction-factor matrices, with \mathcal{S} denoting the velocity induced by a unit source distribution, and with \mathcal{D} denoting the velocity induced by a unit dipole distribution. However, \mathcal{D} has an equivalent physical interpretation connected with a specific way of calculation. According to Politis lemma (Batista, 2016) and the definition of dipole velocity component \mathbf{V}_d in Eq.(2.35), there is a connection between the velocity induced by dipoles distributed on a boundary element i and the velocity induced by surface vortices distributed on the same element. The second can be decomposed to a surface integral on the element and a line (Biot-Savart) integral along the boundary of the element; see Eq.(2.35). In the present case of constant unit dipole distribution $\mu(\xi, \eta) = \mu_i = 1$ on boundary element i , the surface vorticity intensity is zero because $\gamma(\xi, \eta) = \nabla \mu(\xi, \eta) = \nabla \mu_i = 0$. Therefore, in the present approach, that a piecewise constant singularity distribution is used, \mathcal{D} denotes the velocity induced by unit dipole distribution or an equivalent collection of vortex rings (with four straight-line sides that are non coplanar in general) with unit intensity.

Moreover \mathcal{D}_B^{vel} and \mathcal{S}_B^{vel} model the effect of the body on the velocity on the wake, while the additional terms involving the matrices \mathcal{D}_K^{vel} and \mathcal{D}_W^{vel} model the effects of the Kutta strip and the wake on the wake including wake self-induced velocities.

2.5.2 Efficient calculation of the potential surface gradient with curvilinear finite differences

2.5.2.1 Differentiation on the boundary

In the present section an efficient way for the calculation of the tangential to the boundary velocity (surface gradient of the potential) will be presented. The boundary can be a general shaped 2D manifold under the restrictions discussed in Gunter (1967) and Politis (2011b). The description will be done using a general curvilinear (non-Cartesian and non-orthogonal) coordinated system; see also Politis (2011a). Aiming to this, we will apply the method of reciprocal bases³⁸. In the following discussion we will use the indices $i, j, k \in \{1, 2, 3\}$. At a few cases the indices $i, j \in \{1, 2\}$ and this would be explicitly stated. Under our assumptions at every point of the boundary a (covariant) base can be defined, that consists of three non-coplanar vectors $\{\mathbf{e}_1, \mathbf{e}_2, \mathbf{e}_3\}$. That base vectors are in general neither orthogonal nor of unit length. In the present case, base vectors $\mathbf{e}_1, \mathbf{e}_2$ are tangential to the boundary³⁹ and $\mathbf{e}_3 = \mathbf{n}$ is the unit normal to the boundary vector that is related with the surface unit vectors as follows $\mathbf{e}_3 = \mathbf{e}_1 \times \mathbf{e}_2 / \|\mathbf{e}_1 \times \mathbf{e}_2\|_2$. The reciprocal or contravariant base $\{\mathbf{e}^1, \mathbf{e}^2, \mathbf{e}^3\}$ can also be defined in order to have orthogonality at the curvilinear system, i.e.

$$\mathbf{e}_i \cdot \mathbf{e}^j = \begin{cases} 0, & \text{if } i \neq j. \\ 1, & \text{if } i = j. \end{cases} \quad (2.54)$$

The volume V of the parallelepiped spanned by the base $\{\mathbf{e}_1, \mathbf{e}_2, \mathbf{e}_3\}$ or the reciprocal base $\{\mathbf{e}^1, \mathbf{e}^2, \mathbf{e}^3\}$ can be obtained by the following triple products $\mathbf{e}_1 \cdot (\mathbf{e}_2 \times \mathbf{e}_3) = \mathbf{e}^1 \cdot (\mathbf{e}^2 \times \mathbf{e}^3)$. Moreover, the reciprocal base components can be calculated when base $\mathbf{e}_3 = \mathbf{e}_1 \times \mathbf{e}_2$ is known, as follows

$$\mathbf{e}^i = \frac{\mathbf{e}_j \times \mathbf{e}_k}{\mathbf{e}_1 \cdot (\mathbf{e}_2 \times \mathbf{e}_3)}. \quad (2.55)$$

At every point of the boundary the second-order metric tensor can be defined \mathbf{g} . That tensor has covariant components g_{ij} , contravariant components g^{ij} and mixed components g_i^j that can

³⁸In the present section we will briefly present and use some basic concepts and results (excluding proofs) of tensor algebra and analysis. For a more thorough introduction to the fundamentals and the concept of vector and tensor algebra, analysis and applications, that includes also rigorous justification see e.g. Borisenko and Tarapov (1979) and McConnell (2014). For a more advanced treatment of tensor fields on manifolds see e.g. Bishop and Goldberg (2012). In the present manuscript when referring to a tensor as an object, we will adopt a vector-style bold-letter notation. Contrarily, when we refer to the covariant, contravariant or mixed components of a tensor, or when some algebra is needed to be done, the index notation will be followed. In the aforementioned references the index notation is used. A classical reference, from the field of continuum mechanics, where the vector notation is used, can be found in the book Gurtin et al. (2010).

³⁹We denote that on the boundary the collection of vectors $\{\mathbf{e}_1, \mathbf{e}_2\}$ is a (covariant) base on the 2D manifold, where tangential to the boundary vectors, can be expanded.

be calculated using the covariant and the contravariant bases as follows

$$g_{ij} = \mathbf{e}_i \cdot \mathbf{e}_j, \quad (2.56)$$

$$g^{ij} = \mathbf{e}^i \cdot \mathbf{e}^j, \quad (2.57)$$

$$g_i^j = \mathbf{e}_i \cdot \mathbf{e}^j. \quad (2.58)$$

We consider now the a vector \mathbf{a} on the boundary. That vector is a first-order tensor with covariant components a_i and contravariant components a^i . On the one hand, that vector can be expanded with respect to the covariant base using its contravariant components as follows⁴⁰

$$\mathbf{a} = a^i \mathbf{e}_i. \quad (2.59)$$

On the other hand, that vector can be expanded with respect to the contravariant base using its covariant components as follows

$$\mathbf{a} = a_i \mathbf{e}^i. \quad (2.60)$$

Moreover, using the covariant and contravariant components of the metric tensor, we can establish two relations between the covariant and the contravariant components of a vector, as follows

$$a_i = g_{ij} a^j, \quad (2.61)$$

and

$$a^i = g^{ij} a_j. \quad (2.62)$$

Consider now the limiting boundary value of the velocity $\nabla \Phi_B$. This is a vector field defined on the boundary ∂D by a limiting process, in order to obtain a continuous expansion on the closure of the domain \bar{D} for the space gradient $\nabla \Phi$, that was initially defined in open D . Consider also the tangential component of $\nabla \Phi_B$ that is the surface gradient of the limiting boundary value of the potential. This is a vector field defined on the boundary ∂D and it is denoted as $\partial_s \Phi \times \mathbf{n}$. That vector has covariant and contravariant components denoted by $(\partial_s \Phi \times \mathbf{n})_i$ and $(\partial_s \Phi \times \mathbf{n})^i$, respectively, where the index $i \in 1, 2$. Those components are the covariant and contravariant derivatives of Φ_B

$$(\partial_s \Phi \times \mathbf{n})_i = (\partial_{e^i} \Phi_B)_i, \quad i \in \{1, 2\}, \quad (2.63)$$

$$(\partial_s \Phi \times \mathbf{n})^i = (\partial_{e^i} \Phi_B)^i, \quad i \in \{1, 2\}, \quad (2.64)$$

respectively. The covariant derivative $(\partial_{e^i} \Phi_B)_j$ of Φ_B can be calculated by curvilinear differentiation⁴¹. Then the contravariant derivative can be obtained using Eq.(2.62), as follows

$$(\partial_{e^i} \Phi_B)^i = g^{ij} (\partial_{e^j} \Phi_B)_j, \quad i, j \in \{1, 2\}. \quad (2.65)$$

⁴⁰In the present section we use Einstein (repeating index) summation convention; e.g. $a_i \mathbf{e}^i = \sum_{i=1}^3 a_i \mathbf{e}_i$.

⁴¹Justification for the argument that the covariant (and not the contravariant) derivative is calculated by curvilinear differentiation can be found in McConnell (2014).

Furthermore, the tangential component of the velocity $\partial_s \Phi \times \mathbf{n}$ can be obtained by expansion with respect to the covariant base $\mathbf{e}_1, \mathbf{e}_2$ that is defined on ∂D , using Eq.(2.59), as follows

$$\partial_s \Phi \times \mathbf{n} = (\partial_{e_i} \Phi_B)^i \mathbf{e}_i, \quad i \in \{1, 2\}. \quad (2.66)$$

Finally, the limiting boundary value of the velocity $\nabla \Phi_B$ is obtained by adding the tangential and the normal to the boundary components

$$\nabla \Phi_B = \partial_s \Phi \times \mathbf{n} + \partial_n \Phi \cdot \mathbf{n}. \quad (2.67)$$

2.5.2.2 Curvilinear finite differences on a non-uniform grid

The present section is dedicated to the approximate calculation of the tangential velocity (covariant derivative of the limiting boundary value of the potential) with curvilinear finite differences. CUFD schemes will be presented for both closed and open curves. In the case of a smooth (non-lifting) body there exists a curvilinear direction that corresponds to the direction along a closed curve. Examples are, at an ellipsoid the direction along the ellipses that do not intersect the poles, the direction along the circumference of smooth pylons at offshore structures. Contrarily, the directions of the meridians of an ellipsoid, that passes from the poles, both directions along a lifting body, the two curvilinear directions on the wavy free surface, in a ship the directions of sections, constitute directions that correspond to open curves.

To proceed, consider a lifting body, for example a foil and the collocation points on its boundary that form a curvilinear non-uniform grid on its surface. Two curvilinear directions are defined, one at the direction of the chord (with parameter ζ and unit vector \mathbf{e}_1) and another at the direction of span (with parameter η and unit vector \mathbf{e}_2). We denote here that the base $\{\mathbf{e}_1(\zeta, \eta), \mathbf{e}_2(\zeta, \eta)\}$ on that boundary is in general neither Cartesian nor orthogonal, also, it is variable with respect to the parameters (ζ, η) and $\mathbf{e}_1, \mathbf{e}_2$ are not of unit length. The boundary ∂D has been approximated by a discretised boundary $\partial D^{(h)}$ ⁴² that consists of $N \in \mathbb{N}$ boundary elements with variable size and shape. Each boundary element has a characteristic length⁴³ $h_i, i \in \{1, \dots, N\}$ and h is an appropriate mean value.

Concerning the numbering of control points, we have in total N control points located at the centroids of the panels. We define two local numberings, one ζ -wise (chordwise) and another η -wise (spanwise)⁴⁴ as follows:

- Concerning ζ -wise (chordwise) numbering, we begin with the first chordwise strip located at the most negative (with respect to x_2 axis) place of $\partial D^{(h)}$. Moving from one collocation point to the other along the direction of chord we define a local chordwise numbering. That numbering begins from 0, at the nearest to the trailing edge collocation

⁴²A similar notation is common in the literature of numerical treatment of partial differential equations (PDEs); see e.g. Grossmann et al. (2007).

⁴³In the case of a quadrilateral bilinear element the characteristic length is the maximum of the two diagonals that connect two non-successive (moving along the circumference of the element) points.

⁴⁴The example of the foil, that is related with the topic of the present thesis, is chosen here in order to demonstrate the numbering. In that case there is chordwise and spanwise direction. However that applies also on an arbitrary shaped boundary with one ζ -wise direction and another η -wise direction. For example, in the case where the wavy free surface, in a numerical wave tank, is the 2D manifold, ζ -wise direction could be the direction of length and η -wise direction could be the direction of breadth; see e.g. Chapters 3 and 4.

point at the lower side of foil. That numbering ends to $N_{loc1} - 1$, at the nearest to the trailing edge collocation point at the upper side of the foil. Therefore in one chordwise strip we have in total N_{loc1} collocation points and boundary elements.

- Concerning η -wise (spanwise) numbering, we begin with the first spanwise strip located at lower side of the foil at the trailing edge. Moving from one collocation point to the other along the direction of span we define a local spanwise numbering. That numbering begins from 0, at the most negative element (with respect to x_2 axis). That numbering ends to $N_{loc1} - 1$, at the at the most positive element (with respect to x_2 axis). Therefore in one chordwise strip we have in total N_{loc2} collocation points and boundary elements.

Therefore, we have in total $N = N_{loc1}N_{loc2}$ collocation points and panels. Moreover, we can define two global numberings, one ζ -major (chord-major) and another η -major (span-major), as follows:

- In the chord-major ordering, we move along the chordwise strips from the lower to the upper-side trailing edge, beginning with the strip located at the most negative place of x_2 axis ending to strip located the most positive strip of x_2 axis.
- In the span-major ordering, we move along the spanwise strips boundary element located at the most negative place of x_2 axis to the boundary element located at the most positive place of x_2 axis, beginning with the strip located at the lower side of trailing edge ending to strip located upper side of trailing edge.

We consider now the collection of discretised data considered as an unordered family of scalars or vectors. However, we can order them, using a mapping between them and a finite subset of physical numbers, following either the chord-major or span-major numbering⁴⁵. In this way, ordered lists (systems) are created, that represent the collocation points (containing vectors of \mathbb{R}^3), the discretised potential field (containing real numbers), the discretised tangential velocity field (containing vectors of \mathbb{R}^3) or the covariant components of the tangential velocity (containing real numbers). In the sequel for demonstration purposes we will follow the chord-major numbering. The systems that are arranged chord-majorly will be denoted using $|_1$ and those that are arranged span-majorly using $|_2$. Therefore, we have the collocation points $\mathbf{x}_0|_1 = \{\mathbf{x}_{0i}\}$, the potential $\Phi|_1 = \{\Phi_i\}$, the tangential velocity⁴⁶ $\mathbf{V}_t|_1 = \{\mathbf{V}_{ti}\}$, the first component (chordwise) of the covariant derivative of the potential $\mathbf{V}_{t1}|_1 = \{V_{t1i}\}$, the second component (spanwise) of the covariant derivative of the potential $\mathbf{V}_{t2}|_1 = \{V_{t2i}\}$, with $i \in \{0, 1, \dots, N - 1\}$. For programming purposes and for clarity, we denote that $i = i(p, q) =$

⁴⁵The necessity of proper ordering of data is of at most practical importance both for the elegant description of the curvilinear finite differences (CUFD) and the efficient parallel programming of that numerical scheme. The CUFD is a data-intensive process, contrary to the calculation of the induction factors that is a compute-intensive process. Therefore, in that case (that GPGPU programming is used), memory coalescing is crucial (Trompoukis 2012). In order to achieve memory coalescing, the proper selection of numbering, the choice of column-major or row-major way of storage data, together with the proper design of the GPU grid of blocks and threads, are of the utmost importance. However, from the point of view of the present developer, it should be mentioned that the integrated process, that contains both calculation of induced factors, inversion of matrices, CUFD and other sub-processes should be characterised as a compute-intensive task. The reason is that, in terms of time complexity, the induced factors calculation and the inversion of matrices are the heaviest tasks. Moreover, at the present initial stage of development, the developer is not concerned with development of code for the efficient inversion of matrices, which is a data-intensive process. For now, this is treated with the selection of the proper GPGPU library, leaving the development of a solver that is better for the specific application as a very interesting subject for future work.

⁴⁶In the present paragraph the tangential velocity is convenient to be denoted as $\mathbf{V}_t = \partial_s \Phi \times \mathbf{n}$.

$pN_{loc1} + q$, where $p \in \{0, \dots, N_{loc2} - 1\}$, $q \in \{0, \dots, N_{loc1} - 1\}$. Also, an ordered list containing boundary element nodes (vectors of \mathbb{R}^3) $\mathbf{x}^{node}|_1 = \{\mathbf{x}_i^{node}\}, i \in \{0, 1, \dots, N^{node} - 1\}$ is created, where $N^{node} = (N_{loc1} + 1)(N_{loc2} + 1)$.

Consider now, a 2D/3D curve that can be either closed or open with a curvilinear direction \mathbf{e}_1 . In the case of a closed curve, a central CUFD scheme is applied everywhere; on the contrary, in the case of an open curve, forward and backward CUFD schemes are applied at the termination ends. The covariant component of the tangential velocity along that curvilinear direction of \mathbf{e}_1 , can be approximated by the following 2^{nd} order CUFD scheme

$$\mathbf{V}_{t1}|_1 = \mathcal{D}(\mathbf{x}_0|_1) \cdot \Phi|_1. \quad (2.68)$$

The above chordwise CUFD matrix $\mathcal{D}(\mathbf{x}_0|_1)$ is a nearly-banded⁴⁷ $N - 1 \times N - 1$ square matrix, that can have the following two forms

$$\mathcal{D} = \begin{pmatrix} \bullet & \bullet & 0 & \dots & 0 & \bullet \\ \bullet & \bullet & \bullet & 0 & \dots & 0 \\ 0 & \dots & \dots & \dots & \dots & \dots \\ \vdots & \vdots & \vdots & \vdots & \vdots & \vdots \\ 0 & \dots & 0 & \bullet & \bullet & \bullet \\ \bullet & 0 & \dots & 0 & \bullet & \bullet \end{pmatrix}, \quad \text{or} \quad \mathcal{D} = \begin{pmatrix} \bullet & \bullet & \bullet & 0 & \dots & 0 \\ \bullet & \bullet & \bullet & 0 & \dots & 0 \\ 0 & \dots & \dots & \dots & \dots & \dots \\ \vdots & \vdots & \vdots & \vdots & \vdots & \vdots \\ 0 & \dots & 0 & \bullet & \bullet & \bullet \\ 0 & \dots & 0 & \bullet & \bullet & \bullet \end{pmatrix}, \quad (2.69)$$

where the non-zero elements are denoted by dots (\bullet). The first CUFD matrix below corresponds to a closed curve and the second to an open curve. To be more specific, in the present 2^{nd} -order approach, excluding the first and last row, \mathcal{D} is a tridiagonal matrix with bandwidth 1. In general by applying a $(2k)^{th}$ -order CUFD scheme we obtain a nearly-banded matrix, that contains a $(1 + 2k)$ -diagonal matrix with bandwidth k , where $k \in \mathbb{N}$.

The non-zero CUFD coefficients in matrix \mathcal{D} that are common in both closed and open curves are calculated as follows

$$\mathcal{D}_{ii-1} = -\frac{d_i^2}{2d_i^1 d_i^2}, \quad \mathcal{D}_{ii} = \frac{d_i^2 - d_i^1}{2d_i^1 d_i^2}, \quad \mathcal{D}_{ii+1} = \frac{d_i^1}{2d_i^1 d_i^2}, \quad i \in \{1, \dots, N_{loc} - 2\}, \quad (2.70)$$

where

$$d_i^1 = d(\mathbf{x}_{0,i-1}, \mathbf{x}_{0i}), \quad d_i^2 = d(\mathbf{x}_{0i}, \mathbf{x}_{0,i+1}), \quad (2.71)$$

and d is a proper distance⁴⁸ of a proper metric space that contains the points of the 2D manifold.

⁴⁷At the present version of the computational code we treat all the matrices as dense. This is mainly due to the fact that calculation of the DtN operator, that is more computationally demanding than the time-evolution problem, is treated using a classical BEM. The BEM induction-factor matrices, whose creation and storage is crucial in terms of time and space complexity, are dense; contrary to the finite element/difference/volume matrices, used in volume discretisation methods, that are banded (in the case of structured grids) or sparse (in the case of unstructured grids). A very interesting subject for future work is the development of fast multipole BEM where the induction-factor matrices are banded. In that case, for improved computational performance, both induction-factor and CUFD matrices should be treated as banded or sparse.

⁴⁸In the present manuscript the terminology metric is used for the metric tensor of the 2D manifold. When referring to the binary operation that defines distance between two objects of a metric space the word distance and not metric will be adopted. For more details on metrics and metric spaces, see any reference related to functional analysis e.g. Kolmogorov and Fomin (1957).

A naive, but adequate for engineering calculations, choice could be the distance that is induced by the Euclidean norm, i.e. $d_2(\mathbf{x}_{0,i-1}, \mathbf{x}_{0i}) = \|\mathbf{x}_{0,i-1} - \mathbf{x}_{0i}\|_2$.

In the case of a closed curve, the non-zero elements of the first and the last row of the CUFD matrix \mathcal{D} are calculated as follows

$$\mathcal{D}_{00} = \frac{d_0^2 - d_0^1}{2d_0^1 d_0^2}, \quad \mathcal{D}_{01} = \frac{d_0^1}{2d_0^1 d_0^2}, \quad \mathcal{D}_{0,N_{loc}-1} = -\frac{d_0^2}{2d_0^1 d_0^2}, \quad (2.72)$$

$$\begin{aligned} \mathcal{D}_{N_{loc}-1,0} &= \frac{d_{N_{loc}-1}^1}{2d_{N_{loc}-1}^1 d_{N_{loc}-1}^2}, & \mathcal{D}_{N_{loc}-1,N_{loc}-2} &= -\frac{d_{N_{loc}-1}^2}{2d_{N_{loc}-1}^1 d_{N_{loc}-1}^2}, \\ \mathcal{D}_{N_{loc}-1,N_{loc}-1} &= \frac{d_{N_{loc}-1}^2 - d_{N_{loc}-1}^1}{2d_{N_{loc}-1}^1 d_{N_{loc}-1}^2}, \end{aligned} \quad (2.73)$$

where

$$\begin{aligned} d_0^1 &= d(\mathbf{x}_{0,N_{loc}-1}, \mathbf{x}_{00}), & d_0^2 &= d(\mathbf{x}_{00}, \mathbf{x}_{01}), \\ d_{N_{loc}-1}^1 &= d(\mathbf{x}_{0,N_{loc}-2}, \mathbf{x}_{0,N_{loc}-1}), & d_{N_{loc}-1}^2 &= d(\mathbf{x}_{0,N_{loc}-1}, \mathbf{x}_{00}). \end{aligned} \quad (2.74)$$

In the case of an open curve, the non-zero elements of the first and the last row of the CUFD matrix \mathcal{D} are calculated as follows

$$\mathcal{D}_{00} = -\frac{3}{3d_0^1 - d_0^2}, \quad \mathcal{D}_{01} = \frac{4}{3d_0^1 - d_0^2}, \quad \mathcal{D}_{02} = -\frac{1}{3d_0^1 - d_0^2}, \quad (2.75)$$

$$\begin{aligned} \mathcal{D}_{N_{loc}-1,N_{loc}-3} &= \frac{1}{3d_{N_{loc}-1}^2 - d_{N_{loc}-1}^1}, & \mathcal{D}_{N_{loc}-1,N_{loc}-2} &= -\frac{4}{3d_{N_{loc}-1}^2 - d_{N_{loc}-1}^1}, \\ \mathcal{D}_{N_{loc}-1,N_{loc}-1} &= \frac{3}{3d_{N_{loc}-1}^2 - d_{N_{loc}-1}^1}, \end{aligned} \quad (2.76)$$

where in that case

$$\begin{aligned} d_0^1 &= d(\mathbf{x}_{00}, \mathbf{x}_{01}), & d_0^2 &= d(\mathbf{x}_{01}, \mathbf{x}_{02}), \\ d_{N_{loc}-1}^1 &= d(\mathbf{x}_{0,N_{loc}-3}, \mathbf{x}_{0,N_{loc}-2}), & d_{N_{loc}-1}^2 &= d(\mathbf{x}_{0,N_{loc}-2}, \mathbf{x}_{0,N_{loc}-1}). \end{aligned} \quad (2.77)$$

In order to calculate the covariant component of the tangential velocity along the other curvilinear direction of \mathbf{e}_2 we rearrange the systems of collocation points and potential, obtaining $\mathbf{x}_0|_2 = \{\mathbf{x}_{0n(i)}\}$ and potential $\Phi|_2 = \{\Phi_{n(i)}\}$ where $i, n(i) \in \{0, \dots, N-1\}$. In that case $n = n(p, q; i) = qN_{loc2} + p$, where $p \in \{0, \dots, N_{loc2} - 1\}, q \in \{0, \dots, N_{loc1} - 1\}$. The reordering⁴⁹

⁴⁹Concerning programming, there are two ways for rearranging data in memory. The first way is implemented by copying the data in another location allocated in the heap, resulting in a new array, where the data are stored sequentially according to the new ordering. This way, although is inefficient in terms of space complexity, is sometimes more efficient in terms of time complexity, because ordered data can be processed faster by either single or multiple threads. The second way is implemented by rearranging an array of pointers (pointers to pointers) while the data are still stored in their initial location. Those techniques are usually termed zero-copy technique. However the data in memory are still stored sequentially according to the old numbering and maybe their postprocess is inefficient in terms of time complexity. The latter technique, that is standard in classical sorting routines, is usually preferred when arrays of large objects should be rearranged or when strict memory limitations exist. In the present case, although GPUs still have memory limitations, the first approach is followed, because the systems of vectors are not that large and for better performance in terms of time complexity.

is done as follows

$$n(p, q; i_{pq}) = i^T(p, q), \quad p \in \{0, \dots, N_{loc2} - 1\}, q \in \{0, \dots, N_{loc1} - 1\}. \quad (2.78)$$

To justify the use of unary operation of transpose in the above equation we denote that n and i are 2^{nd} -order finite systems of physical numbers. To be more specific the above quantities can be interpreted as non-square matrices (2^{nd} - order systems) and could be denoted as i_{pq} and n_{qp} . However, to be implemented in CUDA C/C++ they are stored in RAM (or in VRAM) sequentially in a column major way, using simple pointers. Therefore, for the RAM (or VRAM) they are also vectors (1_{st} - order systems). To proceed, according to their first nature, n may be interpreted as a $N_{loc1} \times N_{loc2}$ non-square matrix, i as a $N_{loc2} \times N_{loc1}$ non-square matrix and i^T is its transpose⁵⁰. Also, the systems \mathbf{x}_0 and Φ have similar double nature⁵¹. However, they are richer because they contain vectors and scalars, respectively. Therefore the following relations hold

$$\mathbf{x}_0|_2 = (\mathbf{x}_0|_1)^T, \quad (2.79)$$

$$\Phi|_2 = (\Phi|_1)^T. \quad (2.80)$$

To proceed, we calculate the spanwise CUFD matrix $\mathcal{D}(\mathbf{x}_0|_2)$, in a similar manner as we calculated the chordwise CUFD matrix $\mathcal{D}(\mathbf{x}_0|_1)$. Then we apply a similar to Eq.(2.68) formula, to the rearranged data

$$\mathbf{V}_{t2}|_2 = \mathcal{D}(\mathbf{x}_0|_2) \cdot \Phi|_2. \quad (2.81)$$

Finally, $\mathbf{V}_{t2}|_1$ can be calculated, if it is necessary, by rearranging $\mathbf{V}_{t2}|_2$, as follows

$$\mathbf{V}_{t2}|_1 = (\mathbf{V}_{t2}|_2)^T. \quad (2.82)$$

2.6 Free-wake analysis

In the present section we will describe an iterative scheme that can be applied to incorporate to implicit nonlinearity, arising in lifting flow problems, that is associated with the free trailing vortex sheet. As described in Sec.2.2, vorticity is emanating from the trailing edge lying on singular surface/curve of potential discontinuity. Vorticity travels at the wake as a material

⁵⁰In order to develop an efficient computational code, it is important to thoroughly understand the double nature of n and i . They are both non-square matrices (2^{nd} -order systems) and vectors (1_{st} - order systems), of physical numbers. In order to use developed libraries, that implement efficiently linear algebraic operations, e.g. the transpose, their first nature is important. In order to store them and develop functions that implement algebra with them, in CUDA C/C++, their second nature is required.

⁵¹That nature is illuminated by noticing that via $i(p, q)$ or $n(p, q; i)$, with $p \in \{0, \dots, N_{loc2} - 1\}$ and $q \in \{0, \dots, N_{loc1} - 1\}$, their data are mapped to the elements of the Cartesian product of the following finite and ordered subsets of \mathbb{N} : $\{0, \dots, N_{loc2} - 1\}$, $\{0, \dots, N_{loc1} - 1\}$. That Cartesian product has a cardinality of $N = N_{loc1}N_{loc2}$, that equals the number of elements that the 1_{st} - order systems contain.

surface/curve, according to the following law

$$D_t \mu_W(\mathbf{x}; t) = 0, \quad \mathbf{x} \in \partial D_W, \quad (2.83)$$

where $\mu_W = \Phi_W^u - \Phi_W^l$ denotes the potential jump (the dipole intensity) on the wake and $D_t(\cdot) = \partial_t(\cdot) + \mathbf{V}_W^m \cdot \nabla(\cdot)$ is the material derivative, based on the mean total velocity $\mathbf{V}_W^m = 0.5(\nabla \Phi_T^u + \nabla \Phi_T^l)$, on the trailing vortex sheet. The above relation states that the boundary ∂D_W evolves in time, as a material curve and its exact motion is part of the solution introducing an implicit nonlinearity to the problem. That problem can be solved using an iterative implicit-coupling scheme, as follows. Assuming that we have already time-marched to time step $t - \Delta t$ and everything is known, including the geometry of the wake $\partial D_W(t - \Delta t)$. In order to proceed to the next timestep, the body is moved generating a new Kutta strip from the trailing edge with unknown dipole intensity. Then as will be described in Sec.2.8 and in Sec.2.9, the unknown hydrodynamic quantities are calculated. Subsequently, we can evolve the material curve $\partial D(t)$ according to the following equation

Then, if we use an explicit time integration scheme (one-way coupling of body and free wake dynamics) for the above equation, the next step follows or if we implement an implicit iterative scheme (strong two-way coupling of body and free wake dynamics), the part of the DtN map that includes the influence of the wake has to be calculated many times and the above procedure has to be repeated before we proceed to the next time step.

Focusing now to the calculation of the velocity, \mathbf{V}_W^m can be calculated by the representation theorem presented in Sec.2.5.1.3, as follows

$$\begin{aligned} \mathbf{V}_W^m(\mathbf{x}_0; t) = & \int_{\partial D_B(t)} b(\mathbf{x}; t) \nabla_0 G(\mathbf{x}_0 | \mathbf{x}) - \partial_s \Phi_B(\mathbf{x}; t) \times \nabla G(\mathbf{x}_0 | \mathbf{x}) ds(\mathbf{x}) + \mathbf{V}_{BS}(\mathbf{x}_0 | \partial D_B; t) \\ & - \int_{\partial D_W(t)} \gamma_W(\mathbf{x}; t) \times \nabla G(\mathbf{x}_0 | \mathbf{x}) ds(\mathbf{x}) + \mathbf{V}_{BS}(\mathbf{x}_0 | \partial D_W; t), \quad \mathbf{x}_0 \in \partial D_W(t), \end{aligned} \quad (2.84)$$

where

$$\mathbf{V}_{BS}(\mathbf{x}_0 | \partial D; t) = \begin{cases} 0, & \partial(\partial D) = \emptyset. \\ \left\{ \begin{array}{l} +\mu(\mathbf{x}_2; t) \cdot \nabla_2 G_v(\mathbf{x}_0 | \mathbf{x}_2; \mathbf{x}; t) \\ -\mu(\mathbf{x}_1; t) \cdot \nabla_1 G_v(\mathbf{x}_0 | \mathbf{x}_1; \mathbf{x}; t), \quad D \subseteq \mathbb{R}^2 \\ \frac{1}{4\pi} \int_{\partial(\partial D_W)(t)} \mu(\mathbf{x}; t) \frac{d\mathbf{l}(\mathbf{x}) \times \mathbf{r}(\mathbf{x}_0 | \mathbf{x})}{[\mathbf{r}(\mathbf{x}_0 | \mathbf{x})]^3}, \quad D \subseteq \mathbb{R}^3 \end{array} \right\}, & \partial(\partial D) \neq \emptyset. \end{cases} \quad (2.85)$$

As also demonstrated in Sec.2.5.1.3, the discretised form of the velocity representation theorem for points on the N^{node} wake nodes, i.e. on $\mathbf{x}^{node} = \{\mathbf{x}_i^{node}\}, i \in \{0, 1, \dots, N^{node} - 1\}$, is as follows

$$\mathbf{V}_W^m(t) = \mathcal{S}_B^{vel}(t) \cdot \mathbf{b}(t) + \begin{cases} \mathcal{D}_B^{vel}(t) \cdot \boldsymbol{\mu}(t) + \mathcal{D}_K^{vel}(t) \cdot \boldsymbol{\mu}_K(t) + \mathcal{D}_W^{vel}(t) \cdot \boldsymbol{\mu}_W, & D \subseteq \mathbb{R}^2. \\ \mathcal{D}_B^{vel}(t) \times \boldsymbol{\mu}(t) + \mathcal{D}_K^{vel}(t) \times \boldsymbol{\mu}_K(t) + \mathcal{D}_W^{vel}(t) \times \boldsymbol{\mu}_W, & D \subseteq \mathbb{R}^3. \end{cases} \quad (2.86)$$

The velocity induction factors are defined as follows

$$\mathbf{S}_{ij}^{vel} = - \int_{\text{element } j} \nabla G(\mathbf{x}_i|\mathbf{x}) ds(\mathbf{x}), \quad (2.87)$$

$$\begin{aligned} \mathbf{D}_{ij}^{vel} &= \int_{\text{element } j} (\mathbf{n}\nabla)[\nabla G(\mathbf{x}_i|\mathbf{x})] ds(\mathbf{x}) \\ &= \begin{cases} \nabla_2 G_v(\mathbf{x}_i|\mathbf{x}_2; \mathbf{x}) - \nabla_1 G_v(\mathbf{x}_i|\mathbf{x}_1; \mathbf{x}), & D \subseteq \mathbb{R}^2. \\ -\frac{1}{4\pi} \int_{\partial(\text{element } j)} \frac{d\mathbf{l}(\mathbf{x}) \times \mathbf{r}(\mathbf{x}_i|\mathbf{x})}{[\mathbf{r}(\mathbf{x}_i|\mathbf{x})]^3}, & D \subseteq \mathbb{R}^3. \end{cases} \end{aligned} \quad (2.88)$$

The induction factors from the body to the wake are regular integrals and can be easily calculated⁵². However, in 3D case⁵³, the Kutta-strip induction factors and the self-induction factors on the wake are highly-singular non-integrable (in the usual sense) integrals; see also Politis (2004). In the present case of bilinear quadrilateral elements with constant dipole intensity, those Biot-Savart integrals has a straight-line support (the sides of the elements). Therefore, an analytical formula can be obtained. However, the velocity calculated by that formula, in the neighborhood of the node, is still highly singular, and the desingularisation processes that will be followed is described later in the present section. To proceed, in the 3D case the following decomposition, of the boundary of the element to the four straight-line edges, can be done $\partial(\text{element } j) = \bigcup_{k=0}^3 L_{jk}$. Therefore, the line integral (vortex ring velocity) can be decomposed to four straight line integrals on the edges of the element (vortex filaments velocities), as follows

$$\mathbf{D}_{ij}^{vel} = -\frac{1}{4\pi} \int_{\partial(\text{element } j)} \frac{d\mathbf{l}(\mathbf{x}) \times \mathbf{r}(\mathbf{x}_i|\mathbf{x})}{[\mathbf{r}(\mathbf{x}_i|\mathbf{x})]^3} = -\frac{1}{4\pi} \sum_{k=0}^3 \mathbf{D}_{ijk}^L, \quad (2.89)$$

where each vortex filament velocity can be calculated analytically (Katz and Plotkin, 2001), as follows

$$\mathbf{D}_{ijk}^L = \int_{L_{jk}} \frac{d\mathbf{l}(\mathbf{x}) \times \mathbf{r}(\mathbf{x}_i|\mathbf{x})}{[\mathbf{r}(\mathbf{x}_i|\mathbf{x})]^3} = \frac{\mathbf{r}_{ijk}^1 \times \mathbf{r}_{ijk}^2}{\|\mathbf{r}_{ijk}^1 \times \mathbf{r}_{ijk}^2\|_2} \cdot \mathbf{r}_{ijk}^0 \cdot \left(\frac{\mathbf{r}_{ijk}^1}{\|\mathbf{r}_{ijk}^1\|_2} - \frac{\mathbf{r}_{ijk}^2}{\|\mathbf{r}_{ijk}^2\|_2} \right). \quad (2.90)$$

In the above relation upper indices are used to distinguish between the different vector distances. To be more specific, \mathbf{r}_{ijk}^0 is the vector distance between two nodes on the filaments, \mathbf{r}_{ijk}^1 is the vector distance between the first node of the filament and the control point and \mathbf{r}_{ijk}^2 is the vector distance between the second node of the filament and the control point. It is clear that when the control point tend to one of the nodes that quantity tend to infinity.

The velocity representation theorem is accurate for the calculation of the shear layer dynamics

⁵²In 2D case, that calculation can be done analytically in the context of the present low order panel method; see e.g. Moran (2003) or Katz and Plotkin (2001). In 3D case, the calculation can be done either analytically, using far-field approximate formulas or numerically, with simple (non-adaptive) quadrature rules.

⁵³In 2D case the induction factors are single vortices located on the nodes of the panel and their self-induced velocities are singular. The desingularisation of those velocities will be discussed later in the present paragraph.

in the context of the present inviscid approximation. However, dipole self-induced velocity on a boundary element is singular at its nodes. Moreover, from the physical point of view, the mechanisms (a) of vortex sheet evolution, especially at highly unsteady cases, and (b) of the strong interaction between the vortex sheet and itself and other boundaries⁵⁴, are mainly viscous and they are excluded from the present modeling. Furthermore, as denoted in Politis (2011a): "the mathematical flow fields in the vicinity of vortex sheets present peculiar/non-physical performance due to the following reasons: (a) the boundary of a shear layer induces infinite velocities in its neighborhood, Saffman (1992); (b) approaching a point of a shear layer from either sides results in different values of self-induced velocities and induced potentials. Thus formulas for induced velocities/potentials used in BEM cannot be applied to strong interaction cases, where viscosity rules without modification". Moreover, in Politis (2016) it is stated that: "Free vortex sheets are inherently unstable and amenable to two well-known instabilities: the Kelvin-Helmholtz instability⁵⁵ and the roll-up of their free edges⁵⁶. As a result, they show chaotic behavior with the passage of time. On the other hand, experimental evidence on flows around lift producing devices shows that the wake vorticity is organized in specific, problem dependent roll-up patterns". In Politis (2004), a cut-off based filtering technique is applied in order to encounter that problem, achieving reasonably smooth wake shapes, in cases of moderate unsteadiness. However, in Politis (2011a, 2016), a more efficient and elegant desingularisation technique is introduced⁵⁷, that is able to produce smooth wake shapes in highly-unsteady operating conditions. That technique, as explained in Politis (2011a), is inspired by the by exact solutions (like the Batchelor, Oseen-Lamb or the Burgers vortices⁵⁸) of simplified forms of Navier-Stokes equations, as will be described in the sequel. In that approach, smooth desingularisation kernels remove the generic singularities from the self-induced velocities, by introducing artificial viscosity to the modeling. In this way the small-scale instabilities are suppressed, leaving the large-scale organized vortices to govern the evolution of the vortex sheet, generating smooth roll-up patterns, even at highly loaded conditions.

A detailed demonstration of the way that vortices can be obtained, as solutions of simplified forms of Navier-Stokes equations, can be found in Chapters 2 and 6 of Wu et al. (2007). Here just a brief discussion on that topic will be presented, together with the formula of the specific vortex solution we exploit for filtering purposes. To proceed, we start with Navier-Stokes equation, see Eq.(2.161) in the aforementioned work. We cast the left-hand-side material derivative

⁵⁴The interaction of free shear layer and the water free surface, in initially still water and in waves, are studied in Sec.3.2 and Sec.4.4, respectively.

⁵⁵Strictly speaking, the Kelvin-Helmholtz instability refer to continuous dilatation of an initially disturbed vortex sheet with uniform vorticity. A discussion concerning stability on non-uniform shear layers, like unsteady vortex sheets, can be found in Hocking (1964, 1965).

⁵⁶On the one hand, Kelvin-Helmholtz instability refers to the roll-up of the wake about a spanwise axis forming a reverse Karman vortex wake (at thrust-producing operation), that can also be modeled in the 2D formulation of a flapping foil; see e.g. Politis (2011a), Saffman (1992), Batchelor (2000), Wu et al. (2007), Lewis (2005). On the other hand, the termination edges of a finite vortex sheet induce infinite velocities to their self and this is related with the tip vortex rollup; see also Politis (2016).

⁵⁷We denote here, that those filter functions have already been introduced in vortex particle methods; see e.g. Winckelmans and Leonard (1993) and Krasny et al. (2002).

⁵⁸Batchelor and Oseen-Lamb are stretch-free vortices and will be discussed in the sequel. The Burgers vortex (Burgers, 1948), that is referenced in Politis (2016), is the first stretched vortex solution to model turbulent eddies and includes as a special case the Oseen-Lamp vortex; for more details see Sec.6.2.2 of Wu et al. (2007).

to the vorticity form, revealing the inertial term, the gradient of kinetic energy and the Coriolis-type Lamb-vector term. Next, at the right hand side, by applying the first law of thermodynamics in the enthalpy form⁵⁹, we replace pressure gradient with enthalpy gradient temperature and entropy gradient, obtaining the viscous Crocco-Vazsonyi equation; see Eqs.(2.163, 2.164) in the aforementioned reference, where the total enthalpy is used. Writing that relation with respect to a cylindrical coordinated system one can obtain Crocco-Vazsonyi equation, in a form, suitable for the pursuit of vortice-type solutions; see Eq.(6.4) in the aforementioned reference. When seeking for axisymmetric and stretch-free columnar vortices, by introducing the appropriate assumptions we obtain a simplified form for Crocco-Vazsonyi equation; see Eq.(6.18) in the aforementioned reference. Following Wu et al: "if the flow is effectively inviscid, the only equation we can use is (6.18a) in which the pressure can automatically adjust itself to balance whatever centrifugal acceleration. Thus, a stretch-free inviscid vortex can have arbitrary radial dependence, providing a big freedom for constructing various inviscid vortex models. The most familiar example is the q-vortex, which fits many experimental data pretty well". The azimuthal velocity of that vortex, known also a Batchelor vortex⁶⁰, is given by the following formula⁶¹

$$u_{\theta}(r) = \frac{\Gamma}{2\pi r} \left[1 - e^{-c\left(\frac{r}{R}\right)^p} \right], \quad p = 2. \quad (2.91)$$

In the above formula, the second multiplicative factor is the kernel-smoothing function that will be applied to desingularise the Biot-Savart integral. To be more specific, Γ denotes the vortex filament intensity, r is the radial Euclidean distance of the reference point from the core, R is a characteristic radius (that will be further analysed in the sequel) to make r non-dimensional. Moreover, c is a constant characterising the range of action of the filter. In the present work, following Politis (2016), we select $c = \ln 2$. Furthermore, p is a parameter that, in the context of a kernel-smoothing process, depends on the order of the singularity of the kernel function. In the present work, that parameter is selected to be $p = 2$. This is a suitable choice for, both 2D vortex (i.e. infinite vortex filament) and 3D (finite) vortex filament, self-induced velocity desingularisation. That choice is supported by the aforementioned theoretical analysis and by parametric study conducted by professor Politis, that is partially presented in the aforementioned reference. Applying that selection of parameters, we conclude to the following form of

⁵⁹That procedure was followed by Alexander Friedmann in order to produce the result known as Crocco's theorem, that is an inviscid form of Crocco-Vazsonyi equation. That result is an aerodynamic theorem relating the flow velocity, vorticity, and pressure (or entropy) of a potential flow. Crocco's theorem gives a relation between the thermodynamics and fluid kinematics. The theorem was first enunciated by Alexander Friedmann for the particular case of a perfect gas and published in 1922 in the work entitled "An essay on hydrodynamics of compressible fluid". That work is archived at the Wayback Machine in 1934, under the editorship of Nikolai Kochin (see the first formula on page 198 of the reprint). However, usually this theorem is connected with the name of Italian scientist Luigi Crocco.

⁶⁰As stated in Wu et al. (2007), q-vortex "is actually the canonical form of an approximate viscous solution suitable to describe a wake vortex far downstream of an aircraft, found by Batchelor in 1964. So the q-vortex is also called the Batchelor vortex."; see also Batchelor (1964). In that specific case "the vorticity has a Gaussian distribution, and hence the q-vortex is one of the family called Gaussian vortices."

⁶¹That formula is a specific form of Eq.(6.19) of Wu et al. (2007), that is initially introduced, for filtering purposes, in Politis (2011a) and further analysed and extended in Politis (2016).

the kernel-smoothing function⁶²

$$m(r; R) = 1 - e^{-(\ln 2) \left(\frac{r}{R}\right)^2}. \quad (2.92)$$

Concerning the filter radius R in the present work a constant (time independent⁶³) value will be adopted following the guidelines suggested in Politis (2016). According to the aforementioned reference proper values of R are 0.5% to 15% of the diameter of the convex hull that of the system of interacting objects. In the present case it is the convex hull of the single foil. Exact selection of the value is case dependent and varies with respect to the complexity of the geometry, unsteadiness and the Reynolds number.

The application of filtering in 2D case, where a 2D vortex (or equivalently a 3D infinite vortex filament) has to be desingularised, is straightforward and is standard in vortex particle methods. The smoothed velocities can be calculated by multiplying the vortex singularity with the kernel-smoothing function m . In the 3D case, of finite length vortex filaments the desingularisation technique is described in Politis (2011a, 2016). The resulting desingularised velocity induction factors can be calculated by the following formula

$$\mathbf{D}_{ij}^{vel}|_m = \begin{cases} m[r(\mathbf{x}_i|\mathbf{x}_2); R] \nabla_2 G_v(\mathbf{x}_i|\mathbf{x}_2; \mathbf{x}) - m[r(\mathbf{x}_i|\mathbf{x}_1); R] \nabla_1 G_v(\mathbf{x}_i|\mathbf{x}_1; \mathbf{x}), & D \subseteq \mathbb{R}^2, \\ -\frac{1}{4\pi} \sum_{k=0}^3 \mathbf{D}_{ijk}^L m(h_{ijk}; R), & D \subseteq \mathbb{R}^3, \end{cases} \quad (2.93)$$

where $\mathbf{D}_{ij}^{vel}|_m$ denotes the desingularised induction factor and h_{ijk} stands for the normal distance from the control point i to the vortex filament k lying at the k^{th} edge of the element j .

2.7 Pressure calculation

In the present section we deal with the calculation of pressure by means of an approximate Bernoulli theorem, including the effect of an unsteady nonuniform background field, that is not irrotational in general. In the context of the adopted approximation, the total flow consists of an irrotational part that corresponds to the disturbance field and a weakly rotational background field. In that case we will begin with Euler equations, that expresses Newton's second law, for the total velocity and pressure fields $\nabla\Phi = \nabla\Phi + \mathbf{V}_G$ and $p_T = p + p_G$, respectively, where p_T and p_G are the disturbance and the background pressure fields, respectively. The Euler

⁶²Professor Politis, that initially introduced that technique for the desingularisation of Biot-Savart velocities in free-wake analysis of lifting surfaces for purposes of marine hydrodynamics, named that function mollifier. Therefore we will denote that filtering function with the letter m , following the nomenclature used in Politis (2016).

⁶³In Politis (2016) a time dependent radius is selected $R = 2\sqrt{\nu t}$, where ν is the kinematic viscosity. This leads to the Oseen-Lamp vortex; see Oseen (1912) and Lamb (1993). As described in Wu et al. (2007), that vortex form is also the zeroth mode of a Laguerre-polynomial based series expansion. That spectral representation is used in order to solve Laguerre equation in which Navier-Stokes equations can be transformed to, under the appropriate assumptions. That process is described thoroughly in the aforementioned reference. The extension of the of present method in order to include age-dependent kernel-smoothing functions, that could also include additional modes of the Laguerre series, or more complex core structure, consisting of many regions (as shown in Fig.8.2 of the aforementioned reference) is straightforward.

equations for the total fields are given bellow

$$\partial_t \nabla \Phi(\mathbf{x}; t) + \frac{1}{2} \nabla [\nabla \Phi(\mathbf{x}; t)]^2 - \mathbf{V}_T(\mathbf{x}; t) \times [\nabla \times \mathbf{V}_T(\mathbf{x}; t)] + \frac{\nabla p_T(\mathbf{x}; t)}{\rho} = 0, \quad \mathbf{x} \in D, \quad (2.94)$$

$$\begin{aligned} \Rightarrow \partial_t (\nabla \Phi + \mathbf{V}_G) + \frac{1}{2} \nabla (\nabla \Phi + \mathbf{V}_G)^2 \\ - (\nabla \Phi + \mathbf{V}_G) \times [\nabla \times (\nabla \Phi + \mathbf{V}_G)] + \frac{\nabla (p + p_G)}{\rho} = 0. \end{aligned} \quad (2.95)$$

In the equation above ρ is the density of the fluid and $\partial_t(\cdot)$ denotes the rate of change with respect to an earth-fixed (inertial) observer (i.e. with regard to an inertial reference frame). The disturbance velocity field is assumed to be irrotational, therefore Eq.(2.95) becomes

$$\begin{aligned} \partial_t (\nabla \Phi + \mathbf{V}_G) + \frac{1}{2} \nabla (\nabla \Phi)^2 + \nabla (\nabla \Phi \cdot \mathbf{V}_G) + \frac{1}{2} \nabla \mathbf{V}_G^2 \\ - \nabla \Phi \times (\nabla \times \mathbf{V}_G) - \mathbf{V}_G \times (\nabla \times \mathbf{V}_G) + \frac{\nabla (p + p_G)}{\rho} = 0. \end{aligned} \quad (2.96)$$

We apply now Euler equations on the background field and we obtain

$$\partial_t \mathbf{V}_G(\mathbf{x}; t) + \frac{1}{2} \nabla \mathbf{V}_G^2(\mathbf{x}; t) - \mathbf{V}_G(\mathbf{x}; t) \times [\nabla \times \mathbf{V}_G(\mathbf{x}; t)] + \frac{\nabla p_G(\mathbf{x}; t)}{\rho} = 0, \quad \mathbf{x} \in D. \quad (2.97)$$

Subtracting now Eq.(2.97) from Eq.(2.96) we produce the following equation Eq.(2.95) becomes

$$\partial_t (\nabla \Phi) + \frac{1}{2} \nabla (\nabla \Phi)^2 + \nabla (\nabla \Phi \cdot \mathbf{V}_G) - \nabla \Phi \times (\nabla \times \mathbf{V}_G) + \frac{\nabla p}{\rho} = 0. \quad (2.98)$$

Furthermore we assume that the rotational term $\nabla \Phi \times (\nabla \times \mathbf{V}_G)$ is of higher order and, in the context of the present weakly rotational approximation, can be neglected, and thus Eq.(2.98) becomes

$$\nabla \left[\partial_t \Phi + \frac{1}{2} (\nabla \Phi)^2 + \nabla \Phi \cdot \mathbf{V}_G + \frac{p}{\rho} \right] = 0, \quad \mathbf{x} \in D. \quad (2.99)$$

Finally, integrating the above equation along a curve in D we obtain

$$\frac{p(\mathbf{x}; t)}{\rho} + \partial_t \Phi(\mathbf{x}; t) + \frac{1}{2} [\nabla \Phi(\mathbf{x}; t)]^2 + \mathbf{V}_G(\mathbf{x}; t) \nabla \Phi(\mathbf{x}; t) = C(t), \quad (2.100)$$

where the \mathbf{x} -integration constant $C(t)$ is time dependent. However $C(t)$ can be set to zero by redefining the potential as follows

$$\Phi(\mathbf{x}; t) = \Phi_1(\mathbf{x}; t) + \int^t C(\tau) d\tau, \quad (2.101)$$

thus Eq.(2.100) becomes

$$\frac{p(\mathbf{x};t)}{\rho} + \partial_t \Phi_1(\mathbf{x};t) + \frac{1}{2} [\nabla \Phi_1(\mathbf{x};t)]^2 + \mathbf{V}_G(\mathbf{x};t) \nabla \Phi_1(\mathbf{x};t) = C(t), \quad (2.102)$$

To sum up, we have obtained a formula for the calculation of disturbance pressure that is written, after dropping the index 1, in the following form

$$\frac{p(\mathbf{x};t)}{\rho} + \partial_t \Phi(\mathbf{x};t) + \frac{1}{2} [\nabla \Phi(\mathbf{x};t)]^2 + \mathbf{V}_G(\mathbf{x};t) \nabla \Phi(\mathbf{x};t) = 0, \quad \mathbf{x} \in D. \quad (2.103)$$

where p is the disturbance pressure field, ρ is the density of the fluid and $\partial_t(\cdot)$ denotes the rate of change with respect to an earth-fixed (inertial) observer (i.e. with regard to an inertial reference frame).

The time derivative of the potential with respect to the moving, with the body velocity, frame of reference can be calculated by the following formula

$$d_t \Phi(\mathbf{x};t) = \nabla \Phi(\mathbf{x};t) \cdot \mathbf{V}_B(\mathbf{x};t) + \partial_t \Phi(\mathbf{x};t), \quad \mathbf{x} \in \partial D_B(t). \quad (2.104)$$

More details concerning the derivation of the above formula can be found e.g. in the following references Katz and Plotkin (2001), Politis (2004), Politis (2011b), Filippas (2013). By replacing Eq.(2.104) into Eq.(2.103), we obtain a formula for pressure calculation on body boundary, as follows

$$\frac{p(\mathbf{x};t)}{\rho} = -d_t \Phi(\mathbf{x};t) + \nabla \Phi(\mathbf{x};t) \cdot [\mathbf{V}_B(\mathbf{x};t) - \mathbf{V}_G(\mathbf{x};t)] - \frac{1}{2} [\nabla \Phi(\mathbf{x};t)]^2, \quad \mathbf{x} \in \partial D_B(t). \quad (2.105)$$

Moreover, the trace on the body boundary of the space gradient of the potential can be decomposed to its tangential and the vertical components according to Eq.(2.67) and the body boundary condition (Eq.2.4), as follows⁶⁴

$$\begin{aligned} \nabla \Phi(\mathbf{x};t) &= \partial_s \Phi(\mathbf{x};t) \times \mathbf{n}(\mathbf{x};t) + \partial_n \Phi(\mathbf{x};t) \cdot \mathbf{n}(\mathbf{x};t) \\ &= \mathbf{V}_t(\mathbf{x};t) + \{[\mathbf{V}_B(\mathbf{x};t) - \mathbf{V}_G(\mathbf{x};t)] \cdot \mathbf{n}(\mathbf{x};t)\} \cdot \mathbf{n}(\mathbf{x};t) \\ &= \mathbf{V}_t(\mathbf{x};t) + b(\mathbf{x};t) \mathbf{n}(\mathbf{x};t), \quad \mathbf{x} \in \partial D_B(t). \end{aligned} \quad (2.106)$$

Therefore, Eq.(2.105), after some algebra, becomes

$$\begin{aligned} \frac{p(\mathbf{x};t)}{\rho} &= -d_t \Phi(\mathbf{x};t) + \mathbf{V}_t(\mathbf{x};t) \cdot [\mathbf{V}_B(\mathbf{x};t) - \mathbf{V}_G(\mathbf{x};t)] \\ &\quad - \frac{1}{2} [\mathbf{V}_t(\mathbf{x};t)]^2 + \frac{1}{2} b^2(\mathbf{x};t), \quad \mathbf{x} \in \partial D_B(t). \end{aligned} \quad (2.107)$$

The above form of approximate Bernoulli's equation is utilised for pressure calculations on the body boundary. Then the boundary pressure can be integrated to obtain generalised forces (forces and moments) and by exploiting also the local generalised velocity (linear and angular), the power of the studied hydromechanical systems can be obtained, leading to the estimation of appropriate metrics of the efficiency or the performance (power take-off).

⁶⁴In the present paragraph the tangential velocity is convenient to be denoted as $\mathbf{V}_t = \partial_s \Phi \times \mathbf{n}$.

2.8 Pressure-type Kutta condition

The classical Pressure-type Kutta condition can be produced from the dynamic boundary condition on the wake by demanding that the pressure field (and therefore the pressure jump) ought to be continuous in \overline{D} . Recall, the dynamic boundary condition (Eq.2.7) on the wake ∂D_W

$$p_W^u(\mathbf{x};t) = p_W^l(\mathbf{x};t), \quad \mathbf{x} \in \partial D_W. \quad (2.108)$$

The above equation necessitates that the surface of potential and tangential velocity discontinuity, that represents the vortex wake, cannot carry loading and thus the pressure at the both sides of it should be the same. We assume that the pressure jump must be continuous while moving from the trailing vortex sheet to the body and therefore it must be zero at the trailing edge, i.e. at $\partial D_B \cap \partial D_W$. The pressure fields at the upper and the lower side of the trailing edge, approaching from the lifting body, are given by the following formulas

$$p_B^u(\mathbf{x}_{TE};t) = \lim_{\xi \rightarrow \xi_{TE}} p_B^u[\mathbf{x}_B(\xi, \eta);t], \quad \mathbf{x}_B \in \partial D_B(t) \text{ and } \mathbf{x}_{TE} \in \partial D_B(t) \cup \partial D_W(t), \quad (2.109)$$

$$p_B^l(\mathbf{x}_{TE};t) = \lim_{\xi \rightarrow \xi_{TE}} p_B^l[\mathbf{x}_B(\xi, \eta);t], \quad \mathbf{x}_B \in \partial D_B(t) \text{ and } \mathbf{x}_{TE} \in \partial D_B(t) \cup \partial D_W(t). \quad (2.110)$$

Moreover, the pressure fields at the upper and the lower side of the trailing edge, approaching from the wake, are the same according to Eq.(2.108) and are given by the following formulas

$$p_W(\mathbf{x}_{TE};t) = p_W^u(\mathbf{x}_{TE};t) = \lim_{\xi \rightarrow \xi_{TE}} p_W^u[\mathbf{x}_W(\xi, \eta);t], \quad \mathbf{x}_W \in \partial D_W(t) \text{ and } \mathbf{x}_{TE} \in \partial D_B(t) \cup \partial D_W(t), \quad (2.111)$$

$$p_W(\mathbf{x}_{TE};t) = p_W^l(\mathbf{x}_{TE};t) = \lim_{\xi \rightarrow \xi_{TE}} p_W^l[\mathbf{x}_W(\xi, \eta);t], \quad \mathbf{x}_W \in \partial D_W(t) \text{ and } \mathbf{x}_{TE} \in \partial D_B(t) \cup \partial D_W(t). \quad (2.112)$$

Assuming continuity of the pressure field and taking into account Eqs.(2.108-2.112) we obtain the pressure-type Kutta condition

$$\lim_{\xi \rightarrow \xi_{TE}} \left\{ p_B^u[\mathbf{x}_B(\xi, \eta);t] - p_B^l[\mathbf{x}_B(\xi, \eta);t] \right\} = 0, \quad \mathbf{x}_B \in \partial D_B(t) \text{ and } \mathbf{x}_{TE} \in \partial D_B(t) \cup \partial D_W(t), \quad (2.113)$$

2.8.1 Analytical form

To proceed, we recall an appropriate form of the approximate Bernoulli's theorem, Eq.(2.103), derived in Sec.2.7

$$\frac{p(\mathbf{x};t)}{\rho} = -\partial_t \Phi(\mathbf{x};t) - \frac{1}{2} [\nabla \Phi(\mathbf{x};t)]^2 - \mathbf{V}_G(\mathbf{x};t) \nabla \Phi(\mathbf{x};t), \quad \mathbf{x} \in D. \quad (2.114)$$

By rearranging terms, making common factor $-1/2$ and adding and subtracting the quantity $-1/2\mathbf{V}_G^2$, factorising and using the binomial theorem for the sum of squares, we obtain the following formula

$$\frac{p(\mathbf{x};t)}{\rho} = -\partial_t\Phi(\mathbf{x};t) - \frac{1}{2} [\nabla\Phi(\mathbf{x};t) + \mathbf{V}_G(\mathbf{x};t)]^2 - \frac{1}{2}\mathbf{V}_G^2(\mathbf{x};t), \quad \mathbf{x} \in D. \quad (2.115)$$

Moreover, we apply the above form of approximate Bernoulli's theorem to the upper and lower side of the trailing edge, we use pressure-type Kutta condition (Eq.2.113) and we factorise the difference of squares to construct the following form of the condition

$$\lim_{\xi \rightarrow \xi_{TE}} F^{PK}[\mathbf{x}_B(\xi, \eta); t] = 0, \quad \mathbf{x}_B \in \partial D_B \text{ and } \mathbf{x}_{TE} \in \partial D_B \cup \partial D_W, \quad (2.116)$$

where the operator $F^{PK}(\cdot)$ is defined as follows

$$F^{PK}[\mathbf{x}_B(\xi, \eta); t] = \left\{ \partial_t(\Phi^u - \Phi^l) + \left[0.5(\nabla\Phi^u + \nabla\Phi^l) + 0.5(\mathbf{V}_G^u + \mathbf{V}_G^l) \right] \cdot (\nabla\Phi^u - \nabla\Phi^l + \mathbf{V}_G^u - \mathbf{V}_G^l) - 0.5 \left[(\mathbf{V}_G^u)^2 - (\mathbf{V}_G^l)^2 \right] \right\}. \quad (2.117)$$

The above form of pressure-type Kutta condition written with respect to the inertial reference frame, is appropriate for the modeling of lifting flows in a weakly rotational background field, and has already been used in the mathematical formulation of the problem in Sec.2.2, Eqs.(2.12&2.13). For the calculation of pressure from the boundary values of the potential, that is the primary unknown is the present direct formulation, the reformulation of the above relation with respect to the moving reference frame is required. Aiming to the construction of the aforementioned formula we begin with Eq.(2.105), that is rewritten bellow

$$\frac{p(\mathbf{x};t)}{\rho} = -d_t\Phi(\mathbf{x};t) + \nabla\Phi(\mathbf{x};t) \cdot [\mathbf{V}_B(\mathbf{x};t) - \mathbf{V}_G(\mathbf{x};t)] - \frac{1}{2} [\nabla\Phi(\mathbf{x};t)]^2, \quad \mathbf{x} \in \partial D_B(t). \quad (2.118)$$

By rearranging terms, making common factor $-1/2$ and adding and subtracting the quantity $-1/2 [\mathbf{V}_B(\mathbf{x};t) - \mathbf{V}_G(\mathbf{x};t)]^2$, we obtain the following formula

$$\frac{p}{\rho} = -d_t\Phi - \frac{1}{2} \left[(\nabla\Phi)^2 - 2\nabla\Phi \cdot (\mathbf{V}_B - \mathbf{V}_G) + (\mathbf{V}_B - \mathbf{V}_G)^2 - (\mathbf{V}_B - \mathbf{V}_G)^2 \right]. \quad (2.119)$$

Moreover, we factorise the difference of squares to construct the following form

$$\frac{p}{\rho} = -d_t\Phi - \frac{1}{2} (\nabla\Phi + \mathbf{V}_G - \mathbf{V}_B)^2 + \frac{1}{2} (\mathbf{V}_G - \mathbf{V}_B)^2. \quad (2.120)$$

The last relation, in which $\nabla\Phi + \mathbf{V}_G - \mathbf{V}_B$ is the total fluid velocity and $\mathbf{V}_G - \mathbf{V}_B$ is the background field velocity relative to an observer build that follows foil's motions, is the approximate form of Bernoulli's theorem with respect to the Body fixed reference frame. To proceed further, we apply the above form of approximate Bernoulli's theorem to the upper and lower

side of the trailing edge, we use pressure-type Kutta condition (Eq.2.113) to construct the following form of the operator $F^{PK}(\cdot)$

$$\begin{aligned} F^{PK}[\mathbf{x}_B(\xi, \eta); t] &= d_t(\Phi^u - \Phi^l) + \frac{1}{2}(\nabla\Phi^u + \mathbf{V}_G^u - \mathbf{V}_B^u)^2 - \frac{1}{2}(\nabla\Phi^l + \mathbf{V}_G^l - \mathbf{V}_B^l)^2 \\ &\quad + \frac{1}{2}(\mathbf{V}_G^l - \mathbf{V}_B^l)^2 - \frac{1}{2}(\mathbf{V}_G^u - \mathbf{V}_B^u)^2. \end{aligned} \quad (2.121)$$

Moreover, the limiting value on the body boundary of the space gradient of the potential can be decomposed to its tangential and the vertical components according to Eq.(2.67) and the body boundary condition (Eq.2.4), as follows

$$\begin{aligned} \nabla\Phi(\mathbf{x}; t) &= \partial_s\Phi(\mathbf{x}; t) \times \mathbf{n}(\mathbf{x}; t) + \partial_n\Phi(\mathbf{x}; t) \cdot \mathbf{n}(\mathbf{x}; t) \\ &= \mathbf{V}_t(\mathbf{x}; t) + \{[\mathbf{V}_B(\mathbf{x}; t) - \mathbf{V}_G(\mathbf{x}; t)] \cdot \mathbf{n}(\mathbf{x}; t)\} \cdot \mathbf{n}(\mathbf{x}; t) \\ &= \mathbf{V}_t(\mathbf{x}; t) + b(\mathbf{x}; t)\mathbf{n}(\mathbf{x}; t), \quad \mathbf{x} \in \partial D_B(t). \end{aligned} \quad (2.122)$$

With the aid of Eq.(2.122), the operator $F^{PK}(\cdot)$ becomes

$$\begin{aligned} F^{PK}[\mathbf{x}_B(\xi, \eta); t] &= d_t(\Phi^u - \Phi^l) + \frac{1}{2}(\mathbf{V}_t^u + b^u\mathbf{n}^u + \mathbf{V}_G^u - \mathbf{V}_B^u)^2 - \frac{1}{2}(\mathbf{V}_t^l + b^l\mathbf{n}^l + \mathbf{V}_G^l - \mathbf{V}_B^l)^2 \\ &\quad + \frac{1}{2}(\mathbf{V}_G^l - \mathbf{V}_B^l)^2 - \frac{1}{2}(\mathbf{V}_G^u - \mathbf{V}_B^u)^2. \end{aligned} \quad (2.123)$$

Moreover, by factorising the difference of the squares and rearranging terms, we obtain the following form of pressure-type Kutta condition

$$\lim_{\xi \rightarrow \xi_{TE}} F^{PK}[\mathbf{x}_B(\xi, \eta); t] = 0, \quad \mathbf{x}_B \in \partial D_B \text{ and } \mathbf{x}_{TE} \in \partial D_B \cup \partial D_W, \quad (2.124)$$

where

$$\begin{aligned} F^{PK}[\mathbf{x}_B(\xi, \eta); t] &= d_t(\Phi^u - \Phi^l) + \left(\frac{\mathbf{V}_t^u + \mathbf{V}_t^l}{2} + \frac{b^u\mathbf{n}^u + b^l\mathbf{n}^l}{2} + \frac{\mathbf{V}_G^u + \mathbf{V}_G^l}{2} - \frac{\mathbf{V}_B^u + \mathbf{V}_B^l}{2} \right) \\ &\quad \left[\mathbf{V}_t^u - \mathbf{V}_t^l + b^u\mathbf{n}^u - b^l\mathbf{n}^l + \mathbf{V}_G^u - \mathbf{V}_G^l - (\mathbf{V}_B^u - \mathbf{V}_B^l) \right] \\ &\quad - \left(\frac{\mathbf{V}_G^u + \mathbf{V}_G^l}{2} - \frac{\mathbf{V}_B^u + \mathbf{V}_B^l}{2} \right) \left[\mathbf{V}_G^u - \mathbf{V}_G^l - (\mathbf{V}_B^u - \mathbf{V}_B^l) \right]. \end{aligned} \quad (2.125)$$

The above relation⁶⁵ is the pressure-type Kutta condition with respect to the body fixed reference frame. That equation includes a quadratic nonlinear form of the unknown boundary value of the tangential velocity \mathbf{V}_t and linear terms. It also includes the unknown boundary value of the potential Φ at the body contour as approaching the trailing edge. As will be demonstrated in the following section the continuous boundary field \mathbf{V}_t is approximated by

⁶⁵The terms in the Eq.(2.125) are mean values and differences of the upper and lower side traces on the body boundary. Some of those fields are continuous at the trailing edge, however when discretisation is applied and a BEM is exploited for calculations, the vicinity of the trailing edge is modeled by neighboring to the trailing edge panels. In that case, the upper and lower elements are not identical and the same applies to the boundary field values. Therefore, it is important for the accurate and stable imposition of Kutta condition, those mean values and differences to be considered in the calculations.

a discrete tangential velocity field that is projected to a curvilinear coordinated system (see also Sec.2.5.2.1). Moreover, it is approximated by CUFDM (see also Sec.2.5.2.2) and replaced with linear combinations of Φ . Then the DtN (Sec.2.4) will be exploited to replace all the unknowns by linear functions of the dynamic variable of the problem that will be the potential jump (dipole intensity) at the Kutta strip.

2.8.2 Discretised form - The dynamical system

We apply discretisation with BEM and collocation as described in detail in Secs.2.4 & 2.5.2.2. We consider the collection of discretised data that are families of scalars or vectors. They are ordered following span-major numbering. In this way, ordered lists (systems) are created, that represent the collocation points (containing vectors of \mathbb{R}^3), the discretised potential field (containing real numbers), the discretised tangential velocity field (containing vectors of \mathbb{R}^3) or the covariant components of the tangential velocity (containing real numbers). The systems that are arranged span-majorly will be denoted using $|_2$. To proceed, the pressure-type Kutta condition is applied at the body-collocation points at the upper and lower side of the trailing edge⁶⁶ and the corresponding operator is discretised as follows $\mathbf{F}^{PK}|_2 = \{F_i^{PK}\}$, with $i \in \{0, 1, \dots, N_{PK} - 1\}$, where N_{PK} is the total number of collocation points that Kutta condition is applied. Therefore, we have the aforementioned collocation points $\mathbf{x}_0|_2 = \{\mathbf{x}_{0i}\}$, the potential $\Phi|_2 = \{\Phi_i\}$, the tangential velocity $\mathbf{V}_t|_2 = \{\mathbf{V}_{ti}\}$, the first component (chordwise) of the covariant derivative of the potential $\mathbf{V}_{t1}|_2 = \{V_{t1i}\}$, the second component (spanwise) of the covariant derivative of the potential $\mathbf{V}_{t2}|_2 = \{V_{t2i}\}$. Moreover, the known-Neumann-data-times-the-normal-vector discretised vector field is $\mathbf{N}|_2 = \{b_i \mathbf{n}_i\}$ the background-field velocity $\mathbf{V}_G|_2 = \{\mathbf{V}_{Gi}\}$ and the body velocity $\mathbf{V}_B|_2 = \{\mathbf{V}_{Bi}\}$.

The discretised form of pressure-type Kutta condition is as follows

$$\mathbf{F}^{PK}(\mathbf{x}_0|_2; t)|_2 = 0, \quad \mathbf{x}_0|_2 \in \partial D_B(t), \quad (2.126)$$

where

$$\begin{aligned} \mathbf{F}^{PK}(\mathbf{x}_0|_2; t)|_2 &= d_t(\Phi^u|_2 - \Phi^l|_2) \\ &+ \left(\frac{\mathbf{V}_t^u|_2 + \mathbf{V}_t^l|_2}{2} + \frac{\mathbf{N}^u|_2 + \mathbf{N}^l|_2}{2} + \frac{\mathbf{V}_G^u|_2 + \mathbf{V}_G^l|_2}{2} - \frac{\mathbf{V}_B^u|_2 + \mathbf{V}_B^l|_2}{2} \right) \\ &\left[\mathbf{V}_t^u|_2 - \mathbf{V}_t^l|_2 + \mathbf{N}^u|_2 - \mathbf{N}^l|_2 + \mathbf{V}_G^u|_2 - \mathbf{V}_G^l|_2 - \left(\mathbf{V}_B^u|_2 - \mathbf{V}_B^l|_2 \right) \right] \\ &- \left(\frac{\mathbf{V}_G^u|_2 + \mathbf{V}_G^l|_2}{2} - \frac{\mathbf{V}_B^u|_2 + \mathbf{V}_B^l|_2}{2} \right) \left[\mathbf{V}_G^u|_2 - \mathbf{V}_G^l|_2 - \left(\mathbf{V}_B^u|_2 - \mathbf{V}_B^l|_2 \right) \right]. \end{aligned} \quad (2.127)$$

The discretised tangential velocity vector field \mathbf{V}_t is expanded with respect to a curvilinear coordinate system and its covariant base, using the velocity contravariant components (see

⁶⁶A single numbering is used for both the upper and the lower collocation points; i.e. the collection $i \in \{0, 1, \dots, N_{PK} - 1\}$ is mapped to the upper side data denoted with upper index u and to the lower side data denoted with l .

Sec.2.5.2.1), as follows

$$\mathbf{V}_t|_2 = (\mathbf{V}_{tj})^j|_2 \cdot \mathbf{e}_j|_2, \quad j \in \{1, 2\}. \quad (2.128)$$

where \mathbf{e}_j are the systems of vectors that represents the base vectors discretised vector fields $\mathbf{e}_j|_2 = \{\mathbf{e}_{ji}\}, j \in \{1, 2\}, i \in \{0, 1, \dots, N_{PK} - 1\}$ and the dot product is between systems of vectors.

The contravariant components of the velocity can be calculated when the covariant components are known as follows

$$(\mathbf{V}_{tj})^j|_2 = \mathbf{g}^{jk}|_2 (\mathbf{V}_{tk})_k|_2, \quad j, k \in \{1, 2\}. \quad (2.129)$$

where \mathbf{g}^{jk} is a system that contains the contravariant components of the metric tensor at the collocation points; i.e. $\mathbf{g}^{jk}|_2 = \{g_i^{jk}\}, j, k \in \{1, 2\}, i \in \{0, 1, \dots, N_{PK} - 1\}$.

By applying CUFD we can approximate the covariant component of the tangential velocities by the neighboring potential values (see Sec.2.5.2.2) as follows

$$(\mathbf{V}_{t1})_1|_2 = [\mathcal{D}(\mathbf{x}_0|_1) \cdot \Phi|_1]^\top = \left[\mathcal{D}(\mathbf{x}_0|_1) \cdot (\Phi|_2)^\top \right]^\top. \quad (2.130)$$

$$(\mathbf{V}_{t2})_2|_2 = \mathcal{D}(\mathbf{x}_0|_2) \cdot \Phi|_2. \quad (2.131)$$

The above detailed analysis enlightens the fact that the discretised boundary value of the tangential velocity \mathbf{V}_t can be expressed as a function of the discretised boundary value of the potential Φ in the context of our approximation; i.e. $\mathbf{V}_t = \mathcal{V}_{CUFDM}(\Phi)$.

At the final stage the discretised pressure-type Kutta condition (Eqs.2.126&2.127) will be exploited for the construction of the dynamical-system equations in the form $d_t \mathbf{U} = \mathbf{f}(\mathbf{U})$, where the system-derivative \mathbf{f} is a function of the dynamic variable $\mathbf{U} = \mu_K$. In order to obtain that form of Kutta condition we recall the discretised DtN operator constructed in Sec.2.4, Eq.(2.29)

$$\Phi(t) = \mathcal{G} \cdot \mathbf{b}(t) + \mathcal{Z} \cdot \mu_K(t) + \mathcal{P}(t) \cdot \mu_W \quad (2.132)$$

In the above linear relation the only unknown discretised fields are represented by the systems of Dirichlet data on the body and the Kutta strip; i.e. the potential Φ and the potential jump μ_K . The Neumann data on the body \mathbf{b} and are known from the prescribed kinematics and the Dirichlet data on the wake μ_W have been determined from the time history of the system evolution. Therefore, the discretised pressure-type Kutta condition (Eqs.2.126&2.127) together with the discretised DtN operator Eq.(2.132) are a system of (spatially and temporarily) nonlocal differential equations, with explicit and implicit nonlinearities and a linear algebraic constraint.

In the sequel, the algebraic constraint is used in order to express the system-derivative \mathbf{f} as a function of the dynamic variable $\mathbf{U} = \mu_K$. First of all, the discretised potential field with the aid of Eq.(2.132) becomes a function of μ_K ; i.e. $\Phi = \mathcal{DTN}(\mu_K)$. In this way the discretised trace tangential velocity can be expressed as a function of μ_K ; i.e. $\mathbf{V}_t = \mathcal{V}_{DTN}(\mu_K)$. Therefore, the pressure-Kutta operator is also a function of the unknown μ_K (and other known quantities);

i.e. $F^{PK} = \mathcal{F}^{PK}(\boldsymbol{\mu}_K)$. The pressure-type Kutta condition becomes

$$\begin{aligned}
d_t \left[\mathcal{DTN}^u(\boldsymbol{\mu}_K) - \mathcal{DTN}^l(\boldsymbol{\mu}_K) \right] = & \\
& - \left[\frac{\mathcal{V}_{DTN}^u(\boldsymbol{\mu}_K) + \mathcal{V}_{DTN}^l(\boldsymbol{\mu}_K)}{2} + \frac{\mathbf{N}^u + \mathbf{N}^l}{2} + \frac{\mathbf{V}_G^u + \mathbf{V}_G^l}{2} - \frac{\mathbf{V}_B^u + \mathbf{V}_B^l}{2} \right] \\
& \left[\mathcal{V}_{DTN}^u(\boldsymbol{\mu}_K) - \mathcal{V}_{DTN}^l(\boldsymbol{\mu}_K) + \mathbf{N}^u - \mathbf{N}^l + \mathbf{V}_G^u - \mathbf{V}_G^l - (\mathbf{V}_B^u - \mathbf{V}_B^l) \right] \\
& + \left(\frac{\mathbf{V}_G^u + \mathbf{V}_G^l}{2} - \frac{\mathbf{V}_B^u + \mathbf{V}_B^l}{2} \right) \left[\mathbf{V}_G^u - \mathbf{V}_G^l - (\mathbf{V}_B^u - \mathbf{V}_B^l) \right]. \tag{2.133}
\end{aligned}$$

In the equation above, the upper indices u and l refer to the discretised tangential velocity and potential at the upper and lower sides the discretised boundary, respectively. To be more specific to the corresponding values of the discretised fields at the collocation points located at the centroids of the boundary elements that represent the upper and lower sides of the body at the vicinity of the trailing edge. Those values are global functions of the total discretised field of the potential jump at the Kutta-strip $\boldsymbol{\mu}_K$ and that relation is expressed by the global DtN operator (second term at the right hand side of Eq.2.132). For example the velocity and the potential at the left tip of the foil, depends on the intensity of the dipoles that are distributed at Kutta-strip in the vicinity of the right tip. Moreover, it is a function of the total Neumann data on the body (first term at the right hand side of Eq.2.132) and the time history of the total Dirichlet data that are stored as dipoles in the wake (third term at the right hand side of Eq.2.132). In this way the spatial and temporal nonlocal character of the problem, that is preserved through discretisation via BEM, is illustrated.

To proceed further, it is necessary to perform some operations to the time derivative of the DtN operator appeared at the left hand side of Eq.(2.133).

$$\begin{aligned}
d_t \left[\mathcal{DTN}^u(\boldsymbol{\mu}_K) - \mathcal{DTN}^l(\boldsymbol{\mu}_K) \right] = & \\
= d_t[\mathcal{G}^u - \mathcal{G}^l] \cdot \mathbf{b}(t) + [\mathcal{Z}^u - \mathcal{Z}^l] \cdot \boldsymbol{\mu}_K(t) + [\mathcal{P}^u(t) - \mathcal{P}^l(t)] \cdot \boldsymbol{\mu}_W. & \tag{2.134}
\end{aligned}$$

We define the following matrices $\mathcal{G}^{u \setminus l} = [\mathcal{G}^u - \mathcal{G}^l]$, $\mathcal{Z}^{u \setminus l} = [\mathcal{Z}^u - \mathcal{Z}^l]$, $\mathcal{P}^{u \setminus l} = [\mathcal{P}^u - \mathcal{P}^l]$ as differences of matrices with one dimension that equals the number of Kutta-strip collocation points N_{PK} and the other defined by the number of the panels (on body, Kutta-strip and wake, respectively) that induce potential at the collocation points. By adopting that notation and using the Leibniz rule for differentiation we obtain the following relation

$$\begin{aligned}
d_t \left[\mathcal{DTN}^u(\boldsymbol{\mu}_K) - \mathcal{DTN}^l(\boldsymbol{\mu}_K) \right] = & \\
= d_t[\mathcal{G}^{u \setminus l}] \cdot \mathbf{b}(t) + \mathcal{P}^{u \setminus l}(t) \cdot \boldsymbol{\mu}_W + d_t[\mathcal{Z}^{u \setminus l}] \cdot \boldsymbol{\mu}_K(t) + \mathcal{Z}^{u \setminus l} \cdot d_t[\boldsymbol{\mu}_K(t)]. & \tag{2.135}
\end{aligned}$$

By replacing Eq.(2.135) into Eq.(2.133) and multiplying both sides with the inverse of $\mathcal{Z}^{u\setminus l}$, we obtain the final form of the discretised pressure-type Kutta condition

$$\begin{aligned}
d_t[\boldsymbol{\mu}_K(t)] = & (\mathcal{Z}^{u\setminus l})^{-1} \cdot \{ -d_t[\mathcal{G}^{u\setminus l} \cdot \mathbf{b}(t) + \mathcal{P}^{u\setminus l}(t) \cdot \boldsymbol{\mu}_W] - d_t[\mathcal{Z}^{u\setminus l}] \cdot \boldsymbol{\mu}_K(t) + \\
& - \left[\frac{\mathcal{V}_{DTN}^u(\boldsymbol{\mu}_K) + \mathcal{V}_{DTN}^l(\boldsymbol{\mu}_K)}{2} + \frac{\mathbf{N}^u + \mathbf{N}^l}{2} + \frac{\mathbf{V}_G^u + \mathbf{V}_G^l}{2} - \frac{\mathbf{V}_B^u + \mathbf{V}_B^l}{2} \right] \\
& \left[\mathcal{V}_{DTN}^u(\boldsymbol{\mu}_K) - \mathcal{V}_{DTN}^l(\boldsymbol{\mu}_K) + \mathbf{N}^u - \mathbf{N}^l + \mathbf{V}_G^u - \mathbf{V}_G^l - (\mathbf{V}_B^u - \mathbf{V}_B^l) \right] \\
& + \left(\frac{\mathbf{V}_G^u + \mathbf{V}_G^l}{2} - \frac{\mathbf{V}_B^u + \mathbf{V}_B^l}{2} \right) \left[\mathbf{V}_G^u - \mathbf{V}_G^l - (\mathbf{V}_B^u - \mathbf{V}_B^l) \right] \}. \tag{2.136}
\end{aligned}$$

We have finally obtained a system of (spatially and temporarily) nonlocal differential equations, with explicit and implicit nonlinearities, with unknown the dynamic variable $\boldsymbol{\mu}_K$ that approximately describe the dynamics of the system

$$d_t \mathbf{U} = \mathbf{f}(\mathbf{U}), \quad \text{where } \mathbf{U} = \boldsymbol{\mu}_K, \tag{2.137}$$

and

$$\begin{aligned}
\mathbf{f}(\mathbf{U}) = & (\mathcal{Z}^{u\setminus l})^{-1} \cdot \{ -d_t[\mathcal{G}^{u\setminus l} \cdot \mathbf{b}(t) + \mathcal{P}^{u\setminus l}(t) \cdot \boldsymbol{\mu}_W] - d_t[\mathcal{Z}^{u\setminus l}] \cdot \mathbf{U} + \\
& - \left[\frac{\mathcal{V}_{DTN}^u(\mathbf{U}) + \mathcal{V}_{DTN}^l(\mathbf{U})}{2} + \frac{\mathbf{N}^u + \mathbf{N}^l}{2} + \frac{\mathbf{V}_G^u + \mathbf{V}_G^l}{2} - \frac{\mathbf{V}_B^u + \mathbf{V}_B^l}{2} \right] \\
& \left[\mathcal{V}_{DTN}^u(\mathbf{U}) - \mathcal{V}_{DTN}^l(\mathbf{U}) + \mathbf{N}^u - \mathbf{N}^l + \mathbf{V}_G^u - \mathbf{V}_G^l - (\mathbf{V}_B^u - \mathbf{V}_B^l) \right] \\
& + \left(\frac{\mathbf{V}_G^u + \mathbf{V}_G^l}{2} - \frac{\mathbf{V}_B^u + \mathbf{V}_B^l}{2} \right) \left[\mathbf{V}_G^u - \mathbf{V}_G^l - (\mathbf{V}_B^u - \mathbf{V}_B^l) \right] \}. \tag{2.138}
\end{aligned}$$

Eqs.(2.137&2.138) can be numerically integrated in order to calculate evolution of the dynamic variable $\boldsymbol{\mu}_K$, based on information concerning the function $\boldsymbol{\mu}_K$ at previous time steps, in conjunction with the history of the wake dipole intensity $\boldsymbol{\mu}_W$, and the Neumann data $\mathbf{N}|_2 = \{b_i \mathbf{n}_i\}$, known at every time step from unsteady background field and the body motion as described by the body boundary condition Eq.(2.4). Subsequently, the discretised DtN map Eq.(2.132) is used to calculate the remaining unknown discretised Dirichlet boundary field values Φ as follows

$$\Phi(t)|_1 = \mathcal{G} \cdot \mathbf{b}(t)|_1 + \mathcal{Z} \cdot \boldsymbol{\mu}_K(t)|_2 + \mathcal{P}(t) \cdot \boldsymbol{\mu}_W|_2. \tag{2.139}$$

2.9 Time integration of the system

Starting from a prescribed initial condition, e.g. from rest, a time-stepping method is applied to obtain the numerical solution. After evaluation of different explicit time-integration schemes, we found that the higher-order Adams-Bashforth-Moulton predictor-corrector method provides the required accuracy, stability and efficiency. The used scheme requires calculation of only two derivative equations at each time, and the error is of order (Δt^5) , where Δt is the

timestep, ensuring that good convergence is achieved. To be more precise, if we know $\mathbf{U}(t)$ at time t , we have at the corrector step

$$\mathbf{U}(t + \Delta t) = \mathbf{U}(t) + \frac{\Delta t}{24} [9\mathbf{f}_{pre}(t + \Delta t) + 19\mathbf{f}(t) - 5\mathbf{f}(t - \Delta t) + \mathbf{f}(t - 2\Delta t)]. \quad (2.140)$$

with predictor

$$\mathbf{f}_{pre}(t + \Delta t) = \mathbf{f}_{t+\Delta t} [\mathbf{U}_{pre}(t + \Delta t)]. \quad (2.141)$$

and

$$\mathbf{U}_{pre}(t + \Delta t) = \mathbf{U}(t) + \frac{\Delta t}{24} [55\mathbf{f}(t) - 59\mathbf{f}(t - \Delta t) + 37\mathbf{f}(t - 2\Delta t) - 9\mathbf{f}(t - 3\Delta t)]. \quad (2.142)$$

2.10 Numerical results and discussion

2.10.1 Stability and convergence

We begin with a discussion about the stability and convergence of the present scheme. Extensive numerical investigation has been performed for cases of flapping motion in great submergence and near the free surface, as well as in cases of operation in waves. In all cases numerical stability is achieved when a condition of CFL-type is satisfied, as follows

$$\frac{C\Delta t}{\Delta x} \leq \delta = O(1). \quad (2.143)$$

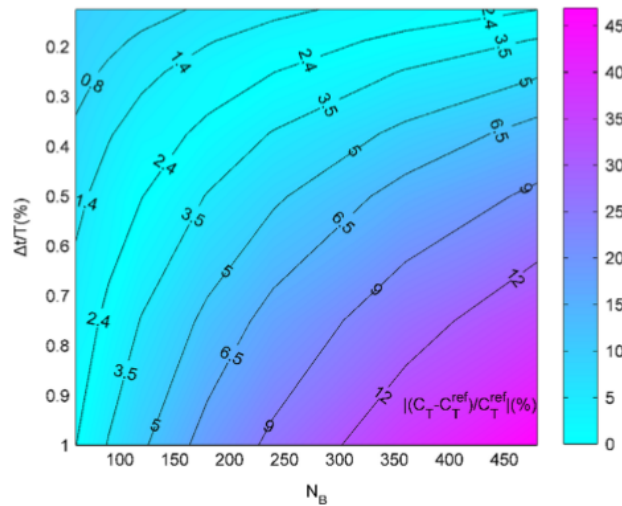


Figure 2.8: Convergence of thrust coefficient C_T as a function of the number of body panels N_B and the time-step $\Delta t/T(\%)$, for a NACA0012 hydrofoil in flapping motion. The error of thrust coefficient (%) is shown using colorscale. Contour lines indicate the ratio $\Delta s_W/\Delta s_B$ of the length of panels in the vicinity of the trailing edge.

where C is in general the celerity of the generated waves on the free-surface and in the present unbounded domain case is the foil velocity ($C = U$) that corresponds to an equivalent vorticity wave on the wake; see linear unsteady hydrofoil theory Filippas (2013) or Newman (1977). Concerning the convergence characteristics of the numerical scheme it is found that there exists an optimum relation between the size Δs_B of the neighboring to the trailing edge panels of the body and those that represent the nearby wake Δs_W ⁶⁷.

As an example, we present in Fig.2.8 a color plot of the error $\left| (C_T - C_T^{ref}) / C_T^{ref} \right|$ associated with the thrust coefficient $C_T = -F_x / \rho U^2 h_0$, as a function of the number of panels on the body N_B and the time-step expressed as a portion of the period $\Delta t / T(\%)$, in the case of flapping NACA0012 hydrofoil in unbounded domain. In this case, the Strouhal number is $St = \omega h_0 / \pi U = 0.4$, the vertical (heaving) amplitude $h_0 / c = 1$ and the rotational (pitching) amplitude $\theta_0 = 45^\circ$.

The thrust coefficient error is calculated with respect to the value C_T^{ref} as obtained by the present method, based on the finest discretization in both space and time ($N_B = 500, \Delta t = 0.00125T$). In the same figure the curves corresponding to different values of $\Delta s_W / \Delta s_B$ are shown using solid lines. We clearly observe that an optimal ratio exists, which in the examined case is $\Delta s_W / \Delta s_B = 2.4$. Extensive numerical evidence has shown that for $0.2 \leq St \leq 0.45$ and $15^\circ \leq \theta_0 \leq 50^\circ$ the optimal ratio varies in the interval $2 \leq \Delta s_W / \Delta s_B \leq 3.25$ with greater values corresponding to lower Strouhal numbers.

In the case of oscillating hydrofoil under the free surface (including also the flapping mode) selection of numerical parameters for convergence also ensures stability of the numerical scheme. This is due to the fact that the wavelength of the wake is usually significantly smaller than the wavelength of the generated waves on the free surface. Thus, a small enough time-step is required in order to capture the wake dynamics, which in most cases suffices for satisfaction of the above criterion, Eq.2.143.

2.10.2 Validation and GPU performance

In the present section validation of the present method against a simpler steady nonlifting problem that can be solved analytically is presented. Moreover the performance of the 3D steady version of the GPU code is compared against a serial 3D steady CPU code that was developed for that purpose. For the comparison, an Intel i5-2300 CPU and a single GTX1080 GPU with 2560 NVIDIA CUDA cores were used. Moreover, comparison of performance of the mixed precision instance of the GPU code against the double precision instance, is presented. The superior performance of mixed precision GPU calculations without significant harm at the accuracy of the solution, is demonstrated.

The method was tested for the calculation of the potential on the surface of an ellipsoid with semi-axis ratio selected to be 0.5:2.5:0.06, to have similar shape with a foil. The results were then compared to the steady analytical solution that can be found in Milne-Thomson (1996). In Figs.2.9 & 2.10, the total calculation time was analyzed to the individual operations for mixed and double precision calculations, respectively. The two operations that require significant

⁶⁷The present section analysis have been obtained using the 2D version of the code. Similar results have been obtained with the 3D version where Δs is a mean value of the maximum diagonal of the boundary elements.

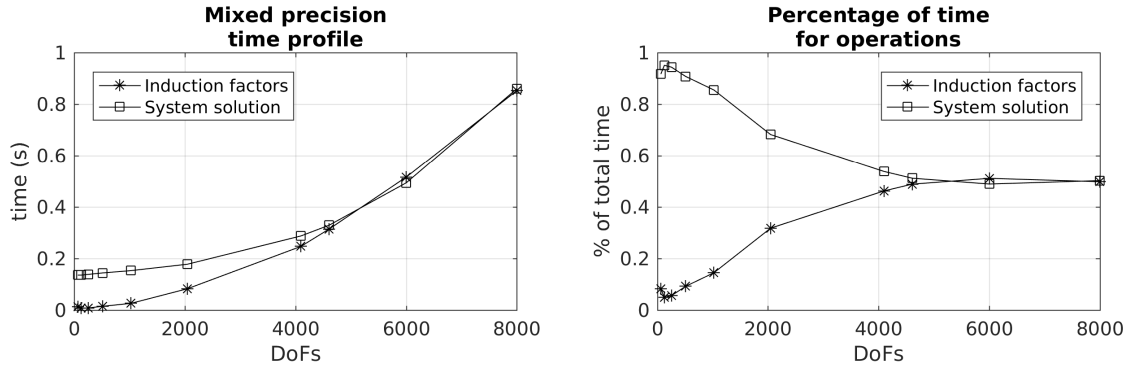


Figure 2.9: Double precision execution time profile for the calculation of the potential on an ellipsoid with semi-axis ratio selected to be 0.5:2.5:0.06, to have similar shape with a foil.

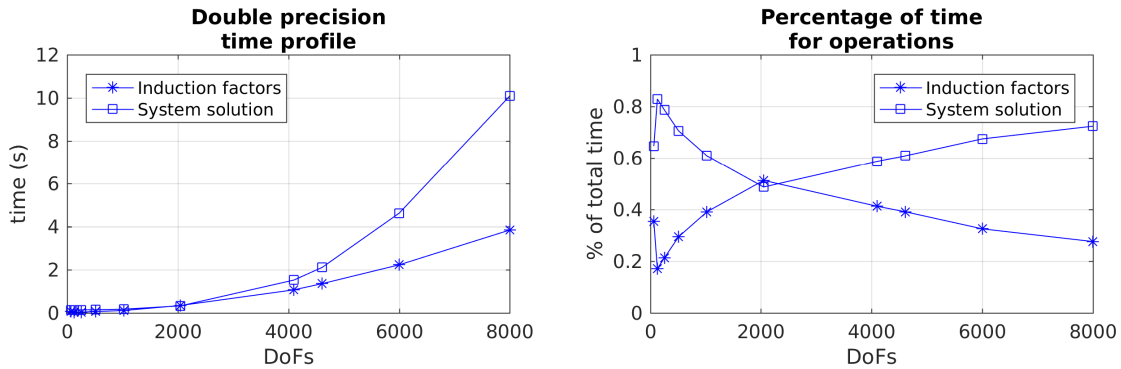


Figure 2.10: Mixed precision execution time profile for the calculation of the potential on the ellipsoid of figure 2.9.

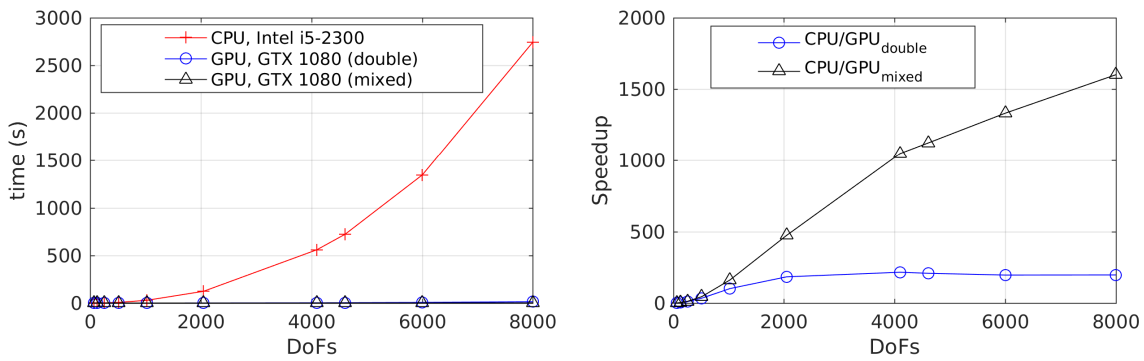


Figure 2.11: Benchmarking between a single threaded CPU core (Intel i5-2300 3.4GHz) and an GTX1080 GPU with 2560 NVIDIA CUDA Cores for the problem of Fig.2.9.

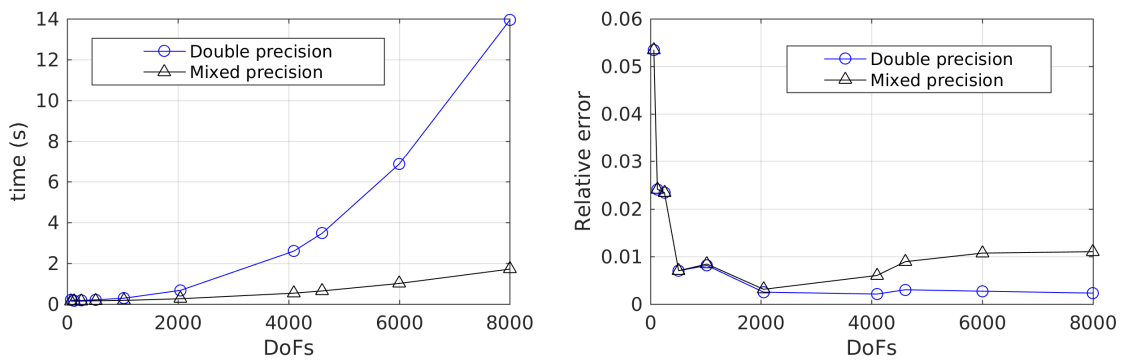


Figure 2.12: Validation against analytical solution and demonstration of the performance using mixed-precision arithmetics for the example of Fig.2.9.

time are the calculation of the induction-factor matrices and the solution of the linear system using LU decomposition and the cuSOLVER function from the CUDA Toolkit v10.0.130. It is observed that for both mixed and double precision calculations the linear-system solution takes more than 50% of the total time exceeding the 80% for the coarser grids. Moreover for the mixed precision instance of the code and for DoFs more than 4000 the computational time for the induction factor reaches similar levels.

In Fig.2.11, the performance of the GPU code is compared with the performance of the code running on a single CPU thread. The double precision instance of the GPU code completes the task up to 197 times faster than the CPU code, while the mixed precision instance is more than 1600 times faster.

In Fig.2.12, the execution times for the calculation of the potential on the test ellipsoid, using the mixed precision scheme are compared with the same calculation using double precision arithmetics, also the relative error is plotted for validation purposes. The mixed precision is almost 7 times faster for the finer discretisation with 8000 DoFs. It is significant that the error of the mixed precision remains close to that of double precision. With mixed precision arithmetics more demanding problems (that will be presented in the sequel and in the following chapters) can be solved due to lower memory usage and the more efficient exploitation of GPU resources.

2.10.3 Biomimetic flapping-foil thruster

In this section numerical results are presented and discussed concerning the performance of hydrofoils in flapping motion at great distance from both the free surface and the bottom, corresponding practically to operating conditions in unbounded domain. Also, comparisons are presented with experiments and other methods from the literature. Except of forward translation with constant speed U , the hydrofoil also performs combined heaving and pitching motions, the latter defined with respect to a pivot axis located at a specific distance X_R from the leading edge. The phase difference between pitching and heaving motion is denoted by ψ , and is appropriately selected $|\psi| = 90^\circ$; see, e.g., Anderson et al. (1998) or Rozhdestvensky and Ryzhov (2003). The Strouhal number of the hydrofoil is $St = \omega h_0 / \pi U = 0.4$ and $\epsilon = \theta_0 U / \omega h_0$ is the feathering parameter, where θ_0 is the pitch and h_0 is the heave amplitude.

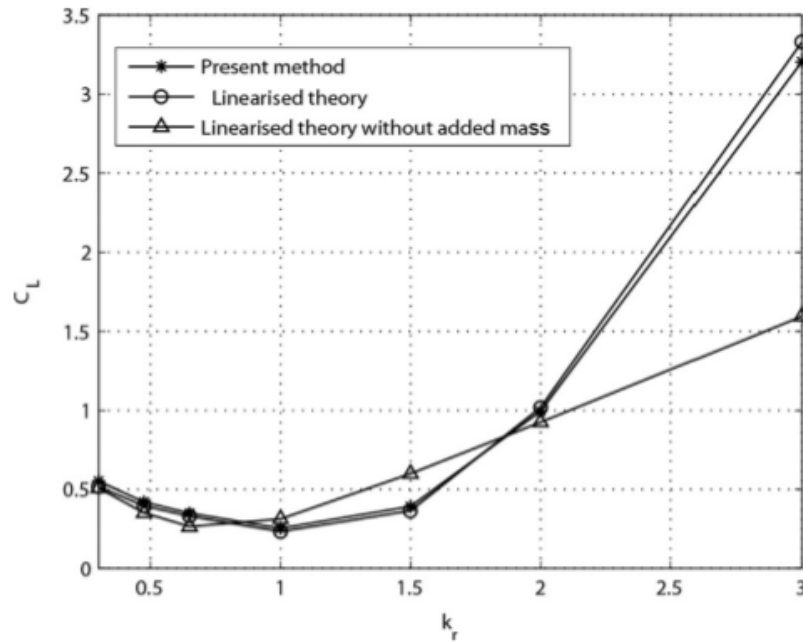


Figure 2.13: Amplitude of lift coefficient of NACA0012 hydrofoil, in low-amplitude flapping motion $h_0/c = 0.1$, $\theta_0 = 10^\circ$, $\psi = -90^\circ$, $X_R/c = 0.5$ in infinite domain. Present method results against linearized theory predictions with and without the contribution of added mass effects.

In order to show the compatibility of the present method with thin hydrofoil theory (Filipapas, 2013; Newman, 1977), in Fig.2.13 a comparison between our calculations (shown using stars) and linearized theory predictions (shown by circles) is shown concerning the amplitude of lift coefficient $C_L = F_L/0.5\rho U^2 c$, in the case of a NACA0012 flapping hydrofoil at small amplitude heaving and pitching oscillations $h_0/c = 0.1$ and $\theta_0 = 10^\circ$, respectively. The pivot axis is located at a distance $X_R/c = 0.5$ from the leading edge and the phase difference is $\psi = -90^\circ$. The amplitude of the lift coefficient is plotted for various values of the reduced frequency $k_r = \omega c/2U = Str(\pi c/2h)$, ranging in the interval $0.3 \leq k_r \leq 3$. We clearly observe in the examined case that present method results are in very good agreement with theoretical predictions. Furthermore, in order to illustrate the significance of the added mass effect to the unsteady responses of the flapping hydrofoil, in the same figure the theoretical predictions, obtained by omitting the added mass effect (expressed by the last term in the right-hand side of Eq.(225) of Newman (1977)), are also shown using triangles. The significance of added mass effect has been recently examined and thoroughly discussed in the works by La Mantia and Dabnichki (2012, 2013) where it is also shown that its omission could lead to great underestimation of both integrated forces and structural loads. On the other hand, it is obvious that the present method is fully capable of providing the total responses fully including the added mass effect, which is expected to become even more significant in the case of flapping foil operating under the free surface. This is another important direction that is planned for future research.

Next, in Fig.2.14 we consider the traveling hydrofoil to perform high-amplitude heaving motion, $h_0/c = 1$, simultaneously with pitching oscillations with amplitude ranging in $10^\circ \leq \theta_0 \leq 55^\circ$. The pivot axis is located at $X_r/c = 0.33$ from the leading edge and $\psi = -90^\circ$.

Calculations concerning the mean value of thrust coefficient $C_T = -F_x/\rho U^2 h_0$, for various Strouhal numbers St , are compared against experimental measurements by Read et al. (2003).

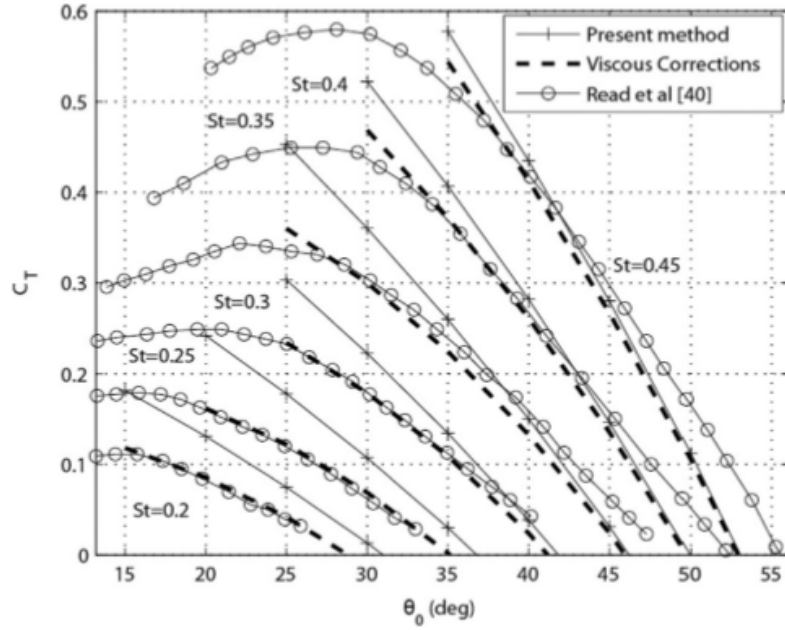


Figure 2.14: Thrust coefficient for NACA0012 hydrofoil, in flapping motion with $h_0/c = 1$, $\psi = -90^\circ$, $X_R/c = 0.33$. Present method compared against experimental data from Read et al. (2003).

We observe in this figure that for small and moderate angles of attack (large θ_0), where leading edge separation and dynamic stall effects are not strong, present results are in good agreement with measured data, while for larger angles of attack and Strouhal numbers, our 2D ideal-flow method does not provide satisfactory predictions. Discrepancies at high loading conditions are attributed to non-linear effects due to 3D effects and vortex wake rollup dynamics that are included in the present simulation. Consideration of viscous effects is also included in the figure, indicated using dashed lines, as calculated using the following empirical formula for the skin friction resistance coefficient c_r (Blevins, 1984; Filippas and Belibassakis, 2014), as a function of Reynolds number $Re = Uc/v$ (where v is the kinematic viscosity)

$$c_r = \frac{0.0858}{[\log_{10} Re - 1.22]^2} + c_a (Re) a^2. \quad (2.144)$$

The above formula includes the effect of the effective angle of attack a through an empirical coefficient c_a , which increases friction coefficient at higher angles of attack leading to better predictions, as shown in Fig.2.14 (dashed lines). We observe in Fig.2.14 that, in comparison with the experimental data (Read et al., 2003), the present results obtained with the 2D version of the code leads to an overestimation of the slope $|dC_T/d\theta_0|$ of the thrust curves from 15% to 45% (depending mainly on St). Part of this discrepancy is due to nonlinearity of the wake dynamics. However, the basic reason cause could be 3D effects intruding the experiments. As it is recently presented in Politis and Tsarsitalidis (2013), the measured data agree well with calculations of a flapping wing of finite aspect ratio $AR = 6$, and the overestimation of $|dC_T/d\theta_0|$ by the present 2D analysis is (on the average) compatible with corresponding estimation provided by quasi-steady lifting line theory, i.e. $2/AR = 33\%$.

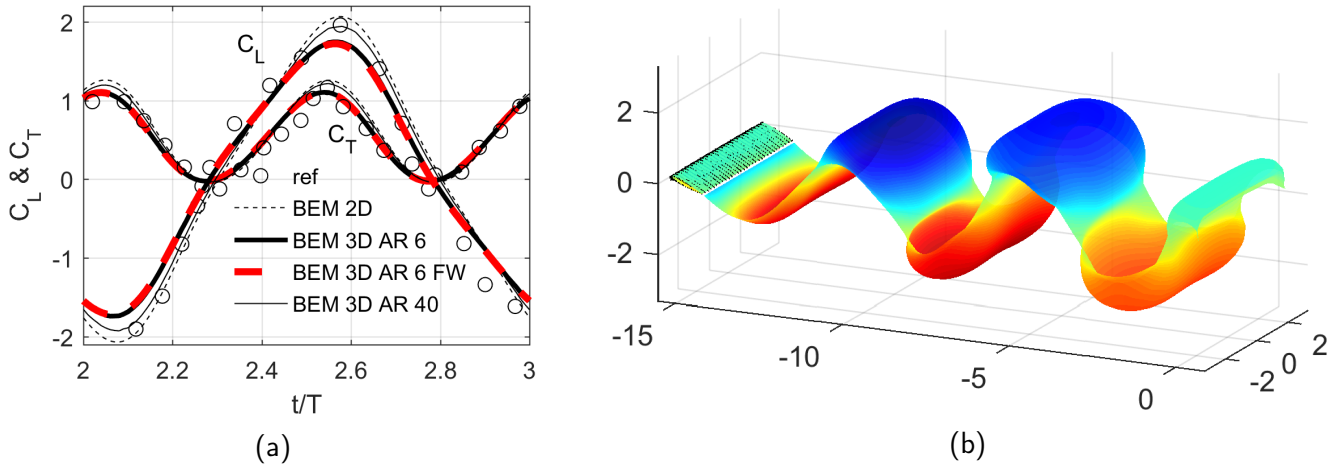


Figure 2.15: Simulation of biomimetic flapping-foil thruster in unbounded domain: (a) Time history of lift and thrust coefficients, comparison of the fully nonlinear 3D calculations with $AR = 6$ & $AR = 40$ against experimental results, 3D calculations with a prescribed wake model and 2D calculations. (b) Potential and velocities on the body and potential jump on the wake (fully nonlinear calculations). For a constant-chord foil with NACA0012 sections and $St = 0.3$, $h_0/c = 0.75$, $\theta_0 = 23.3^\circ$, pivot point $X_R/c = 0.33$ and phase lag $\psi = -90^\circ$.

A specific example, corresponding to one operating condition, for a constant-chord foil with NACA0012 sections, $St = 0.3$, heave amplitude $h_0/c = 0.75$, pitch amplitude $\theta_0 = 23.3^\circ$, pivot point $X_R/c = 0.33$ and phase lag $\psi = -90^\circ$, is shown in Fig.2.15. In Fig.2.15a the time history of lift ($C_L = F_3/0.5\rho U^2 A$) and thrust ($C_T = -F_1/0.5\rho U^2 A$) coefficients is presented. A is the surface of the foil. Calculations have been performed using the present approach with the fully nonlinear 3D model with $AR = 6$ and $AR = 40$, the 3D model with a prescribed wake model and the fully nonlinear 2D model. Experimental measurements by Schouveiler et al. (2005) are also provided. In general, we observe quite satisfactory agreement of the present method with experimental data concerning both the amplitude and the phase lag of the integrated force coefficients. Moreover, it is clear from the trend of the 3D calculations as the AR raises that the 3D version of the numerical method is compatible the the 2D. In Fig.2.15b the potential and velocities on the body and potential jump on the wake are depicted, as calculated with the fully nonlinear 3D model. Regarding the performance of the numerical method and the GPU accelerated computational code, we provide some information fro the case of $AR = 6$. The simulation is in time domain and the foil begins from the rest reaching harmonic state after 2 periods T , the time-step is $\Delta t/T = 1\%$. A total number of $N_B = 1860$ body boundary elements are used. Mixed-precision arithmetics have been used, 1.3GB were required from the VRAM and the simulation time was 21 sec in the case of the prescribed wake model and 88 sec in the case of the free-wake model. In the present case of moderate unsteadiness the fully non-linear wake model does not provide significant improvement to the predictions in comparison with the prescribed wake model, as expected (see relevant discussion in Sec.2.2, below Eq.2.10).

In the sequel, numerical results are presented in order to demonstrate whether or not the formulation of the fully non-linear wake is important. In Fig.2.16 calculations concerning he thrust coefficient $C_T = -F_x/\rho U^2 h_0$ for the NACA0012 hydrofoil are presented, for flapping motion with $h_0/c = 1$, $\psi = -90^\circ$, $X_R/c = 0.33$. Results are obtained by the present method using

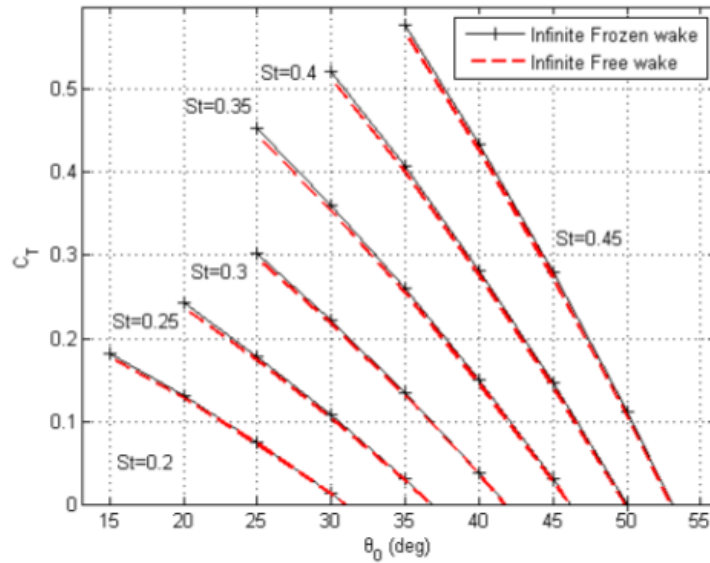
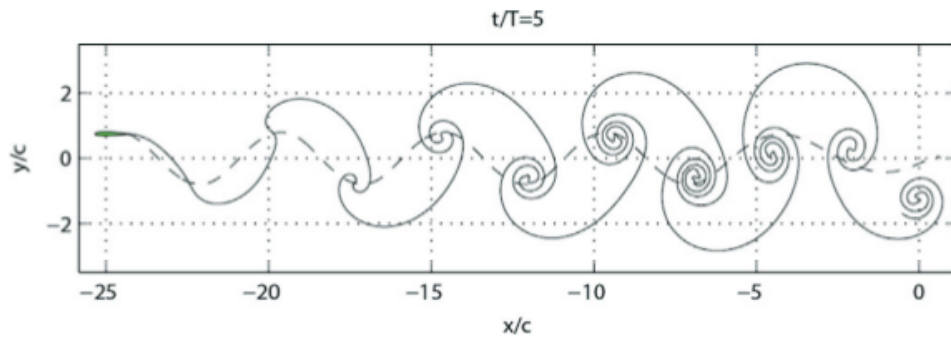


Figure 2.16: Systematic results of averaged thrust coefficient for a 2D NACA0012 hydrofoil, in flapping motion with parameters as in Fig.2.14. Frozen wake model (linearized wake dynamics) compared against free wake formulation in unbounded domain.

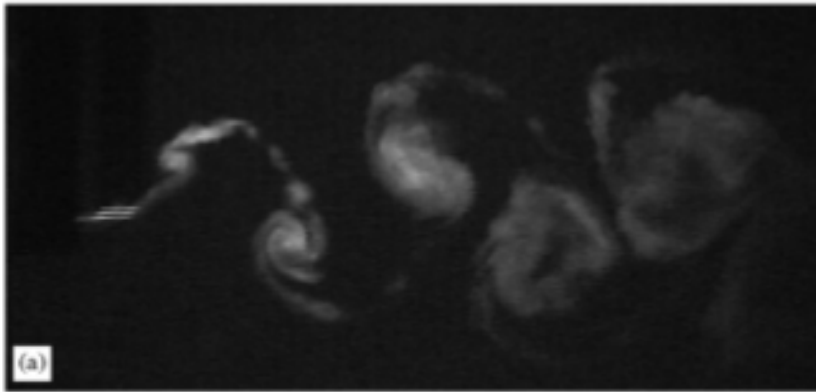
frozen wake model (linearized dynamics) or free wake analysis, are shown using solid and dashed lines, respectively. We observe that the effect of free wake is to reduce the thrust coefficient and it is noticeable only at the greater Strouhal numbers and angles of attack.

However for wake visualization purposes the free wake analysis is the only model that can be applied. To illustrate further this fact, the development of trailing vortex sheet after 5 periods from start is plotted in Fig.2.17a, using free wake analysis, and compared with the shape of the linearized wake model, shown in the same figure using dashed line. We observe that the free wake curve spirals around the peaks of the trailing vortex intensity, shaping an expanding reverse Karman vortex street, which is characteristic feature of thrust production by the foil. Quite similar wake patterns have been observed in experiments Schouveiler et al. (ibid.) (Fig.2.17b).

As we have already mentioned in the case of lifting flow around sharp-ended body like a hydrofoil, the problem is supplemented by the Kutta condition, necessitating finite velocity at the trailing edge. An alternative to the classic Pressure-type condition could be a Morino-type version of the Kutta condition; see Eq.2.11 and the relevant discussion below. That approximation permits the direct calculation of vorticity transport on the free trailing vortex sheet in terms of the potential difference at the trailing edge. In order to compare with Pressure-type Kutta condition we use the example of Fig.2.14, where the traveling hydrofoil performs high-amplitude heaving motion, $h_0/c = 1$, simultaneously with pitching oscillations with amplitude $10^\circ \leq \theta_0 \leq 55^\circ$. The pivot axis s located at $X_R/c = 0.33$ from the leading edge and $\psi = -90^\circ$. Calculations concerning the mean value of thrust coefficient $C_T = -F_x/\rho U^2 h_0$, for various Strouhal numbers St using pressure-type or Morino-type conditions, are compared in Fig.2.18 against experimental measurements by Read et al. (2003), that have been presented in Fig.2.14. We clearly observe that the calculations with Morino-type condition lead to an overestimation of thrust coefficient especially at heavier loads (i.e. higher Strouhal numbers



(a)



(b)

Figure 2.17: (a) Trailing vortex sheet development in 2D for the case of Fig.2.15. (b) Trailing vortex sheet visualization from experiments by Schouveiler et al. (2005).

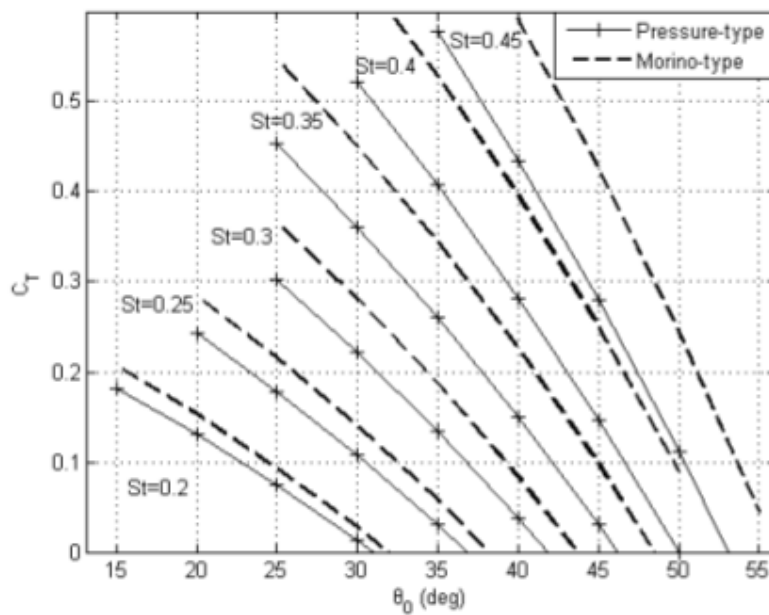


Figure 2.18: Systematic results of averaged thrust coefficient for a 2D NACA0012 hydrofoil, in flapping motion with parameters as in Fig.2.14. Pressure-type Kutta condition compared against Morino-type condition.

and angles of attack). This is reasonable due to the fact that the simpler linear Morino-type condition is a quasi-steady approximation of the more accurate quadratic Pressure-type Kutta condition.

Finally for the same case, in Fig.2.19 we present the evolution of the pressure coefficient ($c_p = p/0.5\rho U^2$) distribution for 5 periods starting from the rest for $St = 0.2, \theta_0 = 35^\circ$ at the upper subplots and $St = 0.35, \theta_0 = 35^\circ$ at the lower subplots, Morino-type Kutta condition at the left is compared against Pressure-type condition at the right. In general we can notice that the pressure difference at specific points (x/c) is larger at the case of Morino-type Kutta conditions and that causes the total overestimation of the integrated thrust coefficient. As we expected, that difference is more significant at the higher Strouhal number and more specifically at the moments when the pressure reaches local extremes. Moreover we can notice that the pressure difference at the trailing edge has finite values at the trailing edge when using Morino-type condition especially for the case of large Strouhal number. This means that a physical quantity like the pressure is discontinuous when we pass from the foil to the wake which is not correct in the context of potential theory. Concerning the above the pressure type condition, although is quadratic and more difficult to be applied, is required for modeling of moderate to higher unsteady phenomena like the flapping foil propulsion beneath the free surface.

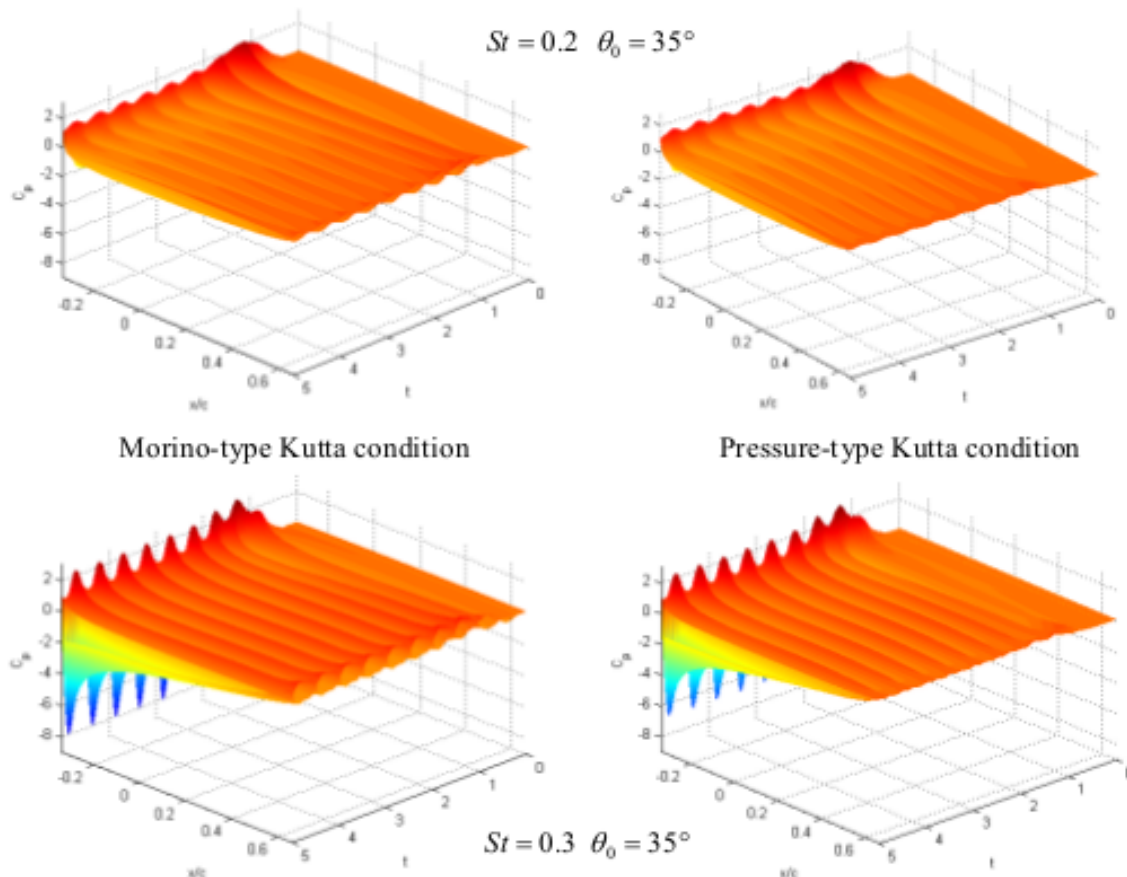


Figure 2.19: Pressure coefficient distribution for a 2D NACA0012 hydrofoil, in flapping motion with $h_0/c = 1$ and $\psi = -90^\circ$ at the upper subplots, $St = 0.35, \theta_0 = 35^\circ$ at the lower subplots, in infinite domain for five periods starting from rest. Morino-type Kutta condition (left) compared against Pressure-type condition (right).

2.11 Remarks and conclusions

In the first part of the present thesis a fully nonlinear time domain method is developed for the general unsteady problem of flow around lifting bodies of general shape in unbounded domain. Also effects of a nonuniform background velocity field (gust) supplementing the future study of the ship-foil self-propulsion problem are modeled. The formulation of the problem is based on the potential theory and the boundary integral equations (BIE). For the numerical solution of the 3D, unsteady and nonlinear problem an efficient (in terms of both time and space complexity) GPU-accelerated boundary element method (BEM) is developed, based on a formulation that is direct with respect to the potential.

The method is applied to the hydrodynamic analysis of foils in several conditions focusing to the 3D effects the nonlinear wake dynamics and the nonlinearity of the Kutta conditions and the performance of the developed GPU computational code. Present work supplements the evidence of previous studies that such biomimetic systems when operate at optimum conditions could achieve high thrust and efficiency levels. Results are obtained, illustrating the numerical performance of the developed method and validating its accuracy through comparisons with other methods and experimental data. Numerical predictions include lift and thrust coefficients of the system, over a range of motion parameters, as reduced frequency, Strouhal number, maximum angle of attack. Comparison between the prescribed and the fully nonlinear wake model, as well as between quasi-steady linearised Morino-type and nonlinear pressure-type Kutta conditions are included, identifying the range of applicability and the limitations of the studied approaches.

Future extensions include the treatment of leading edge separation and dynamic stall effects to extend method's applicability to operation conditions corresponding to large angles of attack. Also, friction resistance could be taken into account using boundary layer theory (Papadakis, 2014; Riziotis and Voutsinas, 2007) and experimental and empirical coefficients. All the above extensions would provide in the future even better comparison with experimental measurements, and support the derivation of systematic results for the detailed investigation of various arrangements of flapping hydrofoil systems operating in stationary fluid or in nonuniform background fields. Moreover, the experimental and numerical study of the self-propulsion problem of a ship with biomimetic flapping foil propulsors is of the utmost importance. Also the effects of chordwise and spanwise elasticity could improve the performance of the biomimetic thruster, as have been demonstrated in our work (Priovolos et al. 2018) and in the diploma thesis Anevlavi (2019) and in references cited there. Finally, we conclude that the present method and GPU code, can serve as a useful and efficient tool for assessment and the preliminary design and control of biomimetic systems such as flapping foils for efficient marine propulsion and maneuvering.

Chapter 3

Hydrodynamic analysis of bodies beneath the free surface

3.1 Summary

The method presented in Chapter 2 is extended to study the effect of the free-surface boundary and the interaction of the latter with the trailing vortex sheet without simplifications concerning their nonlinear character. Oscillating wings are investigated as unsteady thrusters, beneath the free surface and the modeling also includes finite depth effects. The motion and the geometry of the body are general, thus no linearisation has been applied. The body contour is modeled as a surface of potential discontinuity. In the present chapter, the body motion is prescribed, however the whole formulation is directly extended to solve problems that include free motions of finite degrees of freedom; see e.g. the problem of the semi-activated foil in Sec.4.5.4. We consider moderate submergence and speed, permitting us to approximately neglect effects of breaking waves and cavitation. The formulation of the problem is based on the potential theory and the boundary integral equations (BIE). For the numerical solution of the fully nonlinear, 3D and unsteady problem the GPU-accelerated boundary element method (BEM) is extended to treat hydrodynamic flows beneath the free surface. The calculation of generalised forces is obtained by pressure integration without any additional assumption. The latter is calculated using the Bernoulli's equation as presented in Sec.3.3.

We begin with the definition of the unsteady initial boundary value problem (IBVP) problem in the present case. The free-surface boundary conditions and pressure-type Kutta condition will serve for the construction of the equations of the dynamical system and the other kinematic boundary conditions will provide appropriate constraints. Then the analytical form of Bernoulli's equation and of the pressure-type Kutta condition will be presented. For simplicity in the description of the present method, and especially as concerns the treatment of the free-surface conditions (including the conditions at infinity), we will start our presentation with the boundary integral formulation in the case of non-lifting flow around a body of smooth but arbitrary geometry, undergoing general motion. This problem contains as cases of special interest the wave-resistance problem due to constant-speed forward motion and the enforced radiation problem due to body oscillations. Then, in Sec.3.5 the whole methodology is extended to the case of an oscillating hydrofoil in forward motion beneath the free-surface radiating waves, giving special attention to the treatment of the discretised form of pressure-type Kutta condition and free-surface boundary conditions that, along with the discretised extended DtN

operator, form a system of (spatially and temporarily) nonlocal differential equations, with explicit and implicit nonlinearities and linear algebraic constraints. The application of Green's formula on the body boundary and the exact free-surface boundary will be used to obtain a weakly singular Boundary Integral Equation (BIE) for the unknown boundary fields. For the numerical solution we use a potential based boundary element method (BEM) and a collocation method to obtain the discretised BIE. The latter along discretisation will be used for the construction of the discretised extended Dirichlet-to-Neumann (DtN) operator that will serve as an algebraic constraint to the equations of the dynamic system that will be constructed from the free-surface boundary conditions and the Kutta condition. A curvilinear finite difference method (CUFDM), in variable, non Cartesian and non orthogonal coordinate systems (see also Sec.2.5.2) is exploited to express the potential, included in free-surface conditions and the Kutta condition, in terms of the dynamic variables of the problem. Exploiting the free-surface and Kutta conditions we proceed to the construction of the dynamic system equations in the form of a system of (spatially and temporarily) nonlocal differential equations, with explicit and implicit nonlinearities, with a linear algebraic constraint. Next, a method for time integration is presented.

Concerning numerical results and applications, the problem of thrust production using biomimetic flapping-foil systems beneath the free-surface including wave resistance and finite depth effects is numerically investigated. The importance of free-surface and 3D effects, nonlinearity as well as the superior performance of the developed GPU code, are illustrated. Both prescribed and free wake models are investigated for foils beneath the free surface leading to similar results concerning the integrated quantities in the region of interest to the problem and therefore the first simplest scheme which demands also lower computational cost is more efficient and suitable for engineering application at the present problem. However for the detailed prediction of the free-surface elevation and of the velocity and pressure field the fully nonlinear models are important.

Last but not least, it is discussed in Sec.3.6, that the problem of flapping foil in fully non-linear water waves can be treated in the context of the method if part of the lateral boundary could model a 3D wavemaker.

3.2 Mathematical formulation of lifting bodies beneath the free surface

The studied configuration is depicted in Fig.3.1. The problem is time dependent and the oscillating lifting body is represented by a moving boundary $\partial D_B(t)$, with respect to the earth-fixed frame of reference. The domain of definition of the problem is an open semi-bounded domain $D \subseteq \mathbb{R}^n$ (where $n = 2, 3$) with boundary ∂D which is supposed to be smooth everywhere except the trailing edge. Moreover the wake of the body is modeled by another deformable boundary $\partial D_W(t)$, whose length grows emanating continuously from the body sharp edge. The level of the free-surface, when it is still, is shown in Fig.3.1 as a horizontal plane. We consider moderate submergence and speed, permitting us to approximately neglect effects of breaking waves and cavitation. Moreover, the body is considered to be rigid and its motion is prescribed. However, the present method is nonlinear; i.e. a) the shape of the body and b) its motion are not linearised, c) the nonlinear dynamics of the free wake are included and d) the

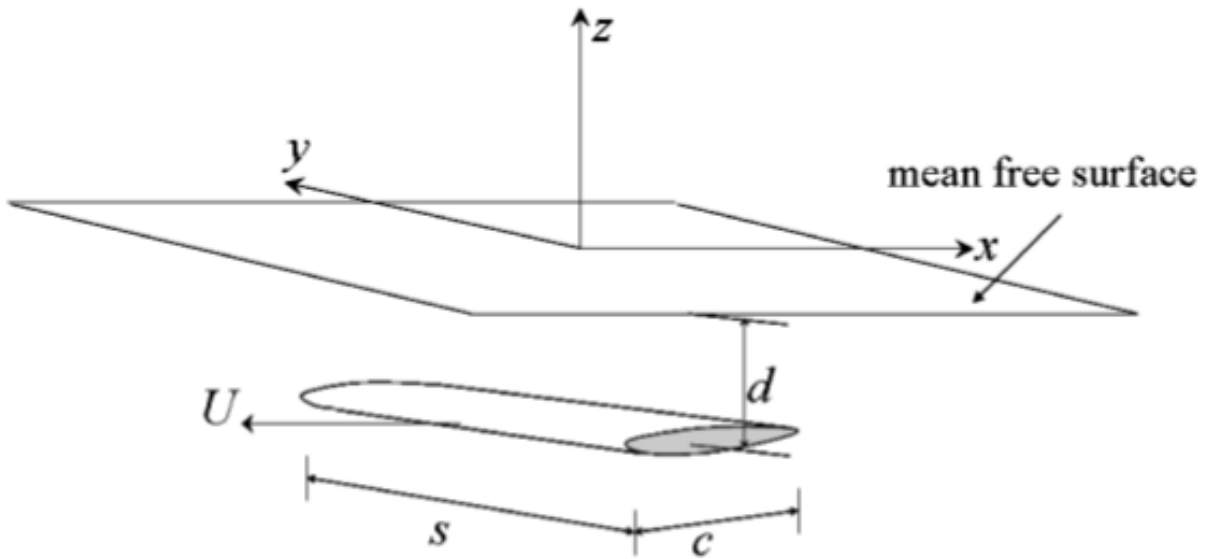


Figure 3.1: Definition of the studied problem (Zhu et al. 2006) in the case of a foil (of mid-chord c_0) moving under the free surface (at mean submergence d). The free surface is initially still and the waves are generated from the motion of moving boundaries.

fully nonlinear free-surface boundary conditions are satisfied at the exact location of the free-surface elevation, that is a result of the rigid-boundaries wave-making motion. In the present work we are interested in design, operation and control problems, aiming to the simulation of the system during many periods and not to its response to extreme cases of overturning and nearly-breaking waves. The latter can be simulated in the context of potential theory, with accepted accuracy, only until the breaking and not after. Therefore, we assume that the free surface is a function defined on the horizontal plane, that is the still free-surface level; see e.g. Hague and Swan (2009) and Spinneken et al. (2014). For the surface tracking, we follow a semi-Lagrangian approach (the horizontal velocities of the free-surface particles are omitted), leaving the extension to the fully Lagrangian method, as a straightforward extension for future work; for fully Lagrangian methods see e.g. Grilli et al. (2001), Fochesato et al. (2007), Touboul et al. (2006), Touboul and Kharif (2010) and Manolas (2015). A Cartesian coordinate system is introduced with x_3 -axis pointing upwards, x_1 -axis and x_2 -axis lying on the still free-surface plane, with x_1 -axis at the direction of body's characteristic motion.

The wave potential Φ satisfies Laplace equation

$$\Delta\Phi(\mathbf{x};t) = 0, \quad \mathbf{x} \in D(t), \quad (3.1)$$

supplemented by the body boundary condition

$$\partial_{n_B}\Phi(\mathbf{x};t) = \mathbf{V}_B(\mathbf{x};t) \cdot \mathbf{n}_B(\mathbf{x};t), \quad \mathbf{x} \in \partial D_B(t), \quad (3.2)$$

and the hard bottom no-entrance condition

$$\partial_{n_H}\Phi(\mathbf{x};t) = 0, \quad \mathbf{x} \in \partial D_H. \quad (3.3)$$

The first is a non-homogeneous Neumann boundary condition and the second, for impermeable and motionless bottom, is a homogeneous Neumann boundary condition. The present method can also tackle problems of impermeable but deformable bottom, however the analysis of those interesting problems that belong to the fields of coastal engineering is left as a subject for future work.

Moreover, the fully non-linear dynamic and kinematic boundary conditions are imposed on the exact free-surface elevation, generated by the wave-making motion of the body. Those equations are given here

$$\partial_t \Phi(\mathbf{x}_F, \eta; t) = -g\eta(\mathbf{x}_F; t) - \frac{1}{2}[\nabla \Phi(\mathbf{x}_F, \eta; t)]^2, \quad \mathbf{x} \in \partial D_F(t), \quad (3.4)$$

$$\partial_t \eta(\mathbf{x}_F; t) = -\partial_{n_F} \Phi(\mathbf{x}_F, \eta; t) \sqrt{1 - [\partial_{x_1} \eta(\mathbf{x}_F; t)]^2 - [\partial_{x_2} \eta(\mathbf{x}_F; t)]^2}, \quad \mathbf{x} \in \partial D_F(t), \quad (3.5)$$

where $\mathbf{x}_F = \{x_1, x_2\}$ and $\mathbf{x} = \{\mathbf{x}_F, \eta\} = \{x_1, x_2, \eta\}$. The dynamic boundary condition of the free surface Eq.(3.4), is similar to the one applied on the free wake of a lifting body examined in Chapter 2, and in the present case, it requires that the hydrodynamic pressure as approaching the free surface equals the atmospheric pressure¹. This assumption using Bernoulli's theorem Eq.(3.4). The kinematic boundary condition Eq.(3.4), is also of the same type as the one used in the modeling of the free wake, it necessitates that the normal velocities of the fluid and of the free-surface boundary must be equal and thus $D_t(x_3 - \eta = 0)$, where $D_t(\cdot)$ is the material derivative. The last constraint, leads to Eq.(3.5).

Moreover, the trace on the free-surface boundary of the space gradient of the potential can be decomposed to its tangential and the vertical components according to Eq.(2.67), as follows²

$$\begin{aligned} \nabla \Phi(\mathbf{x}_F, \eta; t) &= \partial_s \Phi(\mathbf{x}_F, \eta; t) \times \mathbf{n}(\mathbf{x}_F, \eta; t) + \partial_n \Phi(\mathbf{x}_F, \eta; t) \cdot \mathbf{n}(\mathbf{x}_F, \eta; t) \\ &= \mathbf{V}_{F,t}(\mathbf{x}_F, \eta; t) + \partial_n \Phi(\mathbf{x}_F, \eta; t) \cdot \mathbf{n}(\mathbf{x}_F, \eta; t), \quad \mathbf{x} \in \partial D_F(t). \end{aligned} \quad (3.6)$$

With the aid of Eq.(3.6) and the fact that the square root in Eq.(3.5) is the square root of the metric a of the free-surface boundary, the free-surface boundary conditions become

$$\partial_t \Phi(\mathbf{x}_F, \eta; t) = -g\eta(\mathbf{x}_F; t) - \frac{1}{2}[\mathbf{V}_{F,t}(\mathbf{x}_F, \eta; t) + \partial_n \Phi(\mathbf{x}_F, \eta; t) \cdot \mathbf{n}(\mathbf{x}_F, \eta; t)]^2, \quad \mathbf{x} \in \partial D_F(t), \quad (3.7)$$

$$\partial_t \eta(\mathbf{x}_F; t) = -\partial_{n_F} \Phi(\mathbf{x}_F, \eta; t) \sqrt{a(\mathbf{x}_F, \eta; t)}, \quad \mathbf{x} \in \partial D_F(t). \quad (3.8)$$

We treat the above as an initial and boundary value problem (IBVP) and we assume that far from the body the radiated wavefield tends to zero. In the above equations η denotes the generated free-surface elevation and g is the acceleration of gravity. Furthermore, H is the constant

¹The surface tension generates a pressure difference between the atmospheric pressure and the internal pressure of the water at the free surface boundary. Although that effect is significant for the study of high-frequency capillary waves in hydroacoustics, it can be neglected when wave-body interaction is of the main interest. Therefore the surface tension effect is neglected in the present modeling.

²In the present paragraph the tangential to the boundary velocity are denoted as $\mathbf{V}_{F,t} = \partial_s \Phi \times \mathbf{n}$.

(finite) depth, d is the mean submergence of the body and \mathbf{V}_B denotes the instantaneous velocity of the body (due its own motion) at each point on the boundary. Finally, \mathbf{n} is the unit normal vector pointing into the interior of $D(t)$.

In the case of lifting flow around bodies with sharp edges, the problem is supplemented by the kinematic and dynamic conditions on the trailing vortex sheet $\partial D_W(t)$. The dynamic boundary condition

$$p_W^u(\mathbf{x};t) = p_W^l(\mathbf{x};t), \quad \mathbf{x} \in \partial D_W(t), \quad (3.9)$$

necessitates that a free shear layer cannot carry loading and thus the pressure at the both sides of it should be the same. The kinematic boundary condition

$$\partial_{n_W} \Phi_W^u(\mathbf{x};t) = \partial_{n_W} \Phi_W^l(\mathbf{x};t), \quad \mathbf{x} \in \partial D_W(t), \quad (3.10)$$

demands that the upper and the lower side of the shear layer cannot be separated to two distinct surfaces during the flow, thus the normal to the surface velocity is continuous through $\partial D_W(t)$. The indices B, W, F, H are used to denote values of the potential field, its derivative and potential jump, at the body surface and the wake of the foil, the free surface and the bottom, respectively. Using Eqs.(3.9) and Eq.(3.10) in conjunction with the appropriate form of Bernoulli's equation (see also Sec.3.3),

$$\frac{p(\mathbf{x};t) - p_{atm}}{\rho} + \partial_t \Phi(\mathbf{x};t) + \frac{1}{2} [\nabla \Phi(\mathbf{x};t)]^2 + gx_3 = 0, \quad \mathbf{x} \in D(t), \quad (3.11)$$

we obtain

$$D_t \mu_W(\mathbf{x};t) = 0, \quad \mathbf{x} \in \partial D_W(t). \quad (3.12)$$

In the equations above $\mu_W = \Phi_W^u - \Phi_W^l$ denotes the potential jump (the dipole intensity) on the wake and $D_t(\cdot) = \partial_t(\cdot) + \mathbf{V}_W^m \cdot \nabla(\cdot)$ is the material derivative, based on the mean total velocity $\mathbf{V}_W^m = 0.5(\nabla \Phi^u + \nabla \Phi^l)$, on the trailing vortex sheet.

In the lifting case, enforcement of the Kutta condition is required in order to fix the circulation at each time instant. The non-linear (quadratic), pressure-type Kutta condition, requiring zero pressure difference at the trailing edge, is imposed as follows

$$\lim_{\xi \rightarrow \xi_{TE}} F_{fs}^{PK}[\mathbf{x}_B(\xi, \eta); t] = 0, \quad \mathbf{x}_B \in \partial D_B(t) \text{ and } \mathbf{x}_{TE} \in \partial D_B(t) \cup \partial D_W(t), \quad (3.13)$$

where the operator $F_{fs}^{PK}(\cdot)$ is defined as follows

$$F_{fs}^{PK}[\mathbf{x}_B(\xi, \eta); t] = \partial_t(\Phi^u - \Phi^l) + 0.5(\nabla \Phi^u + \nabla \Phi^l)(\nabla \Phi^u - \nabla \Phi^l) + g(x_3^u - x_3^l). \quad (3.14)$$

The above form of pressure-type Kutta condition can be derived using the Bernoulli's theorem on the body at upper and lower sides of trailing edge; see Sec.3.3, Eq.(3.25).

3.3 Pressure calculation and Kutta condition

In the first part of the present section we will present the derivation of an appropriate form of Bernoulli's theorem for the calculation of pressure distribution in the case of lifting flows beneath the nonlinear free surface and in the presence of nonlinear waves. Then we will develop the analytical form of pressure-type Kutta condition for free-surface flows. That form of Kutta condition is exploited in the present section for the study of lifting bodies beneath the free surface in the absence of incident waves. Moreover it could be exploited in the problem of lifting flows around bodies in nonlinear waves in a numerical wave tank as explained in Sec.3.6 or by following the approach presented in Chapter 4 were the Bernoulli's equation and the Kutta condition that will be presented here are exploited (Sec.4.4.3).

In contrary with the case of weakly rotational background field (Sec.2.7), the present wave field is irrotational integration of Euler equations can be performed leading to the classical Bernoulli's theorem for the total potential and pressure fields Φ and p , respectively. Therefore, conservation of energy along a stream line in $D(t)$ can be written as follows

$$\frac{p(\mathbf{x};t) - p_{atm}}{\rho} + \partial_t \Phi(\mathbf{x};t) + \frac{1}{2} [\nabla \Phi(\mathbf{x};t)]^2 + gx_3 = C(t) \quad \mathbf{x} \in D(t), \quad (3.15)$$

where the \mathbf{x} -integration constant $C(t)$ is time dependent. However $C(t)$ can be set to zero by redefining the potential as follows

$$\Phi(\mathbf{x};t) = \Phi_1(\mathbf{x};t) + \int^t C(\tau) d\tau, \quad (3.16)$$

thus Eq.(3.15) becomes

$$\frac{p(\mathbf{x};t) - p_{atm}}{\rho} + \partial_t \Phi_1(\mathbf{x};t) + \frac{1}{2} [\nabla \Phi_1(\mathbf{x};t)]^2 + gx_3 = C(t), \quad (3.17)$$

To sum up, we have obtained a formula for the calculation of pressure that is written, after dropping the index 1, in the following form

$$\frac{p(\mathbf{x};t) - p_{atm}}{\rho} + \partial_t \Phi(\mathbf{x};t) + \frac{1}{2} [\nabla \Phi(\mathbf{x};t)]^2 + gx_3 = 0, \quad \mathbf{x} \in D. \quad (3.18)$$

in the above equations p is the pressure at $\mathbf{x} = \{x_1, x_2, x_3\}$, p_{atm} is the atmospheric pressure on the free surface, ρ is the density of the fluid, g is the acceleration of gravity and the last term is the hydrostatic component. When using that form of Bernoulli's equation to calculate forces acting on the body (especially for free-floating or semi-activated systems; see Sec.4.5.4) we should either omit the hydrostatic term or include to the calculation the gravitational force acting on the body that depends to its mass. Moreover, $\partial_t(\cdot)$ denotes the rate of change with respect to an earth-fixed (inertial) observer (i.e. with regard to an inertial reference frame).

The time derivative of the potential with respect to the moving, with the body velocity, frame of reference can be calculated by the following formula

$$d_t \Phi(\mathbf{x};t) = \nabla \Phi(\mathbf{x};t) \cdot \mathbf{V}_B(\mathbf{x};t) + \partial_t \Phi(\mathbf{x};t), \quad \mathbf{x} \in \partial D_B(t). \quad (3.19)$$

More details concerning the derivation of the above formula can be found e.g. in the following references Katz and Plotkin (2001), Politis (2004), Politis (2011b), Filippas (2013). By replacing Eq.(3.19) into Eq.(3.18), we obtain a formula for pressure calculation on body boundary, as follows

$$\frac{p(\mathbf{x};t) - p_{atm}}{\rho} = -d_t\Phi(\mathbf{x};t) + \nabla\Phi(\mathbf{x};t) \cdot \mathbf{V}_B(\mathbf{x};t) - \frac{1}{2} [\nabla\Phi(\mathbf{x};t)]^2 - gx_3, \quad \mathbf{x} \in \partial D_B(t). \quad (3.20)$$

Moreover, the boundary value of the space gradient of the potential can be decomposed to its tangential and vertical components according to Eq.(2.67) and the body boundary condition (Eq.3.2), as follows³

$$\begin{aligned} \nabla\Phi(\mathbf{x};t) &= \partial_s\Phi(\mathbf{x};t) \times \mathbf{n}(\mathbf{x};t) + \partial_n\Phi(\mathbf{x};t) \cdot \mathbf{n}(\mathbf{x};t) \\ &= \mathbf{V}_t(\mathbf{x};t) + [\mathbf{V}_B(\mathbf{x};t) \cdot \mathbf{n}(\mathbf{x};t)] \cdot \mathbf{n}(\mathbf{x};t) \\ &= \mathbf{V}_t(\mathbf{x};t) + b(\mathbf{x};t)\mathbf{n}(\mathbf{x};t), \quad \mathbf{x} \in \partial D_B(t). \end{aligned} \quad (3.21)$$

Therefore, Eq.(3.20), after some algebra, becomes

$$\begin{aligned} \frac{p(\mathbf{x};t) - p_{atm}}{\rho} &= -d_t\Phi(\mathbf{x};t) + \mathbf{V}_t(\mathbf{x};t) \cdot \mathbf{V}_B(\mathbf{x};t) \\ &\quad - \frac{1}{2} [\mathbf{V}_t(\mathbf{x};t)]^2 + \frac{1}{2} b^2(\mathbf{x};t) - gx_3, \quad \mathbf{x} \in \partial D_B(t). \end{aligned} \quad (3.22)$$

The above form of Bernoulli's equation is utilised for pressure calculations on the body boundary. Then the boundary pressure can be integrated to obtain generalised forces (forces and moments) and by exploiting also the local generalised velocity (linear and angular).

The classical Pressure-type Kutta condition in the following form can be produced from the dynamic boundary condition on the wake by demanding that the pressure field (and therefore the pressure jump) ought to be continuous in \bar{D} as explained in Sec.2.8

$$\lim_{\xi \rightarrow \xi_{TE}} \left\{ p_B^u[\mathbf{x}_B(\xi, \eta); t] - p_B^l[\mathbf{x}_B(\xi, \eta); t] \right\} = 0, \quad \mathbf{x}_B \in \partial D_B(t) \text{ and } \mathbf{x}_{TE} \in \partial D_B(t) \cup \partial D_W(t), \quad (3.23)$$

To proceed, we apply Bernoulli's theorem (Eq.3.18) to the upper and lower side of the trailing edge, we use pressure-type Kutta condition (Eq.3.23) and we factorise the difference of squares to construct the following form of the condition

$$\lim_{\xi \rightarrow \xi_{TE}} F_{fs}^{PK}[\mathbf{x}_B(\xi, \eta); t] = 0, \quad \mathbf{x}_B \in \partial D_B \text{ and } \mathbf{x}_{TE} \in \partial D_B \cup \partial D_W, \quad (3.24)$$

where the operator $F_{fs}^{PK}(\cdot)$ is defined as follows

$$F_{fs}^{PK}[\mathbf{x}_B(\xi, \eta); t] = \partial_t(\Phi^u - \Phi^l) + 0.5(\nabla\Phi^u + \nabla\Phi^l) \cdot (\nabla\Phi^u - \nabla\Phi^l) + g(x_3^u - x_3^l). \quad (3.25)$$

The above form of pressure-type Kutta condition written with respect to the inertial reference frame has already been used in the mathematical formulation of the present problem in Sec.3.2,

³In the present paragraph the tangential velocity is convenient to be denoted as $\mathbf{V}_t = \partial_s\Phi \times \mathbf{n}$.

Eqs.(3.13&3.14). For the calculation of pressure from the boundary values of the potential, that is the primary unknown is the present direct formulation, the reformulation of the above relation with respect to the moving reference frame is required. Aiming to the construction of the aforementioned formula we begin with Eq.(3.20), that is rewritten bellow

$$\frac{p(\mathbf{x};t) - p_{atm}}{\rho} = -d_t\Phi(\mathbf{x};t) + \nabla\Phi(\mathbf{x};t) \cdot \mathbf{V}_B(\mathbf{x};t) - \frac{1}{2} [\nabla\Phi(\mathbf{x};t)]^2 - gx_3, \quad \mathbf{x} \in \partial D_B(t). \quad (3.26)$$

By rearranging terms, making common factor $-1/2$ and adding and subtracting the quantity $-1/2 [\mathbf{V}_B(\mathbf{x};t)]^2$, we obtain the following formula

$$\frac{p(\mathbf{x};t) - p_{atm}}{\rho} = -d_t\Phi - \frac{1}{2} \left[(\nabla\Phi)^2 - 2\nabla\Phi \cdot \mathbf{V}_B + (\mathbf{V}_B)^2 - (\mathbf{V}_B)^2 \right]. \quad (3.27)$$

Moreover, we factorise the difference of squares to construct the following form of Bernoulli's theorem

$$\frac{p(\mathbf{x};t) - p_{atm}}{\rho} = -d_t\Phi - \frac{1}{2} (\nabla\Phi - \mathbf{V}_B)^2 + \frac{1}{2} (\mathbf{V}_B)^2. \quad (3.28)$$

To proceed further, we apply the above form of Bernoulli's theorem to the upper and lower side of the trailing edge, we use pressure-type Kutta condition (Eq.3.23) to construct the following form of the operator $F_{fs}^{PK}(\cdot)$

$$\begin{aligned} F_{fs}^{PK}[\mathbf{x}_B(\xi, \eta); t] &= d_t(\Phi^u - \Phi^l) + \frac{1}{2} (\nabla\Phi^u - \mathbf{V}_B^u)^2 - \frac{1}{2} (\nabla\Phi^l - \mathbf{V}_B^l)^2 \\ &\quad + \frac{1}{2} (\mathbf{V}_B^l)^2 - \frac{1}{2} (\mathbf{V}_B^u)^2. \end{aligned} \quad (3.29)$$

Moreover, the boundary value of the space gradient of the potential can be decomposed to its tangential and the vertical components according to Eq.(2.67) and the body boundary condition (Eq.2.4), as follows

$$\begin{aligned} \nabla\Phi(\mathbf{x};t) &= \partial_s\Phi(\mathbf{x};t) \times \mathbf{n}(\mathbf{x};t) + \partial_n\Phi(\mathbf{x};t) \cdot \mathbf{n}(\mathbf{x};t) \\ &= \mathbf{V}_t(\mathbf{x};t) + \{[\mathbf{V}_B(\mathbf{x};t) - \mathbf{V}_G(\mathbf{x};t)] \cdot \mathbf{n}(\mathbf{x};t)\} \cdot \mathbf{n}(\mathbf{x};t) \\ &= \mathbf{V}_t(\mathbf{x};t) + b(\mathbf{x};t)\mathbf{n}(\mathbf{x};t), \quad \mathbf{x} \in \partial D_B(t). \end{aligned} \quad (3.30)$$

With the aid of Eq.(3.30), the operator $F_{fs}^{PK}(\cdot)$ becomes

$$\begin{aligned} F_{fs}^{PK}[\mathbf{x}_B(\xi, \eta); t] &= d_t(\Phi^u - \Phi^l) + \frac{1}{2} (\mathbf{V}_t^u + b^u\mathbf{n}^u - \mathbf{V}_B^u)^2 - \frac{1}{2} (\mathbf{V}_t^l + b^l\mathbf{n}^l - \mathbf{V}_B^l)^2 \\ &\quad + \frac{1}{2} (\mathbf{V}_B^l)^2 - \frac{1}{2} (\mathbf{V}_B^u)^2. \end{aligned} \quad (3.31)$$

Moreover, by factorising the difference of the squares and rearranging terms, we obtain the following form of pressure-type Kutta condition

$$\lim_{\xi \rightarrow \xi_{TE}} F_{fs}^{PK}[\mathbf{x}_B(\xi, \eta); t] = 0, \quad \mathbf{x}_B \in \partial D_B \text{ and } \mathbf{x}_{TE} \in \partial D_B \cup \partial D_W, \quad (3.32)$$

where

$$F_{fs}^{PK}[\mathbf{x}_B(\xi, \eta); t] = d_t(\Phi^u - \Phi^l) + \left(\frac{\mathbf{V}_t^u + \mathbf{V}_t^l}{2} + \frac{b^u \mathbf{n}^u + b^l \mathbf{n}^l}{2} - \frac{\mathbf{V}_B^u + \mathbf{V}_B^l}{2} \right) \left[\mathbf{V}_t^u - \mathbf{V}_t^l + b^u \mathbf{n}^u - b^l \mathbf{n}^l - (\mathbf{V}_B^u - \mathbf{V}_B^l) \right] - \left(\frac{\mathbf{V}_B^u + \mathbf{V}_B^l}{2} \right) (\mathbf{V}_B^u - \mathbf{V}_B^l). \quad (3.33)$$

The above relation⁴ is the pressure-type Kutta condition with respect to the body-fixed reference frame. That equation includes a quadratic nonlinear form of the unknown boundary value of the tangential velocity \mathbf{V}_t and linear terms. It also includes the unknown boundary value of the potential Φ at the body contour as approaching the trailing edge. As will be demonstrated in the following section the continuous boundary field \mathbf{V}_t is approximated by a discrete tangential velocity field that is projected to a curvilinear coordinated system (see also Sec.2.5.2.1). Moreover, it is approximated by CUFDM (see also Sec.2.5.2.2) and replaced with linear combinations of Φ . Then an extended form of the DtN operator (see Sec.3.5.1 and Sec.3.5.2) will be exploited to replace all the unknowns by linear functions of the dynamic variables of the problem that will be the potential on the free surface, the free-surface elevation and potential jump (dipole intensity) at the Kutta strip.

For simplicity in the description of the present method, and especially as concerns the treatment of the free-surface conditions (including the conditions at infinity), we will start our presentation with the boundary integral formulation in the case of non-lifting flow around a body of smooth but arbitrary geometry, undergoing general motion. This problem contains as cases of special interest the wave-resistance problem due to constant-speed forward motion and the enforced radiation problem due to body oscillations. Then, in Sec.3.5 the whole methodology is extended to the case of an oscillating hydrofoil in forward motion beneath the free surface radiating waves.

3.4 Boundary integral formulation of non-lifting bodies beneath the free surface

Applying Green's theorem to the present nonlifting problem Eqs.(3.1-3.8), we obtain the following two integral representations for the potential in \bar{D} in terms of the potential Φ (dipole intensity) and its normal derivative $\partial_n \Phi$ (source intensity), the first on the body boundary and

⁴The terms in the Eq.(2.125) are mean values and differences of the upper and lower side functions on the body boundary. Some of those fields are continuous at the trailing edge, however when discretisation is applied and a BEM is exploited for calculations, the vicinity of the trailing edge is modeled by neighboring to the trailing edge panels. In that case, the upper and lower elements are not identical and the same applies to the boundary field values. Therefore, it is important for the accurate and stable imposition of Kutta condition, those mean values and differences to be considered in the calculations.

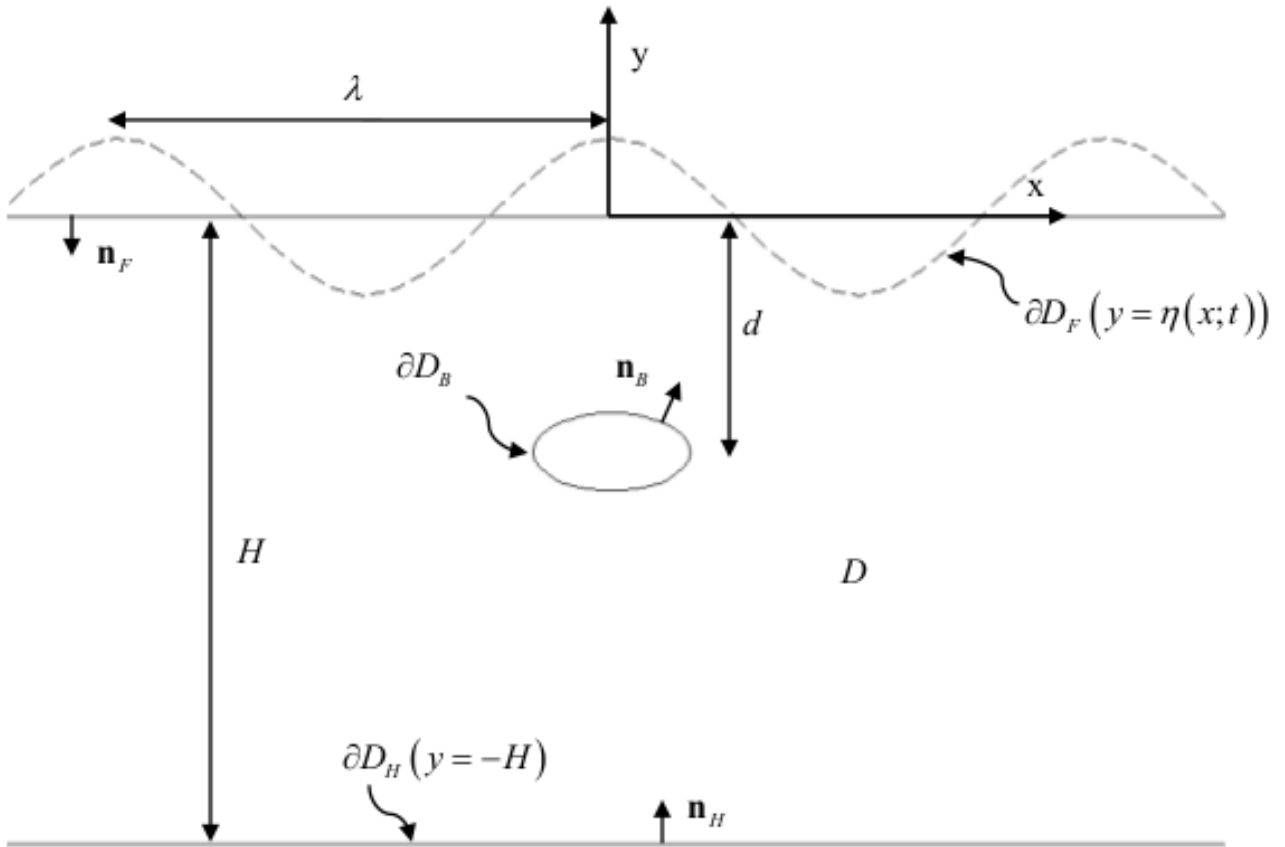


Figure 3.2: Definition of the studied problem in the case of a smooth nonlifting body, moving under the free surface (at mean submergence d). The free surface is initially still and the waves are generated from the motion of moving boundaries.

the second on the free-surface boundary, written compactly as follows

$$\begin{aligned} \Phi(\mathbf{x}_0; t) - \Phi_J(\mathbf{x}_0; t) = & \int_{\partial D_B(t)} \partial_n \Phi_B(\mathbf{x}; t) G_s(\mathbf{x}_0 | \mathbf{x}) - \Phi_B(\mathbf{x}; t) \partial_n G_s(\mathbf{x}_0 | \mathbf{x}) ds(\mathbf{x}) \\ & + \int_{\partial D_F(t)} \partial_n \Phi_F(\mathbf{x}; t) G_s(\mathbf{x}_0 | \mathbf{x}) - \Phi_F(\mathbf{x}; t) \partial_n G_s(\mathbf{x}_0 | \mathbf{x}) ds(\mathbf{x}), \quad \mathbf{x}_0 \in \partial D_B(t) \cup \partial D_F(t) \end{aligned} \quad (3.34)$$

where

$$\Phi(\mathbf{x}_0; t) - \Phi_J(\mathbf{x}_0; t) = \begin{cases} \Phi(\mathbf{x}_0; t), & \mathbf{x}_0 \in D, \\ \Phi_B(\mathbf{x}_0; t) - \frac{\text{sign}(\mathbf{r} \cdot \mathbf{n})}{2} \Phi_B(\mathbf{x}_0; t), & \mathbf{x}_0 \in \partial D_B, \\ \Phi_F(\mathbf{x}_0; t) - \frac{\text{sign}(\mathbf{r} \cdot \mathbf{n})}{2} \Phi_F(\mathbf{x}_0; t), & \mathbf{x}_0 \in \partial D_F, \end{cases} \quad (3.35)$$

In the above relation we have used Green's function (Eq.2.16), consisted of the fundamental solution of 2D/3D Laplace equation corresponding to a Rankine source plus a regular part,

corresponding to a mirror source with respect to the bottom surface and the normal to the boundary derivative of the total Green's function. The total Green's function is denoted with G_s and its normal derivative with $\partial_n G_s$. In this way and in the case of flat bottom, the boundary condition Eq.(3.3) is identically satisfied and the corresponding boundary term of the integral representation is dropped. For simplicity, the case of general bathymetry is not presented in the present section; for more details in that interesting problem see Sec.4.5.1, Sec.4.5.4 and Filippas et al. (2018).

The first integral in Eq.(3.34) represents the effect of the body while the second the effect of the free-surface, on the potential. The first term in the integrals is the potential induced at \mathbf{x}_0 from a source with intensity $\partial_n \Phi(\mathbf{x})$ located on the boundary at \mathbf{x} , while the second term represents similarly the effect of normal to the boundary dipole with intensity $\Phi(\mathbf{x})$. In this way the whole information for the potential in the domain D is stored on the boundary ∂D whose dimension is of one order lower. Therefore, if the trace of the potential and the derivative on the boundary are known, using Green's formula Eqs.(3.34, 3.35) we can evaluate potential everywhere in D .

Replacing body boundary condition Eq.(3.2) into the representation theorem on the boundary Eqs.(3.34, 3.35), we obtain the following two Fredholm 2nd kind weakly singular integral equations

$$\begin{aligned} & - \int_{\partial D_F(t)} \partial_n \Phi_F(\mathbf{x}; t) G_s(\mathbf{x}_0 | \mathbf{x}) ds(\mathbf{x}) \\ \frac{1}{2} \Phi_B(\mathbf{x}_0; t) + \int_{\partial D_B(t)} \Phi_B(\mathbf{x}; t) \partial_n G_s(\mathbf{x}_0 | \mathbf{x}) ds(\mathbf{x}) = & - \int_{\partial D_F(t)} \Phi_F(\mathbf{x}; t) \partial_n G_s(\mathbf{x}_0 | \mathbf{x}) ds(\mathbf{x}) \\ & + \int_{\partial D_B(t)} b(\mathbf{x}; t) G_s(\mathbf{x}_0 | \mathbf{x}) ds(\mathbf{x}), \quad \mathbf{x}_0 \in \partial D_B(t) \end{aligned} \quad (3.36)$$

and

$$\begin{aligned} & - \int_{\partial D_F(t)} \partial_n \Phi_F(\mathbf{x}; t) G_s(\mathbf{x}_0 | \mathbf{x}) ds(\mathbf{x}) \\ + \int_{\partial D_B(t)} \Phi_B(\mathbf{x}; t) \partial_n G_s(\mathbf{x}_0 | \mathbf{x}) ds(\mathbf{x}) = & - \frac{1}{2} \Phi_F(\mathbf{x}_0; t) - \int_{\partial D_F(t)} \Phi_F(\mathbf{x}; t) \partial_n G_s(\mathbf{x}_0 | \mathbf{x}) ds(\mathbf{x}) \\ & + \int_{\partial D_B(t)} b(\mathbf{x}; t) G_s(\mathbf{x}_0 | \mathbf{x}) ds(\mathbf{x}), \quad \mathbf{x}_0 \in \partial D_F(t) \end{aligned} \quad (3.37)$$

The weakly singular boundary integral equation Eqs.(3.36 & 3.37) and the free-surface boundary conditions Eqs.(3.7 & 3.8), provide us with a system of equations for the unknown boundary fields Φ_B on the body and $\Phi_F, \partial_n \Phi_F$ at the free-surface. The above system of equations can be solved numerically after the appropriate discretisation, implemented with a boundary element method (BEM) and collocation, as we will see in the following section. Furthermore, numerical solution of the system can be achieved following two different paths. Either by time integration, where free-surface conditions are treated as a dynamic system and BIE as an algebraic constraint, or using a finite difference method (FDM) for the temporal discretisation of

free-surface conditions. In the later case, BIE and free-surface conditions are treated similarly forming a non-linear algebraic system. The first approach is adopted in the present work and is described in detail at the following sections.

3.4.1 Discretisation the DtN map

The spacial discretisation mainly consists of the following approximations of the analytical model:

- Concerning the geometry, a C^0 representation of the boundary is used as follows:
 - in 2D formulation, following a low-order panel method, the body contour is replaced by a closed polygonal line, and N_B denotes the number of panels. The free surface is also approximated by open polygonal lines composed of N_F panels, respectively.
 - in 3D formulation, the boundary is approximated using bilinear-quadrilateral elements.
- Concerning the representation of the functions on the boundary, the potential and its normal derivative at each time step, are approximated by piecewise constant distributions, as follows:

$$\begin{aligned}
 \Phi_F(\mathbf{x}; t) &= \Phi_{Ff}(t), \quad \text{at free-surface element } f, \quad f = 0, 1, \dots, N_F - 1, \\
 \partial_n \Phi_F(\mathbf{x}; t) &= \partial_n \Phi_{Ff}(t), \quad \text{at free-surface element } f, \quad f = 0, 1, \dots, N_F - 1, \\
 \Phi_B(\mathbf{x}; t) &= \Phi_{Bi}(t), \quad \text{at body element } i, \quad i = 0, 1, \dots, N_B - 1, \\
 \partial_n \Phi_B(\mathbf{x}; t) &= \partial_n \Phi_{Bi}(t) = b_i(t), \quad \text{at body element } i, \quad i = 0, 1, \dots, N_B - 1.
 \end{aligned} \tag{3.38}$$

- Finally, following a collocation scheme, the BIEs (Eqs.3.36 & 3.37) are satisfied in a finite number of points (or control points) and in order to avoid singularities the centroids of the elements have been chosen as collocation points.

To proceed, the discretised form the of the BIEs (Eqs.3.36 & 3.37) is as follows

$$\mathcal{A}_{F,B}^{pot}(t) \cdot \begin{pmatrix} \mathbf{N}_F(t) \\ \Phi_B(t) \end{pmatrix} = \mathcal{B}_{F,B}^{pot}(t) \cdot \begin{pmatrix} \Phi_F(t) \\ \mathbf{b}(t) \end{pmatrix}, \tag{3.39}$$

where

$$\mathcal{A}_{F,B}^{pot}(t) = \begin{pmatrix} \mathcal{A}_{F,B,00}^{pot}(t) & \mathcal{A}_{F,B,01}^{pot}(t) \\ \mathcal{A}_{F,B,10}^{pot}(t) & \mathcal{A}_{F,B,11}^{pot}(t) \end{pmatrix} \quad \text{and} \quad \mathcal{B}_{F,B}^{pot}(t) = \begin{pmatrix} \mathcal{B}_{F,B,00}^{pot}(t) & \mathcal{B}_{F,B,01}^{pot}(t) \\ \mathcal{B}_{F,B,10}^{pot}(t) & \mathcal{B}_{F,B,11}^{pot}(t) \end{pmatrix}. \tag{3.40}$$

In the above equations $\mathcal{A}_{F,B}^{pot}(t), \mathcal{B}_{F,B}^{pot}(t)$ are the potential induction-factor matrices at the left hand side and the right hand side of Eqs.(3.36 & 3.37), respectively. They model free surface-free surface, body-body and free surface-body interactions. The above matrices are defined as

follows

$$\begin{aligned}
\mathcal{A}_{F,B,00}^{pot}(t) &= \{-S_{fs}^{pot}(t)\}, \quad \mathcal{A}_{F,B,01}^{pot}(t) = \{D_{fj}^{pot}(t)\}, \\
\mathcal{A}_{F,B,10}^{pot}(t) &= \{-S_{is}^{pot}(t)\}, \quad \mathcal{A}_{F,B,11}^{pot} = \{0.5\delta_{ij} + D_{ij}^{pot}\}, \\
\mathcal{B}_{F,B,00}^{pot}(t) &= \{-0.5\delta_{fs} - D_{fs}^{pot}(t)\}, \quad \mathcal{B}_{F,B,01}^{pot}(t) = \{S_{fj}^{pot}(t)\}, \\
\mathcal{B}_{F,B,10}^{pot}(t) &= \{-D_{is}^{pot}(t)\}, \quad \mathcal{B}_{F,B,11}^{pot} = \{S_{ij}^{pot}\},
\end{aligned} \tag{3.41}$$

with \mathcal{S} denoting source or single-layer integrals, and with \mathcal{D} denoting dipole or double-layer integrals see Eq.(2.23). Moreover, the indices belong to the following subsets of \mathbb{N}

$$f, s \in \{0, 1, \dots, N_F - 1\}, \quad i, j \in \{0, 1, \dots, N_B - 1\}. \tag{3.42}$$

In Eq.(3.39) $\Phi_F = \{\Phi_{Fs}\}$, $\mathbf{N}_F = \{\partial_n \Phi_{Fs}\}$, $\Phi_B = \{\Phi_{Bj}\}$, $\mathbf{b} = \{b_j\}$. In the sequel, we will denote with bold, vectors containing the values of piecewise constant trace functions on the boundary elements, at various parts of the boundary.

Next we multiply Eq.(3.39) with $[\mathcal{A}_{F,B}^{pot}(t)]^{-1}$ and we obtain

$$\begin{pmatrix} \mathbf{N}_F(t) \\ \Phi_B(t) \end{pmatrix} = \mathcal{G}(t) \cdot \begin{pmatrix} \Phi_F(t) \\ \mathbf{b}(t) \end{pmatrix}, \tag{3.43}$$

or

$$\begin{pmatrix} \mathbf{N}_F(t) \\ \Phi_B(t) \end{pmatrix} = \begin{pmatrix} \mathcal{G}_{00}(t) & \mathcal{G}_{01}(t) \\ \mathcal{G}_{10}(t) & \mathcal{G}_{11}(t) \end{pmatrix} \cdot \begin{pmatrix} \Phi_F(t) \\ \mathbf{b}(t) \end{pmatrix}, \tag{3.44}$$

where

$$\mathcal{G}(t) = [\mathcal{A}_{F,B}^{pot}(t)]^{-1} \cdot \mathcal{B}_{F,B}^{pot}(t). \tag{3.45}$$

The above mapping is a discrete Dirichlet-to-Neumann (DtN) operator⁵ that connects the potential (Dirichlet data) with its normal derivative (Neumann data) on body boundary ∂D_B . We observe in the above equation that the effect of the body velocity is considered through the component \mathbf{V}_B , included in \mathbf{b} , as described by the body boundary condition Eq.(3.2). In Sec.3.4.2 using the appropriate part of the DtN map, Eqs.(3.43-3.45), in the discretised form free-surface boundary conditions, we will obtain a system of (spatially and temporarily) nonlocal differential equations, with explicit and implicit nonlinearities, that approximately describe the dynamics of the system.

⁵The terminology DtN operator is common in the modeling of inviscid water waves. Here we derive a DtN operator for non-lifting flow around smooth bodies beneath the free surface. In Sec.3.5.1 the extended form of the DtN operator, that is suitable for lifting flows beneath the free surface, will be constructed.

3.4.2 Discretised free-surface boundary conditions and the dynamical system

We apply discretisation with BEM and collocation as described in detail in Secs.3.4.1 & 2.5.2.2. We consider the collection of discretised data that are families of scalars or vectors. They are ordered following x_1 -major numbering. In this way, ordered lists (systems) are created, that represent the collocation points (containing vectors of \mathbb{R}^3), the discretised potential field (containing real numbers), the discretised gradient of the free-surface potential field (containing vectors of \mathbb{R}^3) or the covariant components of the tangential velocity (containing real numbers). The systems that are arranged x_1 -majorly will be denoted using $|_1$. To proceed, the free-surface conditions are applied at the free-surface collocation points. Therefore, we have the aforementioned collocation points $\mathbf{x}_0|_1 = \{\mathbf{x}_{0f}\}$ with $f \in \{0, 1, \dots, N_F - 1\}$, where N_F is the total number of the free-surface collocation points, the free-surface potential $\Phi_F|_1 = \{\Phi_{F,f}\}$, the free-surface elevation $\eta|_1 = \{\eta_f\}$, the trace of the gradient of the free-surface potential $\mathbf{V}_F|_1 = \{\nabla\Phi_f\}$, the metric of the free surface $\mathbf{a}|_1 = \{\sqrt{a_f}\}$, the free-surface tangential velocity $\mathbf{V}_{F,t}|_1 = \{\mathbf{V}_{F,t,f}\}$, the first component (x_1 -wise) of the covariant derivative of the free-surface potential $\mathbf{V}_{F,t,1}|_1 = \{V_{F,t,1,f}\}$, the second component (x_2 -wise) of the covariant derivative of the free-surface potential $\mathbf{V}_{F,t,2}|_1 = \{V_{F,t,2,f}\}$. Moreover, the free-surface Neumann-data discretised vector field is $\mathbf{N}_F|_1 = \{\partial_n\Phi_{F,f}\}$ and the discretised normal vector field $\mathbf{n}_F|_1 = \{\mathbf{n}_{F,f}\}$. The discretised form of free-surface boundary conditions (Eqs.3.7 & 3.8) are as follows

$$\partial_t\Phi_F|_1 = -g\eta|_1 - \frac{1}{2}[\mathbf{V}_{F,t}|_1 + \mathbf{N}_F|_1 \cdot \mathbf{n}_F|_1]^2, \quad \mathbf{x} \in \partial D_F(t), \quad (3.46)$$

$$\partial_t\eta|_1 = -\mathbf{N}_F|_1 \cdot \mathbf{a}|_1, \quad \mathbf{x} \in \partial D_F(t), \quad (3.47)$$

The discretised free-surface tangential velocity vector field $\mathbf{V}_{F,t}$ is expanded with respect to a curvilinear coordinate system and its covariant base, using the velocity contravariant components (see Sec.2.5.2.1), as follows

$$\mathbf{V}_{F,t}|_1 = (\mathbf{V}_{F,t,j})^j|_1 \cdot \mathbf{e}_j|_1, \quad j \in \{1, 2\}. \quad (3.48)$$

where \mathbf{e}_j are the systems of vectors that represents the base vectors discretised vector fields $\mathbf{e}_j|_2 = \{\mathbf{e}_{ji}\}$, $j \in \{1, 2\}$, $i \in \{0, 1, \dots, N_F - 1\}$ and the dot product is between systems of vectors.

The contravariant components of the velocity can be calculated when the covariant components are known as follows

$$(\mathbf{V}_{F,t,j})^j|_1 = \mathbf{g}^{jk}|_1 (\mathbf{V}_{F,t,k})_k|_1, \quad j, k \in \{1, 2\}. \quad (3.49)$$

where \mathbf{g}^{jk} is a system that contains the contravariant components of the metric tensor at the collocation points; i.e. $\mathbf{g}^{jk}|_2 = \{g_i^{jk}\}$, $j, k \in \{1, 2\}$, $i \in \{0, 1, \dots, N_{PK} - 1\}$.

By applying CUFD we can approximate the covariant component of the free-surface tangential velocities by the neighboring free-surface potential values (see Sec.2.5.2.2) as follows

$$(\mathbf{V}_{F,t,1})_1|_1 = \mathcal{D}(\mathbf{x}_0|_1) \cdot \Phi_F|_1. \quad (3.50)$$

$$(\mathbf{V}_{F,t,2})_2|_1 = [\mathcal{D}(\mathbf{x}_0|_2) \cdot \Phi_F|_2]^\top = \left[\mathcal{D}(\mathbf{x}_0|_2) \cdot (\Phi_F|_1)^\top \right]^\top. \quad (3.51)$$

The above detailed analysis enlightens the fact that the discretised trace tangential velocity $\mathbf{V}_{F,t}$ can be expressed as a function of the discretised trace of the free-surface potential Φ_F in the context of our approximation; i.e. $\mathbf{V}_{F,t}|_1 = \mathcal{V}_{CUFDM}(\Phi_F|_1)$.

At the final stage the discretised free-surface conditions (Eqs.3.46 & 3.47) will be exploited for the construction of the dynamical-system equations in the form $d_t \mathbf{U} = \mathbf{f}(\mathbf{U})$, where the system-derivative \mathbf{f} is a function of the dynamic variables collected into the 1st-order system $\mathbf{U} = \{\Phi_F, \eta\}$. In order to obtain that form of free-surface conditions we recall the appropriate part of the discretised DtN operator constructed in Sec.3.4.1, Eqs.(3.43-3.45)

$$\mathbf{N}_F(t)|_1 = \mathcal{G}_{00}(t) \cdot \Phi_F(t)|_1 + \mathcal{G}_{01}(t) \cdot \mathbf{b}(t)|_1. \quad (3.52)$$

In the above linear relation the unknown discretised fields are the systems of Neumann and Dirichlet data on the free-surface; i.e. the normal derivative of the free-surface potential $\mathbf{N}_F|_1$ and the free-surface potential $\Phi_F|_1$. The Neumann data on the body \mathbf{b} and are known from the prescribed kinematics. Therefore, the discretised free-surface conditions (Eqs.3.46 & 3.47) together with the appropriate part of the discretised DtN operator Eq.(3.52) are a system of (spatially and temporarily) nonlocal partial differential equations, with explicit and implicit nonlinearities and a linear algebraic constraint.

In the sequel, the algebraic constraint is used in order to express the system-derivative \mathbf{f} as a function of the dynamic variables collected into the 1st-order system $\mathbf{U} = \{\Phi_F, \eta\}$. To proceed, the discretised normal derivative of the free-surface potential field \mathbf{N}_F with the aid of Eq.(3.52) becomes a function of Φ_F ; i.e. $\mathbf{N}_F(t)|_1 = \mathcal{DTN}_0(\Phi_F(t)|_1)$. The free-surface boundary conditions become

$$\partial_t \Phi_F|_1 = -g\eta|_1 - \frac{1}{2}[\mathcal{V}_{CUFDM}(\Phi_F|_1) + \mathcal{DTN}_0(\Phi_F(t)|_1) \cdot \mathbf{n}_F|_1]^2, \quad \mathbf{x} \in \partial D_F(t), \quad (3.53)$$

$$\partial_t \eta|_1 = -\mathcal{DTN}_0(\Phi_F(t)|_1) \cdot \mathbf{a}|_1, \quad \mathbf{x} \in \partial D_F(t), \quad (3.54)$$

Eqs.(3.53 & 3.54) can be numerically integrated in order to calculate evolution of the dynamic variables collected into the 1st-order system $\mathbf{U} = \{\Phi_F, \eta\}$, based on information concerning the functions Φ_F, η at previous time steps, in conjunction with the Neumann data \mathbf{b} on the body boundary, known at every time step from the body motion as described by the body boundary condition Eq.(3.2).

Moreover, the free-surface-boundary nodes are updated every time that the the free-surface at the collocation points changes. However the free-surface elevation is known only at the collocation points and its values are stored in η . The bilinear 4-node boundary elements construct a basic grid with global nodes located at the local element nodes. The values of the free-surface elevation can be obtained everywhere by interpolation, when the nodal values of the free-surface are known. In order to calculate the nodal values of the free-surface elevation a staggered grid, with nodes at the collocation points, is exploited. The staggered-grid nodal values are given by the free-surface elevation η . Then by interpolation, using the staggered grid, the basic-grid nodal values are obtained. Next by interpolation, using the basic grid, the free-surface potential is obtained everywhere. In this way, the free-surface boundary is updated

and the relative quantities like the metric $\mathbf{a}|_1$ and the free-surface unit normal vector $\mathbf{n}_F|_1$ are updated.

Subsequently, following part of the updated discretised DtN map (Eqs.3.43 - 3.45) is used to calculate the remaining unknown discretised body Dirichlet boundary field values Φ_B

$$\Phi_B(t)|_1 = \mathcal{G}_{10}(t) \cdot \Phi_F(t)|_1 + \mathcal{G}_{11}(t) \cdot \mathbf{b}(t)|_1. \quad (3.55)$$

3.4.3 Numerical time integration of the system

Starting from a prescribed initial condition, e.g. from rest, a time-stepping method is applied to obtain the numerical solution. After evaluation of different methods, we found that the higher-order Adams-Bashforth-Moulton predictor-corrector method provides the required accuracy, stability and efficiency; see Sec.2.9, Longuet-Higgins and Cokelet (1976) and Johannessen and Swan (1997). To be more precise, if we know $\mathbf{U}(t)$ at time t , we have at the corrector step

$$\mathbf{U}(t + \Delta t) = \mathbf{U}(t) + \frac{\Delta t}{24} [9\mathbf{f}_{pre}(t + \Delta t) + 19\mathbf{f}(t) - 5\mathbf{f}(t - \Delta t) + \mathbf{f}(t - 2\Delta t)]. \quad (3.56)$$

with predictor

$$\mathbf{f}_{pre}(t + \Delta t) = \mathbf{f}_{t+\Delta t} [\mathbf{U}_{pre}(t + \Delta t)]. \quad (3.57)$$

and

$$\mathbf{U}_{pre}(t + \Delta t) = \mathbf{U}(t) + \frac{\Delta t}{24} [55\mathbf{f}(t) - 59\mathbf{f}(t - \Delta t) + 37\mathbf{f}(t - 2\Delta t) - 9\mathbf{f}(t - 3\Delta t)]. \quad (3.58)$$

The used scheme requires calculation of only two derivative equations at each time, and the error is of order (Δt^5) , where Δt is the timestep, ensuring that good convergence is achieved. To be more specific, at the predictor step, for the calculation of $\mathbf{U}_{pre}(t + \Delta t)$ in Eq.(3.58), the calculation of derivative $\mathbf{f}(t)$ at the present time t and the corresponding DtN are required, together with the values of the derivatives $\mathbf{f}(t - i\Delta t)$, $i \in \{1, 2, 3\}$ from the past, that have already been obtained. Moreover, at the corrector step in Eq.(3.56), the calculation of $\mathbf{U}(t + \Delta t)$ requires a prediction of the derivative $\mathbf{f}_{pre}(t + \Delta t)$ at the future time $t + \Delta t$. Aiming to this, we use the prediction $\mathbf{U}_{pre}(t + \Delta t)$ into Eq.(3.57) and the DtN is calculated again, that time at the predicted free-surface elevation η_{pre} included in \mathbf{U}_{pre} .

3.4.4 Conditions at infinity - Implementation of PML model

An important task concerning the present time-domain scheme deals with the treatment of the horizontally infinite domain and the implementation of appropriate radiation-type conditions at infinity. Although in the case of purely linear waves, conditions at infinity could be treated using the appropriate time-dependent Green's function, the present work is based on the truncation of the domain and on the use of Perfectly Matched Layer (PML) model, as e.g. described by Berenger (1994) and Turkel and Yefet (1998). The latter model permits the numerical absorption of the waves reaching the ends of the truncated domain with minimum reflection. This selection is motivated by the fact that PML model supports the efficient treatment of the

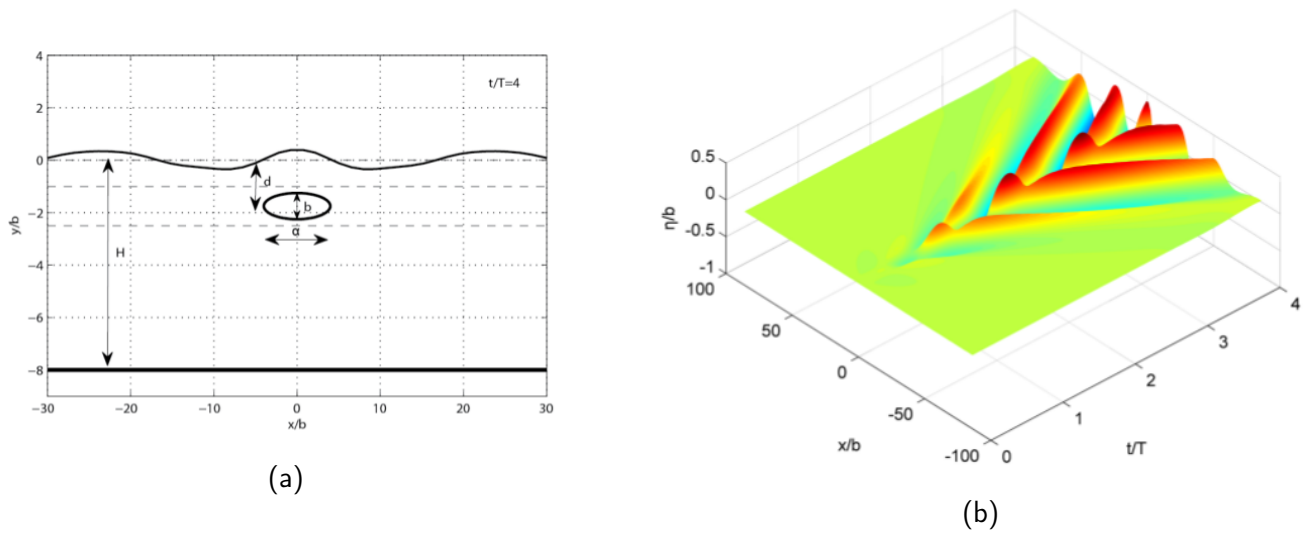


Figure 3.3: Free-surface elevation generated by moderate-amplitude oscillations of an elliptically shaped, fully immersed body at $\omega^2 H/g = 1.63$. (a) Snapshot where The upper and lower limits of heaving motion are shown using dashed lines. (b) Time history of the free-surface elevation.

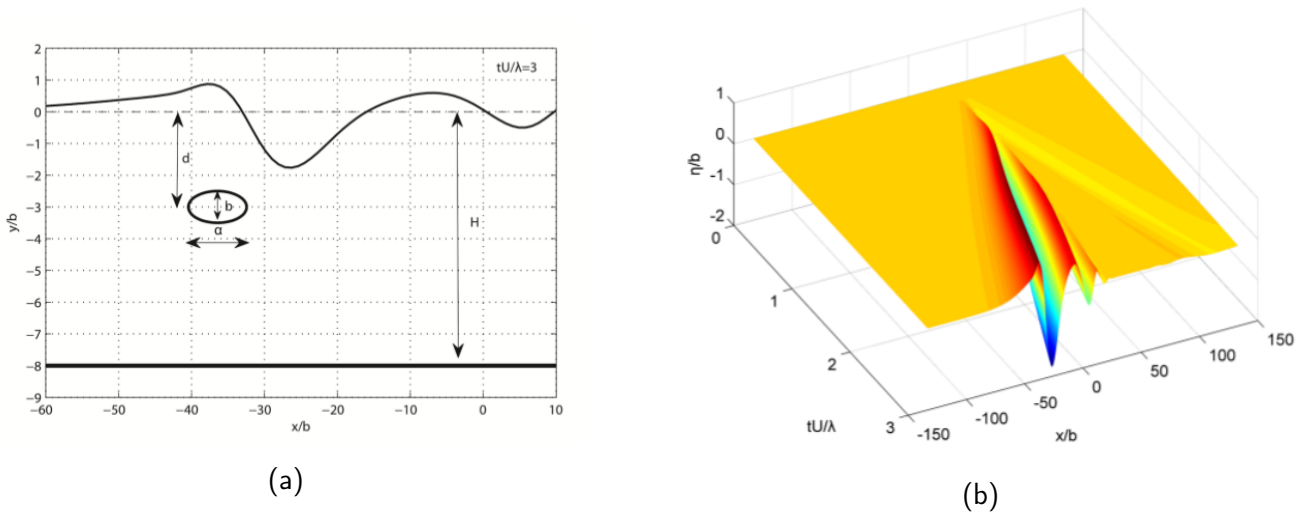


Figure 3.4: Free-surface elevation generated by an elliptically shaped, fully immersed body traveling with constant forward speed at $Fn = U/\sqrt{g a} = 0.71$. (a) Snapshot. (b) Time history of the free-surface elevation.

problem of generation and propagation of non-linear waves excited due to large motion(s) of the moving body at low-submergence depths; see also Belibassakis and Athanassoulis (2011). In order to apply the PML-type absorbing layer, the time-derivative operator in the left hand-side of the dynamical system equations is substituted by the following mixed-type operator:

$$d_t \mathbf{U} + \sigma(\mathbf{x}_F) \mathbf{U} = \mathbf{f}(\mathbf{U}), \quad \text{where } \mathbf{U} = \boldsymbol{\mu}_K, \quad (3.59)$$

where the PML-parameter $\sigma(\mathbf{x}_F)$ is a positive absorption coefficient with support of characteristic size l extended over several wavelengths from the artificial end-type boundaries used in

order to truncate the computational domain. In the present work we use optimum PML coefficients, as described by Collino and Monk (1998) and applied by Belibassakis et al. (2001) and Belibassakis and Athanassoulis (2011) to water wave problems. More details about the PML can be found in our published work Filippas and Belibassakis (2014).

3.4.5 Numerical results and discussion

3.4.5.1 2D calculations

As an example of the forced radiation problem we present in Fig.3.3 the calculated free-surface elevation in the case of an elliptically-shaped, fully immersed body of axis ratio $a/b = 8$ (where a is the length and b the height of the body), performing oscillations in heaving motion with moderate amplitude $h/b = 0.25$, in water of depth $H/b = 8$, after 4 periods starting from rest. The mean submergence is $d/b = 1.75$ and thus, the vertical oscillation is limited in the interval $-2.5 < y/b < -1$, shown using dashed lines in Fig.3.3a. In the examined case the frequency parameter is $\omega^2 H/g$, corresponding to intermediate wave conditions H/λ , where H is water depth and λ the wavelength of the free waves in the water strip at the examined frequency, as predicted by the linear theory $\omega^2 = kg \tanh(kH)$, where $k = 2\pi/\lambda$ is the corresponding wavenumber. Furthermore, the time history of calculated free-surface elevation is plotted in Fig.3.3b all over the horizontal domain for the first 4 periods of oscillation starting from rest. We clearly observe the generation of symmetrical waves propagating to both directions with phase speed C and wavelength $\lambda/b = 28.8$ that is found to be in reasonable compatibility with linearized water-wave theory $\lambda/b = 28.9$.

Moreover, in Fig.3.4, an example concerning the wave-resistance problem is presented. The calculated free-surface elevation generated by the same as before elliptically-shaped, fully immersed body, in constant-speed forward motion at $Fn = U/\sqrt{ga}$, where a is the length of the body, is plotted. The water depth is the same as before $H/b = 8$, while the mean submergence now is greater $d/b = 3$. The examined case corresponds to intermediate wave conditions H/λ , where λ is the wavelength of the free-surface waves in the water strip at the examined constant speed, given by the dispersion relation $F_H^{-2} = kH \tanh(kH)$ corresponding to the bathymetric Froude number $F_H = U/\sqrt{gH} = 0.71$. In this case, the time history of calculated free-surface elevation is plotted in Fig.3.4b, all over the horizontal domain, starting from rest until the nondimensional time $tU/\lambda = 3$. We clearly observe the generation of a small-amplitude transient wave pattern that travels to the positive x -direction while the main wave pattern travels with the speed of the body. After the transient effects have died out, the characteristic wave length of the main pattern $\lambda/b = 24$ is again found in reasonably good compatibility with the predictions by linear theory $\lambda/b = 24.3$.

Moreover, the performance of the PML model is examined in Figs.3.5-3.7 for the example of Fig.3.3. More specifically, the calculated free-surface elevation, after 4 and 8 periods starting from rest, is plotted in the upper and lower subplots of these figures, respectively, as obtained using the PML absorbing layer with parameters $\sigma_0 \in \{0, 2, 4\}$, $p \in \{2, 3, 4\}$ and $l \in \{1\lambda, 1.5\lambda, 2\lambda\}$. In addition, in these figures, our results are compared against a reference numerical solution (indicated using crosses) which is obtained using a very long (characterized as infinite) computational domain ensuring that the generated wave disturbance has not reached its horizontal ends at the two times considered ($t/T = 4$ and 8).

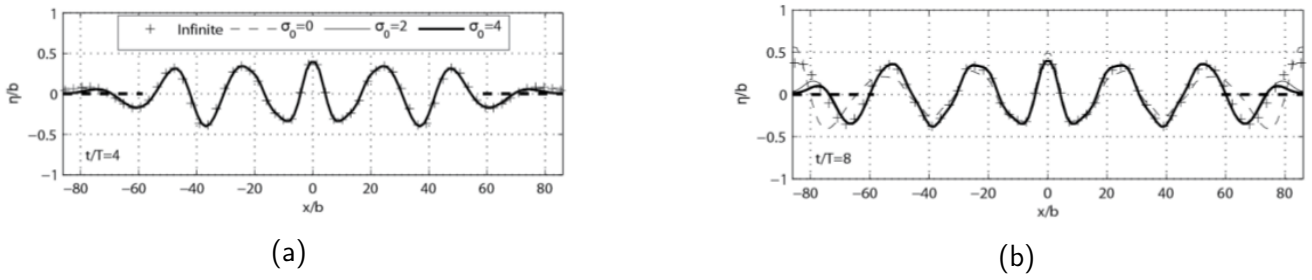


Figure 3.5: Effect of σ_0 -parameter on the efficiency of the PML, for the example of Fig.3.3. The position of PML is indicated by bold dashed lines. The parameter σ_0 controls the magnitude of the $\sigma(x_F)$ distribution.

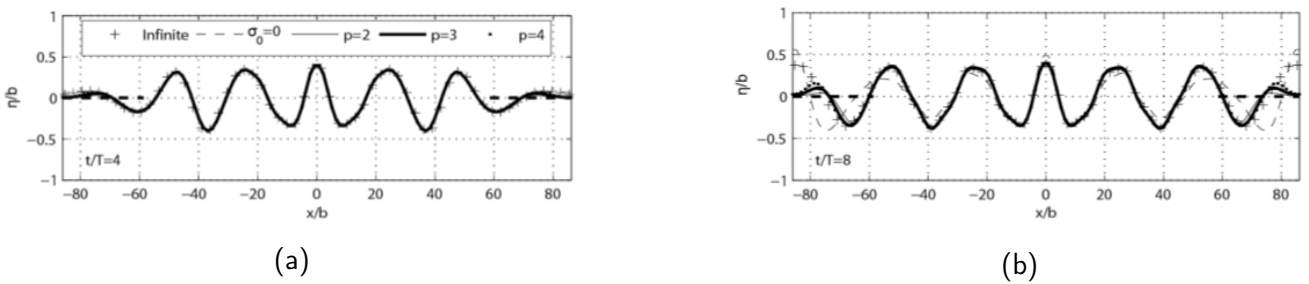


Figure 3.6: Effect of p -parameter on the efficiency of the PML, for the example of Fig.3.3. The position of PML is indicated by bold dashed lines. p is positive parameter that controls the rate of absorption in the PML

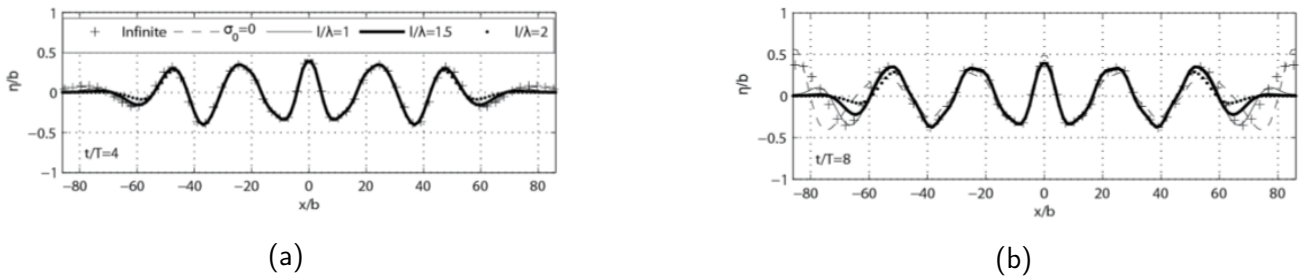


Figure 3.7: Effect of PML thickness λ on the efficiency of the PML, for the example of Fig.3.3. The position of PML is indicated by bold dashed lines. λ adjusts the support of $\sigma(x_F)$ and is comparable to the characteristic wave length of the generated wave

We clearly observe in these figures that the wave presents fast decay within the PML while the numerical solution remains in very good compatibility to the reference solution outside the absorbing layer. Moreover, the performance of the PML becomes better as its length is increased. Based on extensive numerical evidence, we finally conclude that the PML parameters should be $2 \leq \sigma_0 \leq 4$, $2 \leq p \leq 4$ and, $1 \leq l/\lambda \leq 2$ for optimum performance in the studied problem.

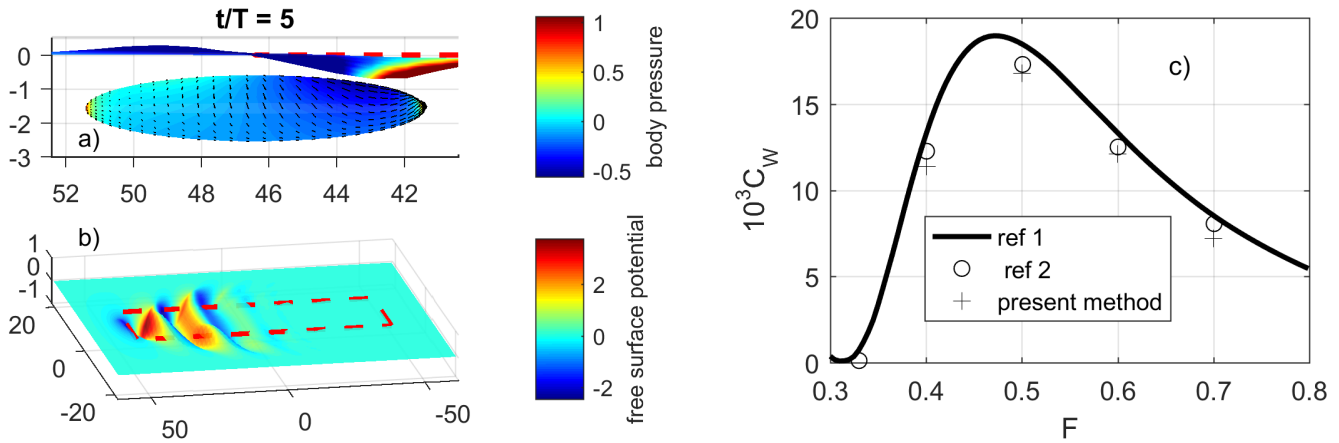


Figure 3.8: Wave resistance study of a prolate spheroid. a) Pressure and velocity fields on the body boundary and free-surface potential and free-surface elevation. b) Total potential field on the free-surface. c) Wave resistance coefficient and comparison against calculations from Belibassakis et al. (2013a).

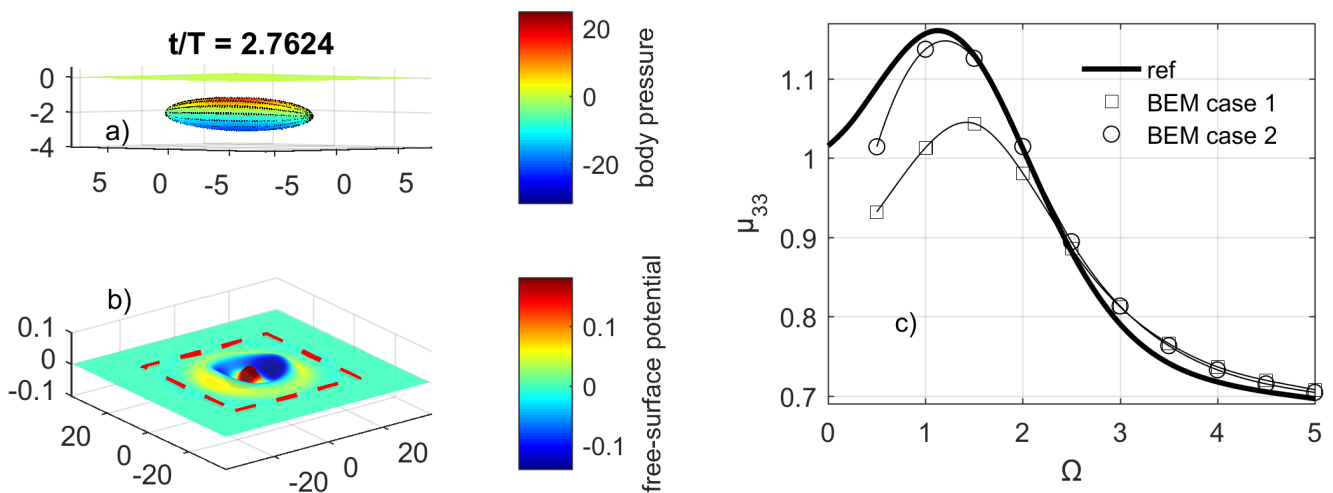


Figure 3.9: Enforced radiation study of a prolate spheroid. a) Pressure and velocity fields on the body boundary and free-surface potential and free-surface elevation. b) Total potential field on the free-surface. c) Added mass coefficient and comparison against calculations from Chatjigeorgiou and Miloh (2015). In the case 1 $N_F = 5400$, in the case 2 $N_F = 10000$.

3.4.5.2 3D calculations and GPU performance

In Fig.3.8 calculations are presented concerning the wave-resistance problem of a fully immersed prolate spheroid of axis ratio 5 : 1 : 1, in constant-speed forward motion at Froude number $F = U/\sqrt{gL}$ in the interval $[0.4, 0.7]$, where L is the length of the body and U its velocity. The body was initially in rest and accelerates smoothly until the steady state condition. The body advances beneath the initially calm free-surface with its longitudinal axis in submergence $d = 0.16L$. A snapshot of the simulation for $t/T = 5$ is presented in Figs.3.8(a,b) for $F = 0.5$.

Moreover, in Fig.3.8(c) the wave resistance coefficient $C_W = R_W/0.5\rho U^2 S_W$ is presented as a function of Froude number (F) and S_W is the wetted surface. The results are in quite good agreement with the calculations from the literature (Belibassakis et al., 2013a).

For the convergence of the present method two sets of numerical parameters have been used. The first is selected to achieve convergence of the distributed quantities and the second is selected for the accurate wave-resistance calculation and corresponds to coarse space-time discretisation. The timestep is 1% (4% in the second case) of the period, on the body and the free-surface we have 640 and 8100 (1472 in the second case) boundary elements, respectively. For the accurate prediction of the surface velocity field at the vicinity of the poles double precision arithmetics have been used, leaving the development of the mixed precision version of the code for the present problem as a subject for future work. For this reason the present implementation of the algorithm in the specific GPU⁶ is characterised by high space complexity and relatively large time complexity. To be more specific 3.2GB (but only 1.5GB in the second case) were required by the VRAM and the execution time of the code reached the 1174 sec (but only 31 sec for the second case). It is worthwhile to mention that the performance of the GPGPU computational code, both in terms of time and space complexity, is substantially higher than the performance of corresponding serial or parallel CPU codes, implemented by exploiting resources of similar cost.

In Fig.3.9 calculations are presented concerning the enforced radiation problem of a fully immersed prolate spheroid of axis ratio 6 : 1 : 1, performing enforced heaving motion with nondimensional frequency $\Omega = \omega^2 a/g$ in the interval $[0.5, 5]$, beneath the initially calm free-surface with its longitudinal axis in submergence $d = 2b$, where a is the large and b is the small semiaxis of the body, respectively and ω is the heaving frequency. A snapshot of the simulation at $t/T \approx 2.76$ and $\Omega = 2.5$ is presented in Figs.3.9(a,b). Moreover, in Fig.3.9(c) the added mass coefficient μ_{33} is presented as a function of Ω . It is clear from the convergence trend of the 3D calculations that our calculations are in the limit compatible with the results from the literature (Chatjigeorgiou and Miloh, 2015). More specifically, in Fig.3.9(a) the potential and velocities on the body together with the free-surface potential are depicted. In Fig.3.9(b) the free-surface elevation and potential are presented and with red dashed line is denoted the limit of the PML. Regarding the performance of the numerical method and the GPU accelerated computational code. In the present time-domain simulation the body begins from the rest reaching harmonic state after 2 periods T , the time-step is $\Delta t/T = 1\%$. A total number of $N_B = 1350$ body boundary elements and $N_F = 10000$ free-surface boundary element are used. Mixed-precision arithmetics have been used, 4.8GB were required from the VRAM and the simulation time was 322 sec.

3.5 Boundary integral formulation and BEM for lifting bodies beneath the free surface

Applying Green's theorem to the lifting problem Eqs.(3.1 - 3.14), we obtain the following two integral representations for the potential in \bar{D} in terms of the potential Φ (dipole intensity) and

⁶The present GPU is a GTX1080 and is designed mainly for graphic processing and not for scientific calculations. The ratio of single to double precision units is 1:32.

its normal derivative $\partial_n \Phi$ (source intensity), the first on the body boundary and the second on the free-surface boundary⁷, written compactly as follows

$$\begin{aligned} \Phi(\mathbf{x}_0; t) - \Phi_J(\mathbf{x}_0; t) = & \int_{\partial D_B(t)} \partial_n \Phi_B(\mathbf{x}; t) G_s(\mathbf{x}_0 | \mathbf{x}) - \Phi_B(\mathbf{x}; t) \partial_n G_s(\mathbf{x}_0 | \mathbf{x}) ds(\mathbf{x}) \\ & + \int_{\partial D_F(t)} \partial_n \Phi_F(\mathbf{x}; t) G_s(\mathbf{x}_0 | \mathbf{x}) - \Phi_F(\mathbf{x}; t) \partial_n G_s(\mathbf{x}_0 | \mathbf{x}) ds(\mathbf{x}) \\ & + \int_{\partial D_W(t)} \left[\partial_n \Phi_W^u(\mathbf{x}; t) - \partial_n \Phi_W^l(\mathbf{x}; t) \right] G_s(\mathbf{x}_0 | \mathbf{x}) ds(\mathbf{x}) \\ & - \int_{\partial D_W(t)} \left[\Phi_W^u(\mathbf{x}; t) - \Phi_W^l(\mathbf{x}; t) \right] \partial_n G_s(\mathbf{x}_0 | \mathbf{x}) ds(\mathbf{x}), \quad \mathbf{x}_0 \in \partial D_B(t) \cup \partial D_F(t) \end{aligned} \quad (3.60)$$

where

$$\Phi(\mathbf{x}_0; t) - \Phi_J(\mathbf{x}_0; t) = \begin{cases} \Phi(\mathbf{x}_0; t), & \mathbf{x}_0 \in D. \\ \Phi_B(\mathbf{x}_0; t) - \frac{\text{sign}(\mathbf{r} \cdot \mathbf{n})}{2} \Phi_B(\mathbf{x}_0; t), & \mathbf{x}_0 \in \partial D_B, \\ \Phi_F(\mathbf{x}_0; t) - \frac{\text{sign}(\mathbf{r} \cdot \mathbf{n})}{2} \Phi_F(\mathbf{x}_0; t), & \mathbf{x}_0 \in \partial D_F, \end{cases} \quad (3.61)$$

In the above relation we have used Green's function (Eq.2.16), consisted of the fundamental solution of 2D/3D Laplace equation corresponding to a Rankine source plus a regular part, corresponding to a mirror source with respect to the bottom surface and the normal to the boundary derivative of the total Green's function. The total Green's function is denoted with G_s and its normal derivative with $\partial_n G_s$. In this way and in the case of flat bottom, the boundary condition Eq.(3.3) is identically satisfied and the corresponding boundary term of the integral representation is dropped. For simplicity, the case of general bathymetry is not presented in this section; for more details in that interesting problem see Sec.4.5.1, Sec.4.5.4 and Filippas et al. (2018). .

The first integral in Eq.(3.60) represents the effect of the body, the second the effect of the free-surface and the third and fourth integrals the effect of the wake on the potential. The first term in the integrals is the potential induced at \mathbf{x}_0 from a source with intensity $\partial_n \Phi(\mathbf{x})$ located on the boundary at \mathbf{x} , while the second term represents similarly the effect of normal to the boundary dipole with intensity $\Phi(\mathbf{x})$. In this way the whole information for the potential in the domain D is stored on the boundary ∂D whose dimension is of one order lower. Therefore, if the trace of the potential and the derivative on the boundary are known, using Green's formula Eqs.(3.60, 3.61) we can evaluate potential everywhere in D .

The non-local form of the operator in the right hand side of Eq.(3.60), that is demonstrated by

⁷The representation theorem is written for the body and the free-surface boundaries and the boundary fields on those two boundaries are mainly governed by the corresponding boundary conditions. However, there exists also the wake boundary emanating from body's trailing edge. The values of the potential jump on the wake are governed by the corresponding boundary conditions and the appropriate Kutta condition. Due to the Kutta condition the mathematical structure of that boundary is essentially different. Moreover, the numerical treatment of the wake boundary in the present case is different and is done following a Lagrangian approach.

the boundary integral and the necessity of accurate description of the boundary and the data⁸ on them, is radicated to the character of free-surface waves and lifting flows. That character is preserved in the context of potential theory and Boundary Integral Equations (BIE) in an optimal way. To be more specific:

- From the point of view of analytical modeling, in potential methods the absence of physical dissipation, due to the neglect of viscosity, strengthens⁹ the interaction between the boundaries.
- Concerning numerical modeling, the BEM, that is based on a boundary integral reformulation of the Boundary Value Problem (BVP), is mesh-free (in the interior of the domain). In this way numerical diffusion, connected with mesh-based methods (e.g. Finite Element/Difference/Volume methods), that weakens the interaction between the boundaries, is avoided.

Replacing body boundary condition Eq.(3.2) and wake kinematic condition Eq.(3.10) into the representation theorem on the boundary Eqs.(3.60, 3.61), we obtain the following two Fredholm 2nd kind weakly singular integral equations

$$\begin{aligned}
 & - \int_{\partial D_F(t)} \partial_n \Phi_F(\mathbf{x}; t) G_s(\mathbf{x}_0 | \mathbf{x}) ds(\mathbf{x}) \\
 \frac{1}{2} \Phi_B(\mathbf{x}_0; t) + \int_{\partial D_B(t)} \Phi_B(\mathbf{x}; t) \partial_n G_s(\mathbf{x}_0 | \mathbf{x}) ds(\mathbf{x}) = & - \int_{\partial D_F(t)} \Phi_F(\mathbf{x}; t) \partial_n G_s(\mathbf{x}_0 | \mathbf{x}) ds(\mathbf{x}) \\
 & + \int_{\partial D_B(t)} b(\mathbf{x}; t) G_s(\mathbf{x}_0 | \mathbf{x}) ds(\mathbf{x}) \\
 & - \int_{\partial D_W(t)} \mu_W(\mathbf{x}; t) \partial_n G(\mathbf{x}_0 | \mathbf{x}) ds(\mathbf{x}), \quad \mathbf{x}_0 \in \partial D_B(t), \quad (3.62)
 \end{aligned}$$

and

$$\begin{aligned}
 & - \int_{\partial D_F(t)} \partial_n \Phi_F(\mathbf{x}; t) G_s(\mathbf{x}_0 | \mathbf{x}) ds(\mathbf{x}) \\
 + \int_{\partial D_B(t)} \Phi_B(\mathbf{x}; t) \partial_n G_s(\mathbf{x}_0 | \mathbf{x}) ds(\mathbf{x}) = & - \frac{1}{2} \Phi_F(\mathbf{x}_0; t) - \int_{\partial D_F(t)} \Phi_F(\mathbf{x}; t) \partial_n G_s(\mathbf{x}_0 | \mathbf{x}) ds(\mathbf{x}) \\
 & + \int_{\partial D_B(t)} b(\mathbf{x}; t) G_s(\mathbf{x}_0 | \mathbf{x}) ds(\mathbf{x}) \\
 & - \int_{\partial D_W(t)} \mu_W(\mathbf{x}; t) \partial_n G(\mathbf{x}_0 | \mathbf{x}) ds(\mathbf{x}), \quad \mathbf{x}_0 \in \partial D_F(t), \quad (3.63)
 \end{aligned}$$

⁸The boundary values of the potential and the normal to the boundary derivative correspond to the intensity of the singularities (Green function - source and normal derivative - dipole) located on the boundary. The knowledge of those boundary fields is necessary and sufficient for the calculation of the hydrodynamic fields (potential, velocity, pressure, etc) in the interior of the domain. The magnitude of those functions at a specific boundary area is a measure of the influence of the specific part of the boundary to the fluid flow and other boundaries.

⁹In real flows between two boundaries viscosity, due to dissipation mechanisms, allows interaction of boundaries at a specific level. In ideal flow models, that interaction is stronger and this is the reason the verb "strengthen" is used.

where $\mu_W = \Phi_W^u - \Phi_W^l$ denotes the potential jump or the dipole intensity on the wake. The weakly singular boundary integral equations Eqs.(3.62&3.63), free-surface boundary conditions Eqs.(3.7, 3.8) and the Pressure-type Kutta condition Eqs.(3.13&3.14) provide us with a system of equations for the unknown boundary fields Φ_B on the body, Φ_F and $\partial_n \Phi_F$ at the free-surface and μ_W at the vicinity of trailing edge. The above system of equations can be solved numerically after the appropriate discretisation, implemented with a boundary element method (BEM) and collocation, as we will see in the following section. Furthermore, numerical solution of the system can be achieved following two different paths. Either by time integration, where free-surface conditions are treated as a dynamic system and BIE as an algebraic constraint, or using a finite difference method (FDM) for the temporal discretisation of free-surface conditions. In the later case, BIE and free-surface conditions are treated similarly forming a non-linear algebraic system. The first approach is adopted in the present work and is described in detail at the following sections.

3.5.1 Discretisation and the extended DtN map

The spacial discretisation mainly consists of the following approximations of the analytical model:

- Concerning the geometry, a C^0 representation of the boundary is used as follows:
 - in 2D formulation, following a low-order panel method, the body contour is replaced by a closed polygonal line, and N_B denotes the number of panels. The free surface and the trailing vortex sheet are also approximated by open polygonal lines composed of N_F and $N_W(t)$ panels, respectively.
 - in 3D formulation, the boundary is approximated using bilinear-quadrilateral elements.
- Concerning the representation of the functions on the boundary, the potential, its normal derivative and the potential jump at each time step, are approximated by piecewise constant distributions, as follows:

$$\begin{aligned}
 \Phi_F(\mathbf{x}; t) &= \Phi_{Ff}(t), \quad \text{at free-surface element } f, \quad f = 0, 1, \dots, N_F - 1, \\
 \partial_n \Phi_F(\mathbf{x}; t) &= \partial_n \Phi_{Ff}(t), \quad \text{at free-surface element } f, \quad f = 0, 1, \dots, N_F - 1, \\
 \Phi_B(\mathbf{x}; t) &= \Phi_{Bi}(t), \quad \text{at body element } i, \quad i = 0, 1, \dots, N_B - 1, \\
 \partial_n \Phi_B(\mathbf{x}; t) &= \partial_n \Phi_{Bi}(t) = b_i(t), \quad \text{at body element } i, \quad i = 0, 1, \dots, N_B - 1, \\
 \mu_W(\mathbf{x}; t) &= \mu_{Ww}(t), \quad \text{at wake element } w, \quad w = 0, 1, \dots, N_W(t) - 1.
 \end{aligned} \tag{3.64}$$

- Finally, following a collocation scheme, the BIEs (Eqs.3.62 & 3.63) are satisfied in a finite number of points (or control points) and in order to avoid singularities the centroids of the elements have been chosen as collocation points.

To proceed, the discretised form the of the BIEs (Eqs.3.62 & 3.63) is as follows

$$\mathcal{A}_{F,B}^{pot}(t) \cdot \begin{pmatrix} \mathbf{N}_F(t) \\ \Phi_B(t) \end{pmatrix} = \mathcal{B}_{F,B}^{pot}(t) \cdot \begin{pmatrix} \Phi_F(t) \\ \mathbf{b}(t) \end{pmatrix} + \mathcal{D}_{F,B,K}^{pot}(t) \cdot \boldsymbol{\mu}_K(t) + \mathcal{D}_{F,B,W}^{pot}(t) \cdot \boldsymbol{\mu}_W, \tag{3.65}$$

where

$$\begin{aligned} \mathcal{A}_{F,B}^{pot}(t) &= \begin{pmatrix} \mathcal{A}_{F,B,00}^{pot}(t) & \mathcal{A}_{F,B,01}^{pot}(t) \\ \mathcal{A}_{F,B,10}^{pot}(t) & \mathcal{A}_{F,B,11}^{pot}(t) \end{pmatrix}, & \mathcal{B}_{F,B}^{pot}(t) &= \begin{pmatrix} \mathcal{B}_{F,B,00}^{pot}(t) & \mathcal{B}_{F,B,01}^{pot}(t) \\ \mathcal{B}_{F,B,10}^{pot}(t) & \mathcal{B}_{F,B,11}^{pot}(t) \end{pmatrix}, \\ \mathcal{D}_{F,B,K}^{pot}(t) &= \begin{pmatrix} \mathcal{D}_{F,B,K,0}^{pot}(t) \\ \mathcal{D}_{F,B,K,1}^{pot}(t) \end{pmatrix}, & \mathcal{D}_{F,B,W}^{pot}(t) &= \begin{pmatrix} \mathcal{D}_{F,B,W,0}^{pot}(t) \\ \mathcal{D}_{F,B,W,1}^{pot}(t) \end{pmatrix}. \end{aligned} \quad (3.66)$$

In the above equations $\mathcal{A}_{F,B}^{pot}$, $\mathcal{B}_{F,B}^{pot}$ are the potential induction-factor matrices at the left hand side and the right hand side of Eqs.(3.62)&(3.63), respectively. They model free surface-free surface, body-body and free surface-body interactions. Also $\mathcal{D}_{F,B,K}^{pot}$, $\mathcal{D}_{F,B,W}^{pot}$ are double layer potential induction-factor matrices modeling the effects of the Kutta strip and the wake on the free-surface and the body. The above matrices are defined as follows

$$\begin{aligned} \mathcal{A}_{F,B,00}^{pot}(t) &= \{-S_{fs}^{pot}(t)\}, & \mathcal{A}_{F,B,01}^{pot}(t) &= \{D_{fj}^{pot}(t)\}, \\ \mathcal{A}_{F,B,10}^{pot}(t) &= \{-S_{is}^{pot}(t)\}, & \mathcal{A}_{F,B,11}^{pot}(t) &= \{0.5\delta_{ij} + D_{ij}^{pot}(t)\}, \\ \mathcal{B}_{F,B,00}^{pot}(t) &= \{-0.5\delta_{fs} - D_{fs}^{pot}(t)\}, & \mathcal{B}_{F,B,01}^{pot}(t) &= \{S_{fj}^{pot}(t)\}, \\ \mathcal{B}_{F,B,10}^{pot}(t) &= \{-D_{is}^{pot}(t)\}, & \mathcal{B}_{F,B,11}^{pot}(t) &= \{S_{ij}^{pot}(t)\}, \\ \mathcal{D}_{F,B,K,0}^{pot}(t) &= \{-D_{fk}^{pot}(t)\}, & \mathcal{D}_{F,B,K,1}^{pot}(t) &= \{-D_{bk}^{pot}(t)\}, \\ \mathcal{D}_{F,B,W,0}^{pot}(t) &= \{-D_{fw}^{pot}(t)\}, & \mathcal{D}_{F,B,W,1}^{pot}(t) &= \{-D_{iw}^{pot}(t)\}, \end{aligned} \quad (3.67)$$

with \mathcal{S} denoting source or single-layer integrals, and with \mathcal{D} denoting dipole or double-layer integrals see Eq.(2.23). Moreover, the indices belong to the following subsets of \mathbb{N}

$$f, s \in \{0, 1, \dots, N_F - 1\}, \quad i, j \in \{0, 1, \dots, N_B - 1\}, \quad k \in \{0, 1, \dots, N_K - 1\}, \quad w \in \{0, 1, \dots, N_W(t) - 1\}. \quad (3.68)$$

In Eq.(3.65) $\Phi_F = \{\Phi_{Fs}\}$, $\mathbf{N}_F = \{\partial_n \Phi_{Fs}\}$, $\Phi_B = \{\Phi_{Bj}\}$, $\mathbf{b} = \{b_j\}$, $\boldsymbol{\mu}_K = \{\mu_{Kk}\}$, $\boldsymbol{\mu}_W = \{\mu_{Ww}\}$. In the sequel, we will denote with bold, vectors containing the values of piecewise constant trace functions on the boundary elements, at various parts of the boundary.

Next we multiply Eq.(3.65) with $[\mathcal{A}_{F,B}^{pot}(t)]^{-1}$ and we obtain

$$\begin{pmatrix} \mathbf{N}_F(t) \\ \Phi_B(t) \end{pmatrix} = \mathcal{G}(t) \cdot \begin{pmatrix} \Phi_F(t) \\ \mathbf{b}(t) \end{pmatrix} + \mathcal{Z}(t) \cdot \boldsymbol{\mu}_K(t) + \mathcal{P}(t) \cdot \boldsymbol{\mu}_W, \quad (3.69)$$

or

$$\begin{pmatrix} \mathbf{N}_F(t) \\ \Phi_B(t) \end{pmatrix} = \begin{pmatrix} \mathcal{G}_{00}(t) & \mathcal{G}_{01}(t) \\ \mathcal{G}_{10}(t) & \mathcal{G}_{11}(t) \end{pmatrix} \cdot \begin{pmatrix} \Phi_F(t) \\ \mathbf{b}(t) \end{pmatrix} + \begin{pmatrix} \mathcal{Z}_0(t) \\ \mathcal{Z}_1(t) \end{pmatrix} \cdot \boldsymbol{\mu}_K(t) + \begin{pmatrix} \mathcal{P}_0(t) \\ \mathcal{P}_1(t) \end{pmatrix} \cdot \boldsymbol{\mu}_W, \quad (3.70)$$

where

$$\begin{aligned}\mathfrak{G}(t) &= \left[\mathcal{A}_{F,B}^{pot}(t) \right]^{-1} \cdot \mathcal{B}_{F,B}^{pot}(t), \quad \mathfrak{Z}(t) = \left[\mathcal{A}_{F,B}^{pot}(t) \right]^{-1} \cdot \mathcal{D}_{F,B,K}^{pot}(t), \\ \mathcal{P}(t) &= \left[\mathcal{A}_{F,B}^{pot}(t) \right]^{-1} \cdot \mathcal{D}_{F,B,W}^{pot}(t).\end{aligned}\quad (3.71)$$

The above mapping is the discrete form of the extended Dirichlet-to-Neumann (DtN) operator that is suitable for lifting flows beneath the free surface. That operator connects the potential (Dirichlet data) with its normal derivative (Neumann data) on body boundary ∂D_B , but also involves the unknown values of the dipole intensity $\boldsymbol{\mu}_K$ (Dirichlet data) on the Kutta strip ∂D_K , as well as the (known from the past) potential jump $\boldsymbol{\mu}_W$ (Dirichlet data) on the wake ∂D_W . We observe in the above equation that the influence of the wake, that introduces memory effects, is taken into account through $\mathcal{P}(t) \cdot \boldsymbol{\mu}_W$. Also, the effect of the body velocity is considered through the component \mathbf{V}_B , included in \mathbf{b} , as described by the body boundary condition Eq.(3.2). In Sec.3.5.2 using the appropriate parts of the DtN map, Eqs.(3.69 - 3.71), in the discretised form of free-surface boundary conditions and pressure-type Kutta condition, we will obtain a system of (spatially and temporarily) nonlocal differential equations, with explicit and implicit nonlinearities, that approximately describe the dynamics of the system.

3.5.2 Discretised free-surface and Kutta conditions and the dynamical system

The discretised free-surface conditions are the same in case of lifting and nonlifting flows and have been already presented in Sec.3.4.2. Those discretised boundary conditions are rewritten here

$$\partial_t \Phi_F|_1 = -g\eta|_1 - \frac{1}{2}[\mathbf{V}_{F,t}|_1 + \mathbf{N}_F|_1 \cdot \mathbf{n}_F|_1]^2, \quad \mathbf{x} \in \partial D_F(t), \quad (3.72)$$

$$\partial_t \eta|_1 = -\mathbf{N}_F|_1 \cdot \mathbf{a}|_1, \quad \mathbf{x} \in \partial D_F(t), \quad (3.73)$$

The discretised free-surface tangential velocity vector field $\mathbf{V}_{F,t}$ is expanded with respect to a curvilinear coordinate system and its covariant base, using the velocity contravariant components (see Sec.2.5.2.1), as follows

$$\mathbf{V}_{F,t}|_1 = (\mathbf{V}_{F,t,j})^j|_1 \cdot \mathbf{e}_j|_1, \quad j \in \{1,2\}. \quad (3.74)$$

where \mathbf{e}_j are the systems of vectors that represents the base vectors discretised vector fields $\mathbf{e}_j|_1 = \{\mathbf{e}_{ji}\}, j \in \{1,2\}, i \in \{0,1,\dots, N_F - 1\}$ and the dot product is between systems of vectors.

The contravariant components of the velocity can be calculated when the covariant components are known as follows

$$(\mathbf{V}_{F,t,j})^j|_1 = \mathbf{g}^{jk}|_1 (\mathbf{V}_{F,t,k})_k|_1, \quad j, k \in \{1,2\}. \quad (3.75)$$

where \mathbf{g}^{jk} is a system that contains the contravariant components of the metric tensor at the collocation points; i.e. $\mathbf{g}^{jk}|_2 = \{g_i^{jk}\}, j, k \in \{1, 2\}, i \in \{0, 1, \dots, N_F - 1\}$.

By applying CUFD we can approximate the covariant component of the free-surface tangential velocities by the neighboring free-surface potential values (see Sec.2.5.2.2) as follows

$$(\mathbf{V}_{F,t,1})_1|_1 = \mathcal{D}(\mathbf{x}_0|_1) \cdot \Phi_F|_1. \quad (3.76)$$

$$(\mathbf{V}_{F,t,2})_2|_1 = [\mathcal{D}(\mathbf{x}_0|_2) \cdot \Phi_F|_2]^\top = \left[\mathcal{D}(\mathbf{x}_0|_2) \cdot (\Phi_F|_1)^\top \right]^\top. \quad (3.77)$$

The above detailed analysis enlightens the fact that the discretised boundary value of the tangential velocity $\mathbf{V}_{F,t}$ can be expressed as a function of the discretised boundary value of the potential Φ_F in the context of our approximation; i.e. $\mathbf{V}_{F,t}|_1 = \mathcal{V}_{CUFDM}(\Phi_F|_1)$.

At the final stage the discretised free-surface conditions (Eqs.3.72 & 3.73) together with the discretised Kutta condition that will be presented in the sequel, will be exploited for the construction of the dynamical-system equations in the form $d_t \mathbf{U} = \mathbf{f}(\mathbf{U})$, where the system-derivative \mathbf{f} is a function of the dynamic variables collected into the 1st-order system $\mathbf{U} = \{\Phi_F, \eta, \mu_K\}$. In order to obtain that form of free-surface conditions we recall the appropriate part of the discretised extended DtN operator constructed in Sec.3.5.1, Eqs.(3.69 - 3.71)

$$\mathbf{N}_F(t)|_1 = \mathcal{G}_{00}(t) \cdot \Phi_F(t)|_1 + \mathcal{G}_{01}(t) \cdot \mathbf{b}(t)|_1 + \mathcal{Z}_0(t) \cdot \mu_K(t)|_2 + \mathcal{P}_0(t) \cdot \mu_W|_2. \quad (3.78)$$

In the above linear relation the unknown discretised fields are the systems of Neumann and Dirichlet data on the free-surface; i.e. the normal derivative of the free-surface potential $\mathbf{N}_F|_1$ and the free-surface potential $\Phi_F|_1$ and the system of Dirichlet data on the Kutta strip; i.e. the potential jump μ_K . The Neumann data on the body \mathbf{b} and are known from the prescribed kinematics and the Dirichlet data on the wake μ_W have been determined from the time history of the system evolution. Therefore, the discretised free-surface conditions (Eqs.3.72 & 3.73) together with the appropriate part of the discretised DtN operator Eq.(3.78) are a system of (spatially and temporarily) nonlocal differential equations, with explicit and implicit nonlinearities and a linear algebraic constraint. This is only the half part of the total system of equations. The remaining part that is based on the pressure-type Kutta condition will be constructed later in the same section. The other part of the system is also constrained and another part of the extended *DtN* operator serves as a linear constraint this will be also discussed later.

In the sequel, the algebraic constraint is used in order to express the system-derivative \mathbf{f} as a function of the dynamic variables collected into the 1st-order system $\mathbf{U} = \{\Phi_F, \eta, \mu_K\}$. To proceed, the discretised normal derivative of the free-surface potential field \mathbf{N}_F with the aid of Eq.(3.78) becomes a function of Φ_F and μ_K ; i.e. $\mathbf{N}_F(t)|_1 = \mathcal{DTN}_0(\Phi_F(t)|_1, \mu_K|_2)$. The free-surface boundary conditions become

$$\partial_t \Phi_F|_1 = -g\eta|_1 - \frac{1}{2}[\mathcal{V}_{CUFDM}(\Phi_F|_1) + \mathcal{DTN}_0(\Phi_F(t)|_1, \mu_K|_2) \cdot \mathbf{n}_F|_1]^2, \quad \mathbf{x} \in \partial D_F(t), \quad (3.79)$$

$$\partial_t \eta|_1 = -\mathcal{DTN}_0(\Phi_F(t)|_1, \mu_K|_2) \cdot \mathbf{a}|_1, \quad \mathbf{x} \in \partial D_F(t), \quad (3.80)$$

The discretised free-surface conditions in the form of Eqs.(3.79 & 3.80) together with the discretised pressure-type Kutta condition, that will be constructed in the sequel, are a system of (spatially and temporarily) nonlocal differential equations, with explicit and implicit nonlinearities, in the form $d_t \mathbf{U} = \mathbf{f}(\mathbf{U})$, where the system-derivative \mathbf{f} is a function of the dynamic variables collected into the 1st-order system $\mathbf{U} = \{\Phi_F, \eta, \mu_K\}$.

Moreover concerning the lifting part of the problem and the pressure-type Kutta condition, we apply discretisation with BEM and collocation as described in detail in Sec.2.4 and in Sec.2.5.2.2. We consider the collection of discretised data that are families of scalars or vectors. They are ordered following span-major numbering. In this way, ordered lists (systems) are created, that represent the collocation points (containing vectors of \mathbb{R}^3), the discretised potential field (containing real numbers), the discretised tangential velocity field (containing vectors of \mathbb{R}^3) or the covariant components of the tangential velocity (containing real numbers). The systems that are arranged span-majorly will be denoted using $|_2$. To proceed, the pressure-type Kutta condition is applied at the body-collocation points at the upper and lower side of the trailing edge¹⁰ and the corresponding operator is discretised as follows $\mathbf{F}_{fs}^{PK}|_2 = \{F_{fs,i}^{PK}\}$, with $i \in \{0, 1, \dots, N_{PK} - 1\}$, where N_{PK} is the total number of collocation points that Kutta condition is applied. Therefore, we have the aforementioned collocation points $\mathbf{x}_0|_2 = \{\mathbf{x}_{0i}\}$, the potential $\Phi_B|_2 = \{\Phi_{B,i}\}$, the tangential velocity $\mathbf{V}_t|_2 = \{\mathbf{V}_{ti}\}$, the first component (chordwise) of the covariant derivative of the potential $\mathbf{V}_{t1}|_2 = \{V_{t1i}\}$, the second component (spanwise) of the covariant derivative of the potential $\mathbf{V}_{t2}|_2 = \{V_{t2i}\}$. Moreover, the known-Neumann-data-times-the-normal-vector discretised vector field is $\mathbf{N}|_2 = \{b_i \mathbf{n}_i\}$ and the body velocity $\mathbf{V}_B|_2 = \{\mathbf{V}_{Bi}\}$.

The discretised form of pressure-type Kutta condition is as follows

$$\mathbf{F}_{fs}^{PK}(\mathbf{x}_0|_2; t)|_2 = 0, \quad \mathbf{x}_0|_2 \in \partial D_B(t), \quad (3.81)$$

where

$$\begin{aligned} \mathbf{F}_{fs}^{PK}(\mathbf{x}_0|_2; t)|_2 = d_t(\Phi_B^u|_2 - \Phi_B^l|_2) + & \left(\frac{\mathbf{V}_t^u|_2 + \mathbf{V}_t^l|_2}{2} + \frac{\mathbf{N}^u|_2 + \mathbf{N}^l|_2}{2} - \frac{\mathbf{V}_B^u|_2 + \mathbf{V}_B^l|_2}{2} \right) \\ & \left[\mathbf{V}_t^u|_2 - \mathbf{V}_t^l|_2 + \mathbf{N}^u|_2 - \mathbf{N}^l|_2 - (\mathbf{V}_B^u|_2 - \mathbf{V}_B^l|_2) \right] \\ & - \left(\frac{\mathbf{V}_B^u|_2 + \mathbf{V}_B^l|_2}{2} \right) (\mathbf{V}_B^u|_2 - \mathbf{V}_B^l|_2). \end{aligned} \quad (3.82)$$

The discretised tangential velocity vector field \mathbf{V}_t is expanded with respect to a curvilinear coordinate system and its covariant base, using the velocity contravariant components (see Sec.2.5.2.1), as follows

$$\mathbf{V}_t|_2 = (\mathbf{V}_{tj})^j|_2 \cdot \mathbf{e}_j|_2, \quad j \in \{1, 2\}. \quad (3.83)$$

where \mathbf{e}_j are the systems of vectors that represents the base vectors discretised vector fields $\mathbf{e}_j|_2 = \{\mathbf{e}_{ji}\}$, $j \in \{1, 2\}$, $i \in \{0, 1, \dots, N_{PK} - 1\}$ and the dot product is between systems of vectors.

¹⁰A single numbering is used for both the upper and the lower collocation points; i.e. the collection $i \in \{0, 1, \dots, N_{PK} - 1\}$ is mapped to the upper side data denoted with upper index u and to the lower side data denoted with l .

The contravariant components of the velocity can be calculated when the covariant components are known as follows

$$(\mathbf{V}_{tj})^j|_2 = \mathbf{g}^{jk}|_2 (\mathbf{V}_{tk})_k|_2, \quad j, k \in \{1, 2\}. \quad (3.84)$$

where \mathbf{g}^{jk} is a system that contains the contravariant components of the metric tensor at the collocation points; i.e. $\mathbf{g}^{jk}|_2 = \{g_i^{jk}\}, j, k \in \{1, 2\}, i \in \{0, 1, \dots, N_{PK} - 1\}$.

By applying CUFD we can approximate the covariant component of the tangential velocities by the neighboring potential values (see Sec.2.5.2.2) as follows

$$(\mathbf{V}_{t1})_1|_2 = [\mathcal{D}(\mathbf{x}_0|_1) \cdot \Phi_B|_1]^\top. \quad (3.85)$$

$$(\mathbf{V}_{t2})_2|_2 = \mathcal{D}(\mathbf{x}_0|_2) \cdot \Phi_B|_2. \quad (3.86)$$

The above detailed analysis enlightens the fact that the discretised trace tangential velocity \mathbf{V}_t can be expressed as a function of the discretised trace of the potential Φ_B in the context of our approximation; i.e. $\mathbf{V}_t|_2 = \mathcal{V}_{CUFDM}(\Phi_B)$.

At the final stage the discretised pressure-type Kutta condition (Eqs.3.81 & 3.82) together with the discretised free-surface conditions (Eqs.3.72 & 3.73) will be exploited for the construction of the dynamical-system equations in the form $d_t \mathbf{U} = \mathbf{f}(\mathbf{U})$, where the system-derivative \mathbf{f} is a function of the dynamic variables collected into the 1st-order system $\mathbf{U} = \{\Phi_F, \eta, \mu_K\}$. In order to obtain that form of Kutta condition we recall the discretised DtN operator constructed in Sec.3.5.1, Eqs.(3.69 - 3.71)

$$\Phi_B(t) = \mathcal{G}_{10}(t) \cdot \Phi_F(t) + \mathcal{G}_{11}(t) \cdot \mathbf{b}(t) + \mathcal{Z}_1(t) \cdot \mu_K(t) + \mathcal{P}_1(t) \cdot \mu_W. \quad (3.87)$$

In the above linear relation the unknown discretised fields are the system of Dirichlet data on the body boundary; i.e. the body potential $\mathbf{N}_B|_1$, the system of Dirichlet data on the free-surface; i.e. the free-surface potential $\mathbf{N}_F|_1$ and the system of Dirichlet data on the Kutta strip; i.e. the potential jump μ_K . The Neumann data on the body \mathbf{b} and are known from the prescribed kinematics and the Dirichlet data on the wake μ_W have been determined from the time history of the system evolution. Therefore, the discretised pressure-type Kutta condition (Eqs.3.81 & 3.82) together with the appropriate part of the discretised DtN operator Eq.(3.87) and the discretised free-surface boundary conditions (Eqs.3.72 & 3.73) together with the appropriate part of the discretised DtN operator Eq.(3.78) are a system of (spatially and temporarily) nonlocal differential equations, with explicit and implicit nonlinearities and linear algebraic constraints.

We proceed with the pressure-type Kutta condition. The algebraic constraint is used in order to express the system-derivative \mathbf{f} as a function of the dynamic variables collected into the 1st-order system $\mathbf{U} = \{\Phi_F, \eta, \mu_K\}$. First of all, the discretised potential field with the aid of Eq.(3.87) becomes a function of Φ_F and μ_K ; i.e. $\Phi = \mathcal{DTN}(\Phi_F, \mu_K)$. In this way the discretised trace tangential velocity can be expressed as a function of Φ_F and μ_K ; i.e. $\mathbf{V}_t = \mathcal{V}_{DTN}(\Phi_F, \mu_K)$. Therefore, the pressure-Kutta operator is also a function of the unknown Φ_F and μ_K (and other

known quantities); i.e. $F_{fs}^{PK} = \mathcal{F}_{fs}^{PK}(\Phi_F, \mu_K)$. The pressure-type Kutta condition becomes

$$\begin{aligned}
d_t \left[\mathcal{DTN}_1^u(\Phi_F, \mu_K) - \mathcal{DTN}_1^l(\Phi_F, \mu_K) \right] = & \\
& - \left[\frac{\mathcal{V}_{DTN}^u(\Phi_F, \mu_K) + \mathcal{V}_{DTN}^l(\Phi_F, \mu_K)}{2} + \frac{\mathbf{N}^u + \mathbf{N}^l}{2} - \frac{\mathbf{V}_B^u + \mathbf{V}_B^l}{2} \right] \\
& \left[\mathcal{V}_{DTN}^u(\Phi_F, \mu_K) - \mathcal{V}_{DTN}^l(\Phi_F, \mu_K) + \mathbf{N}^u - \mathbf{N}^l - (\mathbf{V}_B^u - \mathbf{V}_B^l) \right] \\
& + \left(\frac{\mathbf{V}_B^u + \mathbf{V}_B^l}{2} \right) (\mathbf{V}_B^u - \mathbf{V}_B^l). \tag{3.88}
\end{aligned}$$

In the equation above, the upper indices u and l refer to the discretised fields at the upper and lower sides the discretised boundary, respectively. To be more specific to the corresponding values of the discretised fields at the collocation points located at the centroids of the boundary elements that represent the upper and lower sides of the body at the vicinity of the trailing edge. Those values are global functions of the total discretised field of the potential jump at the Kutta-strip μ_K and that relation is expressed by the global DtN_1 operator (third term at the right hand side of Eq.3.87). Moreover they are global functions of the total discretised field of the potential jump on the free-surface boundary Φ_F and that relation is expressed by the global DtN_1 operator (first term at the right hand side of Eq.3.87). For example the velocity and the potential at the left tip of the foil, depends on the intensity of the dipoles that are distributed at Kutta-strip in the vicinity of the right tip. Also they depend on the intensity of the dipoles that are distributed at whole free-surface boundary. Moreover, it is a function of the total Neumann data on the body (second term at the right hand side of Eq.3.87) and the time history of the total Dirichlet data that are stored as dipoles in the wake (forth term at the right hand side of Eq.3.87). In this way the spatial and temporal nonlocal character of the problem, that is preserved through discretisation via BEM, is illustrated.

To proceed further, it is necessary to perform some operations to the time derivative of the DtN operator appeared at the left hand side of Eq.(3.88).

$$\begin{aligned}
d_t \left[\mathcal{DTN}_1^u(\Phi_F, \mu_K) - \mathcal{DTN}_1^l(\Phi_F, \mu_K) \right] = & \\
= \left\{ d_t [\mathcal{G}_{10}^u(t) - \mathcal{G}_{10}^l(t)] \cdot \Phi_F(t) + [\mathcal{G}_{11}^u(t) - \mathcal{G}_{11}^l(t)] \cdot \mathbf{b}(t) \right. & \\
& \left. + [\mathcal{Z}_1^u(t) - \mathcal{Z}_1^l(t)] \cdot \mu_K(t) + [\mathcal{P}_1^u(t) - \mathcal{P}_1^l(t)] \cdot \mu_W \right\}. \tag{3.89}
\end{aligned}$$

We define the following matrices $\mathcal{G}_{10}^{u \setminus l} = [\mathcal{G}_{10}^u - \mathcal{G}_{10}^l]$, $\mathcal{G}_{11}^{u \setminus l} = [\mathcal{G}_{11}^u - \mathcal{G}_{11}^l]$, $\mathcal{Z}_1^{u \setminus l} = [\mathcal{Z}_1^u - \mathcal{Z}_1^l]$, $\mathcal{P}_1^{u \setminus l} = [\mathcal{P}_1^u - \mathcal{P}_1^l]$ as differences of matrices with one dimension that equals the number of Kutta-strip collocation points N_{PK} and the other defined by the number of the panels (on free-surface, body, Kutta-strip and wake, respectively) that induce potential at the collocation points. By adopting that notation and using the Leibniz rule for differentiation we obtain the following

relation

$$\begin{aligned}
 d_t \left[\mathcal{DTN}_1^u(\Phi_F, \mu_K) - \mathcal{DTN}_1^l(\Phi_F, \mu_K) \right] &= \\
 &= d_t[\mathcal{G}_{10}^{u\setminus l}(t)] \cdot \Phi_F(t) + \mathcal{G}_{10}^{u\setminus l}(t) \cdot d_t[\Phi_F(t)] \\
 &\quad + d_t[\mathcal{G}_{11}^{u\setminus l}(t)] \cdot \mathbf{b}(t) + \mathcal{P}_1^{u\setminus l}(t) \cdot \mu_W \\
 &\quad + d_t[\mathcal{Z}_1^{u\setminus l}(t)] \cdot \mu_K(t) + \mathcal{Z}_1^{u\setminus l}(t) \cdot d_t[\mu_K(t)].
 \end{aligned} \tag{3.90}$$

Next, using the dynamic boundary condition (Eq.3.79) and considering that the body-fixed time derivative of the free-surface potential is the same with the inertial¹¹, we can replace time derivative of the free-surface potential with functions of the dynamic variables as follows

$$\begin{aligned}
 d_t \left[\mathcal{DTN}_1^u(\Phi_F, \eta, \mu_K) - \mathcal{DTN}_1^l(\Phi_F, \eta, \mu_K) \right] &= \\
 &= d_t[\mathcal{G}_{10}^{u\setminus l}(t)] \cdot \Phi_F(t) \\
 &\quad + \mathcal{G}_{10}^{u\setminus l}(t) \cdot \left\{ -g\eta - \frac{1}{2}[\mathcal{V}_{CUFDM}(\Phi_F) + \mathcal{DTN}_0(\Phi_F, \mu_K) \cdot \mathbf{n}_F]^2 \right\} \\
 &\quad + d_t[\mathcal{G}_{11}^{u\setminus l}(t)] \cdot \mathbf{b}(t) + \mathcal{P}_1^{u\setminus l}(t) \cdot \mu_W \\
 &\quad + d_t[\mathcal{Z}_1^{u\setminus l}(t)] \cdot \mu_K(t) + \mathcal{Z}_1^{u\setminus l}(t) \cdot d_t[\mu_K(t)].
 \end{aligned} \tag{3.91}$$

By replacing Eq.(3.91) into Eq.(3.88) and multiplying both sides with the inverse of $\mathcal{Z}_1^{u\setminus l}$, we obtain the final form of the discretised pressure-type Kutta condition

$$\begin{aligned}
 d_t[\mu_K(t)] &= \left[\mathcal{Z}_1^{u\setminus l}(t) \right]^{(-1)} \cdot \left\{ -d_t[\mathcal{G}_{10}^{u\setminus l}(t)] \cdot \Phi_F(t) \right. \\
 &\quad \left. - \mathcal{G}_{10}^{u\setminus l}(t) \cdot \left\{ -\frac{1}{2}[\mathcal{V}_{CUFDM}(\Phi_F) + \mathcal{DTN}_0(\Phi_F, \mu_K) \cdot \mathbf{n}_F]^2 - g\eta \right\} \right. \\
 &\quad \left. - d_t[\mathcal{G}_{11}^{u\setminus l}(t)] \cdot \mathbf{b}(t) + \mathcal{P}_1^{u\setminus l}(t) \cdot \mu_W \right\} - d_t[\mathcal{Z}_1^{u\setminus l}(t)] \cdot \mu_K(t) \\
 &\quad - \left[\frac{\mathcal{V}_{DTN}^u(\Phi_F, \mu_K) + \mathcal{V}_{DTN}^l(\Phi_F, \mu_K)}{2} + \frac{\mathbf{N}^u + \mathbf{N}^l}{2} - \frac{\mathbf{V}_B^u + \mathbf{V}_B^l}{2} \right] \\
 &\quad \left[\mathcal{V}_{DTN}^u(\Phi_F, \mu_K) - \mathcal{V}_{DTN}^l(\Phi_F, \mu_K) + \mathbf{N}^u - \mathbf{N}^l - (\mathbf{V}_B^u - \mathbf{V}_B^l) \right] \\
 &\quad + \left(\frac{\mathbf{V}_B^u + \mathbf{V}_B^l}{2} \right) (\mathbf{V}_B^u - \mathbf{V}_B^l) \left. \right\}.
 \end{aligned} \tag{3.92}$$

The discretised free-surface conditions in the form of Eqs.(3.79 & 3.80) together with the discretised pressure-type Kutta condition (Eq.3.92) are a system of (spatially and temporarily) non-local differential equations, with explicit and implicit nonlinearities, written here in the form $d_t \mathbf{U} = \mathbf{f}(\mathbf{U})$, where the system-derivative \mathbf{f} is a function of the dynamic variables collected into the 1st-order system $\mathbf{U} = \{\Phi_F, \eta, \mu_K\}$. That system can be numerically integrated in order to calculate evolution of $\{\Phi_F, \eta\}$, based on information concerning the functions Φ_F, η, μ_K at previous time steps, in conjunction with the history of the wake dipole intensity μ_W , and the

¹¹The free-surface elevation and the free-surface potential are functions defined at the initially calm free-surface level, following an Eulerian approach.

Neumann data \mathbf{b} on the body boundary, known at every time step from the body motion as described by the body boundary condition Eq.(3.2). The time derivatives at the right hand side of Eq.(3.92) are numerically calculated using backward finite difference schemes.

Moreover, the free-surface-boundary nodes are updated every time that the the free-surface at the collocation points changes. However the free-surface elevation is known only at the collocation points and its values are stored in η . The bilinear 4-node boundary elements construct a basic grid with global nodes located at the local element nodes. The values of the free-surface elevation can be obtained everywhere by interpolation, when the nodal values of the free-surface are known. In order to calculate the nodal values of the free-surface elevation a staggered grid, with nodes at the collocation points, is exploited. The staggered-grid nodal values are given by the free-surface elevation η . Then by interpolation, using the staggered grid, the basic-grid nodal values are obtained. Next by interpolation, using the basic grid, the free-surface potential is obtained everywhere. In this way, the free-surface boundary is updated and the relative quantities like the metric $\mathbf{a}|_1$ and the free-surface unit normal vector $\mathbf{n}_F|_1$ are updated.

Subsequently, following part of the updated discretised extended DtN map (Eqs.3.69 - 3.71) is used to calculate the remaining unknown discretised body Dirichlet boundary field values Φ_B

$$\Phi_B(t)|_1 = \mathcal{G}_{10}(t) \cdot \Phi_F(t)|_1 + \mathcal{G}_{11}(t) \cdot \mathbf{b}(t)|_1 + \mathcal{Z}_1(t) \cdot \boldsymbol{\mu}_K(t)|_2 + \mathcal{P}_1(t) \cdot \boldsymbol{\mu}_W|_2. \quad (3.93)$$

3.5.3 Numerical results and discussion

In this section numerical results are presented and discussed concerning the performance of hydrofoils in steady and oscillatory motion under the free surface. Calculations are compared with other methods and experimental results from the literature, in order to illustrate the range of applicability, as well as the limitations of the developed method. In particular, in Sec.3.5.3.1 the hydrofoil in steady motion beneath the free surface is examined. In Sec.3.5.3.2 the additional effects of oscillatory motion(s) are presented, the unsteady thruster operates beneath the free-surface and in sea with finite depth, while in Sec.3.5.3.3 the nonlinear wake effect is studied. Finally, in Sec.3.5.3.4 results are presented with the 3D fully nonlinear version of the method.

3.5.3.1 Steady foil beneath the free surface

Numerical calculation for NACA4412 hydrofoil at a stationary angle of attack 5° and a variety of Froude numbers $Fn = U/\sqrt{g\bar{c}}$ (where c is the chord) and submergence ratio d/c of the foil are shown in Fig.3.10. In all cases deep water conditions ($H/\lambda \gg 0.5$) are assumed. Present-method results are based on $N_B = 60$ panels on the body, the number of free-surface panels per wavelength is $N_F/\lambda = 25$, and the time step $U\Delta t/\lambda = 4\%$. Transition from rest to steady state condition has been accomplished after a traveled distance of 10 chord lengths. Results for both distributed and integrated quantities are presented in comparison with numerical results from steady panel methods reported by various authors and experimental measurements by Ausman (1954). In particular, the wave elevation for $Fn = 0.9$ and $d/c = 1$ is shown in

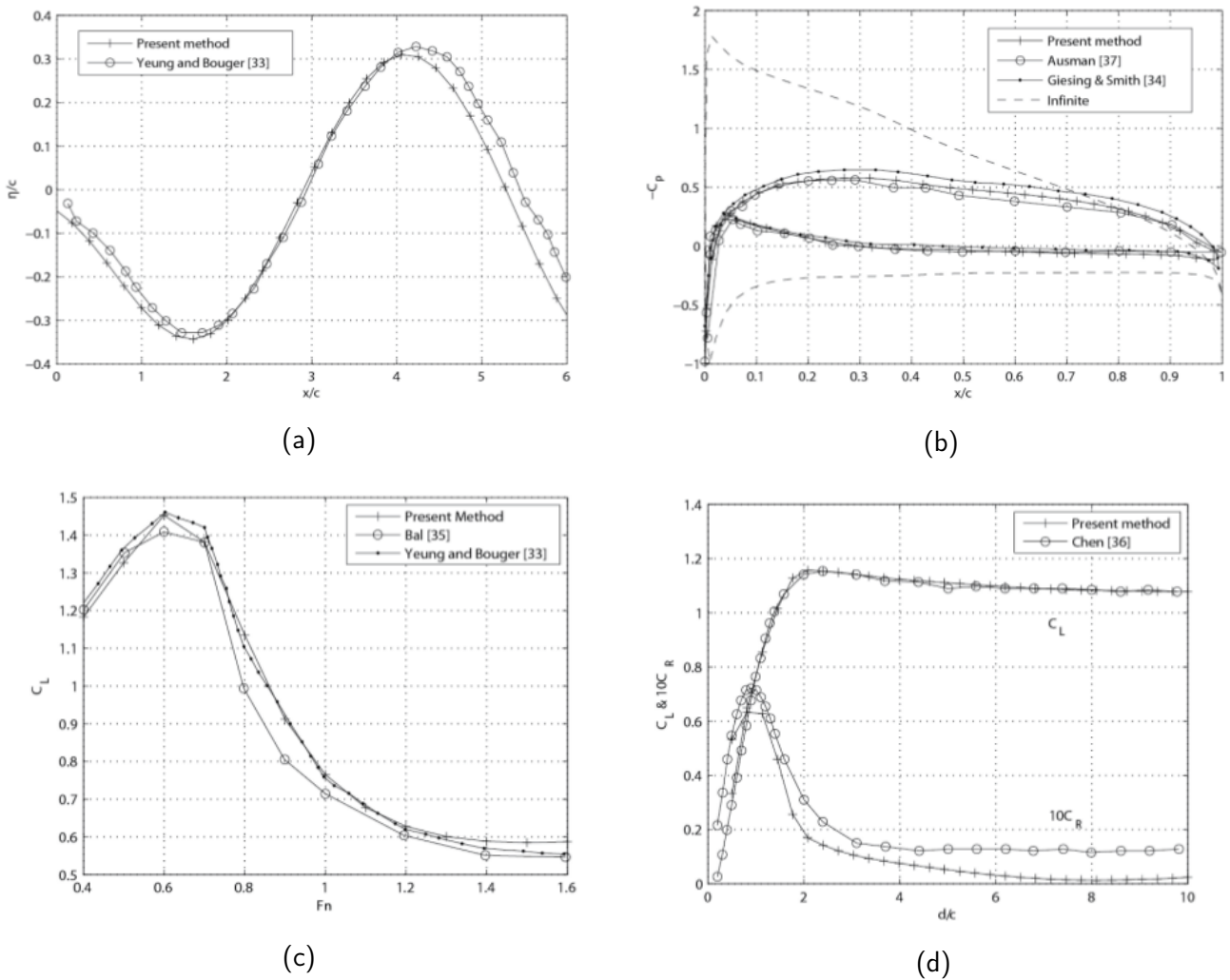


Figure 3.10: NACA4412 hydrofoil, at 5° angle of attack beneath the free surface: (a) Free surface elevation for $Fn = 0.9$ and submergence $d/c = 1$ (with respect to the leading edge of the foil). (b) Pressure coefficient at $Fn = 1.03$ and submergence $d/c = 0.6$ (with respect to the midchord of the foil). (c) Lift coefficient for submergence $d/c = 1$ (with respect to the leading edge of the foil), against Froude number. (d) Lift and wave resistance coefficients at $Fn = 1$, against submergence (with respect to the midchord of the foil).

Fig.3.10a against numerical predictions by Yeung and Bouger (1979). Also, the pressure coefficient ($C_p = p/0.5\rho U^2$) at somewhat greater Froude number $Fn = 1.03$ and smaller submergence of the foil $d/c = 1$ is plotted in Fig.3.10b against calculated data from Giesing and Smith (1967) and experimental data by Ausman (1954). In both cases we observe that present results are in very good agreement with other methods and experimental data. To illustrate the effects of the free surface on the generation of the lift, we include in Fig.3.10b a calculation with the foil at great distance from the free surface, corresponding practically to infinite domain which is in perfect agreement with the steady panel method by Hess & Smith see e.g. Moran (2003), Sec.4.8. We notice that free-surface effects result in significant decrease of pressure difference on the foil and thus, reduction of lift and suction force at the leading edge. The latter is also responsible for the increase of the wave resistance, as it will be illustrated in the sequel.

Moreover, in Fig.3.10c the effect of Froude number on the lift coefficient $C_L = F_Y/0.5\rho U^2 c$ for foil submergence $d/c = 1$ is shown, and compared with predictions by Yeung and Bouger (1979) and Bal (1998). It is seen that the free surface causes a drop in C_L as Froude number increases. The effect of free surface on lift and wave-resistance coefficient ($C_R = F_X/0.5\rho U^2 c$), for $Fn = 1$, is presented in Fig.3.10d and compared against predictions by Chen (2012). We observe in this figure that as the submergence increases the lift coefficient converges to its value in unbounded domain and that wave resistance tends to zero, as it is naturally expected.

3.5.3.2 Free surface and finite depth effects on flapping-foil thrusters

In this subsection we examine the effects of free surface on the performance of the biomimetic flapping hydrofoil operating as an unsteady thruster. In particular, in Fig.3.11a we compare integrated results, obtained by the present method concerning the thrust coefficient defined here as $C_T = -F_x/\rho g h_0^2$, against predictions by linearised theory for thin uncambered hydrofoil beneath the free surface, developed by Grue et al. (1988). For compatibility with the thin hydrofoil theory, we examine here a thin symmetrical NACA0006 hydrofoil, in small-amplitude oscillations. Results have been obtained for heaving oscillatory and flapping motion, respectively, and are plotted in Fig.3.11a against the non-dimensional frequency $\Omega = \omega^2 c/2g$. We can see in the above that present method predictions are in very good agreement with thin hydrofoil theory.

Furthermore, calculations concerning the thrust coefficient $C_T = -F_x/\rho U^2 h_0$ for the NACA0012 hydrofoil are presented in Fig.3.11b, for flapping motion with $0.2 \leq St \leq 0.45$ and $10^\circ \leq \theta_0 \leq 55^\circ$. Results obtained by the present method with a flapping foil operating at two different submergence ratios $d/c = 2.5, 1.5$ and Froude number $Fn = 1.5$, in water layer of constant depth $H/c = 5$, are shown using dashed lines and symbols, respectively, and compared against results with the same flapping foil operating in infinite fluid, indicated in the same figure using continuous lines. We remark here that the characteristic wavelength associated with forward translation of the foil is $\lambda/H = 2.76$ and is found to be much greater than the corresponding wavelengths of all oscillatory frequencies, associated with all Strouhal numbers considered. We observe in this figure that, the main effect of finite submergence is to reduce the thrust coefficient essentially due to development of wave resistance. The reduction is of the order 0.7-13%, in the case of $d/c = 2.5$, and, as it is naturally expected, it becomes quite more significant as submergence decreases, reaching almost 20% for $d/c = 1.5$, at high loading conditions. As already remarked, the above free-surface effect is attributed to the development of wave resistance associated with the generation the complex wave system due to both steady translation of the body and radiating waves due to flapping oscillations.

Although we have concentrated so far on the free-surface effects, that are expected to be more significant for flapping thrusters operating at small submergence, the effect of other boundaries can also be conveniently studied by the present method, as for example, the bottom boundary effects that could be found to be important especially for inland shipping. In fact, a very interesting example of full scale application of flapping foil propulsion is coming from the inland shipping industry. The Dutch company O-foil developed main flapping-foil propulsion mechanism and equipped the Ms Triade inland vessel (Fig.3.11c) reporting 50% fuel savings.

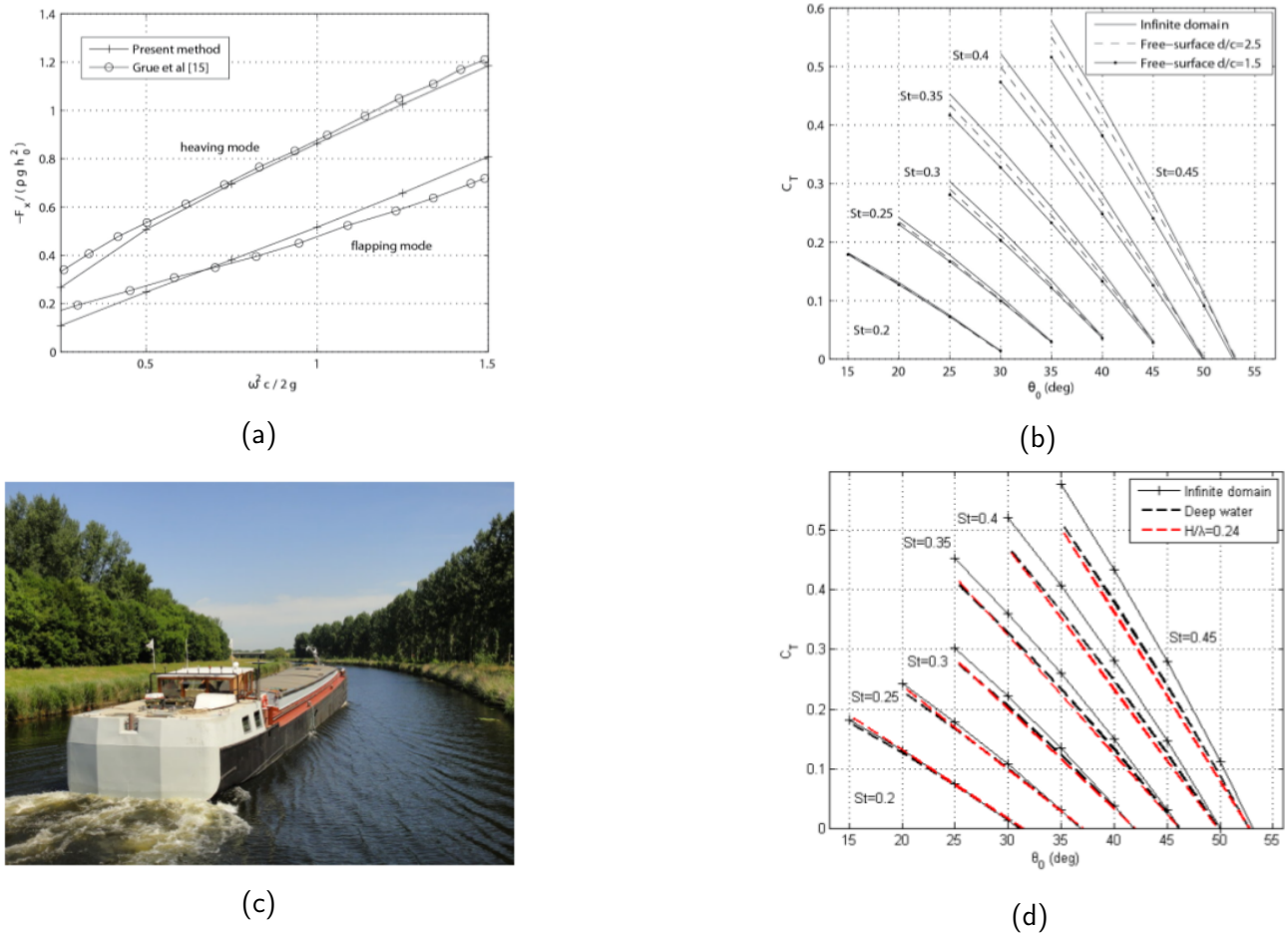


Figure 3.11: (a) Thrust coefficient $C_T = -F_x / \rho g h_0^2$ against non dimensional frequency $\Omega = \omega^2 c / 2g$, for NACA0006 hydrofoil at $d/c = 0.5$, in heaving and flapping low-amplitude motions. Feathering parameter $\epsilon = 0.6$, pivot point $X_R/c = 0.5$, and heave-pitch phase lag $|\psi| = 90^\circ$. (b) Free surface and bottom effects on C_T for NACA0012 hydrofoil for cases of different submergence ratio $d/c = 2.5, 1.5$. The Froude number is $Fn = 1.5$ and the water depth $H/c = 5$. (c) An example of full scale application of flapping foil propulsion is coming from the inland shipping industry. (d) Free surface and bottom effects on C_T for NACA0012 hydrofoil for cases of different water depth conditions. The Froude number is $Fn = 1.5$ and the submergence is $d/c = 1.5$.

Relevant results concerning thrust coefficient $C_T = -F_x / \rho U^2 h_0$ for the NACA0012 hydrofoil are presented in Fig.3.11d, for flapping motion with $0.2 \leq St \leq 0.45$ and $10^\circ \leq \theta_0 \leq 55^\circ$. Results obtained by the present method with a flapping foil operating at submergence ratios $d/c = 1.5$ and Froude number $Fn = 1.5$, in deep water and in intermediate depth $\lambda/H = 0.24$, are shown using black and red dashed lines and symbols, respectively, and compared against results with the same flapping foil operating in unbounded domain, indicated in the same figure using continuous lines. As we have observed before, the main effect of finite submergence is to reduce the thrust coefficient essentially due to development of wave resistance. The reduction is of the order 0.7-20% and is more important at high loading conditions. The effect of finite depth is causes a reduction of thrust at higher Strouhal numbers where it is more important. At small Strouhal numbers there are regions where the effect of finite depth is to increase thrust in comparison with the case of deep water but the increase is of secondary importance at least in the cases studied here.

3.5.3.3 Nonlinear wake effects

In the sequel, numerical results are presented in order to demonstrate whether or not the formulation of the fully non-linear wake is important. In Fig.3.12a calculations concerning the thrust coefficient ($C_T = -F_X/\rho U^2 h_0$) for the NACA0012 hydrofoil are presented, for flapping motion with $h_0/c = 1$, $\psi = -90^\circ$, $X_R/c = 0.33$, $0.2 \leq St \leq 0.45$ and $10^\circ \leq \theta_0 \leq 55^\circ$ in finite submergence $d/c = 2.5$ and the Froude number is $Fn = 1.5$, in deep water condition $H/\lambda \gg 1$. We observe that the effect of free wake is to reduce the thrust coefficient and it is noticeable only at the greater Strouhal numbers and angles of attack; see also Sec.2.10.3. Even in the present case of operation beneath the free surface at small submergence the effect very important. Moreover in Figs. 3.12b & 3.12c the evolution of thrust and lift coefficients is presented concerning the example of Fig.3.12a, for a hydrofoil beneath the free surface at $St = 0.45$, $\theta_0 = 35^\circ$. It is observed again that, for the present cases of moderate unsteadiness, the effect of free wake is of second order and is more significant at the peaks of the signals.

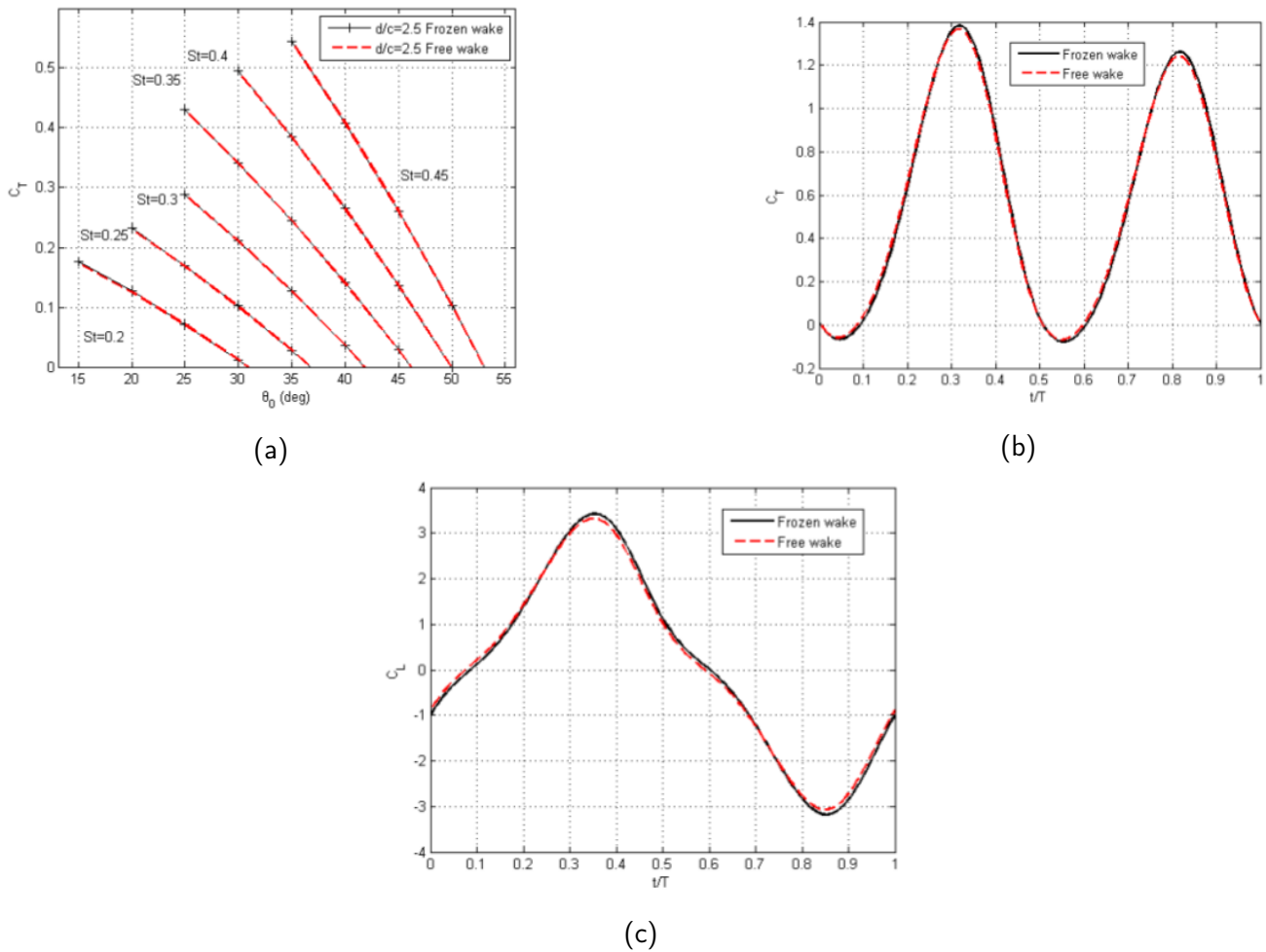


Figure 3.12: Free surface and free-wake effects for NACA0012 hydrofoil for submergence ratio $d/c = 2.5$, $h_0/c = 1$, $\psi = -90^\circ$, $X_R/c = 0.33$, $Fn = 1.5$, in deep water condition $H/\lambda \gg 1$. Frozen wake model (linearized wake dynamics) compared against free wake formulation: (a) Systematic calculations of on thrust coefficient (C_T) for $0.2 \leq St \leq 0.45$ and $10^\circ \leq \theta_0 \leq 55^\circ$. (b) Time history of thrust coefficient in the case of $St = 0.45$, and $\theta_0 = 35^\circ$. (c) Time history of lift coefficient in the case of $St = 0.45$, and $\theta_0 = 35^\circ$.

3.5.3.4 3D effects nonlinearity and GPU performance

In Fig.3.13 we present 3D calculations for the biomimetic propulsor beneath the free-surface. In Fig.3.13a), for validation purposes, present method calculations are compared against 2D unsteady hydrofoil theory from Grue et al. (1988) and 3D BEM calculations from Zhu et al. (2006). To be more specific, two constant-chord (c) foils with NACA0005 and NACA0012 advancing at Froude number $F = U/\sqrt{gc} = 0.18$ in heaving motion with amplitudes $h_0/c = 0.025$ & $h_0/c = 0.1$ and mean submergence $d/c = 0.5$ are simulated. Reasonable agreement is achieved with both the linear theory and the potential solver.

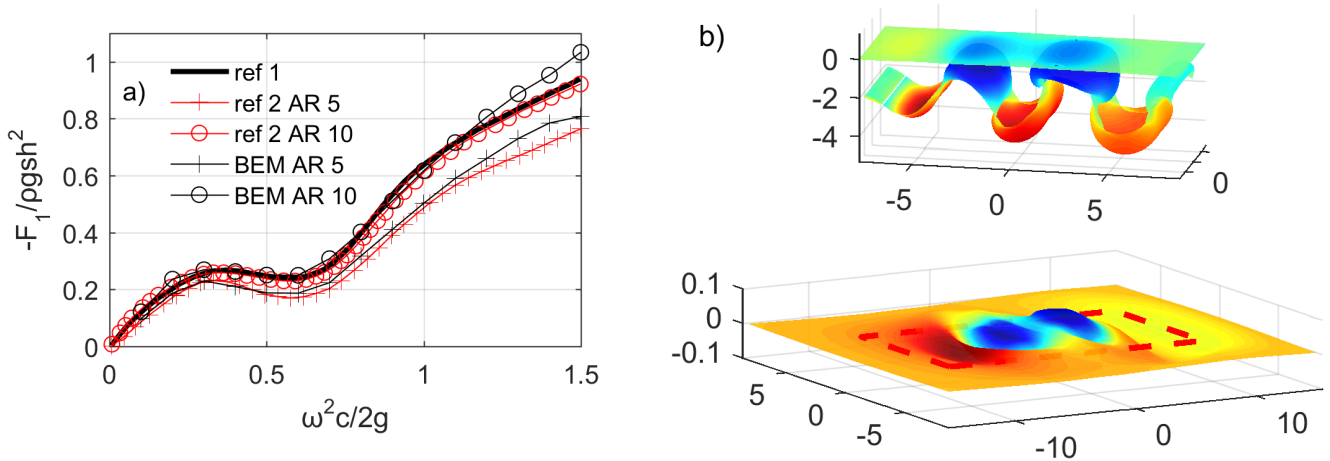


Figure 3.13: Simulation of biomimetic flapping-foil thruster beneath the free-surface. a) Mean value of the thrust coefficient as a function of nondimensional frequency. Comparison of present method for constant-chord foils with NACA0012 sections, $AR = 10$ & $AR = 5$, in heaving motion with $h_0/c = 0.025$ & $h_0/c = 0.1$ and $F = U/\sqrt{gc} = 0.18$, in mean submergence $d/c = 0.5$, against 2D unsteady hydrofoil theory from Grue et al. (1988) and 3D BEM calculations from Zhu et al. (2006). b) Potential and velocities on the body and potential jump on the wake as well as free-surface potential and elevation with the fully nonlinear model. For a constant-chord $AR = 6$ foil with NACA0012 sections and $St = 0.3$, $h_0/c = 0.75$, $\theta_0 = 23.3^\circ$, pivot point $X_R/c = 0.33$ and phase lag $\psi = -90^\circ$, Froude number $F = 0.6$, mean submergence $d/c = 0.5$.

Moreover, in Fig.3.13b) a specific example, corresponding to one operating condition, for a constant-chord foil with NACA0012 sections and $AR = 6$, at Froude number $F = 0.6$, mean submergence $d/c = 0.5$, in flapping foil motions with $St = 0.3$, heave amplitude $h_0/c = 0.75$, pitch amplitude $\theta_0 = 23.3^\circ$, pivot point $X_R/c = 0.33$ and phase lag $\psi = -90^\circ$, is simulated using the fully nonlinear 3D model. To be more specific, the potential on the body and the free-surface and the velocities on the body and potential jump on the wake are depicted. Regarding the performance of the numerical method and the GPU accelerated computational code, we provide some information for the fully nonlinear calculations. The simulation is in time domain and the foil begins from the rest reaching harmonic state after 2 periods T , the time-step is $\Delta t/T = 0.5\%$. A total number of $N_B = 1860$ body boundary elements and $N_F = 2170$ free-surface elements are used. Mixed-precision arithmetics have been used, 1.4GB were required from the VRAM and the simulation time was 270 sec in the case of the prescribed wake model and 847 sec in the case of the free-wake model. It is worthwhile to mention that due to the

specific numerical treatment of the problem (see also Sec.1.3.1), the truncation of the horizontally infinite domain using PML, the exploitation of mixed precision arithmetics and the proper handling of induction-factor matrices (see the discussion below Eq.2.25), the present GPGPU computational code is very efficient in terms of space complexity. To be more specific, in the present case where free-surface discretisation is required the memory demand from the VRAM is only 0.1GB higher in comparison with the infinite domain case. This is crucial if we consider the limited amount of memory available even in modern GPUs.

3.6 Non-linear numerical wave tank

The problem of flapping foil in fully non-linear water waves can be treated in the context of the method described at the present section in the context of a numerical wave tank approach; see e.g. Vinje and Brevig (1981), Grilli et al. (2001), Fochesato et al. (2007), Touboul et al. (2006), Touboul and Kharif (2010) and Manolas (2015). Part of the lateral boundary could be model a 3D wavemaker. Even more general nonlinear waves could be studied when the wavemaker¹² performs general motion. The waves generated will be evolve over flat or nonuniform bathymetry and interact with the body taking into account the fully nonlinear dynamics. The implementation of that approach, as well as the thorough study of the connection between the real nonlinear stochastic waves in open water, the resulting more realistic non-linear waves in the numerical wave tank, are left as a very interesting subject of future work; see e.g. Ning and Teng (2007), Abbasnia et al. (2017). In the next chapter, an efficient method for the hydrodynamic analysis, design and operation of flapping foils in fully developed nonlinear waves will be presented.

3.7 Remarks and conclusions

In the second part of the present thesis the fully nonlinear time domain method for the general unsteady problem of flow around lifting bodies of general shape is extended to treat problems with free-surface flows. Also finite depth effects are included and the the wave-resistance problem due to constant-speed forward motion and the enforced radiation problem due to body oscillations (heaving and pitching) of a nonlifting body are examined. The formulation of the problem is based on the potential theory and the boundary integral equations. For the numerical solution of the 3D, unsteady and nonlinear problem an efficient (in terms of both time and space complexity) GPU-accelerated BEM is developed, based on a formulation that is direct with respect to the potential. For the numerical solution of the fully nonlinear, 3D and unsteady problem the GPU-accelerated BEM is extended to hydrodynamic flows beneath the free surface.

The method is applied to the hydrodynamic analysis of foils in several conditions focusing on the investigation of the free-surface effects, which for relatively low submergence become important and should be included in the modeling. Moreover, the nonlinear vortex wake and the performance of the developed GPU computational code. Results are obtained, illustrating

¹²The effect of the wave maker can be modeled using a moving lateral boundary with geometry and kinematics that fit to the exact shape and motion of a real wavemaker, or using proper inhomogeneous boundary conditions.

the superior numerical performance of the developed method and the GPU code validating the accuracy of the method through comparisons with other methods and experimental data. Comparison between the prescribed and the fully nonlinear wake model are included, identifying the range of applicability and the limitations of the studied approaches. Numerical predictions for the thrust coefficient of the flapping hydrofoil operating beneath the free surface indicate that the present system, after experimental verification, could be exploited for efficient thrust production beneath the free surface, even when the effect of wave-making resistance is considered.

Last but not least, it is discussed, that the problem of flapping foil in fully non-linear water waves can be treated in the context of the method as presented in the present chapter, in the context of a numerical wave tank approach.

Direct extensions include the investigation of added mass effect beneath the free surface for various foil shapes and arrangements. Future research includes the treatment of leading edge separation and dynamic stall effects. Research extensions include the study of 3D flapping-wing thrusters beneath the free-surface and their interaction with the hull of the ship. Finally, the problem of flapping foil in fully non-linear water waves can be treated in the context of the method described at the present section with part of the lateral boundary, modeling a 3D wavemaker.

Chapter 4

Hydrodynamic analysis of bodies in waves

4.1 Summary

The method and the GPU code, that are introduced in previous chapters, are extended in cases of lifting flows beneath the free surface and in fully nonlinear waves. Although, the problem of the system could be treated by the method presented in Chapter 3 using a classical numerical wave tank, a more efficient approach is selected for a number of reasons that will be illustrated in the sequel and summarised in the conclusions.

Exploiting the present method, oscillating wings are investigated as unsteady thrusters, beneath the free surface and in oblique nonlinear waves exploring the possibility of thrust augmentation extracting energy from the incident wave field (wave devouring propulsion), the results are presented in Sec.4.5.2. By employing the two dimensional version of the method and linearizing the free-surface boundary conditions two very interesting and practical problem are studied. In order to examine those problems significant effort has been put to the extension of the method as discussed in the relevant sections and the corresponding publications. Extension of the 3D fully nonlinear version of the method to treat in more detail those problem is a very interesting subject for future work. The first problem is about flapping wings located beneath or to the side of the hull of the ship that are investigated as unsteady thrusters, augmenting the ship's main propulsion in waves; results are presented in Sec.4.5.3. Also, the performance of oscillating hydrofoils in the presence of waves and currents is studied for the exploitation of combined renewable marine energy sources in nearshore and coastal regions; results are presented in Sec.4.5.4.

Turning into more details concerning the method, the body contour is modeled as a surface of potential discontinuity. In the present chapter the body motion is prescribed, however the whole formulation could be extended to solve problems that include free motions of finite degrees of freedom; see e.g. the problem of the semi-activated foil in Sec.4.5.4 where the a specific version of the method has been extended to include induced heaving oscillations. The formulation of the problem is based on the potential theory and the boundary integral equations (BIE). For the numerical solution of the fully nonlinear, 3D and unsteady problem the GPU-accelerated boundary element method (BEM) is extended to hydrodynamic flows beneath the free surface and in nonlinear waves. The calculation of generalised forces is obtained without any further assumption by pressure integration. The latter is calculated using the Bernoulli's equation as presented in Sec.3.3.

We begin with the definition of the unsteady initial boundary value problem (IBVP) problem in the present case. The free-surface boundary conditions and pressure-type Kutta condition will be serve for the construction of the dynamical system equation and the other kinematic boundary conditions with provide appropriate constraints. Then the representation of the total fields, in terms of the initial guess and the corrector field, is introduced. The application of Green's formula on the body boundary and the exact free-surface boundary will be used to obtain a weakly singular Boundary Integral Equation (BIE) for the unknown corrector boundary fields. For the numerical solution we use a potential based boundary element method (BEM) and a collocation method, obtaining the discretised BIE. The latter after discretisation will be used for the construction of the discretised extended Dirichlet-to-Neumann (DtN) operator that will serve as an algebraic constraint to the equations of the dynamic system that will be constructed from the free-surface boundary conditions and the Kutta condition. A curvilinear finite difference method (CUFDM), in variable, non Cartesian and non orthogonal coordinate systems (see also Sec.2.5.2) is exploited to express the corrector potential, included in free-surface conditions and the Kutta condition, in terms of the dynamic variables of the problem. Exploiting the free-surface and Kutta conditions we proceed to the construction of the dynamic system equations in the form of a system of (spatially and temporarily) nonlocal differential equations, with explicit and implicit nonlinearities linear algebraic constraints. The evolution of the unknown corrector dynamic variables is obtained by time integration and the total solution can be constructed using that information and the initial guess fields. Next, a method for time integration together with the algorithm of the constant time iterations that are performed to solve the non-linear problem, are presented.

The importance of free-surface and 3D effects, nonlinearity as well as the performance of the developed GPU code in the case of 3D foils in oblique waves, are illustrated. The problem of augmentation of the ship's main propulsion in waves is studied in Sec.4.5.3. The main arrangement consists of horizontal wing(s) in vertical oscillatory motion which is induced by ship heave and pitch, while rotation about the wing pivot axis is actively controlled. In this work we investigate the energy extraction by the system operating in irregular wave conditions and its performance concerning direct conversion to propulsive thrust. More specifically, we consider operation of the flapping foil in waves characterized by a spectrum, corresponding to specific sea state, taking into account the coupling between the hull and the flapping foil dynamics. The effect of the wavy free surface is accounted for through the satisfaction of the corresponding boundary conditions and the consideration of the wave velocity on the formation of the incident flow. Numerical results concerning thrust and power coefficients are presented, indicating that significant thrust can be produced under general operating conditions. The present work can be exploited for the design and optimum control of such systems extracting energy from sea waves for augmenting marine propulsion in rough seas, with simultaneous reduction of ship responses offering also dynamic stabilization. Also, the performance of biomimetic energy systems in the presence of waves and currents is studied for the exploitation of combined renewable marine energy sources in nearshore and coastal regions is studied in Sec.4.5.4. The system operates as a semi-activated biomimetic energy device, with imposed pitching motion and induced heaving motion in harmonic incident waves and flow. Except of uniform currents also vertically sheared currents are considered. The analysis is based on a Coupled-Mode System, in conjunction with a time-domain BEM, taking into account the effect of the wavy free surface, the velocity due to waves and currents on the formation of the incident flow, and the effects of variable bathymetry. Results are presented concerning the performance of the system for a wide range of parameters, including cases where the wave frequency is

different from the pitching frequency of the hydrofoil. It is indicated that significant energy can be extracted, and that the power gain from the waves increases well above the maximum values predicted for the system in uniform flow. The present method can be applied to the design and optimum control of such biomimetic systems operating in the nearshore/coastal region and extracting energy from waves in the presence of ambient currents.

4.2 Mathematical formulation of lifting bodies in nonlinear waves

The studied configuration is depicted in Fig.4.1. The problem is time dependent and the oscillating lifting body is represented by a moving boundary $\partial D_B(t)$, with respect to the earth-fixed frame of reference. Moreover the wake of the body is modeled by another deformable boundary $\partial D_W(t)$, whose length grows emanating continuously from the body sharp edge. The level of the free-surface, when it is still, is shown in Fig.4.1 using a dashed line. We consider moderate submergence and speed, permitting us to approximately neglect effects of breaking waves and cavitation. Moreover, the body is considered to be rigid and its motion is prescribed. However, the present method is nonlinear; i.e. a) the shape of the body and b) its motion are not linearised, c) the nonlinear dynamics of the free wake are included and d) the fully nonlinear free-surface boundary conditions are satisfied at the exact location of the total free-surface elevation. In the present work we are interested in design, operation and control problems, aiming to the simulation of the system during many periods and not to its response to extreme cases of overturning and nearly-breaking waves. The latter can be simulated in the context of potential theory, with accepted accuracy, only until the breaking and not after. Therefore, we assume that the free surface is a function defined on the horizontal plane, that is the still free-surface level. For the surface tracking, we follow a semi-Lagrangian approach (the horizontal velocities of the free-surface particles are omitted), leaving the extension to the fully Lagrangian method, as a straightforward extension for future work. A Cartesian coordinate system is introduced with x_3 -axis pointing upwards, x_1 -axis and x_2 -axis lying on the still free-surface plane, with x_1 -axis at the direction of body's characteristic motion.

The total wave potential Φ satisfies Laplace equation

$$\Delta\Phi(\mathbf{x};t) = 0, \quad \mathbf{x} \in D(t), \quad (4.1)$$

supplemented by the body boundary condition

$$\partial_{n_B}\Phi(\mathbf{x};t) = \mathbf{V}_B(\mathbf{x};t) \cdot \mathbf{n}_B(\mathbf{x};t), \quad \mathbf{x} \in \partial D_B(t). \quad (4.2)$$

and the hard bottom no-entrance condition

$$\partial_{n_H}\Phi(\mathbf{x};t) = 0, \quad \mathbf{x} \in \partial D_H. \quad (4.3)$$

The first is a non-homogeneous Neumann boundary condition and the second, for impermeable and motionless bottom, is a homogeneous Neumann boundary condition. With the present method problems of deformable bottom can be solved, however the analysis of those

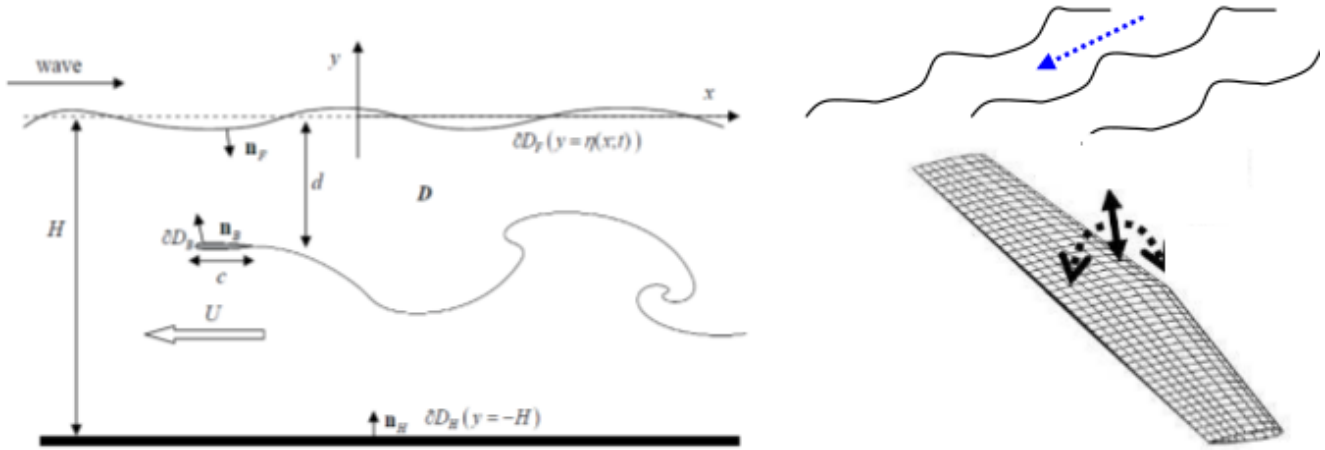


Figure 4.1: Definition of the studied problem in the case of a foil (of mid-chord c_0) moving under the free surface (at mean submergence d) and in waves.

interesting problems that belong to the fields of coastal engineering is left as a subject for future work.

Moreover, the fully non-linear dynamic and kinematic boundary conditions are imposed on the total free-surface elevation, as follows

$$\partial_t \Phi(\mathbf{x}_F, \eta; t) = -g\eta(\mathbf{x}_F; t) - \frac{1}{2} [\nabla \Phi(\mathbf{x}_F, \eta; t)]^2, \quad \mathbf{x} \in \partial D_F(t), \quad (4.4)$$

$$\partial_t \eta(\mathbf{x}_F; t) = -\partial_{n_F} \Phi(\mathbf{x}_F, \eta; t) \sqrt{1 - [\partial_{x_1} \eta(\mathbf{x}_F; t)]^2 - [\partial_{x_2} \eta(\mathbf{x}_F; t)]^2}, \quad \mathbf{x} \in \partial D_F(t), \quad (4.5)$$

or where $\mathbf{x}_F = \{x_1, x_2\}$ and $\mathbf{x} = \{\mathbf{x}_F, \eta\} = \{x_1, x_2, \eta\}$.

We treat the above as an initial and boundary value problem (IBVP) and we assume that far from the body the total field tend to the solution of the equivalent problem in the absence of the body. In the above equations η denotes the total free-surface elevation and g is the acceleration of gravity. Furthermore, H is the constant (finite) depth, d is the mean submergence of the body and \mathbf{V}_B denotes the instantaneous velocity of the body (due its own motion) at each point on the boundary. Finally, \mathbf{n} is the unit normal vector pointing into the interior of $D(t)$.

In the case of lifting flow around bodies with sharp edges, the problem is supplemented by the kinematic and dynamic conditions on the trailing vortex sheet $\partial D_W(t)$. The dynamic boundary condition

$$p_W^u(\mathbf{x}; t) = p_W^l(\mathbf{x}; t), \quad \mathbf{x} \in \partial D_W(t), \quad (4.6)$$

necessitates that a free shear layer cannot carry loading and thus the pressure at the both sides of it should be the same. The kinematic boundary condition

$$\partial_{n_W} \Phi_W^u(\mathbf{x}; t) = \partial_{n_W} \Phi_W^l(\mathbf{x}; t), \quad \mathbf{x} \in \partial D_W(t), \quad (4.7)$$

demands that the upper and the lower side of the shear layer cannot be separated to two distinct surfaces during the flow, thus the normal to the surface velocity is continuous through

$\partial D_W(t)$. The indices B, W, F, H are used to denote values of the total potential field, its derivative and potential jump, at the body surface and the wake of the foil, the free surface and the bottom, respectively. Using Eqs.(4.6) and Eq.(4.7) in conjunction with the appropriate form of Bernoulli's equation¹,

$$\frac{p(\mathbf{x};t) - p_{atm}}{\rho} + \partial_t \Phi(\mathbf{x};t) + \frac{1}{2} [\nabla \Phi(\mathbf{x};t)]^2 + gx_3 = 0, \quad \mathbf{x} \in D(t), \quad (4.8)$$

we obtain

$$D_t \mu_W(\mathbf{x};t) = 0, \quad \mathbf{x} \in \partial D_W(t), \quad (4.9)$$

$\mu_W = \Phi_W^u - \Phi_W^l$ denotes the potential jump (the dipole intensity) on the wake and $D_t(\cdot) = \partial_t(\cdot) + \mathbf{V}_W^m \cdot \nabla(\cdot)$ is the material derivative, based on the mean total velocity $\mathbf{V}_W^m = 0.5(\nabla \Phi^u + \nabla \Phi^l)$, on the trailing vortex sheet, that includes also the velocity of the waves.

In the lifting case, enforcement of the Kutta condition is required in order to fix the circulation at each time instant. The non-linear (quadratic), pressure-type Kutta condition, requiring zero pressure difference at the trailing edge, is imposed as follows

$$\lim_{\zeta \rightarrow \zeta_{TE}} F_{fs}^{PK}[\mathbf{x}_B(\zeta, \eta); t] = 0, \quad \mathbf{x}_B \in \partial D_B(t) \text{ and } \mathbf{x}_{TE} \in \partial D_B(t) \cup \partial D_W(t), \quad (4.10)$$

where the operator $F_{fs}^{PK}(\cdot)$ is defined as follows

$$F_{fs}^{PK}[\mathbf{x}_B(\zeta, \eta); t] = \partial_t(\Phi^u - \Phi^l) + 0.5(\nabla \Phi^u + \nabla \Phi^l)(\nabla \Phi^u - \nabla \Phi^l) + g(x_3^u - x_3^l). \quad (4.11)$$

The above form of pressure-type Kutta condition can be derived using the Bernoulli's theorem on the body at upper and lower sides of trailing edge; see Sec.3.3, Eq.(3.25).

4.3 The representation of the total fields

In the present section, for demonstration purposes, we will present in detail the representation of the potential. Similar representation holds for the other quantities involved, i.e. the free-surface elevation, time and space derivatives and dipole intensities, as well as the shape of the domain. The method is based on an iterative scheme and at a specific time t , iterations are performed, following a general iterative method

$$\Phi_{I+1}(\mathbf{x};t) = \mathcal{G}_I[\Phi_I(\mathbf{x};t)], \quad I \in \mathbb{N}. \quad (4.12)$$

At a specific time t , a finite number of N_I iterations are performed, until the total wave potential at the current iteration Φ_I converges² to the solution Φ of the fully nonlinear problem, as

¹When using that form of Bernoulli's equation to calculate forces acting on the body (especially for free-floating or semi-activated systems) we should either omit the hydrostatic term or include to the calculation the gravitational force acting on the body that depends to its mass.

²The theoretical study of the convergence characteristics, of various general iterative schemes that could be applied, is not a subject of the present thesis. Only numerical evidence of the convergence and accuracy is provided in the present work, via demonstration of the boundary conditions' satisfaction and comparisons against calculations from the literature.

follows

$$\Phi(\mathbf{x}; t) \approx \lim_{I \rightarrow N_I} \Phi_I(\mathbf{x}; t) = \Phi_{N_I-1}(\mathbf{x}; t). \quad (4.13)$$

The total wave potential $\Phi_I(\mathbf{x}; t)$ at the iteration I has the following representation

$$\Phi_I(\mathbf{x}; t) = \Phi_0^0(\mathbf{x}; t) + \phi_I^{cor}(\mathbf{x}; t), \quad I \in \mathbb{N}, \quad (4.14)$$

and at the last iteration ($I = N_I - 1$) the representation has the following form

$$\Phi_{N_I-1}(\mathbf{x}; t) = \Phi_0^0(\mathbf{x}; t) + \phi_{N_I-1}^{cor}(\mathbf{x}; t). \quad (4.15)$$

At a specific time t , the first component Φ_0^0 is an initial guess at the specific time t . That can be an exact or an approximate solution of the fully non-linear water-wave problem in the absence of the body, or the linear solution with the presence of the body. The initial-guess could be obtained using couple mode or mild-slope models in the case of variable bathymetry, the Rienecker and Fenton approach for fully non-linear waves over flat bottom, the Stokes or Cnoidal waves, for approximate solution of non-linear waves, in deep to intermediate and intermediate to shallow depth, respectively. Finally, another approach that is less efficient, but capable to treat overturning waves, could be the use of a non-linear BEM. The proper selection of the initial guess affects the efficiency of the numerical scheme. To be more specific, we expect that for wave-lifting body interaction over flat bottom, when choosing initial guess between the possible solutions in the absence of the body, the linearised solution will need more iterations than the 5th order Stokes, that also will require more iterations than the fully nonlinear solution obtained by Rienecker and Fenton approach. The detailed study of the performance of the method and its dependence to the initial guess, is left as a subject of future work.

At a specific timestep, we assume that convergence is achieved when the sequence of the corrector field ϕ_I^{cor} , $I \in \mathbb{N}$ converges to a specific finite field value. The norm of that finite value has a specific interpretation, it is the distance from the initial guess to the fully nonlinear solution. To be more specific concerning the convergence we have

$$\Phi(\mathbf{x}; t) - \Phi_0^0(\mathbf{x}; t) = \Phi_{N_I-1}(\mathbf{x}; t) - \Phi_0^0(\mathbf{x}; t) = \lim_{I \rightarrow (N_I-1)} \phi_I^{cor}(\mathbf{x}; t) = \phi_{N_I-1}^{cor}(\mathbf{x}; t), \quad (4.16)$$

and the convergence of ϕ_I^{cor} can be said that is achieved³ when the following distance (defined in an appropriate Banach space) becomes adequate small

$$d[\phi_{I+1}^{cor}(\mathbf{x}; t) - \phi_I^{cor}(\mathbf{x}; t)] < \epsilon, \quad \epsilon \in \mathbb{R}^+. \quad (4.17)$$

The claim that the iterative procedure converges to the fully nonlinear solution could be supported by calculations, demonstrating that the fully nonlinear boundary conditions are satisfied with controlled accuracy and via comparisons against fully nonlinear solutions of simpler problems from the literature (DtN calculation and comparison against HCMS for the case of a soliton over variable topography, evolution of fully nonlinear waves in deep water with initial guess a 5th order Stokes wave).

³The convergence of the Cauchy sequence is equivalent with the convergence of the series inside a complete metric space. The detailed and rigorous proof of that convergence and the selection of the proper Banach space is not the topic of the present manuscript. The only guideline that will be given here, is that for the proof maybe the Banach fixed point theorem could be used.

To be more specific concerning the algorithm, the only quantities that is chosen by the user is the initial guess fields e.g. the initial guess potential Φ_0^0 . Then, at every iteration step, the unknown is the corrector ϕ_I^{cor} . That is calculated in a way the ensures that the total Φ_I , at the specific iteration, satisfies the nonlinear equations, defined on the approximation of the total free-surface elevation, at the specific iteration. For that calculation, information from the past is exploited and that information remains unchanged during the whole iterative process. Concerning the sequence of the total potential Φ_I that converges to the fully nonlinear solution Φ , we proceed to the next iteration as follows

$$\Phi_{I+1}(\mathbf{x}; t) = \mathcal{G}_I[\Phi_0^0(\mathbf{x}; t) + \phi_I^{cor}(\mathbf{x}; t)], \quad I \in \mathbb{N}. \quad (4.18)$$

In the present work, a computational code is implemented, following an explicit version of that method, using an Adams-Bashforth-Moulton predictor-corrector time-integration scheme, performing $N_I = 2$ sets of similar constant-time calculations. At a specific timestep the initial constant-time iteration step corresponds to $I = 0$ and the second constant-time iteration step corresponds to $I = N_I - 1 = 1$, for more details see Sec.4.4.5. The extension of the code to the case of arbitrary number of constant-time iterations, until a specific convergence criterion to be satisfied, is left as a subject of future work

By replacing Eq.(4.13) and Eq.(4.14) into linear Laplace equation (Eq.4.1), we conclude that the terms of the representation must be harmonic functions. That should be considered when choosing the initial guess Φ_0^0 and for the corrector ϕ_I^{cor} it is satisfied, because it will be constructed by linear superposition of singularities, located on $\partial D(t)$, that are harmonic functions in open $D(t)$. More details on the representation of the corrector potential field are given in Sec.(4.4.1).

Moreover, we replace the representation in the body boundary condition Eq.(4.2) and taking the limit $I \rightarrow N_I - 1$, we obtain

$$\partial_{n_B} \phi_{N_I-1}^{cor}(\mathbf{x}; t) = \mathbf{V}_B(\mathbf{x}; t) \cdot \mathbf{n}_B(\mathbf{x}; t) - \partial_{n_B} \Phi_0^0(\mathbf{x}; t) = b(\mathbf{x}; t), \quad \mathbf{x} \in \partial D_B(t). \quad (4.19)$$

Moreover we denote that at the time t and at the I^{th} iteration $\partial_{n_B} \Phi_0^0$ is known and therefore $\partial_{n_B} \phi_I^{cor} = \partial_{n_B} \phi_{N_I-1}^{cor} = \partial_{n_B} \phi^{cor}$ is obtained by the known Neumann data b , does not change with the iterations and this is the reason the lower index I in term b is dropped. In a similar manner the hard bottom condition (Eq.4.3) becomes

$$\partial_{n_H} \phi_{N_I-1}^{cor}(\mathbf{x}; t) = \partial_{n_H} \phi^{cor}(\mathbf{x}; t) = -\partial_{n_H} \Phi_0^0(\mathbf{x}; t), \quad \mathbf{x} \in \partial D_H. \quad (4.20)$$

If the initial guess Φ_0^0 satisfies the bottom boundary condition the above equation is just a homogeneous Neumann condition for the unknown corrector potential. Furthermore, we replace the representation for Φ and η at the fully non-linear free-surface conditions (Eqs.4.4 & 4.5) and taking the limit $I \rightarrow N_I - 1$, we obtain the following formulas

$$\begin{aligned} \partial_t \phi_{N_I-1}^{cor}(\mathbf{x}_F, \eta_{N_I-1}; t) &= -\partial_t \Phi_0^0(\mathbf{x}_F, \eta_{N_I-1}; t) - g\eta_0^0(\mathbf{x}_F; t) - g\eta_{N_I-1}^{cor}(\mathbf{x}_F; t) \\ &\quad - \frac{1}{2} [\nabla \Phi_0^0(\mathbf{x}_F, \eta_{N_I-1}; t) + \nabla \phi_{N_I-1}^{cor}(\mathbf{x}_F, \eta_{N_I-1}; t)]^2, \quad \mathbf{x} \in \partial D_{F, N_I-1}(t), \end{aligned} \quad (4.21)$$

$$\begin{aligned} \partial_t \eta_{N_I-1}^{cor}(\mathbf{x}_F; t) &= -\partial_t \eta_0^0(\mathbf{x}_F; t) - [\partial_{n_F} \Phi_0^0(\mathbf{x}_F, \eta_{N_I-1}; t) \\ &\quad + \partial_{n_F} \phi_{N_I-1}^{cor}(\mathbf{x}_F, \eta_{N_I-1}; t)] \sqrt{1 - [\partial_{x_1} \eta_{N_I-1}(\mathbf{x}_F; t)]^2 - [\partial_{x_2} \eta_{N_I-1}(\mathbf{x}_F; t)]^2}, \quad \mathbf{x} \in \partial D_{F, N_I-1}(t), \end{aligned} \quad (4.22)$$

where the initial-guess data (Φ_0^0 , η_0^0 and derivatives) are known and the unknowns are the corrector data ($\phi_{N_I-1}^{cor}$, $\eta_{N_I-1}^{cor}$ and derivatives). The above equations (and pressure Kutta condition for the lifting case), after spatial discretisation, together with the discretised BIE- DtN will be a system of (spatially and temporarily) nonlocal differential equations, with explicit and implicit nonlinearities and an integral constraint. The dynamic variables of the above system are the corrector potential $\phi_{N_I-1}^{cor}$ and free-surface elevation $\eta_{N_I-1}^{cor}$ (and Kutta-strip dipole intensity $\mu_{N_I-1,K}^{cor}$ for the lifting case), while the corrector normal derivative $\partial_n \phi_{N_I-1}^{cor}$ is a dependent variable, that will be expressed as a function of the dynamic variables, using discretised BIE- DtN . The above equations are not linearised in any way and the present approach is a non-perturbative one. To be more specific, a) the explicit non-linearities introduced by the quadratic term in Eq.(4.21) and by the metric of the free-surface boundary in Eq.(4.22) are not approximated by any expansion. Also, b) they are satisfied at the total free-surface elevation, introducing an implicit non-linearity, that is treated by the present general iterative numerical scheme.

Moreover, the corrector trace on the free-surface boundary of the space gradient of the potential ($\nabla \phi_{N_I-1}^{cor}$) can be decomposed to its tangential and the vertical components according to Eq.(2.67), as follows⁴

$$\begin{aligned}\nabla \phi_{N_I-1}^{cor} &= \partial_s \phi_{N_I-1}^{cor} \times \mathbf{n} + \partial_n \phi_{N_I-1}^{cor} \mathbf{n} \\ &= \partial_s \phi_{N_I-1}^{cor} \times \mathbf{n} + \partial_n \phi_{N_I-1}^{cor} \mathbf{n} \\ &= \mathbf{V}_{t,N_I-1}^{cor} + \partial_n \phi_{N_I-1}^{cor} \mathbf{n}, \quad \mathbf{x} \in \partial D_{F,N_I-1}(t).\end{aligned}\quad (4.23)$$

With the aid of Eq.(4.23) and the fact that the square root in Eq.(4.22) is the square root of the total metric a_I of the free-surface boundary, the free-surface boundary conditions become

$$\begin{aligned}\partial_t \phi_{N_I-1}^{cor}(\mathbf{x}_F, \eta_{N_I-1}; t) &= -\partial_t \Phi_0^0(\mathbf{x}_F, \eta_{N_I-1}; t) - g \eta_0^0(\mathbf{x}_F; t) - g \eta_{N_I-1}^{cor}(\mathbf{x}_F; t) \\ &\quad - \frac{1}{2} [\nabla \Phi_0^0(\mathbf{x}_F, \eta_{N_I-1}; t) + \mathbf{V}_{t,N_I-1}^{cor}(\mathbf{x}_F, \eta_{N_I-1}; t) \\ &\quad + \partial_n \phi_{N_I-1}^{cor}(\mathbf{x}_F, \eta_{N_I-1}; t) \mathbf{n}(\mathbf{x}_F, \eta_{N_I-1}; t)]^2, \quad \mathbf{x} \in \partial D_{F,N_I-1}(t),\end{aligned}\quad (4.24)$$

$$\begin{aligned}\partial_t \eta_{N_I-1}^{cor}(\mathbf{x}_F; t) &= -\partial_t \eta_0^0(\mathbf{x}_F; t) - [\partial_{n_F} \Phi_0^0(\mathbf{x}_F, \eta_{N_I-1}; t) \\ &\quad + \partial_{n_F} \phi_{N_I-1}^{cor}(\mathbf{x}_F, \eta_{N_I-1}; t)] \sqrt{a_I(\mathbf{x}_F, \eta_{N_I-1}; t)}, \quad \mathbf{x} \in \partial D_{F,N_I-1}(t),\end{aligned}\quad (4.25)$$

Concerning the lifting part of the problem, the vorticity and the trailing vortex sheet evolves with the mean total velocity $\mathbf{V}_{N_I-1}^m = 0.5(\nabla \Phi_0^{0,u} + \nabla \Phi_0^{0,l}) + 0.5(\nabla \phi_{N_I-1}^{cor,u} + \nabla \phi_{N_I-1}^{cor,l})$. Moreover, at the pressure-type Kutta condition the operator $F_{fs}^{PK}(\cdot)$ becomes

$$\begin{aligned}F_{fs,N_I-1}^{PK}[\mathbf{x}_B(\xi, \eta); t] &= \partial_t (\phi_{N_I-1}^{cor,u} - \phi_{N_I-1}^{cor,l}) + \left[0.5 \left(\nabla \phi_{N_I-1}^{cor,u} + \nabla \phi_{N_I-1}^{cor,l} \right) + 0.5 \left(\nabla \Phi_0^{0,u} + \nabla \Phi_0^{0,l} \right) \right] \\ &\quad \cdot (\nabla \phi_{N_I-1}^{cor,u} - \nabla \phi_{N_I-1}^{cor,l} + \nabla \Phi_0^{0,u} - \nabla \Phi_0^{0,l}) + \partial_t (\Phi_0^{0,u} - \Phi_0^{0,l}) + g(x_3^u - x_3^l).\end{aligned}\quad (4.26)$$

The above equation, after spatial discretisation (including CUFDM), will provide an extra equation that complete the dynamic system of the discretised form of Eqs.(4.21 & 4.22), in the case of lifting flows beneath the free surface and in waves. The extra dynamic variable, that

⁴In the present paragraph the tangential velocity is convenient to be denoted as $\mathbf{V}_{t,N_I-1}^{cor} = \partial_s \phi_{N_I-1}^{cor} \times \mathbf{n}$.

is the corrector Kutta-strip intensity $\mu_{N_{l-1},K}^{cor}$, will be appear when the corrector body potential $\phi_{N_{l-1}}^{cor}$ will be replaced using the extended form of the discretised BIE- DtN .

4.4 Boundary integral formulation and BEM for lifting bodies in waves

4.4.1 Representation theorem and BIE for the corrector potential

The corrector potential is a harmonic function therefore by applying Green's theorem to the present problem Eqs.(4.19 - 4.26), we obtain the following two integral representations for the corrector potential in $\bar{D}_{N_{l-1}}$ in terms of the corrector potential $\phi_{N_{l-1}}^{cor}$ (dipole intensity) and its normal derivative $\partial_n \phi_{N_{l-1}}^{cor}$ (source intensity), the first on the body boundary and the second on the total free-surface boundary, written compactly as follows

$$\begin{aligned}
\phi_{N_{l-1}}^{cor}(\mathbf{x}_0; t) - \phi_{J, N_{l-1}}^{cor}(\mathbf{x}_0; t) &= \int_{\partial D_{B, N_{l-1}}(t)} \partial_n \phi_{B, N_{l-1}}^{cor}(\mathbf{x}; t) G_s(\mathbf{x}_0 | \mathbf{x}) - \phi_{B, N_{l-1}}^{cor}(\mathbf{x}; t) \partial_n G_s(\mathbf{x}_0 | \mathbf{x}) ds(\mathbf{x}) \\
&+ \int_{\partial D_{F, N_{l-1}}(t)} \partial_n \phi_{F, N_{l-1}}^{cor}(\mathbf{x}; t) G_s(\mathbf{x}_0 | \mathbf{x}) - \phi_{F, N_{l-1}}^{cor}(\mathbf{x}; t) \partial_n G_s(\mathbf{x}_0 | \mathbf{x}) ds(\mathbf{x}) \\
&+ \int_{\partial D_{W, N_{l-1}}(t)} \left[\partial_n \phi_{W, N_{l-1}}^{cor, u}(\mathbf{x}; t) - \partial_n \phi_{W, N_{l-1}}^{cor, l}(\mathbf{x}; t) \right] G_s(\mathbf{x}_0 | \mathbf{x}) ds(\mathbf{x}) \\
&- \int_{\partial D_{W, N_{l-1}}(t)} \left[\phi_{W, N_{l-1}}^{cor, u}(\mathbf{x}; t) - \phi_{W, N_{l-1}}^{cor, l}(\mathbf{x}; t) \right] \partial_n G_s(\mathbf{x}_0 | \mathbf{x}) ds(\mathbf{x}), \quad \mathbf{x}_0 \in \partial D_{B, N_{l-1}}(t) \cup \partial D_{F, N_{l-1}}(t) \quad (4.27)
\end{aligned}$$

where

$$\phi_{N_{l-1}}^{cor}(\mathbf{x}_0; t) - \phi_{J, N_{l-1}}^{cor}(\mathbf{x}_0; t) = \begin{cases} \phi_{N_{l-1}}^{cor}(\mathbf{x}_0; t), & \mathbf{x}_0 \in D_{N_{l-1}}. \\ \phi_{B, N_{l-1}}^{cor}(\mathbf{x}_0; t) - \frac{\text{sign}(\mathbf{r} \cdot \mathbf{n})}{2} \phi_{B, N_{l-1}}^{cor}(\mathbf{x}_0; t), & \mathbf{x}_0 \in \partial D_{B, N_{l-1}}, \\ \phi_{F, N_{l-1}}^{cor}(\mathbf{x}_0; t) - \frac{\text{sign}(\mathbf{r} \cdot \mathbf{n})}{2} \phi_{F, N_{l-1}}^{cor}(\mathbf{x}_0; t), & \mathbf{x}_0 \in \partial D_{F, N_{l-1}}, \end{cases} \quad (4.28)$$

In the above relation we have used Green's function (Eq.2.16), consisted of the fundamental solution of 2D/3D Laplace equation corresponding to a Rankine source. In the present case the mirror Green's function could not be exploited because the Neumann bottom boundary condition Eq.(4.3) is inhomogeneous therefore in the case of finite depth the bottom integral must be calculated. For simplicity, we assume deep water conditions therefore the bottom integral is dropped.

The first integral in Eq.(4.27) represents the effect of the body, the second the effect of the free-surface and the third and fourth integrals the effect of the wake on the corrector potential. The first term in the integrals is the corrector potential induced at \mathbf{x}_0 from a source with intensity $\partial_n \phi_{N_{l-1}}^{cor}(\mathbf{x})$ located on the boundary at \mathbf{x} , while the second term represents similarly the effect of normal to the boundary dipole with intensity $\phi_{N_{l-1}}^{cor}(\mathbf{x})$. In this way the whole information for the corrector potential in the domain $D_{N_{l-1}}$ is stored on the boundary $\partial D_{N_{l-1}}$ whose

dimension is of one order lower. Therefore, if the trace of the corrector potential and the corrector normal derivative on the boundary are known, using Green's formula Eqs.(4.27, 4.28) we can evaluate corrector potential everywhere in D_{N_I-1} . The initial guess potential is known, therefore the total potential can be obtained.

Replacing body boundary condition Eq.(4.19) and wake kinematic condition into the representation theorem on the boundary Eqs.(3.60, 3.61), we obtain the following two Fredholm 2nd kind weakly singular integral equations

$$\begin{aligned}
& - \int_{\partial D_{F,N_I-1}(t)} \partial_n \phi_{F,N_I-1}^{cor}(\mathbf{x}; t) G_s(\mathbf{x}_0|\mathbf{x}) ds(\mathbf{x}) \\
& \frac{1}{2} \phi_{B,N_I-1}^{cor}(\mathbf{x}_0; t) + \int_{\partial D_{B,N_I-1}(t)} \phi_{B,N_I-1}^{cor}(\mathbf{x}; t) \partial_n G_s(\mathbf{x}_0|\mathbf{x}) ds(\mathbf{x}) = - \int_{\partial D_{F,N_I-1}(t)} \phi_{F,N_I-1}^{cor}(\mathbf{x}; t) \partial_n G_s(\mathbf{x}_0|\mathbf{x}) ds(\mathbf{x}) \\
& \quad + \int_{\partial D_{B,N_I-1}(t)} b(\mathbf{x}; t) G_s(\mathbf{x}_0|\mathbf{x}) ds(\mathbf{x}) \\
& \quad - \int_{\partial D_{W,N_I-1}(t)} \mu_{W,N_I-1}^{cor}(\mathbf{x}; t) \partial_n G(\mathbf{x}_0|\mathbf{x}) ds(\mathbf{x}), \quad \mathbf{x}_0 \in \partial D_{B,N_I-1}(t),
\end{aligned} \tag{4.29}$$

and

$$\begin{aligned}
& - \int_{\partial D_{F,N_I-1}(t)} \partial_n \phi_{F,N_I-1}^{cor}(\mathbf{x}; t) G_s(\mathbf{x}_0|\mathbf{x}) ds(\mathbf{x}) \\
& + \int_{\partial D_{B,N_I-1}(t)} \phi_{B,N_I-1}^{cor}(\mathbf{x}; t) \partial_n G_s(\mathbf{x}_0|\mathbf{x}) ds(\mathbf{x}) = - \frac{1}{2} \phi_{F,N_I-1}^{cor}(\mathbf{x}_0; t) - \int_{\partial D_{F,N_I-1}(t)} \phi_{F,N_I-1}^{cor}(\mathbf{x}; t) \partial_n G_s(\mathbf{x}_0|\mathbf{x}) ds(\mathbf{x}) \\
& \quad + \int_{\partial D_{B,N_I-1}(t)} b(\mathbf{x}; t) G_s(\mathbf{x}_0|\mathbf{x}) ds(\mathbf{x}) \\
& \quad - \int_{\partial D_{W,N_I-1}(t)} \mu_{W,N_I-1}^{cor}(\mathbf{x}; t) \partial_n G(\mathbf{x}_0|\mathbf{x}) ds(\mathbf{x}), \quad \mathbf{x}_0 \in \partial D_{F,N_I-1}(t),
\end{aligned} \tag{4.30}$$

where $\mu_{W,N_I-1}^{cor} = \phi_{W,N_I-1}^{cor,\mu} - \phi_{W,N_I-1}^{cor,l}$ denotes the corrector potential jump or the corrector dipole intensity on the wake. The weakly singular boundary integral equations Eqs.(4.29 & 4.30), free-surface boundary conditions Eqs.(4.24, 4.25) and the Pressure-type Kutta condition Eqs.(4.11 and 4.26) provide us with a system of equations for the unknown boundary fields ϕ_{B,N_I-1}^{cor} on the body, ϕ_{F,N_I-1}^{cor} and $\partial_n \phi_{F,N_I-1}^{cor}$ at the free-surface and μ_{W,N_I-1}^{cor} at the vicinity of trailing edge. The above system of equations can be solved numerically after the appropriate discretisation, implemented with a boundary element method (BEM) and collocation and the free-surface conditions are treated as a dynamic system and BIE as an algebraic constraint, as we will see in the following sections.

4.4.2 Discretisation and the extended DtN map

The spacial discretisation mainly consists of the following approximations of the analytical model:

- Concerning the geometry, a C^0 representation of the boundary is used as follows:
 - in 2D formulation, following a low-order panel method, the body contour is replaced by a closed polygonal line, and N_B denotes the number of panels. The free surface and the trailing vortex sheet are also approximated by open polygonal lines composed of N_F and $N_W(t)$ panels, respectively.
 - in 3D formulation, the boundary is approximated using bilinear-quadrilateral elements.
- Concerning the representation of the functions on the boundary, the corrector potential, its normal derivative and the corrector potential jump at each time step, are approximated by piecewise constant distributions, as follows:

$$\begin{aligned}
 \phi_{F,N_I-1}^{cor}(\mathbf{x};t) &= \phi_{F,N_I-1,f}^{cor}(t), \text{ at free-surface element } f, f = 0, 1, \dots, N_F - 1, \\
 \partial_n \phi_{F,N_I-1}^{cor}(\mathbf{x};t) &= \partial_n \phi_{F,N_I-1,f}^{cor}(t), \text{ at free-surface element } f, f = 0, 1, \dots, N_F - 1, \\
 \phi_{B,N_I-1}^{cor}(\mathbf{x};t) &= \phi_{B,N_I-1,i}^{cor}(t), \text{ at body element } i, i = 0, 1, \dots, N_B - 1, \\
 \partial_n \phi_{B,N_I-1}^{cor}(\mathbf{x};t) &= \partial_n \phi_{B,i}^{cor}(t) = b_i(t), \text{ at body element } i, i = 0, 1, \dots, N_B - 1, \\
 \mu_{W,N_I-1}^{cor}(\mathbf{x};t) &= \mu_{W,N_I-1,w}^{cor}(t), \text{ at wake element } w, w = 0, 1, \dots, N_W(t) - 1.
 \end{aligned} \tag{4.31}$$

- Finally, following a collocation scheme, the BIEs Eqs.(4.29 & 4.30) are satisfied in a finite number of points (or control points) and in order to avoid singularities the centroids of the elements have been chosen as collocation points.

To proceed, the discretised form of the BIEs Eqs.(4.29 & 4.30) is as follows

$$\begin{aligned}
 \mathcal{A}_{F,B,N_I-1}^{pot}(t) \cdot \begin{pmatrix} \mathbf{N}_{F,N_I-1}^{cor}(t) \\ \boldsymbol{\phi}_{B,N_I-1}^{cor}(t) \end{pmatrix} &= \mathcal{B}_{F,B,N_I-1}^{pot}(t) \cdot \begin{pmatrix} \boldsymbol{\phi}_{F,N_I-1}^{cor}(t) \\ \mathbf{b}(t) \end{pmatrix} \\
 &+ \mathcal{D}_{F,B,K,N_I-1}^{pot}(t) \cdot \boldsymbol{\mu}_{K,N_I-1}^{cor}(t) + \mathcal{D}_{F,B,W,N_I-1}^{pot}(t) \cdot \boldsymbol{\mu}_{W,N_I-1}^{cor},
 \end{aligned} \tag{4.32}$$

where

$$\begin{aligned}
 \mathcal{A}_{F,B,N_I-1}^{pot}(t) &= \begin{pmatrix} \mathcal{A}_{F,B,N_I-1,00}^{pot} & \mathcal{A}_{F,B,N_I-1,01}^{pot}(t) \\ \mathcal{A}_{F,B,N_I-1,10}^{pot}(t) & \mathcal{A}_{F,B,11}^{pot} \end{pmatrix}, \\
 \mathcal{B}_{F,B,N_I-1}^{pot}(t) &= \begin{pmatrix} \mathcal{B}_{F,B,N_I-1,00}^{pot} & \mathcal{B}_{F,B,N_I-1,01}^{pot}(t) \\ \mathcal{B}_{F,B,N_I-1,10}^{pot}(t) & \mathcal{B}_{F,B,11}^{pot} \end{pmatrix}, \\
 \mathcal{D}_{F,B,K,N_I-1}^{pot}(t) &= \begin{pmatrix} \mathcal{D}_{F,B,K,N_I-1,0}^{pot}(t) \\ \mathcal{D}_{F,B,K,1}^{pot} \end{pmatrix}, \quad \mathcal{D}_{F,B,W,N_I-1}^{pot}(t) = \begin{pmatrix} \mathcal{D}_{F,B,W,N_I-1,0}^{pot}(t) \\ \mathcal{D}_{F,B,W,1}^{pot}(t) \end{pmatrix}.
 \end{aligned} \tag{4.33}$$

In the above equations $\mathcal{A}_{F,B,N_I-1}^{pot}$, $\mathcal{B}_{F,B,N_I-1}^{pot}$ are the potential induction-factor matrices at the left hand side and the right hand side of Eqs.(4.29 & 4.30), respectively. They model free surface-free surface, body-body and free surface-body interactions. Also $\mathcal{D}_{F,B,K,N_I-1}^{pot}$, $\mathcal{D}_{F,B,W,N_I-1}^{pot}$ are double layer potential induction-factor matrices modeling the effects of the Kutta strip and the wake on the free-surface and the body. The above matrices are defined as follows

$$\begin{aligned}
\mathcal{A}_{F,B,N_I-1,00}^{pot} &= \{-S_{N_I-1,fs}^{pot}\}, \quad \mathcal{A}_{F,B,N_I-1,01}^{pot}(t) = \{D_{N_I-1,fj}^{pot}(t)\}, \\
\mathcal{A}_{F,B,N_I-1,10}^{pot}(t) &= \{-S_{N_I-1,is}^{pot}(t)\}, \quad \mathcal{A}_{F,B,11}^{pot} = \{0.5\delta_{ij} + D_{ij}^{pot}\}, \\
\mathcal{B}_{F,B,N_I-1,00}^{pot} &= \{-0.5\delta_{fs} - D_{N_I-1,fs}^{pot}\}, \quad \mathcal{B}_{F,B,N_I-1,01}^{pot}(t) = \{S_{N_I-1,fj}^{pot}(t)\}, \\
\mathcal{B}_{F,B,N_I-1,10}^{pot}(t) &= \{-D_{N_I-1,is}^{pot}(t)\}, \quad \mathcal{B}_{F,B,11}^{pot} = \{S_{ij}^{pot}\}, \\
\mathcal{D}_{F,B,K,N_I-1,0}^{pot}(t) &= \{-D_{N_I-1,fk}^{pot}(t)\}, \quad \mathcal{D}_{F,B,K,1}^{pot} = \{-D_{bk}^{pot}\}, \\
\mathcal{D}_{F,B,W,N_I-1,0}^{pot}(t) &= \{-D_{N_I-1,fw}^{pot}(t)\}, \quad \mathcal{D}_{F,B,W,1}^{pot}(t) = \{-D_{iw}^{pot}(t)\},
\end{aligned} \tag{4.34}$$

with \mathcal{S} denoting source or single-layer integrals, and with \mathcal{D} denoting dipole or double-layer integrals see Eq.(2.23). Moreover, the indices belong to the following subsets of \mathbb{N}

$$f, s \in \{0, 1, \dots, N_F - 1\}, \quad i, j \in \{0, 1, \dots, N_B - 1\}, \quad k \in \{0, 1, \dots, N_K - 1\}, \quad w \in \{0, 1, \dots, N_W(t) - 1\}. \tag{4.35}$$

In Eq.(4.32) $\boldsymbol{\phi}_{F,N_I-1}^{cor} = \{\phi_{F,N_I-1,s}^{cor}\}$, $\mathbf{N}_{F,N_I-1}^{cor} = \{\partial_n \phi_{F,N_I-1,s}^{cor}\}$, $\boldsymbol{\phi}_{B,N_I-1}^{cor} = \{\phi_{B,N_I-1,j}^{cor}\}$, $\mathbf{b} = \{b_j\}$, $\boldsymbol{\mu}_{K,N_I-1}^{cor} = \{\mu_{K,N_I-1,k}^{cor}\}$, $\boldsymbol{\mu}_{W,N_I-1}^{cor} = \{\mu_{W,N_I-1,w}^{cor}\}$. In the sequel, we will denote with bold, vectors containing the values of piecewise constant functions on the panels, at various parts of the boundary.

Next we multiply Eq.(4.32) with $[\mathcal{A}_{F,B,N_I-1}^{pot}(t)]^{-1}$ and we obtain

$$\begin{aligned}
\begin{pmatrix} \mathbf{N}_{F,N_I-1}^{cor}(t) \\ \boldsymbol{\phi}_{B,N_I-1}^{cor}(t) \end{pmatrix} &= \mathcal{G}_{N_I-1}(t) \cdot \begin{pmatrix} \boldsymbol{\phi}_{F,N_I-1}^{cor}(t) \\ \mathbf{b}(t) \end{pmatrix} \\
&+ \mathcal{Z}_{N_I-1}(t) \cdot \boldsymbol{\mu}_{K,N_I-1}^{cor}(t) + \mathcal{P}_{N_I-1}(t) \cdot \boldsymbol{\mu}_{W,N_I-1}^{cor},
\end{aligned} \tag{4.36}$$

or

$$\begin{aligned}
\begin{pmatrix} \mathbf{N}_{F,N_I-1}^{cor}(t) \\ \boldsymbol{\phi}_{B,N_I-1}^{cor}(t) \end{pmatrix} &= \begin{pmatrix} \mathcal{G}_{N_I-1,00}(t) & \mathcal{G}_{N_I-1,01}(t) \\ \mathcal{G}_{N_I-1,10}(t) & \mathcal{G}_{N_I-1,11}(t) \end{pmatrix} \cdot \begin{pmatrix} \boldsymbol{\phi}_{F,N_I-1}^{cor}(t) \\ \mathbf{b}(t) \end{pmatrix} \\
&+ \begin{pmatrix} \mathcal{Z}_{N_I-1,0}(t) \\ \mathcal{Z}_{N_I-1,1}(t) \end{pmatrix} \cdot \boldsymbol{\mu}_{K,N_I-1}^{cor}(t) + \begin{pmatrix} \mathcal{P}_{N_I-1,0}(t) \\ \mathcal{P}_{N_I-1,1}(t) \end{pmatrix} \cdot \boldsymbol{\mu}_{W,N_I-1}^{cor},
\end{aligned} \tag{4.37}$$

where

$$\begin{aligned}
\mathcal{G}_{N_I-1}(t) &= [\mathcal{A}_{F,B,N_I-1}^{pot}(t)]^{-1} \cdot \mathcal{B}_{F,B,N_I-1}^{pot}(t), \quad \mathcal{Z}_{N_I-1}(t) = [\mathcal{A}_{F,B,N_I-1}^{pot}(t)]^{-1} \cdot \mathcal{D}_{F,B,K,N_I-1}^{pot}(t), \\
\mathcal{P}_{N_I-1}(t) &= [\mathcal{A}_{F,B,N_I-1}^{pot}(t)]^{-1} \cdot \mathcal{D}_{F,B,W,N_I-1}^{pot}(t).
\end{aligned} \tag{4.38}$$

The above mapping is the discrete form of the extended Dirichlet-to-Neumann (DtN) operator

that is suitable for lifting flows beneath the free surface and in waves. That operator connects the corrector potential (Dirichlet data) with its normal derivative (Neumann data) on body boundary ∂D_B , but also involves the unknown values of the corrector dipole intensity μ_{K, N_I-1}^{cor} (Dirichlet data) on the Kutta strip ∂D_K , as well as the (known from the past) corrector potential jump μ_{W, N_I-1}^{cor} (Dirichlet data) on the wake ∂D_W . We observe in the above equation that the influence of the wake, that introduces memory effects, is taken into account through $\mathcal{P}_{N_I-1}(t) \cdot \mu_{W, N_I-1}^{cor}$. Also, the effect of the body velocity and the initial guess velocity are considered through the components \mathbf{V}_B and $\partial_{n_B} \Phi_0^0$, included in \mathbf{b} , as described by the body boundary condition Eq.(4.19). In Sec.4.4.4 using the appropriate parts of the extended DtN map, Eqs.(4.36 - 4.38), in the discretised form of free-surface boundary conditions and pressure-type Kutta condition, we will obtain a system of (spatially and temporarily) nonlocal differential equations, with explicit and implicit nonlinearities, that approximately describe the dynamics of the system.

4.4.3 Pressure calculation and implementation of the pressure-type Kutta condition

In the present section we develop the appropriate form of Bernoulli's theorem for the calculation of pressure distribution in the case of lifting flows beneath the nonlinear free surface and in the presence of nonlinear waves and the analytical form of pressure-type Kutta condition for the same problem. Both expressions will be in terms of the representation of the total fields.

We begin with the appropriate form of Bernoulli's theorem that has been derived in Sec.3.3, Eq.(3.18), that is rewritten here

$$\frac{p(\mathbf{x}; t) - p_{atm}}{\rho} + \partial_t \Phi(\mathbf{x}; t) + \frac{1}{2} [\nabla \Phi(\mathbf{x}; t)]^2 + gx_3 = 0, \quad \mathbf{x} \in D. \quad (4.39)$$

in the above equations p is the pressure at $\mathbf{x} = \{x_1, x_2, x_3\}$, p_{atm} is the atmospheric pressure on the free surface, ρ is the density of the fluid, g is the acceleration of gravity and the last term is the hydrostatic component. When using that form of Bernoulli's equation to calculate forces acting on the body (especially for free-floating or semi-activated systems; see Sec.4.5.4) we should either omit the hydrostatic term or include to the calculation the gravitational force acting on the body that depends to its mass.

Now the representation of the total fields will be replaced in Eq.(3.18). According to Eq.(4.14), the total wave potential $\Phi_I(\mathbf{x}; t)$ and its derivative have the following representation

$$\Phi(\mathbf{x}; t) = \lim_{I \rightarrow N_I-1} \Phi_I(\mathbf{x}; t), \quad \Phi_I(\mathbf{x}; t) = \Phi_0^0(\mathbf{x}; t) + \phi_I^{cor}(\mathbf{x}; t), \quad I \in \mathbb{N}, \quad (4.40)$$

$$\nabla \Phi(\mathbf{x}; t) = \lim_{I \rightarrow N_I-1} \nabla \Phi_I(\mathbf{x}; t), \quad \nabla \Phi_I(\mathbf{x}; t) = \nabla \Phi_0^0(\mathbf{x}; t) + \nabla \phi_I^{cor}(\mathbf{x}; t), \quad I \in \mathbb{N}. \quad (4.41)$$

By replacing Eqs.(4.40 & 4.41) into Eq.(4.39), taking the limit $I \rightarrow (N_I - 1)$ and rearranging terms, we obtain the following relation

$$\frac{p(\mathbf{x};t) - p_{atm}}{\rho} = -\partial_t \phi_{N_I-1}^{cor}(\mathbf{x};t) - \frac{1}{2} \left[\nabla \Phi_0^0(\mathbf{x};t) + \nabla \phi_{N_I-1}^{cor}(\mathbf{x};t) \right]^2 - \partial_t \Phi_0^0(\mathbf{x};t) - gx_3, \quad \mathbf{x} \in D. \quad (4.42)$$

In the equations above, $\partial_t(\cdot)$ denotes the rate of change with respect to an earth-fixed (inertial) observer (i.e. with regard to an inertial reference frame). The time derivative of the corrector potential $d_t \phi_{N_I-1}^{cor}$ with respect to the moving, with the body velocity, frame of reference can be calculated by the following formula

$$d_t \phi_{N_I-1}^{cor}(\mathbf{x};t) = \nabla \phi_{N_I-1}^{cor}(\mathbf{x};t) \cdot \mathbf{V}_B(\mathbf{x};t) + \partial_t \phi_{N_I-1}^{cor}(\mathbf{x};t), \quad \mathbf{x} \in \partial D_B(t). \quad (4.43)$$

More details concerning the derivation of the above formula can be found e.g. in the following references Katz and Plotkin (2001), Politis (2004), Politis (2011b), Filippas (2013). By replacing Eq.(4.43) into Eq.(4.42), we obtain a formula for pressure calculation on body boundary, as follows

$$\begin{aligned} \frac{p(\mathbf{x};t) - p_{atm}}{\rho} &= -d_t \phi_{N_I-1}^{cor}(\mathbf{x};t) + \nabla \phi_{N_I-1}^{cor}(\mathbf{x};t) \cdot \mathbf{V}_B(\mathbf{x};t) \\ &\quad - \frac{1}{2} \left[\nabla \Phi_0^0(\mathbf{x};t) + \nabla \phi_{N_I-1}^{cor}(\mathbf{x};t) \right]^2 - \partial_t \Phi_0^0(\mathbf{x};t) - gx_3, \quad \mathbf{x} \in \partial D_B(t). \end{aligned} \quad (4.44)$$

using binomial theorem for the sum of squares and rearranging terms we obtain the following formula

$$\begin{aligned} \frac{p(\mathbf{x};t) - p_{atm}}{\rho} &= -d_t \phi_{N_I-1}^{cor}(\mathbf{x};t) + \nabla \phi_{N_I-1}^{cor}(\mathbf{x};t) \cdot \left[\mathbf{V}_B(\mathbf{x};t) - \nabla \Phi_0^0(\mathbf{x};t) \right] - \frac{1}{2} \left[\nabla \phi_{N_I-1}^{cor}(\mathbf{x};t) \right]^2 \\ &\quad - \partial_t \Phi_0^0(\mathbf{x};t) - \frac{1}{2} \left[\nabla \Phi_0^0(\mathbf{x};t) \right]^2 - gx_3, \quad \mathbf{x} \in \partial D_B(t). \end{aligned} \quad (4.45)$$

Moreover, $\nabla \phi_{N_I-1}^{cor}$ can be decomposed to its tangential and the vertical components according to Eq.(2.67) and the body boundary condition (Eqs.4.2 & 4.19), as follows⁵

$$\begin{aligned} \nabla \phi_{N_I-1}^{cor}(\mathbf{x};t) &= \partial_s \phi_{N_I-1}^{cor}(\mathbf{x};t) \times \mathbf{n}(\mathbf{x};t) + \partial_n \phi_{N_I-1}^{cor}(\mathbf{x};t) \cdot \mathbf{n}(\mathbf{x};t) \\ &= \partial_s \phi_{N_I-1}^{cor}(\mathbf{x};t) \times \mathbf{n}(\mathbf{x};t) + \partial_n \phi^{cor}(\mathbf{x};t) \cdot \mathbf{n}(\mathbf{x};t) \\ &= \mathbf{V}_{t,N_I-1}^{cor}(\mathbf{x};t) + \left[\mathbf{V}_B(\mathbf{x};t) \cdot \mathbf{n}(\mathbf{x};t) - \partial_{n_B} \Phi_0^0(\mathbf{x};t) \right] \cdot \mathbf{n}(\mathbf{x};t) \\ &= \mathbf{V}_{t,N_I-1}^{cor}(\mathbf{x};t) + b(\mathbf{x};t) \mathbf{n}(\mathbf{x};t), \quad \mathbf{x} \in \partial D_B(t). \end{aligned} \quad (4.46)$$

Therefore, Eq.(4.45), after some algebra, becomes

$$\begin{aligned} \frac{p(\mathbf{x};t) - p_{atm}}{\rho} &= -d_t \phi_{N_I-1}^{cor}(\mathbf{x};t) + \nabla \phi_{N_I-1}^{cor}(\mathbf{x};t) \cdot \left[\mathbf{V}_B(\mathbf{x};t) - \nabla \Phi_0^0(\mathbf{x};t) \right] - \frac{1}{2} \left[\nabla \phi_{N_I-1}^{cor}(\mathbf{x};t) \right]^2 \\ &\quad + \frac{1}{2} [b(\mathbf{x};t)]^2 - \partial_t \Phi_0^0(\mathbf{x};t) - \frac{1}{2} \left[\nabla \Phi_0^0(\mathbf{x};t) \right]^2 - gx_3, \quad \mathbf{x} \in \partial D_B(t). \end{aligned} \quad (4.47)$$

⁵In the present paragraph the tangential velocity is convenient to be denoted as $\mathbf{V}_t = \partial_s \Phi \times \mathbf{n}$.

The above form of Bernoulli's equation is utilised for pressure calculations on the body boundary in the case of (nonlifting or lifting) bodies beneath the free surface and in nonlinear waves and is written in terms of the representation of total fields. Then the boundary pressure can be integrated to obtain generalised forces (forces and moments) and by exploiting also the local generalised velocity (linear and angular), the power of the studied hydromechanical systems can be obtained, leading to the estimation of appropriate metrics of the efficiency or the performance (power take-off).

The classical Pressure-type Kutta condition in the following form can be produced from the dynamic boundary condition on the wake by demanding that the pressure field (and therefore the pressure jump) ought to be continuous in \bar{D} as explained in Sec.2.8

$$\lim_{\xi \rightarrow \xi_{TE}} \left\{ p_B^u[\mathbf{x}_B(\xi, \eta); t] - p_B^l[\mathbf{x}_B(\xi, \eta); t] \right\} = 0, \quad \mathbf{x}_B \in \partial D_B(t) \text{ and } \mathbf{x}_{TE} \in \partial D_B(t) \cup \partial D_W(t), \quad (4.48)$$

To proceed, we apply Bernoulli's theorem (Eq.3.18 or Eq.4.39) to the upper and lower side of the trailing edge, we use pressure-type Kutta condition (Eq.3.23) and we factorise the difference of squares to construct the following form of the condition

$$\lim_{\xi \rightarrow \xi_{TE}} F^{PK}[\mathbf{x}_B(\xi, \eta); t] = 0, \quad \mathbf{x}_B \in \partial D_B \text{ and } \mathbf{x}_{TE} \in \partial D_B \cup \partial D_W, \quad (4.49)$$

where the operator $F^{PK}(\cdot)$ is defined as follows

$$F^{PK}[\mathbf{x}_B(\xi, \eta); t] = \partial_t(\Phi^u - \Phi^l) + 0.5(\nabla\Phi^u + \nabla\Phi^l) \cdot (\nabla\Phi^u - \nabla\Phi^l) + g(x_3^u - x_3^l). \quad (4.50)$$

The above form of pressure-type Kutta condition written with respect to the inertial reference frame has already been used in the mathematical formulation of the present problem in Sec.3.2, Eqs.(4.10 & 4.11). For the calculation of pressure from the boundary values of the potential, that is the primary unknown is the present direct formulation, the reformulation of the above relation with respect to the moving reference frame is required. Aiming to the construction of the aforementioned formula we begin with Eq.(4.45), that is rewritten bellow

$$\begin{aligned} \frac{p(\mathbf{x}; t) - p_{atm}}{\rho} &= -d_t\phi_{N_I}^{cor}(\mathbf{x}; t) + \nabla\phi_{N_I}^{cor}(\mathbf{x}; t) \cdot [\mathbf{V}_B(\mathbf{x}; t) - \nabla\Phi_0^0(\mathbf{x}; t)] - \frac{1}{2} [\nabla\phi_{N_I}^{cor}(\mathbf{x}; t)]^2 \\ &\quad - \partial_t\Phi_0^0(\mathbf{x}; t) - \frac{1}{2} [\nabla\Phi_0^0(\mathbf{x}; t)]^2 - gx_3, \quad \mathbf{x} \in \partial D_B(t). \end{aligned} \quad (4.51)$$

By rearranging terms, making common factor $-1/2$ and adding and subtracting the quantity $-1/2 [\mathbf{V}_B - \nabla\Phi_0^0]^2$ and factorising, we obtain the following formula

$$\begin{aligned} \frac{p(\mathbf{x}; t) - p_{atm}}{\rho} &= -d_t\phi_{N_I-1}^{cor}(\mathbf{x}; t) \\ &\quad - \frac{1}{2} \left\{ [\nabla\phi_{N_I-1}^{cor}(\mathbf{x}; t)]^2 - 2\nabla\phi_{N_I-1}^{cor}(\mathbf{x}; t) \cdot [\mathbf{V}_B(\mathbf{x}; t) - \nabla\Phi_0^0(\mathbf{x}; t)] + [\mathbf{V}_B - \nabla\Phi_0^0]^2 \right\} \\ &\quad + 1/2 [\mathbf{V}_B - \nabla\Phi_0^0]^2 - \partial_t\Phi_0^0(\mathbf{x}; t) - \frac{1}{2} [\nabla\Phi_0^0(\mathbf{x}; t)]^2 - gx_3, \quad \mathbf{x} \in \partial D_B(t). \end{aligned} \quad (4.52)$$

Moreover, we factorise the difference of squares to construct the following form of Bernoulli's theorem

$$\begin{aligned} \frac{p(\mathbf{x};t) - p_{atm}}{\rho} = & -d_t \phi_{N_I-1}^{cor}(\mathbf{x};t) - \frac{1}{2} \left[\nabla \phi_{N_I-1}^{cor}(\mathbf{x};t) + \nabla \Phi_0^0 - \mathbf{V}_B \right]^2 \\ & + 1/2 \left[\nabla \Phi_0^0 - \mathbf{V}_B \right]^2 - \partial_t \Phi_0^0(\mathbf{x};t) - \frac{1}{2} \left[\nabla \Phi_0^0(\mathbf{x};t) \right]^2 - g x_3, \quad \mathbf{x} \in \partial D_B(t). \end{aligned} \quad (4.53)$$

To proceed further, we apply the above form of Bernoulli's theorem to the upper and lower side of the trailing edge, we use pressure-type Kutta condition (Eq.4.48) to construct the following form of the operator $F^{PK}(\cdot)$

$$\begin{aligned} F_{N_I-1}^{PK}[\mathbf{x}_B(\xi, \eta); t] = & d_t(\phi_{N_I-1}^{cor,u} - \phi_{N_I-1}^{cor,l}) + \frac{1}{2} \left(\nabla \phi_{N_I-1}^{cor,u} + \nabla \Phi_0^{0,u} - \mathbf{V}_B^u \right)^2 - \frac{1}{2} \left(\nabla \phi_{N_I-1}^{cor,l} + \nabla \Phi_0^{0,l} - \mathbf{V}_B^l \right)^2 \\ & + \frac{1}{2} \left(\nabla \Phi_0^{0,l} - \mathbf{V}_B^l \right)^2 - \frac{1}{2} \left(\nabla \Phi_0^{0,u} - \mathbf{V}_B^u \right)^2 \\ & + \partial_t \left(\Phi_0^{0,u} - \Phi_0^{0,l} \right) + \frac{1}{2} \left(\nabla \Phi_0^{0,u} \right)^2 - \frac{1}{2} \left(\nabla \Phi_0^{0,l} \right)^2 + g \left(x_3^u - x_3^l \right). \end{aligned} \quad (4.54)$$

Moreover, the trace on the body boundary of the space gradient of the potential can be decomposed to its tangential and the vertical components according to Eq.(2.67) and the body boundary condition (Eqs.4.2 & 4.19), as follows⁶

$$\begin{aligned} \nabla \phi_{N_I-1}^{cor}(\mathbf{x};t) = & \partial_s \phi_{N_I-1}^{cor}(\mathbf{x};t) \times \mathbf{n}(\mathbf{x};t) + \partial_n \phi_{N_I-1}^{cor}(\mathbf{x};t) \cdot \mathbf{n}(\mathbf{x};t) \\ = & \partial_s \phi_{N_I-1}^{cor}(\mathbf{x};t) \times \mathbf{n}(\mathbf{x};t) + \partial_n \phi^{cor}(\mathbf{x};t) \cdot \mathbf{n}(\mathbf{x};t) \\ = & \mathbf{V}_{t,N_I-1}^{cor}(\mathbf{x};t) + \left[\mathbf{V}_B(\mathbf{x};t) \cdot \mathbf{n}(\mathbf{x};t) - \partial_{n_B} \Phi_0^0(\mathbf{x};t) \right] \cdot \mathbf{n}(\mathbf{x};t) \\ = & \mathbf{V}_{t,N_I-1}^{cor}(\mathbf{x};t) + b(\mathbf{x};t) \mathbf{n}(\mathbf{x};t), \quad \mathbf{x} \in \partial D_B(t). \end{aligned} \quad (4.55)$$

With the aid of Eq.(4.55), the operator $F^{PK}(\cdot)$ becomes

$$\begin{aligned} F_{N_I-1}^{PK}[\mathbf{x}_B(\xi, \eta); t] = & d_t(\phi_{N_I-1}^{cor,u} - \phi_{N_I-1}^{cor,l}) \\ & + \frac{1}{2} \left(\mathbf{V}_{t,N_I-1}^{cor,u} + b^u \mathbf{n}^u + \nabla \Phi_0^{0,u} - \mathbf{V}_B^u \right)^2 - \frac{1}{2} \left(\mathbf{V}_{t,N_I-1}^{cor,l} + b^l \mathbf{n}^l + \nabla \Phi_0^{0,l} - \mathbf{V}_B^l \right)^2 \\ & + \frac{1}{2} \left(\nabla \Phi_0^{0,l} - \mathbf{V}_B^l \right)^2 - \frac{1}{2} \left(\nabla \Phi_0^{0,u} - \mathbf{V}_B^u \right)^2 \\ & + \partial_t \left(\Phi_0^{0,u} - \Phi_0^{0,l} \right) + \frac{1}{2} \left(\nabla \Phi_0^{0,u} \right)^2 - \frac{1}{2} \left(\nabla \Phi_0^{0,l} \right)^2 + g \left(x_3^u - x_3^l \right). \end{aligned} \quad (4.56)$$

Moreover, by factorising the difference of the squares and rearranging terms, we obtain the following form of pressure-type Kutta condition

$$\lim_{\xi \rightarrow \xi_{TE}} F_{N_I-1}^{PK}[\mathbf{x}_B(\xi, \eta); t] = 0, \quad \mathbf{x}_B \in \partial D_B \text{ and } \mathbf{x}_{TE} \in \partial D_B \cup \partial D_W, \quad (4.57)$$

⁶In the present paragraph the tangential velocity is convenient to be denoted as $\mathbf{V}_t = \partial_s \Phi \times \mathbf{n}$.

where

$$\begin{aligned}
F_{N_I-1}^{PK}[\mathbf{x}_B(\zeta, \eta); t] = & d_t(\phi_{N_I-1}^{cor,u} - \phi_{N_I-1}^{cor,l}) \\
& + \left(\frac{\mathbf{V}_{t,N_I-1}^{cor,u} + \mathbf{V}_{t,N_I-1}^{cor,l}}{2} + \frac{b^u \mathbf{n}^u + b^l \mathbf{n}^l}{2} + \frac{\nabla \Phi_0^{0,u} + \nabla \Phi_0^{0,l}}{2} - \frac{\mathbf{V}_B^u + \mathbf{V}_B^l}{2} \right) \\
& \left[\mathbf{V}_{t,N_I-1}^{cor,u} - \mathbf{V}_{t,N_I-1}^{cor,l} + b^u \mathbf{n}^u - b^l \mathbf{n}^l + \nabla \Phi_0^{0,u} - \nabla \Phi_0^{0,l} - (\mathbf{V}_B^u - \mathbf{V}_B^l) \right] \\
& - \left(\frac{\nabla \Phi_0^{0,u} + \nabla \Phi_0^{0,l}}{2} - \frac{\mathbf{V}_B^u + \mathbf{V}_B^l}{2} \right) \left[\nabla \Phi_0^{0,u} - \nabla \Phi_0^{0,l} - (\mathbf{V}_B^u - \mathbf{V}_B^l) \right] \\
& + \partial_t (\Phi_0^{0,u} - \Phi_0^{0,l}) + \frac{\nabla \Phi_0^{0,u} + \nabla \Phi_0^{0,l}}{2} (\nabla \Phi_0^{0,u} - \nabla \Phi_0^{0,l}) + g (x_3^u - x_3^l).
\end{aligned} \tag{4.58}$$

The above relation⁷ is the pressure-type Kutta condition with respect to the body fixed reference frame. That equation includes a quadratic nonlinear form of the unknown trace on the boundary of the corrector tangential velocity $\mathbf{V}_{t,N_I-1}^{cor}$, linear terms and the last line that includes known initial guess terms and the hydrostatic term. It also includes the unknown boundary value of the corrector potential ϕ^{cor} at the body contour as approaching the trailing edge. As will be demonstrated in the following section the continuous boundary field $\mathbf{V}_{t,N_I-1}^{cor}$ is approximated by a discrete tangential velocity field that is projected to a curvilinear coordinated system (see also Sec.2.5.2.1). Moreover, it is approximated by CUFDM (see also Sec.2.5.2.2) and replaced with linear combinations of ϕ^{cor} . Then an extended form of the DtN operator (see Sec.4.4.2 and Sec.4.4.4) will be exploited to replace all the unknowns by linear functions of the dynamic variables of the problem that will be the corrector values of the potential on the free surface and of the free-surface elevation as well as and potential jump (dipole intensity) at the Kutta strip.

4.4.4 Discretised free-surface and Kutta conditions and the dynamical system

We apply discretisation with BEM and collocation as described in detail in Secs.2.4 & 2.5.2.2. We consider the collection of discretised data that are families of scalars or vectors. They are ordered following x_1 -major numbering. In this way, ordered lists (systems) are created, that represent the collocation points (containing vectors of \mathbb{R}^3), the discretised potential field (containing real numbers), the discretised gradient of the free-surface potential field (containing vectors of \mathbb{R}^3) or the covariant components of the tangential velocity (containing real numbers). The systems that are arranged x_1 -majorly will be denoted using $|_1$. To proceed, the free-surface conditions are applied at the free-surface collocation points. Therefore, we have the aforementioned collocation points $\mathbf{x}_0|_1 = \{\mathbf{x}_{0f}\}$ with $f \in \{0, 1, \dots, N_F - 1\}$, where N_F is the total number

⁷The terms in the Eq.(4.58) are mean values and differences of the upper and lower side traces on the body boundary. Some of those fields are continuous at the trailing edge, however when discretisation is applied and a BEM is exploited for calculations, the vicinity of the trailing edge is modeled by neighboring to the trailing edge panels. In that case, the upper and lower elements are not identical and the same applies to the boundary field values. Therefore, it is important for the accurate and stable imposition of Kutta condition, those mean values and differences to be considered in the calculations.

of the free-surface collocation points, the initial guess free-surface potential $\Phi_0^0|_1 = \{\Phi_{0,f}^0\}$, the corrector free-surface potential $\phi_{F,N_i-1}^{cor}|_1 = \{\phi_{F,N_i-1,f}^{cor}\}$, the initial guess free-surface elevation $\eta_{0,N_i-1}^0|_1 = \{\eta_{0,f}^0\}$, the corrector free-surface elevation $\eta_{N_i-1}^{cor}|_1 = \{\eta_{N_i-1,f}^{cor}\}$, the initial guess trace of the gradient of the free-surface potential $\mathbf{V}_{F,0}^0|_1 = \{\nabla\Phi_{0,f}^0\}$, the corrector trace of the gradient of the free-surface potential $\mathbf{V}_{F,N_i-1}^{cor}|_1 = \{\nabla\phi_{N_i-1,f}^{cor}\}$, the total metric of the free surface $\mathbf{a}_I|_1 = \{\sqrt{a_{I,f}}\}$, the corrector free-surface tangential velocity $\mathbf{V}_{F,t,N_i-1}^{cor}|_1 = \{\mathbf{V}_{F,t,N_i-1,f}^{cor}\}$, the first component (x_1 -wise) of the covariant derivative of the corrector free-surface potential $\mathbf{V}_{F,t,N_i-1,1}^{cor}|_1 = \{V_{F,t,N_i-1,1,f}^{cor}\}$, the second component (x_2 -wise) of the covariant derivative of the corrector free-surface potential $\mathbf{V}_{F,t,N_i-1,2}^{cor}|_1 = \{V_{F,t,N_i-1,2,f}^{cor}\}$. Moreover, the initial guess free-surface Neumann-data discretised vector field is $\mathbf{N}_0^0|_1 = \{\partial_n\Phi_{0,f}^0\}$ and the corrector free-surface Neumann-data discretised vector field is $\mathbf{N}_{F,N_i-1}^{cor}|_1 = \{\partial_n\phi_{N_i-1,f}^{cor}\}$ and the discretised unit normal to the total free-surface vector field $\mathbf{n}_F|_1 = \{\mathbf{n}_{F,f}\}$. The discretised form of free-surface boundary conditions (Eqs.4.24 & 4.25) in the case of nonlinear waves are as follows

$$\begin{aligned} \partial_t\phi_{N_i-1}^{cor}|_1 = & -\partial_t\Phi_0^0|_1 - g\eta_{0,N_i-1}^0|_1 - g\eta_{N_i-1}^{cor}|_1 \\ & - \frac{1}{2} \left(\mathbf{V}_{F,0}^0|_1 + \mathbf{V}_{F,t,N_i-1}^{cor}|_1 + \mathbf{N}_{F,N_i-1}^{cor}|_1 \cdot \mathbf{n}_F|_1 \right)^2, \quad \mathbf{x} \in \partial D_{F,N_i-1}(t), \end{aligned} \quad (4.59)$$

$$\partial_t\eta_{N_i-1}^{cor}|_1 = -\partial_t\eta_{0,N_i-1}^0|_1 - \left(\mathbf{N}_0^0|_1 + \mathbf{N}_{F,N_i-1}^{cor}|_1 \right) \cdot \mathbf{a}_I|_1, \quad \mathbf{x} \in \partial D_{F,N_i-1}(t), \quad (4.60)$$

where the dot product at the 2nd term at the r.h.s. of Eq.(4.60) and the square at the 4th term at thr r.h.s. of Eq.(4.59) as well as, the product at the expression inside the square, are dot products between 1st-order systems; for more details, see Sec.2.5.1.3.

The discretised tangential corrector free-surface velocity vector field $\mathbf{V}_{F,t,N_i-1}^{cor}$ is expanded with respect to a curvilinear coordinate system and its covariant base, using the velocity contravariant components (see Sec.2.5.2.1), as follows

$$\mathbf{V}_{F,t,N_i-1}^{cor}|_1 = (\mathbf{V}_{F,t,N_i-1,j}^{cor})^j|_1 \cdot \mathbf{e}_j|_1, \quad j \in \{1,2\}. \quad (4.61)$$

where \mathbf{e}_j are the systems of vectors that represents the base vectors discretised vector fields $\mathbf{e}_j|_2 = \{\mathbf{e}_{ji}\}, j \in \{1,2\}, i \in \{0,1,\dots,N_F-1\}$ and the dot product is between systems of vectors.

The contravariant components of the corrector free-surface velocity can be calculated when the covariant components are known as follows

$$(\mathbf{V}_{F,t,N_i-1,j}^{cor})^j|_1 = \mathbf{g}^{jk}|_1 (\mathbf{V}_{F,t,N_i-1,k}^{cor})_k|_1, \quad j,k \in \{1,2\}. \quad (4.62)$$

where \mathbf{g}^{jk} is a system that contains the contravariant components of the metric tensor at the collocation points; i.e. $\mathbf{g}^{jk}|_1 = \{g_i^{jk}\}, j,k \in \{1,2\}, i \in \{0,1,\dots,N_F-1\}$.

By applying CUFD we can approximate the covariant component of the tangential corrector free-surface velocities by the neighboring corrector potential values (see Sec.2.5.2.2) as follows

$$\left(\mathbf{V}_{F,t,N_i-1,1}^{cor} \right)_1|_1 = \mathcal{D}(\mathbf{x}_0|_1) \cdot \phi_{F,N_i-1}^{cor}|_1. \quad (4.63)$$

$$\left(\mathbf{V}_{F,t,N_I-1,2}^{cor}\right)_2|_1 = \left[\mathcal{D}(\mathbf{x}_0|_2) \cdot \boldsymbol{\phi}_{F,N_I-1}^{cor}|_2\right]^T = \left[\mathcal{D}(\mathbf{x}_0|_2) \cdot \left(\boldsymbol{\phi}_{F,N_I-1}^{cor}|_1\right)^T\right]^T. \quad (4.64)$$

The above detailed analysis enlightens the fact that the discretised boundary value of the tangential free-surface corrector velocity $\mathbf{V}_{F,t,N_I-1}^{cor}$ can be expressed as a function of the discretised boundary value of the corrector free-surface potential $\boldsymbol{\phi}_{F,N_I-1}^{cor}$ in the context of our approximation; i.e. $\mathbf{V}_{F,t,N_I-1}^{cor}|_1 = \mathcal{V}_{CUFDM}\left(\boldsymbol{\phi}_{F,N_I-1}^{cor}|_1\right)$.

At the final stage the discretised free-surface conditions (Eqs.4.59 & 4.60) together with discretised Kutta condition that will be presented in the sequel, will be exploited for the construction of the dynamical-system equations in the form $d_t \mathbf{U}_{N_I-1}^{cor} = \mathbf{f}(\mathbf{U}_{N_I-1}^{cor})$, where the system-derivative \mathbf{f} is a function of the dynamic variables collected into the 1st-order system $\mathbf{U}_{N_I-1}^{cor} = \left\{\boldsymbol{\phi}_{F,N_I-1}^{cor}, \boldsymbol{\eta}_{N_I-1}^{cor}, \boldsymbol{\mu}_{N_I-1,K}^{cor}\right\}$. In order to obtain that final form of free-surface conditions we recall the discretised extended DtN operator constructed in Sec.4.4.2, Eqs.(4.36 - 4.38).

$$\begin{aligned} \mathbf{N}_{F,N_I-1}^{cor}(t)|_1 = & \mathcal{S}_{N_I-1,00}(t) \cdot \boldsymbol{\phi}_{F,N_I-1}^{cor}(t)|_1 + \mathcal{S}_{N_I-1,01}(t) \cdot \mathbf{b}(t)|_1 \\ & + \mathcal{Z}_{N_I-1,0}(t) \cdot \boldsymbol{\mu}_{K,N_I-1}^{cor}(t)|_2 + \mathcal{P}_{N_I-1,0}(t) \cdot \boldsymbol{\mu}_{W,N_I-1}^{cor}|_2. \end{aligned} \quad (4.65)$$

In the above linear relation the unknown discretised fields are the systems of Neumann and Dirichlet data on the free-surface; i.e. the normal derivative of the corrector free-surface potential $\mathbf{N}_{F,N_I-1}^{cor}|_1$ and the corrector free-surface potential $\boldsymbol{\phi}_{F,N_I-1}^{cor}|_1$ and the system of Dirichlet data on the Kutta strip; i.e. the potential jump $\boldsymbol{\mu}_{K,N_I-1}^{cor}|_2$. The Neumann data on the body $\mathbf{b}|_1$ and are known from the prescribed kinematics and the initial guess velocity and the Dirichlet data on the wake $\boldsymbol{\mu}_{W,N_I-1}^{cor}|_2$ have been determined from the time history of the system evolution. Therefore, the discretised free-surface conditions (Eqs.4.59 & 4.60) together with the appropriate part of the discretised extended DtN operator Eq.(4.65) are a system of (spatially and temporarily) nonlocal differential equations, with explicit and implicit nonlinearities, with a linear algebraic constraint. This is only the half part of the total system of equations. The remaining part that is based on the pressure-type Kutta condition will be constructed later in the same section. The other part of the system is also constrained and another part of the DtN serves as a linear constraint this will be also discussed later.

In the sequel, the algebraic constraint is used in order to express the system-derivative \mathbf{f} as a function of the dynamic variables collected into the 1st-order system

$$\mathbf{U}_{N_I-1}^{cor} = \left\{\boldsymbol{\phi}_{N_I-1}^{cor}, \boldsymbol{\eta}_{N_I-1}^{cor}, \boldsymbol{\mu}_{N_I-1,K}^{cor}\right\}. \quad (4.66)$$

To proceed, the discretised normal derivative of the corrector free-surface potential field $\mathbf{N}_{F,N_I-1}^{cor}$ with the aid of Eq.(4.65) becomes a function of $\boldsymbol{\phi}_{F,N_I-1}^{cor}$ and $\boldsymbol{\mu}_{N_I-1,K}^{cor}$ as follows

$$\mathbf{N}_{F,N_I-1}^{cor}|_1 = \mathcal{DTN}_0\left(\boldsymbol{\phi}_{F,N_I-1}^{cor}|_1, \boldsymbol{\mu}_{N_I-1,K}^{cor}|_2\right). \quad (4.67)$$

The free-surface boundary conditions become

$$\begin{aligned} \partial_t \boldsymbol{\phi}_{N_I-1}^{cor}|_1 &= -\partial_t \boldsymbol{\Phi}_0^0|_1 - g\boldsymbol{\eta}_{0,N_I-1}^0|_1 - g\boldsymbol{\eta}_{N_I-1}^{cor}|_1 \\ &\quad - \frac{1}{2} \left[\mathbf{V}_{F,0}^0|_1 + \mathcal{V}_{CUFDM} \left(\boldsymbol{\phi}_{F,N_I-1}^{cor}|_1 \right) \right. \\ &\quad \left. + \mathcal{DTN}_0 \left(\boldsymbol{\phi}_{F,N_I-1}^{cor}|_1, \boldsymbol{\mu}_{N_I-1,K}^{cor}|_2 \right) \cdot \mathbf{n}_F|_1 \right]^2, \quad \mathbf{x} \in \partial D_{F,N_I-1}(t), \end{aligned} \quad (4.68)$$

$$\partial_t \boldsymbol{\eta}_{N_I-1}^{cor}|_1 = -\partial_t \boldsymbol{\eta}_{0,N_I-1}^0|_1 - \left[\mathbf{N}_0^0|_1 + \mathcal{DTN}_0 \left(\boldsymbol{\phi}_{F,N_I-1}^{cor}|_1, \boldsymbol{\mu}_{N_I-1,K}^{cor}|_2 \right) \right] \cdot \mathbf{a}_I|_1, \quad \mathbf{x} \in \partial D_{F,N_I-1}(t), \quad (4.69)$$

The discretised free-surface conditions in the form of Eqs.(4.68 & 4.69) together with the discretised pressure-type Kutta condition, that will be constructed in the sequel, are a system of (spatially and temporarily) nonlocal differential equations, with explicit and implicit nonlinearities, in the form $d_t \mathbf{U}_{N_I-1}^{cor} = \mathbf{f}(\mathbf{U}_{N_I-1}^{cor})$, where the system-derivative \mathbf{f} is a function of the dynamic variables collected into the 1st-order system $\mathbf{U}_{N_I-1}^{cor} = \left\{ \boldsymbol{\phi}_{F,N_I-1}^{cor}, \boldsymbol{\eta}_{N_I-1}^{cor}, \boldsymbol{\mu}_{K,N_I-1}^{cor} \right\}$.

Moreover concerning the lifting part of the problem and the pressure-type Kutta condition, we apply discretisation with BEM and collocation as described in detail in Secs.2.4 & 2.5.2.2. We consider the collection of discretised data that are families of scalars or vectors. They are ordered following span-major numbering. In this way, ordered lists (systems) are created, that represent the collocation points (containing vectors of \mathbb{R}^3), the discretised potential field (containing real numbers), the discretised tangential velocity field (containing vectors of \mathbb{R}^3) or the covariant components of the tangential velocity (containing real numbers). The systems that are arranged span-majorly will be denoted using $|_2$. To proceed, the pressure-type Kutta condition is applied at the body-collocation points at the upper and lower side of the trailing edge⁸ and the corresponding operator is discretised as follows $\mathbf{F}_{fs,N_I-1}^{PK}|_2 = \{F_{fs,N_I-1,i}^{PK}\}$, with $i \in \{0, 1, \dots, N_{PK} - 1\}$, where N_{PK} is the total number of collocation points that Kutta condition is applied. Therefore, we have the aforementioned collocation points $\mathbf{x}_0|_2 = \{\mathbf{x}_{0,i}\}$, the corrector potential $\boldsymbol{\phi}_{B,N_I-1}^{cor}|_2 = \{\phi_{B,N_I-1,i}^{cor}\}$, the initial guess potential $\boldsymbol{\Phi}_0^0|_2 = \{\Phi_{0,i}^0\}$, the corrector tangential velocity $\mathbf{V}_{t,N_I-1}^{cor}|_2 = \{\mathbf{V}_{t,N_I-1,i}^{cor}\}$, the first component (chordwise) of the covariant derivative of the corrector potential $\mathbf{V}_{t,N_I-1,1}^{cor}|_2 = \{V_{t,N_I-1,1,i}^{cor}\}$, the second component (spanwise) of the covariant derivative of the corrector potential $\mathbf{V}_{t,N_I-1,2}^{cor}|_2 = \{V_{t,N_I-1,2,i}^{cor}\}$. Moreover, the known-Neumann-data-times-the-normal-vector discretised vector field is $\mathbf{N}|_2 = \{b_i \mathbf{n}_i\}$ the initial guess velocity $\mathbf{V}_0^0|_2 = \{\nabla \Phi_{0,i}^0\}$ and the body velocity $\mathbf{V}_B|_2 = \{\mathbf{V}_{Bi}\}$.

The discretised form of pressure-type Kutta condition is as follows

$$\mathbf{F}_{fs,N_I-1}^{PK}(\mathbf{x}_0|_2; t)|_2 = 0, \quad \mathbf{x}_0|_2 \in \partial D_B(t), \quad (4.70)$$

⁸A single numbering is used for both the upper and the lower collocation points; i.e. the collection $i \in \{0, 1, \dots, N_{PK} - 1\}$ is mapped to the upper side data denoted with upper index u and to the lower side data denoted with l .

where

$$\begin{aligned}
\mathbf{F}_{fs, N_I-1}^{PK}(\mathbf{x}_0|_2; t)|_2 &= d_t(\boldsymbol{\phi}_{B, N_I-1}^{cor, u}|_2 - \boldsymbol{\phi}_{B, N_I-1}^{cor, l}|_2) \\
&+ \left(\frac{\mathbf{V}_{t, N_I-1}^{cor, u}|_2 + \mathbf{V}_{t, N_I-1}^{cor, l}|_2}{2} + \frac{\mathbf{N}^u|_2 + \mathbf{N}^l|_2}{2} + \frac{\mathbf{V}_0^{0, u}|_2 + \mathbf{V}_0^{0, l}|_2}{2} - \frac{\mathbf{V}_B^u|_2 + \mathbf{V}_B^l|_2}{2} \right) \\
&\left[\mathbf{V}_{t, N_I-1}^{cor, u}|_2 - \mathbf{V}_{t, N_I-1}^{cor, l}|_2 + \mathbf{N}^u|_2 - \mathbf{N}^l|_2 + \mathbf{V}_0^{0, u}|_2 - \mathbf{V}_0^{0, l}|_2 - \left(\mathbf{V}_B^u|_2 - \mathbf{V}_B^l|_2 \right) \right] \\
&- \left(\frac{\mathbf{V}_0^{0, u}|_2 + \mathbf{V}_0^{0, l}|_2}{2} - \frac{\mathbf{V}_B^u|_2 + \mathbf{V}_B^l|_2}{2} \right) \left[\mathbf{V}_0^{0, u}|_2 - \mathbf{V}_0^{0, l}|_2 - \left(\mathbf{V}_B^u|_2 - \mathbf{V}_B^l|_2 \right) \right] \\
&+ \partial_t \left(\boldsymbol{\Phi}_0^{0, u}|_2 - \boldsymbol{\Phi}_0^{0, l}|_2 \right) + \frac{\mathbf{V}_0^{0, u}|_2 + \mathbf{V}_0^{0, l}|_2}{2} \left(\mathbf{V}_0^{0, u}|_2 - \mathbf{V}_0^{0, l}|_2 \right) + g \left(\mathbf{x}_0^u|_2 - \mathbf{x}_0^l|_2 \right).
\end{aligned} \tag{4.71}$$

The discretised tangential corrector velocity vector field $\mathbf{V}_{t, N_I-1}^{cor}$ is expanded with respect to a curvilinear coordinate system and its covariant base, using the velocity contravariant components (see Sec.2.5.2.1), as follows

$$\mathbf{V}_{t, N_I-1}^{cor}|_2 = (\mathbf{V}_{t, N_I-1, j}^{cor})^j|_2 \cdot \mathbf{e}_j|_2, \quad j \in \{1, 2\}. \tag{4.72}$$

where \mathbf{e}_j are the systems of vectors that represents the base vectors discretised vector fields $\mathbf{e}_j|_2 = \{\mathbf{e}_{ji}\}, j \in \{1, 2\}, i \in \{0, 1, \dots, N_{PK} - 1\}$ and the dot product is between systems of vectors.

The contravariant components of the corrector velocity can be calculated when the covariant components are known as follows

$$(\mathbf{V}_{t, N_I-1, j}^{cor})^j|_2 = \mathbf{g}^{jk}|_2 (\mathbf{V}_{t, N_I-1, k}^{cor})_k|_2, \quad j, k \in \{1, 2\}. \tag{4.73}$$

where \mathbf{g}^{jk} is a system that contains the contravariant components of the metric tensor at the collocation points; i.e. $\mathbf{g}^{jk}|_2 = \{g_i^{jk}\}, j, k \in \{1, 2\}, i \in \{0, 1, \dots, N_{PK} - 1\}$.

By applying CUFD we can approximate the covariant component of the tangential corrector velocities by the neighboring corrector potential values (see Sec.2.5.2.2) as follows

$$\left(\mathbf{V}_{t, N_I-1, 1}^{cor} \right)_1|_2 = \left[\mathcal{D}(\mathbf{x}_0|_1) \cdot \boldsymbol{\phi}_{B, N_I-1}^{cor}|_1 \right]^\top = \left[\mathcal{D}(\mathbf{x}_0|_1) \cdot \left(\boldsymbol{\phi}_{B, N_I-1}^{cor}|_2 \right)^\top \right]^\top. \tag{4.74}$$

$$\left(\mathbf{V}_{t, N_I-1, 2}^{cor} \right)_2|_2 = \mathcal{D}(\mathbf{x}_0|_2) \cdot \boldsymbol{\phi}_{B, N_I-1}^{cor}|_2. \tag{4.75}$$

The above detailed analysis enlightens the fact that the discretised boundary value of the tangential corrector velocity $\mathbf{V}_{t, N_I-1}^{cor}$ can be expressed as a function of the discretised boundary value of the corrector potential $\boldsymbol{\phi}_{B, N_I-1}^{cor}$ in the context of our approximation; i.e. $\mathbf{V}_{t, N_I-1}^{cor}|_2 = \mathcal{V}_{CUFDM} \left(\boldsymbol{\phi}_{B, N_I-1}^{cor}|_2 \right)$.

At the final stage the discretised pressure-type Kutta condition (Eqs.4.70 & 4.71) together with the discretised free-surface conditions (Eqs.4.59 & 4.60) will be exploited for the construction of the dynamical-system equations in the form $d_t \mathbf{U}_{N_I-1}^{cor} = \mathbf{f}(\mathbf{U}_{N_I-1}^{cor})$, where the system-derivative

\mathbf{f} is a function of the dynamic variables collected into the following 1st-order system

$$\mathbf{U}_{N_I-1}^{cor} = \left\{ \boldsymbol{\phi}_{F,N_I-1}^{cor}, \boldsymbol{\eta}_{N_I-1}^{cor}, \boldsymbol{\mu}_{K,N_I-1}^{cor} \right\}. \quad (4.76)$$

In order to obtain that form of Kutta condition we recall the discretised DtN operator constructed in Sec.4.4.2, Eqs.(4.36 - 4.38)

$$\begin{aligned} \boldsymbol{\phi}_{B,N_I-1}^{cor}(t) = & \mathcal{G}_{N_I-1,10}(t) \cdot \boldsymbol{\phi}_{F,N_I-1}^{cor}(t) + \mathcal{G}_{N_I-1,11}(t) \cdot \mathbf{b}(t) \\ & + \mathcal{Z}_{N_I-1,1}(t) \cdot \boldsymbol{\mu}_{K,N_I-1}^{cor}(t) + \mathcal{P}_{N_I-1,1}(t) \cdot \boldsymbol{\mu}_{W,N_I-1}^{cor}. \end{aligned} \quad (4.77)$$

In the above linear relation the unknown discretised fields are the system of corrector Dirichlet data on the body boundary; i.e. the corrector body potential $\boldsymbol{\phi}_{B,N_I-1}^{cor}$, the system of corrector Dirichlet data on the free-surface; i.e. the corrector free-surface potential $\boldsymbol{\phi}_{F,N_I-1}^{cor}$ and the system of corrector Dirichlet data on the Kutta strip; i.e. the potential jump $\boldsymbol{\mu}_{K,N_I-1}^{cor}$. The Neumann data on the body \mathbf{b} and are known from the prescribed kinematics and the known initial guess free-surface velocity and the corrector Dirichlet data on the wake $\boldsymbol{\mu}_{W,N_I-1}^{cor}$ have been determined from the time history of the system evolution. Therefore, the discretised pressure-type Kutta condition (Eqs.4.70 & 4.71) together with the appropriate part of the discretised DtN operator Eq.(4.77) and the discretised free-surface boundary conditions (Eqs.4.59 & 4.60) together with the appropriate part of the discretised DtN operator Eq.(4.65) are a system of (spatially and temporarily) nonlocal differential equations, with explicit and implicit nonlinearities and linear algebraic constraints.

We proceed with the pressure-type Kutta condition. The algebraic constraint is used in order to express the system-derivative \mathbf{f} as a function of the dynamic variables collected into the 1st-order system $\left\{ \boldsymbol{\phi}_{F,N_I-1}^{cor}, \boldsymbol{\eta}_{N_I-1}^{cor}, \boldsymbol{\mu}_{K,N_I-1}^{cor} \right\}$. First of all, the discretised corrector potential field with the aid of Eq.(4.77) becomes a function of $\boldsymbol{\phi}_{F,N_I-1}^{cor}$ and $\boldsymbol{\mu}_{K,N_I-1}^{cor}$; i.e. $\boldsymbol{\Phi}_{B,N_I-1} = \mathcal{DTN} \left(\boldsymbol{\phi}_{F,N_I-1}^{cor}, \boldsymbol{\mu}_{K,N_I-1}^{cor} \right)$. In this way the discretised corrector tangential velocity can be expressed as a function of $\boldsymbol{\phi}_{F,N_I-1}^{cor}$ and $\boldsymbol{\mu}_{K,N_I-1}^{cor}$; i.e. $\mathbf{V}_{t,N_I-1}^{cor} = \mathcal{V}_{DTN} \left(\boldsymbol{\phi}_{F,N_I-1}^{cor}, \boldsymbol{\mu}_{K,N_I-1}^{cor} \right)$. Therefore, the pressure-Kutta operator is also a function of the unknown $\boldsymbol{\phi}_{F,N_I-1}^{cor}$ and $\boldsymbol{\mu}_{K,N_I-1}^{cor}$ (and other known quantities); i.e. $\mathbf{F}_{fs,N_I-1}^{PK} = \mathcal{F}_{fs,N_I-1}^{PK} \left(\boldsymbol{\phi}_{F,N_I-1}^{cor}, \boldsymbol{\mu}_{K,N_I-1}^{cor} \right)$. The pressure-type Kutta condition becomes

$$\begin{aligned} d_t \left[\mathcal{DTN}_1^u \left(\boldsymbol{\phi}_{F,N_I-1}^{cor}, \boldsymbol{\mu}_{K,N_I-1}^{cor} \right) - \mathcal{DTN}_1^l \left(\boldsymbol{\phi}_{N_I-1}^{cor}, \boldsymbol{\mu}_{N_I-1,K}^{cor} \right) \right] = \\ - \left(\frac{\mathcal{V}_{DTN}^u \left(\boldsymbol{\phi}_{F,N_I-1}^{cor}, \boldsymbol{\mu}_{K,N_I-1}^{cor} \right) + \mathcal{V}_{DTN}^l \left(\boldsymbol{\phi}_{F,N_I-1}^{cor}, \boldsymbol{\mu}_{K,N_I-1}^{cor} \right)}{2} + \frac{\mathbf{N}^u + \mathbf{N}^l}{2} + \frac{\mathbf{V}_0^{0,u} + \mathbf{V}_0^{0,l}}{2} - \frac{\mathbf{V}_B^u + \mathbf{V}_B^l}{2} \right) \\ \left[\mathcal{V}_{DTN}^u \left(\boldsymbol{\phi}_{F,N_I-1}^{cor}, \boldsymbol{\mu}_{K,N_I-1}^{cor} \right) - \mathcal{V}_{DTN}^l \left(\boldsymbol{\phi}_{F,N_I-1}^{cor}, \boldsymbol{\mu}_{K,N_I-1}^{cor} \right) + \mathbf{N}^u - \mathbf{N}^l + \mathbf{V}_0^{0,u} - \mathbf{V}_0^{0,l} - \left(\mathbf{V}_B^u - \mathbf{V}_B^l \right) \right] \\ + \left(\frac{\mathbf{V}_0^{0,u} + \mathbf{V}_0^{0,l}}{2} - \frac{\mathbf{V}_B^u + \mathbf{V}_B^l}{2} \right) \left[\mathbf{V}_0^{0,u} - \mathbf{V}_0^{0,l} - \left(\mathbf{V}_B^u - \mathbf{V}_B^l \right) \right] \\ - \partial_t \left(\boldsymbol{\Phi}_0^{0,u} - \boldsymbol{\Phi}_0^{0,l} \right) - \frac{\mathbf{V}_0^{0,u} + \mathbf{V}_0^{0,l}}{2} \left(\mathbf{V}_0^{0,u} - \mathbf{V}_0^{0,l} \right) - g \left(\mathbf{x}_0^u - \mathbf{x}_0^l \right). \end{aligned} \quad (4.78)$$

In the equation above, the upper indices u and l refer to the discretised fields at the upper

and lower sides the discretised boundary, respectively. To proceed further, it is necessary to perform some operations to the time derivative of the DtN operator appeared at the left hand side of Eq.(4.78).

$$\begin{aligned}
d_t \left[\mathcal{DTN}_1^u \left(\boldsymbol{\phi}_{F,N_{I-1}}^{cor}, \boldsymbol{\mu}_{K,N_{I-1}}^{cor} \right) - \mathcal{DTN}_1^l \left(\boldsymbol{\phi}_{F,N_{I-1}}^{cor}, \boldsymbol{\mu}_{K,N_{I-1}}^{cor} \right) \right] = \\
= d_t \left\{ [\mathcal{G}_{N_{I-1},10}^u(t) - \mathcal{G}_{N_{I-1},10}^l(t)] \boldsymbol{\phi}_{F,N_{I-1}}^{cor}(t) + [\mathcal{G}_{N_{I-1},11}^u(t) - \mathcal{G}_{N_{I-1},11}^l(t)] \cdot \mathbf{b}(t) \right. \\
\left. + [\mathcal{Z}_{N_{I-1},1}^u(t) - \mathcal{Z}_{N_{I-1},1}^l(t)] \cdot \boldsymbol{\mu}_{K,N_{I-1}}^{cor}(t) + [\mathcal{P}_{N_{I-1},1}^u(t) - \mathcal{P}_{N_{I-1},1}^l(t)] \cdot \boldsymbol{\mu}_{W,N_{I-1}}^{cor} \right\}. \tag{4.79}
\end{aligned}$$

We define the following matrices $\mathcal{G}_{N_{I-1},10}^{u \setminus l} = [\mathcal{G}_{N_{I-1},10}^u - \mathcal{G}_{N_{I-1},10}^l]$, $\mathcal{G}_{N_{I-1},11}^{u \setminus l} = [\mathcal{G}_{N_{I-1},11}^u - \mathcal{G}_{N_{I-1},11}^l]$, $\mathcal{Z}_{N_{I-1},1}^{u \setminus l} = [\mathcal{Z}_{N_{I-1},1}^u - \mathcal{Z}_{N_{I-1},1}^l]$, $\mathcal{P}_{N_{I-1},1}^{u \setminus l} = [\mathcal{P}_{N_{I-1},1}^u - \mathcal{P}_{N_{I-1},1}^l]$ as differences of matrices with one dimension that equals the number of Kutta-strip collocation points N_{PK} and the other defined by the number of the panels (on free-surface, body, Kutta-strip and wake, respectively) that induce potential at the collocation points. By adopting that notation and using the Leibniz rule for differentiation we obtain the following relation

$$\begin{aligned}
d_t \left[\mathcal{DTN}_1^u \left(\boldsymbol{\phi}_{F,N_{I-1}}^{cor}, \boldsymbol{\mu}_{K,N_{I-1}}^{cor} \right) - \mathcal{DTN}_1^l \left(\boldsymbol{\phi}_{F,N_{I-1}}^{cor}, \boldsymbol{\mu}_{K,N_{I-1}}^{cor} \right) \right] = \\
= d_t [\mathcal{G}_{N_{I-1},10}^{u \setminus l}(t)] \cdot \boldsymbol{\phi}_{F,N_{I-1}}^{cor}(t) + \mathcal{G}_{N_{I-1},10}^{u \setminus l}(t) \cdot d_t [\boldsymbol{\phi}_{F,N_{I-1}}^{cor}(t)] \\
+ d_t [\mathcal{G}_{N_{I-1},11}^{u \setminus l}(t)] \cdot \mathbf{b}(t) + \mathcal{P}_{N_{I-1},1}^{u \setminus l}(t) \cdot \boldsymbol{\mu}_{W,N_{I-1}}^{cor} \\
+ d_t [\mathcal{Z}_{N_{I-1},1}^{u \setminus l}(t)] \cdot \boldsymbol{\mu}_{K,N_{I-1}}^{cor}(t) + \mathcal{Z}_{N_{I-1},1}^{u \setminus l}(t) \cdot d_t [\boldsymbol{\mu}_{K,N_{I-1}}^{cor}(t)]. \tag{4.80}
\end{aligned}$$

Next, using the dynamic boundary condition (Eq.4.68) and considering that the body-fixed time derivative of the free-surface potential is the same with the inertial⁹, we can replace time derivative of the free-surface potential with functions of the dynamic variables as follows

$$\begin{aligned}
d_t \left[\mathcal{DTN}_1^u \left(\boldsymbol{\phi}_{F,N_{I-1}}^{cor}, \boldsymbol{\mu}_{K,N_{I-1}}^{cor} \right) - \mathcal{DTN}_1^l \left(\boldsymbol{\phi}_{F,N_{I-1}}^{cor}, \boldsymbol{\mu}_{K,N_{I-1}}^{cor} \right) \right] = \\
= d_t [\mathcal{G}_{N_{I-1},10}^{u \setminus l}(t)] \cdot \boldsymbol{\phi}_{F,N_{I-1}}^{cor}(t) \\
+ \mathcal{G}_{N_{I-1},10}^{u \setminus l}(t) \cdot \left\{ -\partial_t \boldsymbol{\Phi}_0^0 - g \boldsymbol{\eta}_{0,N_{I-1}}^0 - g \boldsymbol{\eta}_{N_{I-1}}^{cor} \right. \\
\left. - \frac{1}{2} \left[\mathbf{V}_{F,0}^0 + \mathcal{V}_{CUFDM} \left(\boldsymbol{\phi}_{F,N_{I-1}}^{cor} \right) + \mathcal{DTN}_0 \left(\boldsymbol{\phi}_{F,N_{I-1}}^{cor}, \boldsymbol{\mu}_{N_{I-1},K}^{cor} \right) \cdot \mathbf{n}_F \right]^2 \right\} \\
+ d_t [\mathcal{G}_{N_{I-1},11}^{u \setminus l}(t)] \cdot \mathbf{b}(t) + \mathcal{P}_{N_{I-1},1}^{u \setminus l}(t) \cdot \boldsymbol{\mu}_{W,N_{I-1}}^{cor} \\
+ d_t [\mathcal{Z}_{N_{I-1},1}^{u \setminus l}(t)] \cdot \boldsymbol{\mu}_{K,N_{I-1}}^{cor}(t) + \mathcal{Z}_{N_{I-1},1}^{u \setminus l}(t) \cdot d_t [\boldsymbol{\mu}_{K,N_{I-1}}^{cor}(t)]. \tag{4.81}
\end{aligned}$$

⁹The free-surface elevation and the free-surface potential are functions defined at the initially calm free-surface level, following an Eulerian approach.

By replacing Eq.(4.81) into Eq.(4.78) and multiplying both sides with the inverse of $\mathcal{Z}_{N_i-1,1}^{u,l}$, we obtain the final form of the discretised pressure-type Kutta condition

$$\begin{aligned}
d_t[\boldsymbol{\mu}_{K,N_i-1}^{cor}(t)] &= \left[\mathcal{Z}_{N_i-1,1}^{u,l}(t) \right]^{(-1)} \cdot \left\{ -d_t[\mathcal{G}_{N_i-1,10}^{u,l}(t)] \cdot \boldsymbol{\phi}_{F,N_i-1}^{cor}(t) \right. \\
&\quad - \mathcal{G}_{N_i-1,10}^{u,l}(t) \cdot \left\{ -\partial_t \boldsymbol{\Phi}_0^0 - g\boldsymbol{\eta}_{0,N_i-1}^0 - g\boldsymbol{\eta}_{N_i-1}^{cor} \right. \\
&\quad \left. \left. - \frac{1}{2} \left[\mathbf{V}_{F,0}^0 + \mathcal{V}_{CUFDM}(\boldsymbol{\phi}_{F,N_i-1}^{cor}) + \mathcal{DTN}_0(\boldsymbol{\phi}_{F,N_i-1}^{cor}, \boldsymbol{\mu}_{N_i-1,K}^{cor}) \cdot \mathbf{n}_F \right]^2 \right\} \right. \\
&\quad - d_t[\mathcal{G}_{N_i-1,11}^{u,l}(t)] \cdot \mathbf{b}(t) + \mathcal{P}_{N_i-1,1}^{u,l}(t) \cdot \boldsymbol{\mu}_{W,N_i-1}^{cor} - d_t[\mathcal{Z}_{N_i-1,1}^{u,l}(t)] \cdot \boldsymbol{\mu}_{K,N_i-1}^{cor}(t) \\
&\quad - \left(\frac{\mathcal{V}_{DTN}^u(\boldsymbol{\phi}_{F,N_i-1}^{cor}, \boldsymbol{\mu}_{K,N_i-1}^{cor}) + \mathcal{V}_{DTN}^l(\boldsymbol{\phi}_{F,N_i-1}^{cor}, \boldsymbol{\mu}_{K,N_i-1}^{cor})}{2} + \frac{\mathbf{N}^u + \mathbf{N}^l}{2} + \frac{\mathbf{V}_0^{0,u} + \mathbf{V}_0^{0,l}}{2} - \frac{\mathbf{V}_B^u + \mathbf{V}_B^l}{2} \right) \\
&\quad \left[\mathcal{V}_{DTN}^u(\boldsymbol{\phi}_{F,N_i-1}^{cor}, \boldsymbol{\mu}_{K,N_i-1}^{cor}) - \mathcal{V}_{DTN}^l(\boldsymbol{\phi}_{F,N_i-1}^{cor}, \boldsymbol{\mu}_{K,N_i-1}^{cor}) + \mathbf{N}^u - \mathbf{N}^l + \mathbf{V}_0^{0,u} - \mathbf{V}_0^{0,l} - (\mathbf{V}_B^u - \mathbf{V}_B^l) \right] \\
&\quad + \left(\frac{\mathbf{V}_0^{0,u} + \mathbf{V}_0^{0,l}}{2} - \frac{\mathbf{V}_B^u + \mathbf{V}_B^l}{2} \right) \left[\mathbf{V}_0^{0,u} - \mathbf{V}_0^{0,l} - (\mathbf{V}_B^u - \mathbf{V}_B^l) \right] \\
&\quad \left. - \partial_t (\boldsymbol{\Phi}_0^{0,u} - \boldsymbol{\Phi}_0^{0,l}) - \frac{\mathbf{V}_0^{0,u} + \mathbf{V}_0^{0,l}}{2} (\mathbf{V}_0^{0,u} - \mathbf{V}_0^{0,l}) - g(\mathbf{x}_0^u - \mathbf{x}_0^l) \right\}. \tag{4.82}
\end{aligned}$$

The discretised free-surface conditions in the form of Eqs.(4.68 & 4.69) together with the discretised pressure-type Kutta condition (Eq.4.82) are a system of (spatially and temporarily) non-local differential equations, with explicit and implicit nonlinearities, written here in the form $d_t \mathbf{U}_{N_i-1}^{cor} = \mathbf{f}(\mathbf{U}_{N_i-1}^{cor})$, where the system-derivative \mathbf{f} is a function of the dynamic variables collected into the 1st-order system $\mathbf{U}_{N_i-1}^{cor} = \left\{ \boldsymbol{\phi}_{F,N_i-1}^{cor}, \boldsymbol{\eta}_{N_i-1}^{cor}, \boldsymbol{\mu}_{K,N_i-1}^{cor} \right\}$. That system can be numerically integrated in order to predict the evolution of the dynamic variables collected into the 1st-order system $\mathbf{U}_{N_i-1}^{cor}$ (Eq.4.66), based on information concerning the functions $\boldsymbol{\phi}_{N_i-1}^{cor}, \boldsymbol{\eta}_{N_i-1}^{cor}$ and $\boldsymbol{\mu}_{N_i-1,K}^{cor}$ at previous time steps, in conjunction with the history of the corrector wake dipole intensity $\boldsymbol{\mu}_{W,N_i-1}^{cor}$, and the Neumann data $\mathbf{b}(t)$ on the body boundary, known at every time step from the body motion and the initial guess velocity as described by the body boundary condition Eq.(4.19), as well other known initial-guess quantities included in Eqs.(4.68 & 4.69).

Moreover, the free-surface-boundary nodes are updated every time that the the total free-surface at the collocation points changes. It holds for the total potential that $\eta_{N_i-1} = \eta_0^0 + \eta_{N_i-1}^{cor}$. We assume that the initial guess free-surface elevation is known everywhere and can be updated at the collocation points without interpolation. However the corrector free-surface elevation is known only at the collocation points and its values are stored in $\boldsymbol{\eta}_{N_i-1}^{cor}$. The bilinear 4-node boundary elements construct a basic grid with global nodes located at the local element nodes. The values of the corrector free-surface elevation can be obtained everywhere by interpolation, when the nodal values of the corrector free-surface are known. In order to calculate the nodal values of the corrector free-surface elevation a staggered grid, with nodes at the collocation points, is exploited. The staggered-grid nodal values are given by the corrector free-surface elevation $\boldsymbol{\eta}_{N_i-1}^{cor}$. Then by interpolation, using the staggered grid, the basic-grid nodal values are obtained. Next by interpolation, using the basic grid, the corrector free-surface potential is obtained everywhere. Then we add the initial guess free-surface elevation to the corrector free-surface elevation to obtain the total free-surface everywhere. In this way, the total free-surface boundary is updated and the relative quantities like the total metric \mathbf{a}_I and the

total free-surface unit normal vector \mathbf{n}_F can be calculated.

Subsequently, part of the updated discretised extended DtN map (Eqs.4.36 - 4.38) is used to calculate the remaining unknown discretised body Dirichlet boundary field values $\boldsymbol{\phi}_{B,N_I-1}^{cor}$

$$\begin{aligned} \boldsymbol{\phi}_{B,N_I-1}^{cor}(t)|_1 &= \mathcal{G}_{N_I-1,10}(t) \cdot \boldsymbol{\phi}_{F,N_I-1}^{cor}(t)|_1 + \mathcal{G}_{N_I-1,11}(t) \cdot \mathbf{b}(t)|_1 \\ &+ \mathcal{Z}_{N_I-1,1}(t) \cdot \boldsymbol{\mu}_{K,N_I-1}^{cor}(t)|_2 + \mathcal{P}_{N_I-1,1}(t) \cdot \boldsymbol{\mu}_{W,N_I-1}^{cor}|_2. \end{aligned} \quad (4.83)$$

4.4.5 Numerical time integration of the system

In the present work, a computational code is implemented, following an explicit version of that method, using an Adams-Bashforth-Moulton predictor-corrector time-integration scheme, performing $N_I = 2$ sets of similar constant-time calculations. At a specific timestep the initial constant-time iteration step corresponds to $I = 0$ and the second constant-time iteration step corresponds to $I = N_I - 1 = 1$. The extension of the code to the case of arbitrary number of constant-time iterations, until a specific convergence criterion to be satisfied, is left as a subject of future work. The process begins with known the second ($I = N_I - 1 = 1$) value of the corrector system ($\mathbf{U}_{N_I-1}^{cor} = \mathbf{U}_1^{cor}$) at time t , and the time history of the second ($I = N_I - 1 = 1$) value of the time derivatives ($\mathbf{f}_{N_I-1} = \mathbf{f}_1$). Then, the first ($I = 0$) value of the corrector system $\mathbf{U}_0^{cor}(t + \Delta t)$ at time $t + \Delta t$ is obtained as follows

$$\begin{aligned} \mathbf{U}_0^{cor}(t + \Delta t) &= \mathbf{U}_1^{cor}(t) + \frac{\Delta t}{24} \{55\mathbf{f}_1[\mathbf{U}_1^{cor}(t);t] - 59\mathbf{f}_1[\mathbf{U}_1^{cor}(t - \Delta t);t - \Delta t] \\ &+ 37\mathbf{f}_1[\mathbf{U}_1^{cor}(t - 2\Delta t);t - 2\Delta t] - 9\mathbf{f}_1[\mathbf{U}_1^{cor}(t - 3\Delta t);t - 3\Delta t]\}. \end{aligned} \quad (4.84)$$

The first ($I = 0$) set of calculations also include the approximation of the first ($I = 0$) value of the time derivative $\mathbf{f}_0[\mathbf{U}_0^{cor}(t + \Delta t);t + \Delta t]$ at time $t + \Delta t$. In this way the predictor step of the Adams-Bashforth-Moulton method provides us with a process to implement the first ($I = 0$) set of calculations of the present iterative scheme. For that calculation the extended DtN operator must be calculated with respect to the total free-surface elevation and the updated traces of the data on the updated boundaries. Then it follows the corrector step of Adams-Bashforth-Moulton method that corresponds to the second ($I = 1$) set of calculations of the present iterative scheme

$$\begin{aligned} \mathbf{U}_1^{cor}(t + \Delta t) &= \mathbf{U}_1^{cor}(t) + \frac{\Delta t}{24} \{9\mathbf{f}_0[\mathbf{U}_0^{cor}(t + \Delta t);t + \Delta t] + 19\mathbf{f}_1[\mathbf{U}_1^{cor}(t);t] \\ &- 5\mathbf{f}_1[\mathbf{U}_1^{cor}(t - \Delta t);t - \Delta t] + \mathbf{f}_1[\mathbf{U}_1^{cor}(t - 2\Delta t);t - 2\Delta t]\}. \end{aligned} \quad (4.85)$$

In this way the second ($I = 1$) value of the corrector system $\mathbf{U}_1^{cor}(t + \Delta t)$ at time $t + \Delta t$ is obtained. The second ($I = 1$) set of calculations also includes the approximation of the second ($I = 1$) value of the time derivative $\mathbf{f}_1[\mathbf{U}_1^{cor}(t + \Delta t);t + \Delta t]$ at time $t + \Delta t$ is calculated. The latter requires the recalculation of the extended DtN operator with respect to the new total free-surface elevation and the updated traces of the data on the updated boundaries. The problem of the extra computational cost of the repeated calculation of the DtN is tackled by means of GPGPU programming.

The aforementioned process is performed for every timestep to obtain the time evolution of the $(N_I - 1)^{th}$ value of the corrector potential $\phi_{N_I-1}^{cor}$, and the other dynamic variables collected into the system $\mathbf{U}_{N_I-1}^{cor} = \left\{ \phi_{N_I-1}^{cor}, \eta_{N_I-1}^{cor}, \mu_{N_I-1,K}^{cor} \right\}$. The time evolution of the total potential is obtained by adding at each timestep the $(N_I - 1)^{th}$ value of corrector potential to the initial guess potential as follows $\Phi \approx \lim_{I \rightarrow (N_I-1)} \Phi_I = \Phi_{N_I-1} = \Phi_0^0 + \phi_{N_I-1}^{cor}$. The same applies to the other trace data of the problem. Moreover, the free-surface boundary is recalculated by remeshing at the location of the total free-surface elevation. The later is approximated by interpolation from the control-point values of the total free surface using a staggered grid.

Finally, the evolution of the wake could be obtained explicitly either by calculation at every constant-time iteration step or simpler by calculation at the end of every timestep. In the present work the second approach is followed. Moreover, it could be calculated implicitly; i.e. the first approximation of the wake could be obtained at the end of a specific constant-time iteration or timestep, followed by another wake-iterative scheme with many (interior) iterations at the specific constant-time (exterior) iteration or timestep until a proper convergence criterion (that includes wake related metrics) is achieved. In the present work the explicit approach is adopted and the investigation of the importance of the implicit approaches is left as a subject of future work.

4.5 Numerical results and discussion

4.5.1 DtN calculation in the case of propagation of a solitary wave over general bathymetry

In the present section validation of the present method in the case of propagation of a solitary wave over general bathymetry, exploiting the solution of a fully nonlinear Hamiltonian Coupled-Mode System (HCMS) of equations (Papoutsellis et al., 2018), is presented. Performance analysis of the mixed precision instance of the GPU code is also documented. The GPU calculations have been performed in a GTX1080 GPU with 2560 NVIDIA CUDA Cores.

In the work of Papoutsellis et al. (2018), time domain calculations with the HCMS model are presented, concerning the transformation of a solitary wave over a 3D bathymetry with banks and trenches; more details concerning the geometry and the parameters of the problem can be found in Sec.6.5 of the aforementioned reference. Exploiting the recently presented Hamiltonian Coupled-Mode Theory (HCMT), the authors studied that very interesting problem with a rich physical content and also introduced a new representation of the Dirichlet-to-Neumann operator, which is needed to close the Hamiltonian evolution equations.

In the present section results are obtained by the present method concerning the normal to the free-surface boundary derivative of the potential on the exact location of the free-surface boundary. To be more specific, for the design of the computational domain where the DtN operator is calculated, four time instances (cases) of the evolution of the solitary wave, as been calculated by the HCMS model, are exploited. In Fig.4.2 the boundary-element grid for the four cases is presented. An elliptic boundary value problem is solved in the interior of the domain. The bottom boundary condition is a homogeneous Neumann-type condition while

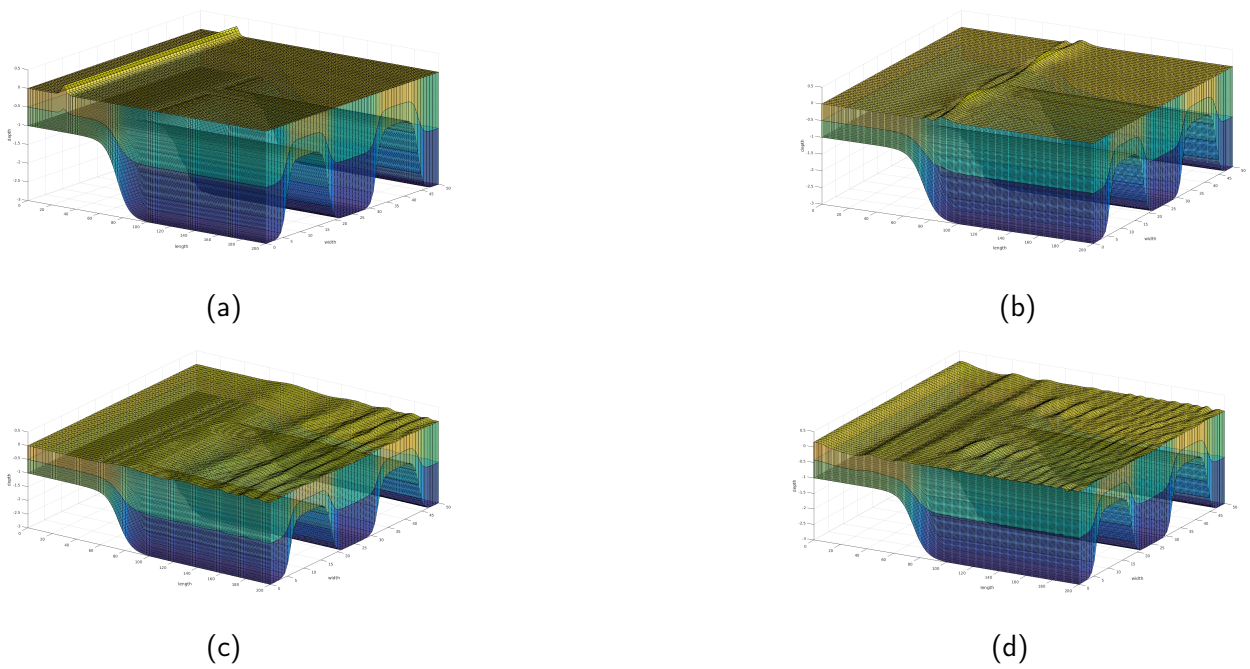


Figure 4.2: Computational domain and boundary element grid for DtN calculation in the case of a solitary wave propagating over a 3D bathymetry with banks and trenches. Four time instances are exploited for the calculations: (a) Case 1. (b) Case 2. (c) Case 3. (d) Case 4.

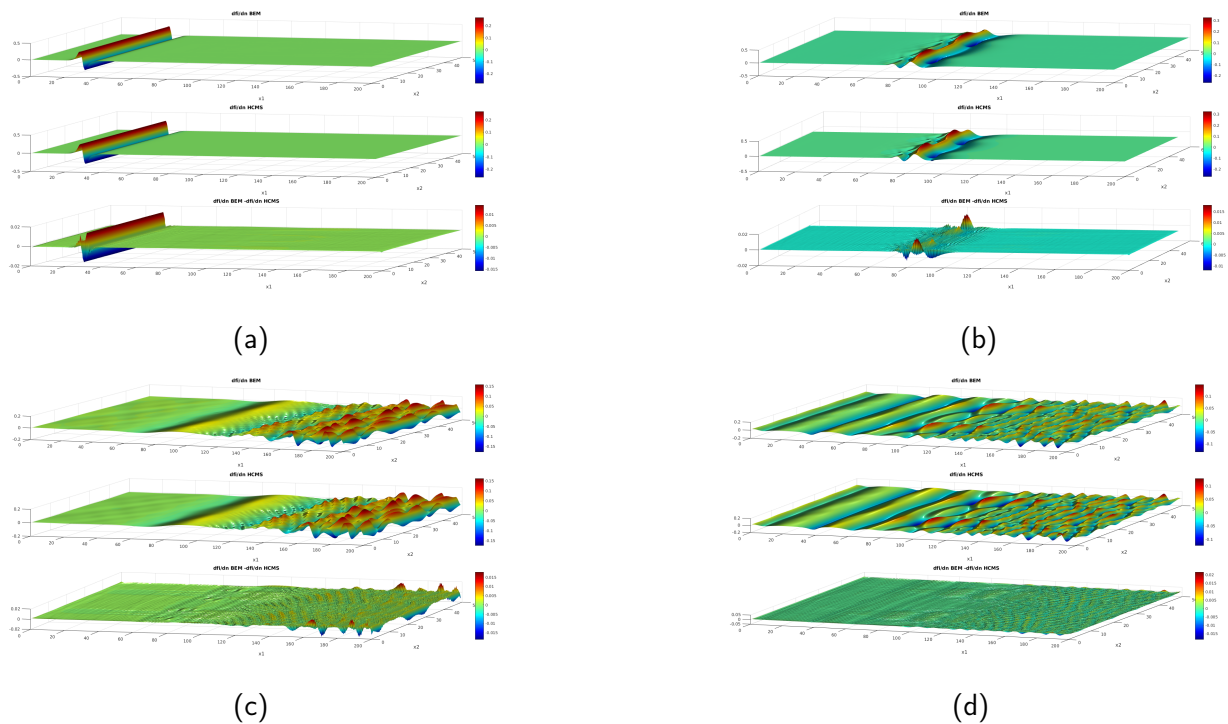


Figure 4.3: Normal-derivative field as calculated by the two methods and the difference of the two fields for the four computational domains depicted in Fig.4.2: (a) Case 1. (b) Case 2. (c) Case 3. (d) Case 4.

```

CASE 1 Grd: 1 2 3 4 5
        Nx: 232 192 152 112 72
        Ny: 58 48 38 28 18
        Nz: 2 2 2 2 2
        DoF: 28072 19392 12312 6832 2952

k:
relTol 58 48 38 28 18
        10^-2 10^-2 10^-2 10^-2 10^-2
relative L2 error(%): ~ 2.99 ~ 4.49 ~ 7.70 ~ 14.22 ~ 30.98
time per run (sec): 16.00 6.89 3.15 1.81 1.19
ind. factors (sec): 5.60 3.07 1.69 1.14 0.73
linear system (sec): 10.05 3.49 1.14 0.35 0.17
GPU memory (MB): 7167 4023 2311 1509 1217
=====
CASE 2 Grd: 1 2 3 4 5
        Nx: 232 192 152 112 72
        Ny: 58 48 38 28 18
        Nz: 2 2 2 2 2
        DoF: 28072 19392 12312 6832 2952

k:
relTol 58 48 38 28 18
        10^-2 10^-2 10^-2 10^-2 10^-2
relative L2 error(%): ~ 1.60 ~ 2.13 ~ 3.44 ~ 6.48 ~ 14.45
time per run (sec): 16.02 6.85 3.15 1.82 1.20
ind. factors (sec): 5.54 3.02 1.68 1.14 0.73
linear system (sec): 10.13 3.50 1.14 0.36 0.17
GPU memory (MB): 7167 4023 2311 1509 1217
=====
CASE 3 Grd: 1 2 3 4 5
        Nx: 232 192 152 112 72
        Ny: 58 48 38 28 18
        Nz: 2 2 2 2 2
        DoF: 28072 19392 12312 6832 2952

k:
relTol 58 48 38 28 18
        10^-2 10^-2 10^-2 10^-2 10^-2
relative L2 error(%): ~ 2.90 ~ 3.95 ~ 6.56 ~ 12.85 ~ 30.34
time per run (sec): 15.94 6.96 3.18 1.80 1.20
ind. factors (sec): 5.54 3.06 1.70 1.14 0.73
linear system (sec): 10.06 3.58 1.16 0.35 0.17
GPU memory (MB): 7167 4023 2311 1509 1217
=====
CASE 4 Grd: 1 2 3 4 5
        Nx: 232 192 152 112 72
        Ny: 58 48 38 28 18
        Nz: 2 2 2 2 2
        DoF: 28072 19392 12312 6832 2952

k:
relTol 58 48 38 28 18
        10^-2 10^-2 10^-2 10^-2 10^-2
relative L2 error(%): ~ 3.01 ~ 4.17 ~ 6.90 ~ 13.42 ~ 29.69
time per run (sec): 16.13 6.91 3.17 1.80 1.22
ind. factors (sec): 5.68 3.07 1.71 1.14 0.73
linear system (sec): 10.09 3.53 1.14 0.36 0.18
GPU memory (MB): 7167 4023 2311 1509 1217
=====

```

Figure 4.4: GPU performance and L^2 error connected with the DtN calculation in the case of a solitary wave propagating over a 3D bathymetry with banks and trenches depicted in Fig.4.2.

inhomogeneous Neumann-type boundary conditions are imposed at the four lateral boundaries and a Dirichlet-type boundary condition is imposed on the free-surface boundary. The values of the normal derivative and the potential as calculated by the HCMS model are exploited. By using the DtN operator, as calculated by the present method, the known Dirichlet data on the free-surface are transformed to Neumann data and the latter can be compared with the HCMS calculations; see Fig.4.3 where the normal-derivative field as calculated by the two methods and the difference of the two fields, are presented.

More details concerning the numerical characteristics and the performance of the present GPU numerical method and the relative L^2 error between the two methods are presented in Fig.4.4. For the four different phases of evolution of the solitary wave (cases 1-4) five different grids have been used, with N_x, N_y, N_z elements along the length, the width and the depth of the computational domain. The finer grid have already been presented in Fig.4.2. The total degrees of freedom (DoF) affecting the size of the induction-factor matrices are also presented in Fig.4.4 and the required VRAM size varies from 1217MB (for the coarser) to 7167MB (for the finer discretisation). The available GPU memory for the GTX1080 GPU is 8000MB, permitting a level of accuracy that corresponds to an L^2 error varying from 1.60% to 3.01%, for the finer discretisation. Moreover, the total calculation time was analyzed to the basic individual operations. The two operations that require significant time are the calculation of the induction-factor matrices and the solution of the linear systems using LU decomposition and the cuSOLVER function from the CUDA Toolkit v10.0.130. It is shown that the calculation of the singular integrals approximately takes up to 30% of the total time for the finer grid case and the total GPU time

does not exceed 16.5 sec in all cases. It is observed that the linear-system solution is significant in terms of computational complexity and therefore spacial care must be put in choosing or even developing more efficient functions for that computational demanding process. The total execution time, as well as the memory footprint can be decreased by employing techniques like the Fast Multipole Method; see e.g. Nishimura (2002). That argument is also supported by the analysis presented in Sec.2.10.2, for an ellipsoid in steady motion, in unbounded domain.

4.5.2 Free-surface effects on wave-augmented propulsion using flapping-foil biomimetic systems

In the present section, we demonstrate the effects of incoming waves and the possibility of wave-energy extraction for exploitation in marine propulsion. A comparison between the present method and recent computations by De Silva and Yamaguchi (2012), based on CFD solver (FLUENT) for three cases of flapping NACA0015 hydrofoil in deep water conditions is presented in Fig.4.5. The parameters of motion are $St = 0.18$, $h_0/c = 0.6$, $\theta_0 = 15.2^\circ$, $X_R/c = 0.3$, $\psi = -105^\circ$ and $Fn = 0.87$, with mean submergence $d/c = 1.28$. Results, in the case of no incident wave are shown using thin lines and are compared against two cases of head incident waves with different phase lag ϕ between heaving foil motion and wave. In this case the encounter frequency ω_0 equals to flapping frequency $\omega_0/\omega_h = 1$, leading to maximum energy extraction; see De Silva and Yamaguchi (2012). In general, present method results, concerning the thrust coefficient ($C_T = -F_X/\rho U^2 h_0$), are found in reasonable agreement with the viscous solver, in all cases examined. We observe in Fig.4.5 that when $\phi = -90^\circ$, the vertical velocities of the wave and the heaving motion have opposite direction resulting in maximum thrust production due to additional energy extraction from the wave. When $\phi = 90^\circ$ the above velocities have the same direction and the thrust production is again positive, but lower in comparison with the case of calm water; see also De Silva and Yamaguchi (2012), sec.6.2. Small differences in calculated C_T observed between present method and CFD analysis are attributed to viscosity effects. The present method is again found to be able to provide good predictions, at least in the examples that are characterized by small and moderate angles of attack, where leading edge separation and dynamic-stall effects are not significant. It is worth noting, that the computational cost of present boundary element method is order(s) of magnitude less, rendering our approach quite competitive and efficient, especially for initial design, optimization and active control development.

Another example concerning the efficiency of the flapping thruster in waves is presented in Fig.4.6. We examine in detail one of the cases of Fig.3.11b, concerning a NACA0012 hydrofoil at $St = 0.4$, $\theta_0 = 35^\circ$ at submergence $d/c = 2.5$, in the presence of an incoming wave of amplitude $\eta_0/h_0 = 0.75$, with flapping frequency equal to encounter frequency $\omega_0/\omega_h = 1$. In this figure the effect of phase difference ϕ between heaving motion and the incident wave on unsteady thrust production is studied. More specifically, in Fig.4.6 the values of the thrust coefficient ($C_T = -F_X/\rho U^2 h_0$) are presented, as a portion of its value at finite submergence below the free surface in calm water. The value at calm water is shown with horizontal bold line at 100% and the value in unbounded domain with horizontal dashed line. We observe that the effect of the free surface is to cause a reduction of thrust (approx. 5% in the examined case, in comparison with value in deep submergence $C_{Tinf} = 0.41$) due to the wave resistance. The results obtained by the present method for the same system operating in head incident

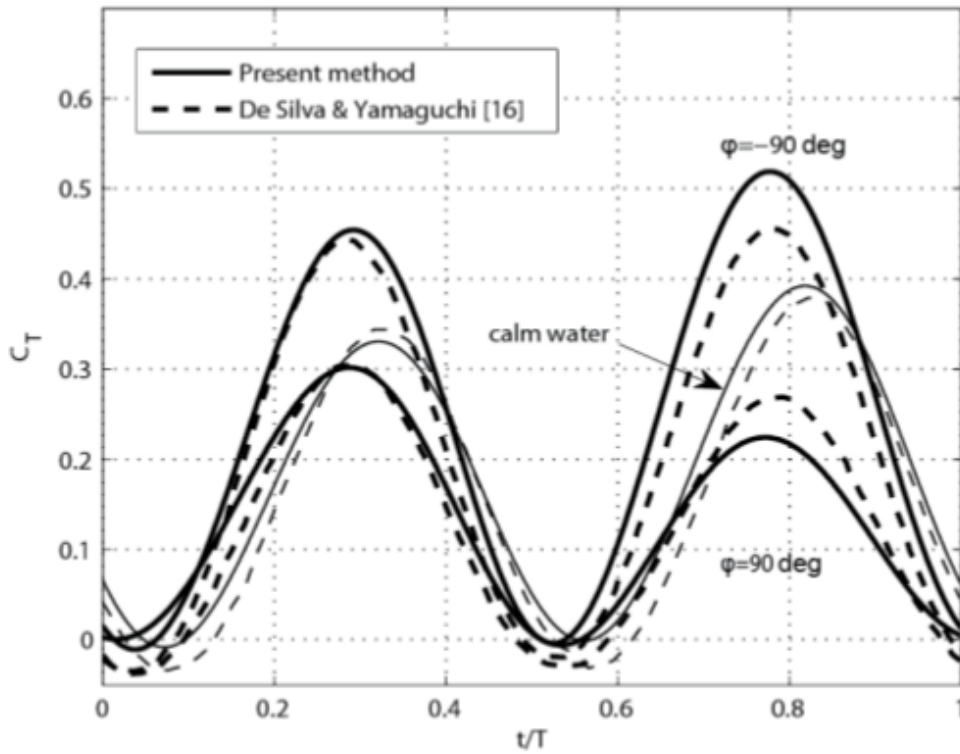


Figure 4.5: Thrust coefficient for NACA0015 at $Fn = 0.87$ and submergence $d/c = 1.28$ and deep water with motion parameters $St = 0.18$, $h_0/c = 0.6$, $\theta_0 = 15.2^\circ$, $X_R/c = 0.3$, $\psi = -105^\circ$, for three cases: (i) without wave, (ii) with an incident wave of amplitude $\eta_0/h_0 = 0.238$, encounter frequency equal to flapping frequency $\omega_0/\omega_h = 1$ and $\phi = -90^\circ$, (iii) the same wave and $\phi = 90^\circ$.

waves are also shown in the same figure using a thick line, for various values of the phase lag ϕ between incident wave and heaving motion. We clearly notice in this figure that there exists an interval, for $-178^\circ \leq \phi \leq 12^\circ$, where energy extraction from the waves raises the total thrust production of the system above its value at calm sea, free of cost. This gain is maximized at $\phi = -90^\circ$, shown using an arrow in the figure, where it becomes of order 20% higher. Moreover, we observe in Fig.4.6 that in the region $-163^\circ \leq \phi \leq 4.7^\circ$ the thrust gain from wave energy extraction overrides significantly the losses due to wave resistance. On the basis of the above findings we expect that the present biomimetic system, with the appropriate active control, could serve for augmenting ship propulsion in rough sea by extracting energy from the waves. That interesting and practical problem is studied in detail in Sec.4.5.3.

In the final example of the present section we present a 3D fully nonlinear simulation of for the biomimetic propulsor beneath the free-surface and in oblique incident waves of moderate amplitude, leaving the systematic examination of angle-of-incidence and nonlinearity effects as a subject of future work. In Fig.4.7 we present 3D calculations for the biomimetic propulsor beneath the free-surface and in waves with angle of incidence $\beta = 45^\circ$ and wave amplitude $\eta_0/c = 0.2$. The calculated incident wave satisfies with controlled accuracy the fully nonlinear free-surface boundary conditions. The initial guess corresponds to a 5th-order Stokes wave; see e.g. Massel (1989) and Fenton (1985). The characteristic wavelength is selected properly to approximately obtain a wave component in x - direction (that is the direction of the foil forward motion) with encounter frequency that equals the flapping foil frequency. For the simulation a constant-chord foils with NACA0012 sections, $AR = 6$, in flapping motion with

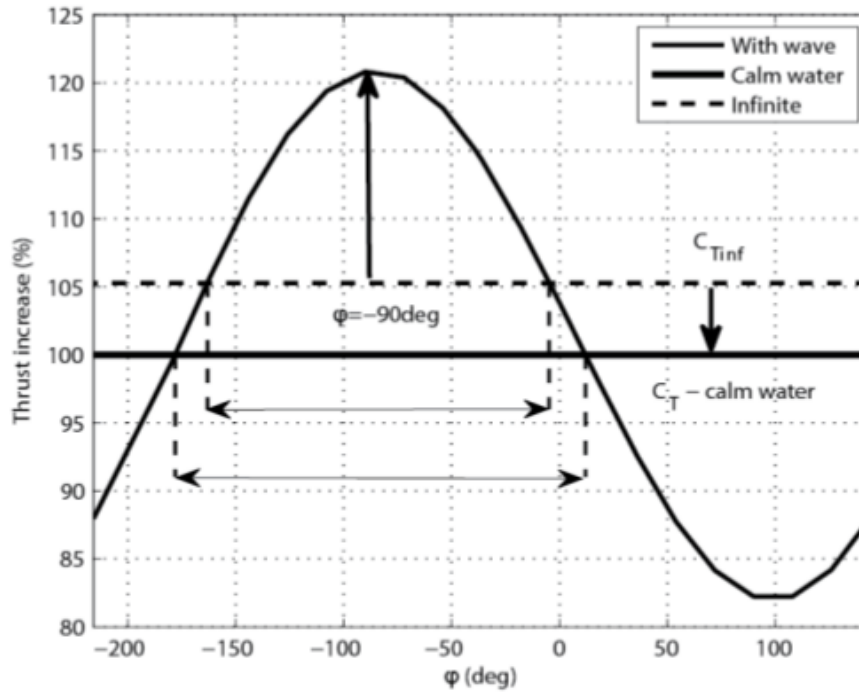


Figure 4.6: Average thrust coefficient for the flapping hydrofoil of Fig.3.11b at $St = 0.4$, $\theta_0 = 35^\circ$ at submergence $d/c = 2.5$, in the presence of an incoming wave of amplitude $\eta_0/h_0 = 0.75$, with flapping frequency equal to encounter frequency $\omega_0/\omega_h = 1$. Comparison between results in deep submergence, beneath the free surface in calm sea, and in head waves.

$St = 0.3$, $h_0/c = 0.75$, $\theta_0 = 23.3^\circ$, pivot point $X_R/c = 0.33$ and phase lag $\psi = -90^\circ$ and $F = U/\sqrt{gc} = 0.6$, in mean submergence $d/c = 0.5$. To be more specific, the corrector potential on the body and the total potential at the free-surface and the potential jump on the wake are depicted. Regarding the performance of the numerical method and the GPU accelerated computational code, we provide some information for the fully nonlinear calculations. The simulation is in time domain and the foil begins from the rest reaching harmonic state after 2 periods T , the time-step is $\Delta t/T = 0.5\%$. A total number of $N_B = 1860$ body boundary elements and $N_F = 2976$ free-surface elements are used. Mixed-precision arithmetics have been used, 1.5GB were required from the VRAM and the simulation time was 350 sec in the case of the prescribed wake model and 981 sec in the case of the free-wake model. It is worthwhile to mention that due to the specific numerical treatment of the problem (see also Sec.1.3.1), the truncation of the horizontally infinite domain using PML, the exploitation of mixed precision arithmetics, the proper handling of induction-factor matrices (see the discussion bellow Eq.2.25) and the special treatment of the nonlinear incident waves (as presented in the present chapter), the present GPGPU computational code is very efficient in terms of space complexity. To be more specific, in the present case where free-surface discretisation is required the memory demand from the VRAM is only 0.2GB higher in comparison with the infinite domain case. This is crucial if we consider the limited amount of memory available even in modern GPUs.

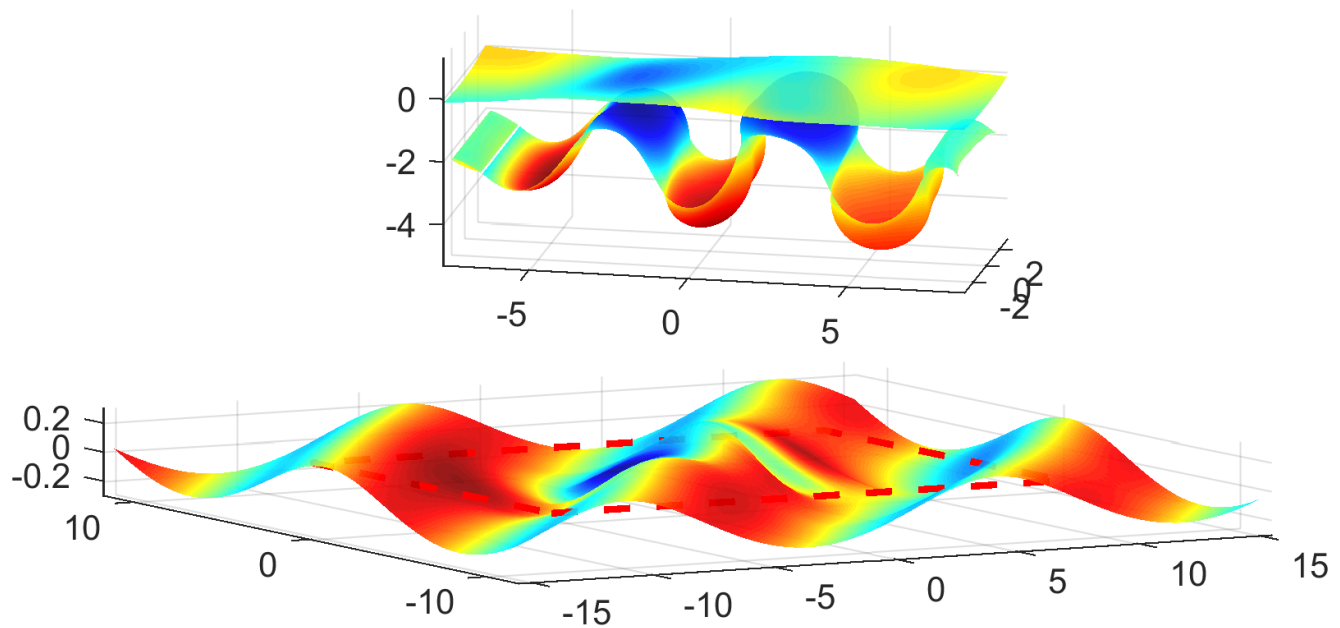


Figure 4.7: 3D nonlinear simulation of biomimetic flapping-foil thruster beneath the free-surface and in waves with angle of incidence $\beta = 45^\circ$ and wave amplitude $\eta_0/c = 0.2$. For the simulation a constant-chord foils with NACA0012 sections, $AR = 6$, in flapping motion with $St = 0.3$, $h_0/c = 0.75$, $\theta_0 = 23.3^\circ$, pivot point $X_R/c = 0.33$ and phase lag $\psi = -90^\circ$ and $F = U/\sqrt{g\bar{c}} = 0.6$, in mean submergence $d/c = 0.5$. Potential and velocities on the body and potential jump on the wake as well as total free-surface potential and elevation, as calculated with the fully nonlinear model, are presented.

4.5.3 Augmenting ship propulsion in waves by actively controlled flapping foils

The present section results and the details in the development of the method are presented in detail in our work (Belibassakis and Filippas, 2015), however here we will present a few interesting and practical results concerning the problem of ship propulsion augmentation in waves by actively controlled flapping foils (Fig.4.8). For that purpose the linearised free-surface conditions and the 2D version of the code have been used. The method has also been extended to treat multichromatic waves that correspond to specific sea states modeled using parametric spectra; more details can be found in the aforementioned reference. For simplicity, only head waves in deep-water conditions are considered here as excitation of the hull oscillatory motion.

To obtain solution the following procedure is adopted: The first step is the calculation of the incident wave-current field in frequency domain by means of a coupled-mode model. Subsequently, the lifting flow problem associated with the flapping foil is solved along with the dynamical heaving response of the foil, where the mechanical system including the energy generator is modeled as an one degree-of-freedom oscillator. Finally, the biomimetic system then is analyzed by means of a time-domain BEM; more details can be found in Belibassakis and Filippas (2015).

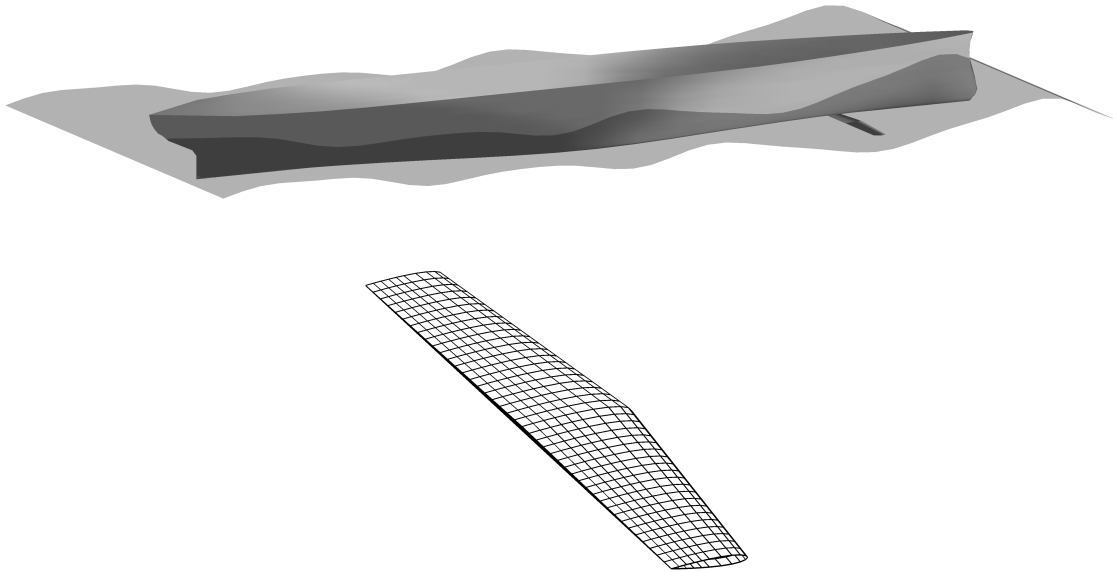


Figure 4.8: Ship hull, advancing in head waves, equipped with a flapping wing located below the keel, at forward station operating in random wave conditions, gaining its vertical motion from ship heave and pitch responses.

The first step is the calculation of the coupled responses of the ship with the operation of the flapping thruster, using linear seakeeping analysis, in conjunction with foil model based on quasi-steady lifting line approximation and spanwise integration of sectional lift forces. The latter can be corrected after the last step calculated by means of a time domain BEM. Subsequently, the wave field and the kinematics of the foil are obtained using the calculated RAO. Then, the behaviour of the above system in random waves, represented by various frequency spectra, is examined by means of time-domain BEM, including the free surface effect and taking into account the ship-induced motions, but disregarding as a first approximation the foil-hull interaction.

To be more specific, we consider a ship in head waves advancing at constant forward speed U . In the present approach we use the equations of motion derived in the body-fixed frame of reference linearised by assuming small oscillatory amplitudes. Seakeeping analysis in the frequency domain is used to obtain the motions and responses of the examined system (ship and flapping wing) in the vertical plane. A simplified lifting-line model to derive expressions of the flapping wing forces. As it has been suggested by Politis and Politis (2014) the controlled foil pitch angle is set proportional to the angle of attack due to heaving motion of the foil, with the pitch control parameter w ranging from 0 to 1. The analysis described in detail in Belibassakis and Politis (2013) and Belibassakis and Filippas (2015), permits us to calculate the ship responses including the effect of the flapping wing operating as an unsteady thruster and compare with the corresponding seakeeping responses concerning the bare hull without the wing. For demonstration purposes, we consider a series 60-Cb0.60 ship hull form and a flapping wing propulsor located at a distance $x_{wing} = 15$ m fore the midship section (station 8 of the ship), at a depth $d = 7$ below the waterline. More the details concerning the geometry can be found in the aforementioned reference.

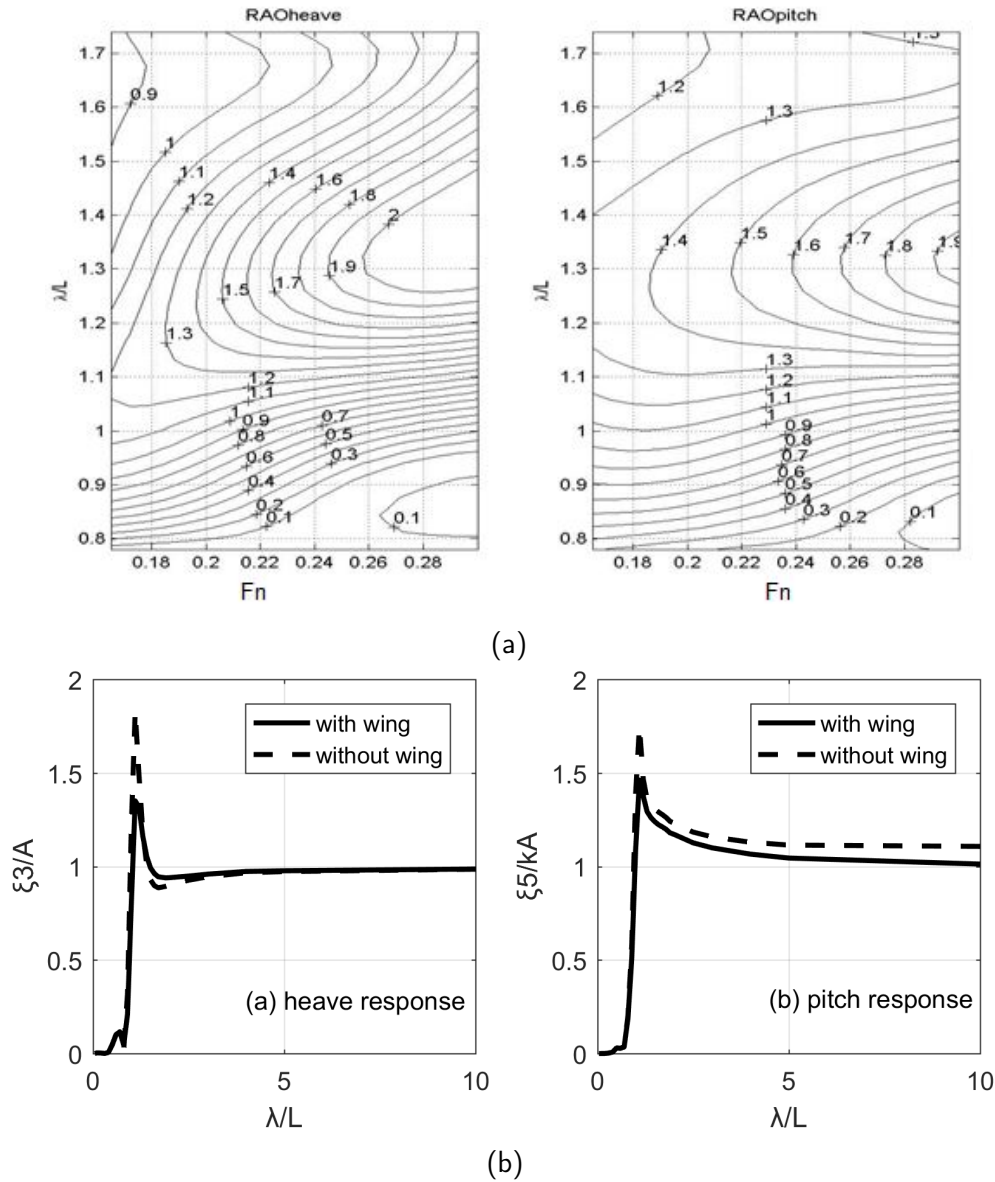


Figure 4.9: (a) Heave ξ_3/A and pitch response ξ_5/kA of the examined ship hull against non-dimensional wavelength λ/L and ship Froude numbers $F_n = U/\sqrt{g}L$. (b) Comparison of heave and pitch responses for ship speed $U = 5.5$ m/s, with (bold line) and without (dashed line) the operation of the flapping wing thruster.

In Fig.4.9 results are presented concerning the response of the system in head seas. To be more specific, in Fig.4.9a the normalised heave response with respect to the incident wave amplitude ξ_3/A of the ship is plotted, without the operation of the wing, for various values of the non-dimensional wavelength λ/L and ship Froude numbers $F_n = U/\sqrt{g}L$. The corresponding, ship-pitch response ξ_5/kA is also shown in Fig.4.9a. To illustrate the effect of foil operation, in Fig.4.9b, the same responses are presented in the case of ship Froude number $F_n = 0.25$ ($U = 5.5$ m/s) using dashed line. The modified responses taking into account the coupled ship-flapping wing dynamics are overplotted in the same figures using a thick solid line. We observe significant reduction of the ship motions, especially in the vicinity of the resonance condition. This result is indicative of the extraction of energy from ship motion by the flapping wing. In the case of ship pitch motion, the operation of the flapping wing propulsor leads

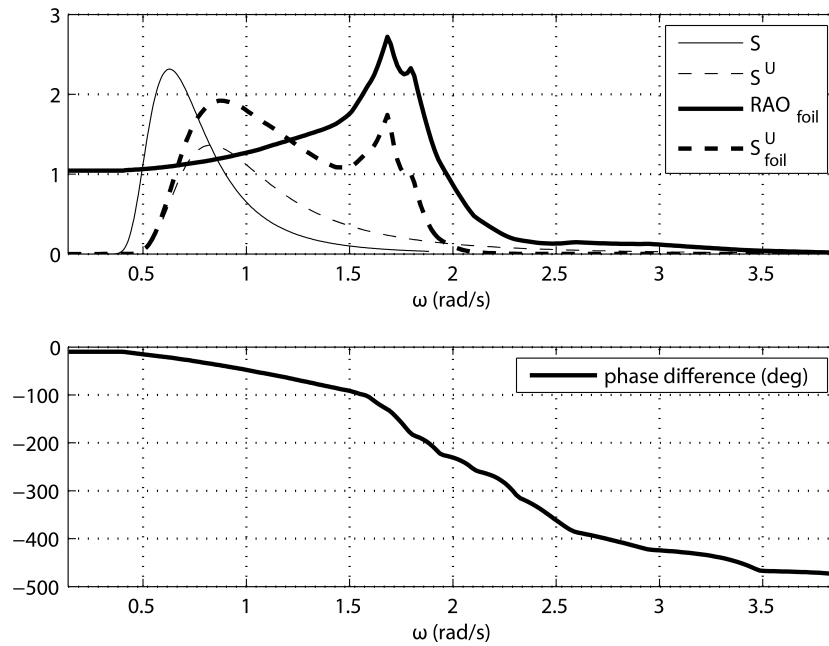


Figure 4.10: Sea spectrum ($H_s = 4$ m and $T_m = 10$ sec) with respect to the inertial (S) and the moving (S^U) frame and foil's motion spectrum at station 8 $x_{wing}/L = 0.33$ where the horizontal flapping wing is located, for head seas and ship speed $U = 10.6$ kn ($Fn = 0.25$). The amplitude and phase of the foil's RAO are also plotted using thick lines in the upper and the lower subplots, respectively.

to reduction of the response, especially for wavelengths longer than the ship length. Thus, the operation of the examined unsteady thruster extracts energy from the waves offering also dynamic stabilisation. An extra effect, strongly connected with the reduction of ship responses, is the expected drop of the added wave resistance of the ship. Indicative results concerning the latter additional benefit are provided in Belibassakis and Politis (2013).

Using the responses of the system, the kinematics of the flapping wing are obtained, permitting the detailed formulation and study of the performance of the wing sections operating in random head waves. For this reason, the present method is applied to analyze numerically the performance of high aspect ration foils beneath the free surface. As a first approximation we use the assumption of waves with small amplitude in comparison with the wavelength and we work in the context of linear free surface wave theory. Realistic sea conditions are modeled using parametric spectra and the realization of the free surface elevation and of other wave signals is implemented using the classical random phase model, more details can be found in our work Belibassakis and Filippas (2015). The final speed of the foil U , reached after acceleration from rest, is connected with the following Froude number $F_{foil} = U/\sqrt{gc}$ based on the chord c of the foil. We denote with $S(\omega)$ the wave spectrum in the earth fixed frame of reference and we can obtain an expression for the spectrum according to a moving observer with the foil mean velocity U denoted by $S^U(\omega_{en})$, where ω_{en} is the encounter frequency. Then we use the response amplitude operator RAO_{foil} at the position x_{wing} of the wing, in order to obtain the spectrum of wings heaving motion (see also Fig.4.10). Furthermore, the rotational motion of the hydrofoil, about an axis at $x_R = 0.33c$ distance from the foils leading edge, is defined as

negative at the clockwise direction. The latter self-pitching motion of the foil is a result of a simple active control law based on its linear oscillation history.

In the sequel numerical results are presented and discussed concerning the performance of a NACA0012 flapping hydrofoil in random waves, at various sea states. The effects of the mean foil submergence d , its horizontal location along the ship x_{wing} and of the pitch control parameter w are investigated. The incident wave field is represented by frequency spectra corresponding to different sea states labelled by an index ranging from 1 to 5. The correspondence of sea conditions with Beaufort scale (BF), sea state and the main spectral wave parameters, i.e., the significant wave height H_s and the modal period T_m are given in the following table:

Sea conditions and spectral parameters.

Sea condtions	BF	Sea State	H_s (m)	T_m (s)
1	3	3	1	7
2	4-5	4	2	8
3	5-6	4-5	3	9
4	6	5	4	10
5	7	6	5	11

Considering the vertical motion of the hydrofoil in head waves, which is described by the combined ship hull-flapping foil responses, in Fig.4.11 the simulation of a flapping foil at mean submergence $d/c = 7$, Froude number $F_{foil} = \sqrt{U}/gc$ ($F_{ship} = 0.25$), advancing in random head waves corresponding to sea state 5 is presented. Numerical results have been obtained using pitch control parameter $w = 0.5$ and setting the pivot-axis concerning the self-pitching motion of the flapping foil at distance $c/3$ from the leading edge. In particular, in Fig.4.11 the profile of the ship travelling in random waves and positioned according to the response of the coupled ship-flapping wing system is shown at five instants within a time interval corresponding to one modal period. The hydrofoil is located at forward station $x_{wing} = 0.3L$ with respect to the midship section of the ship. In the same figure the trailing vortex curve modelling the foil's wake is plotted, including the calculated dipole intensity (potential jump) on the vortex sheet, which is illustrated using arrows normal to the wake curve with length proportional to the local dipole strength. The latter result is associated with the memory effect of the generated lifting flow around the flapping foil operating in random incident waves. Moreover, in the right subplots of Fig.4.11 the instantaneous distribution of the pressure coefficient ($c_p = p - p_{atm}/0.5\rho U^2$) on the hydrofoil, at the same time instants as the plots to the right, as calculated by the present method. From the calculated sectional pressure distributions, lift and thrust components are obtained at each time step by integration. Furthermore, it is worthwhile to notice that the present model is able to predict intermittent cavitation inception, which may significantly affect the performance of flapping hydrofoil, and would be very important particularly at lower foil submergence.

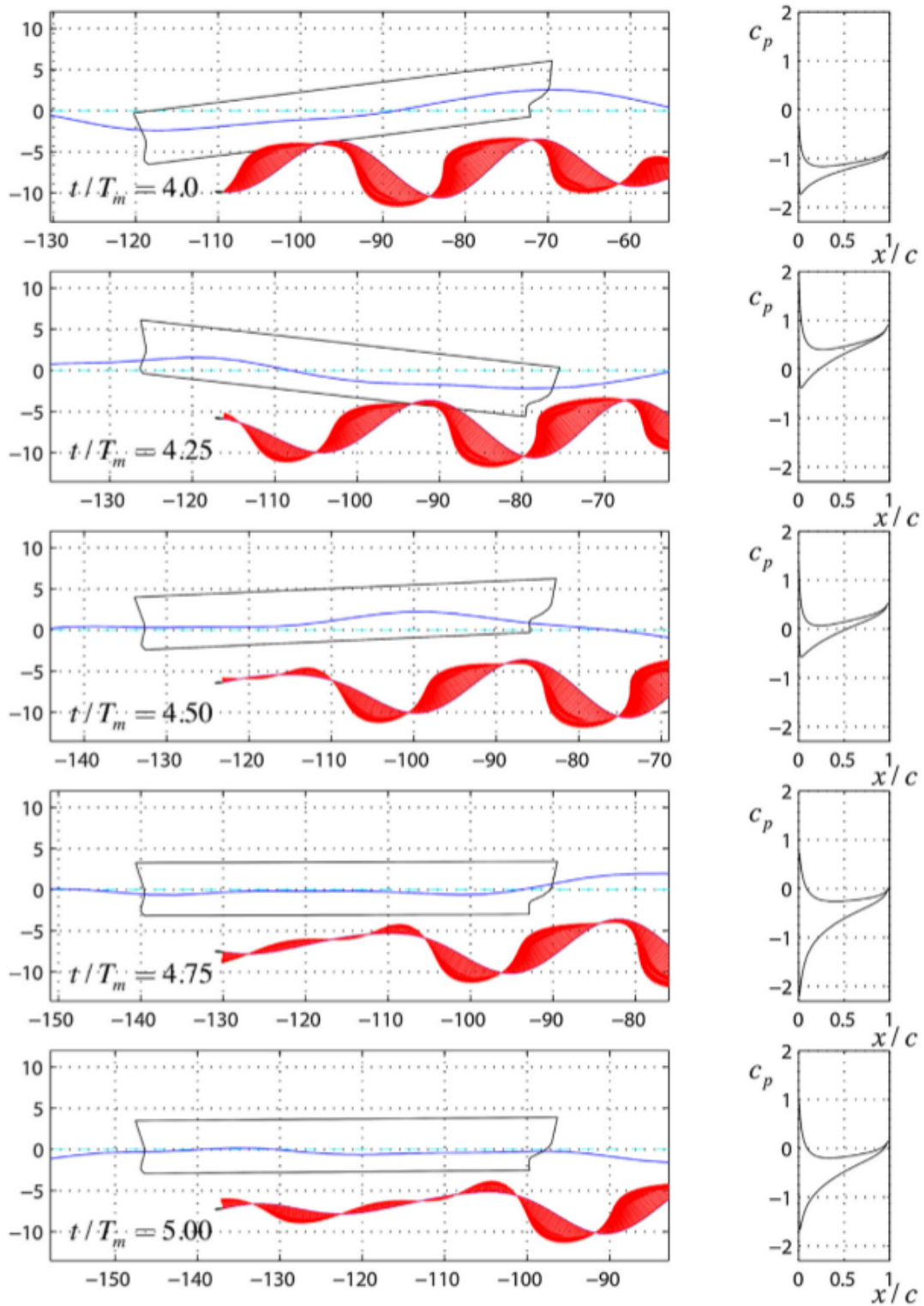
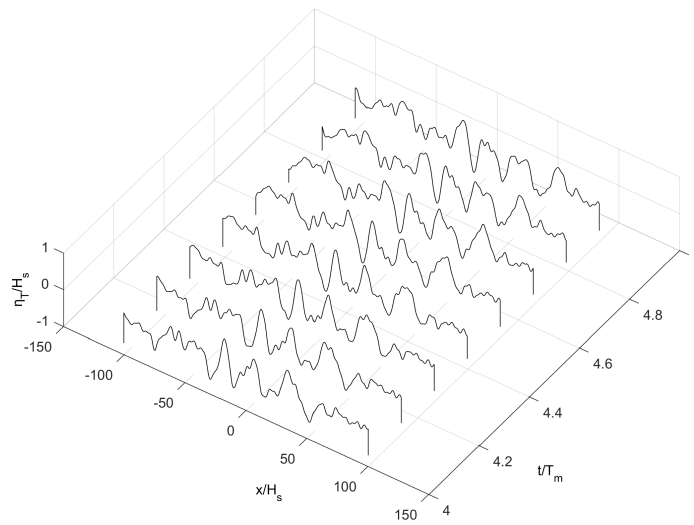
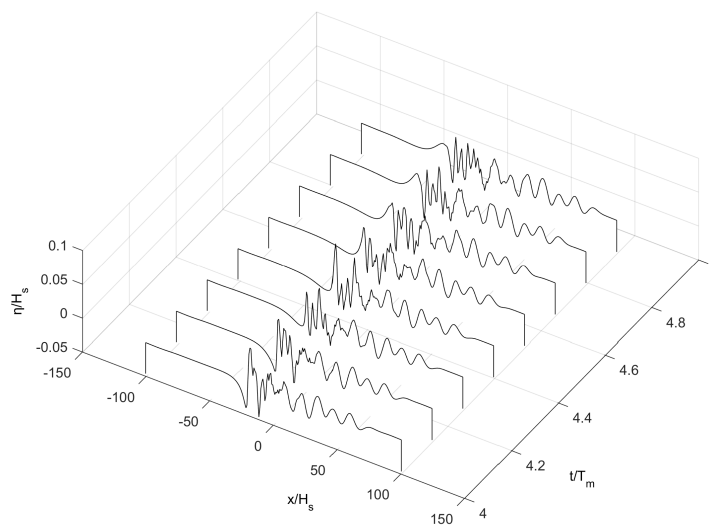


Figure 4.11: Simulation of the system operating in sea state 5. Results plotted at various instants in one modal period. In the right subplots the distribution of the unsteady pressure coefficient ($c_p = p - p_{atm}/0.5\rho U^2$) on the flapping foil, located at station $x_{wing} = 0.3L$ (with respect to the midship section), at the same instants is plotted, as calculated by the present method.



(a)



(b)

Figure 4.12: Time history of (a) the total free-surface elevation and (b) the disturbance component due to the operation of the foil during the same time interval of one modal period, as in Fig.4.11.

In order to illustrate the relative magnitude of the incident and disturbance flow generating by the flapping motion of the foil in waves, for the same as before wave conditions and hydro-foil data, the calculated free-surface elevation normalised with respect to the significant wave height is plotted in Fig.4.12 over the horizontal domain, at some instants during one modal period. In particular, in Fig.4.12(a) the total free surface elevation is plotted during the formation of a high-amplitude wave. The corresponding disturbance component due to the operation of the flapping foil is shown in Fig.4.12(b), as calculated by the present method. Since the flapping foil travels forward at subcritical conditions and the submerged depth is significant, the disturbance wave propagates mainly as a following component, which is characterised by quite smaller amplitude than the incident wave.

Turning into more specific details, we present in Fig.4.13 the time series of important quantities concerning thrust production by the examined system operating in random wave conditions, as calculated by the present method. The same parameters as before are considered concerning the incident wave and the flapping foil data. In the first subplot the time history of heaving motion at the location of the foil at a forward station of the ship, as produced by combined oscillatory heaving and pitching motion of the coupled ship-flapping foil response, is shown together with the generated lift coefficient $C_L = F_Y/0.5\rho U^2 c$. The calculated signals are plotted for 15 modal periods, after transition from rest has been achieved. We observe that significant amplitudes of the lift force are produced. Moreover, the phase lag between foil's motion and lift force is approximately 180° and therefore, the generated lift acts as a restoring force reducing the responses of a ship equipped with flapping hydrofoils. Thus, except of thrust augmentation, the examined system will offer dynamic stabilisation, as it can also be observed in the RAO calculations presented in Fig4.9b. In Fig. 7(b) the dynamic evolution of thrust with respect to the resistance of the ship in calm water $-F_X/R$ is shown, in the same time interval. For the ship travelling at $U = 5.5$ m/s the calm water resistance has been estimated to be $R_s = 14.75$ kN (Belibassakis and Politis, 2013). We observe in this subplot that the thrust oscillations are in the interval $0\% \leq -F_X/R_s \leq 960\%$, with an average value of 79% of R_s , which is indicated in Fig.4.13(b) using thick solid line. Moreover, in Fig.4.13(c) the power extracted by the examined system from the waves is compared against the corresponding power that is necessary for the self-pitching motion of the foil, actually for tuning the instantaneous angle of attack in order to produce positive thrust. A dashed line is used in Fig.4.13(c) to indicate the achieved propulsion power, scaled with respect to the Effective Horse Power of the ship in calm water (which at $U =$ m/s is estimated EHP = 80 kW). In the same subplot a bold line is used to indicate the power required for the self pitching motion of the foil, which is negligible and thus, it is multiplied by 100 in the figure in order to be observable. Negative values indicate power required by the system. Similar findings have been reported by Politis and Politis (2014), in the case of pitching and heaving wing in infinite flow domain, without consideration of the free-surface effects.

Next, in Fig.4.14 we examine the effect of sea state and of the free-surface boundary on the augmentation of the overall propulsion of the ship by the flapping system operating in random waves. In Fig.4.14(a) the mean value of the normalised thrust is plotted for various sea conditions represented by the significant wave height, as listed in previous Table. The same parameters as in the previous example are considered concerning the flapping foil data. We notice in this plot that as the wave height increases, the value of mean thrust also increases. Moreover, appropriate modification of pitch control parameter, can further increase the amplitude of the angle of attack of the flapping foil and thus, the thrust production. The latter is expected to be practically useful in the case of lower severity seas. This could be achieved without passing the limit of leading edge separation, as it will be described in more detail below. Furthermore, in Fig.4.14(b), the variation of the mean thrust generated by the flapping foil is shown as a function of its mean submergence scaled with respect to the modal wavelength. In this case, the corresponding ratio of mean submergence to chord varies in the interval $7 \leq d/c \leq 40$. We can see that the effect of free surface is to reduce the thrust coefficient, which is naturally expected due to increase in the developed wave resistance, as the foil submergence becomes smaller. Another reason for the observed thrust decrease at lower submergence is the reduction of the foil vertical oscillatory motion induced by ship pitching due to smaller radius of rotation.

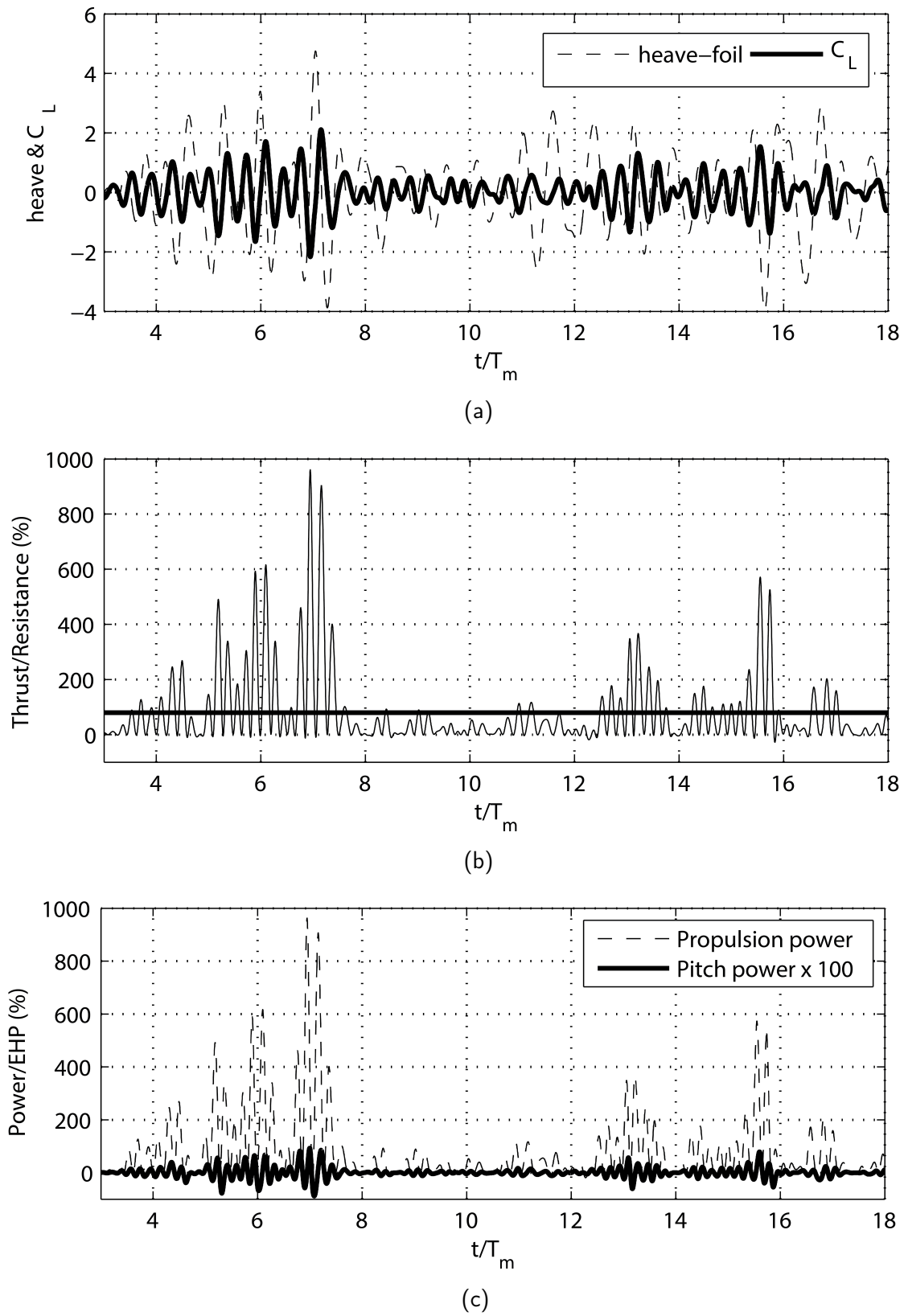


Figure 4.13: Evolution of motion and integrated hydrodynamic quantities for a NACA0012 flapping hydrofoil in random head waves, corresponding to sea state 5, traveling at $F_{foil} = 1.76$, for time duration of 15 modal periods. Foil mean submergence $d/c = 7$ and control parameter $w = 0.5$.

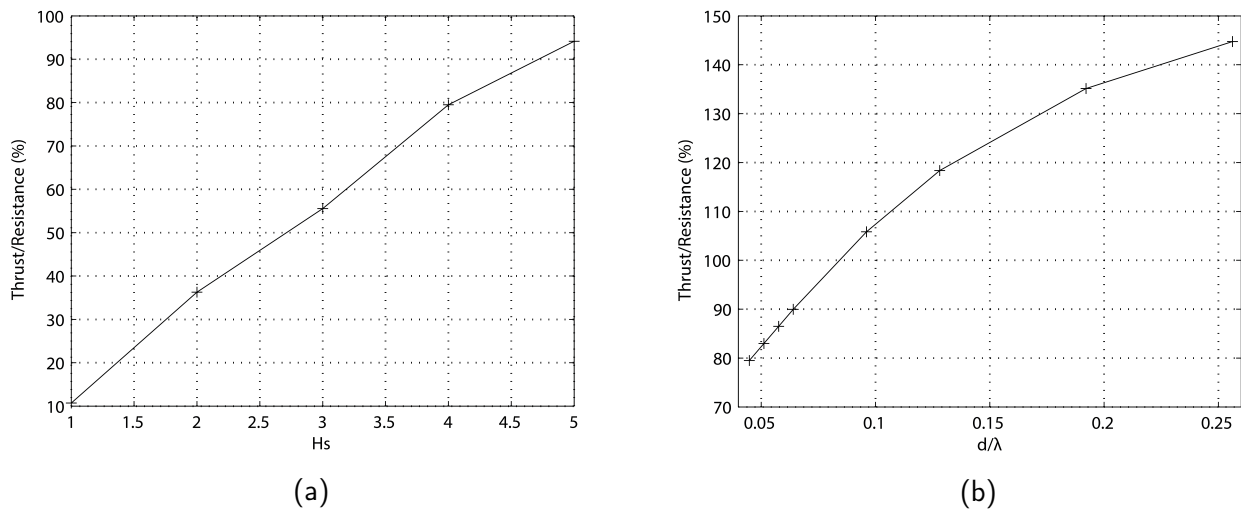


Figure 4.14: Mean thrust to calm water resistance ratio as (a) function of sea conditions represented by significant wave height, and (b) as function of the mean foil submergence to modal wavelength ratio.

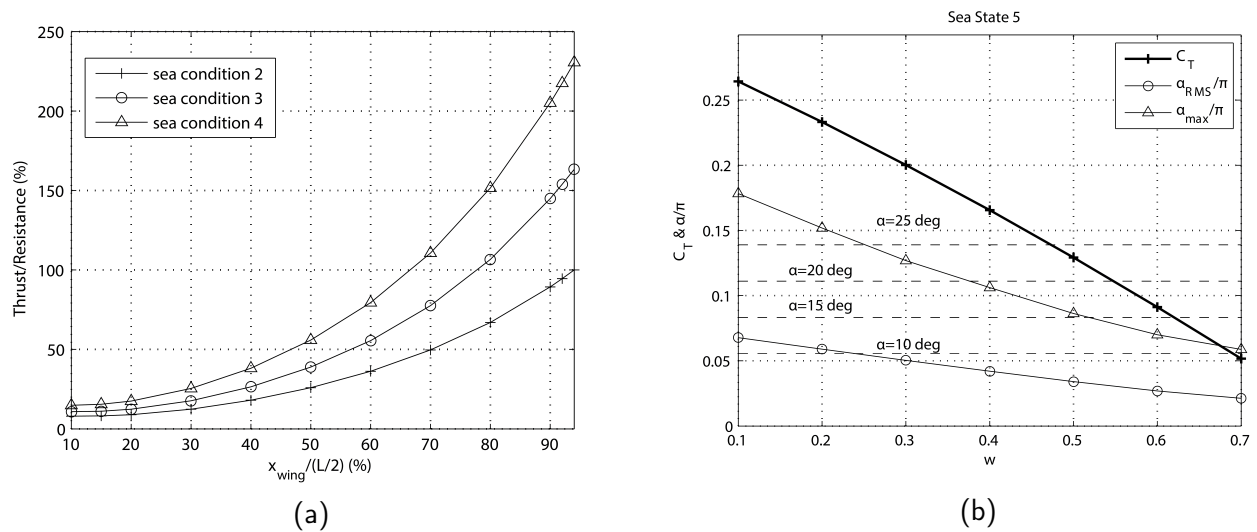


Figure 4.15: (a) Mean thrust to calm-water resistance as a function of the longitudinal position of the flapping foil for various sea conditions. (b) Mean thrust coefficient (bold line) as a function of pitch control parameter w , for the same as before foil parameters.

Next, the effect of the longitudinal position of the flapping wing located at a forward station along the ship is demonstrated in Fig.4.15a. In this plot the mean thrust to resistance ratio is plotted against x wing measured from the midship section and expressed as a portion of ship half length $L/2$. The three curves correspond to various sea conditions; see Table 1. As it is expected, best position for thrust production by the examined unsteady propulsor is near the bow. On the other hand, selection of extreme forward location of the flapping foil is dangerous from the point of view of intense slamming, especially at high wave conditions, and should be avoided. Similar findings based on experimental research have been reported by Naito and Isshiki (2005) and more recently by Bøckmann and Steen (2016). Finally, in Fig.4.15b the effect

of the pitch control parameter w on the thrust production by the flapping foil is investigated. In particular, the mean thrust coefficient is plotted as a function of w using a thick solid line. The foil data are kept the same as before. We clearly observe that as the pitch control parameter is getting smaller, the calculated thrust coefficient increases, as expected due to the increase of the amplitude of the effective angle of attack. However, the present method does not provide quite reliable predictions of the thrust coefficient at large angles of attack (see also Sec.2.10.3) due to dynamic stall effects, which are not presently modeled and will be subject of future extension of the present model. For this reason the root mean square and the maximum value of the angle of attack are also plotted in Fig.4.15b, using circles and triangles, respectively, supporting the selection of the pitch control parameter in order to avoid leading edge separation.

Moreover, in author's work Filippas (2015), a feasibility study on an existing patrol boat of Greek navy fleet is presented. That boat is equipped with two fin stabilized near the midship section for roll reduction purposes. Although, the design wings with small span, located near the pitch rotation center of the ship is optimal for roll reduction and not for extraction of energy from ship heave and pitch, it is shown that existing set up can operate only changing the control law of the wings' rotational motion. Moreover, it is illustrated that with appropriate redesign of the location of the fins the performance of the system can be further enhanced.

Based on the above data we conclude that the present results can be exploited to derive useful guidelines concerning the control and optimum performance of the examined system extracting energy from sea waves for augmenting marine propulsion in rough seas, with simultaneous reduction of ship responses offering dynamic stabilisation. There are several issues that need to be considered before real ship application of the present system becomes feasible. These include clearance under the hull and fouling protection, cavitation, flow separation and structural vibration issues, cost of the support structure and the pitch actuator mechanism. Also, arrangements consisted of multiple oscillating foils, or foils closer to the hull could enhance the whole performance, however, they introduce strong interference effects associated with foil operation in the boundary layer of the ship or in the wake of preceding bodies, requiring special viscous-inviscid interaction techniques of full CFD modelling for numerical simulation. All the above are left to be examined as future tasks associated with the detailed design and implementation of the system.

4.5.4 Semi-activated oscillating hydrofoil as a nearshore biomimetic energy system in waves and currents

The present section results and the details in the development of the method are presented in detail in our work (Filippas et al., 2018), however here we will present a few interesting and practical results concerning the problem of energy extraction from waves and currents nearshore using semi-activated oscillating foil biomimetic systems (Fig.4.16). For that purpose the linearised free-surface conditions and the 2D version of the code have been used. The method has also been extended using a linearised version of the couple mode system (Belibasakis et al., 2017) to consider the effect of non-uniform linearly sheared currents, and the effects of variable bathymetry.

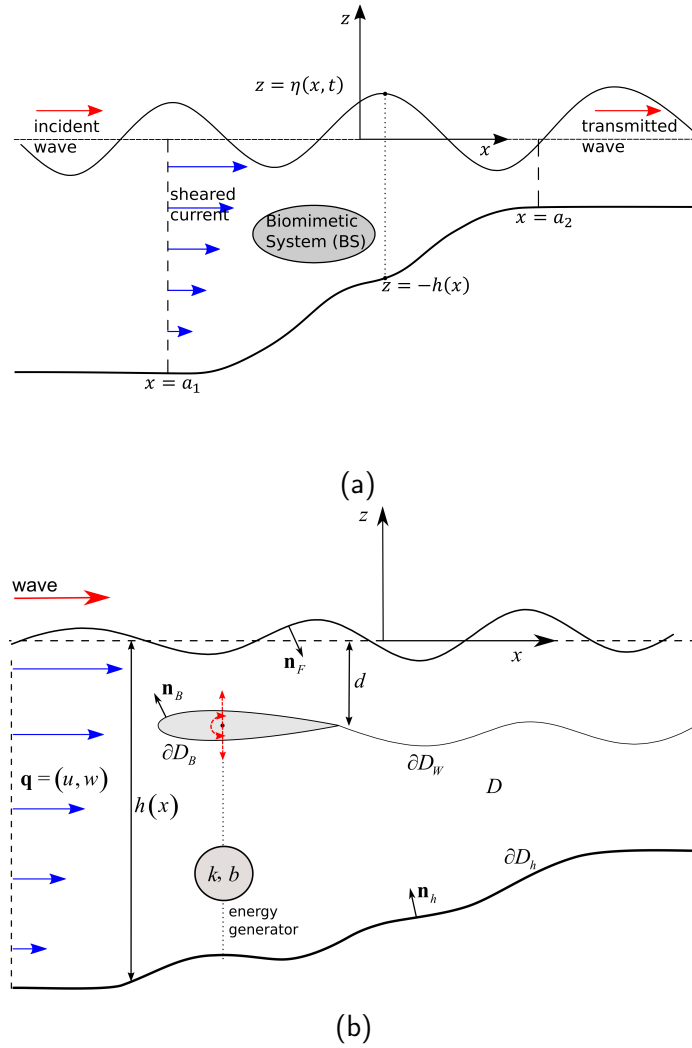


Figure 4.16: (a) Interaction of waves with vertically sheared currents over variable seabed topography around the location where the biomimetic energy converter is installed; see also Belibassakis et al. (2017). (b) Oscillating hydrofoil operating as energy device in waves and sheared currents.

To obtain solution the following procedure is adopted: The first step is the calculation of the incident wave-current field in frequency domain by means of a coupled-mode model. Subsequently, the lifting flow problem associated with the flapping foil is solved along with the dynamical heaving response of the foil, where the mechanical system including the energy generator is modeled as an one degree-of-freedom oscillator. Finally, the biomimetic system then is analyzed by means of a time-domain BEM; more details as well as validation of the method, can be found in the aforementioned references.

In the sequel, we apply the proposed method to study the performance of a NACA0012 hydrofoil, as flow and wave energy converter, operating in nearshore regions. We consider here a hydrofoil of chord c operating in a coastal region, in the presence of propagating waves and vertically sheared currents, over the shoaling environment that is presented in Sec.2.2 of Filippas et al. (2018). In the examined case, the Strouhal number of the incident waves is $St = \omega \sqrt{h_1 / g} = 0.4$, where h_1 is the depth at the entrance of the domain and the wave amplitude is $H / (2c)$. We recall that the current speed at the entrance of the domain corresponds

to bathymetric Froude number $F_d = U/\sqrt{gh_1}$ and the maximum shear in the middle of the domain (where the hydrofoil is located) is $S_{max} = 0.05 \text{ s}^{-1}$. The hydrofoil operates around a mean submergence depth $d = 2c$, and performs enforced pitching and induced heaving oscillations. The pitching motion is about a rotation axis at distance $X_R = 0.33c$ from the leading edge, with amplitude $\theta_0 = 15^\circ$. In general, the oscillation frequency ω_Θ can be different from the incident wave frequency ω . In the present section we consider one case where $\omega_\Theta/\omega = 1$, with corresponding reduced frequency $k_r = \omega_\Theta c/2U = 0.267$ and phase difference between pitch and the incoming wave equal to $\psi = -40^\circ$, and another case with $\omega_\Theta/\omega = 2$, $k_r = 0.533$ and $\psi = -90^\circ$. In the examined cases, the following oscillator parameters of the 1-degree-of-freedom oscillator are used $m^* = 4$, $\zeta = 0.5$, $\omega_0/\omega = 2$; for more details see Filippas et al. (2018), Sec.3.1.

4.5.4.1 Numerical simulation of the biomimetic energy system in waves and currents

First, in Fig.4.17 we consider an example of equal wave and pitching frequency $\omega_\Theta/\omega = 1$ and $\psi = -40^\circ$. Results are presented at various instances in a period T , concerning the position of the foil, together with dipole intensities in the vortex wake (denoted with red arrows), as well as the calculated instantaneous pressure coefficient c_p on the flapping foil and the free-surface elevation η (with red stars we denote the absorbing layer zone). Integrating the pressure distribution on the hydrofoil boundary, we obtain the force and the moment, and subsequently exploiting information about the enforced pitching and induced heaving velocities, the input and output power of the system is calculated.

In the case $\omega_\Theta/\omega = 1$ and $\psi = -40^\circ$, in Fig.4.18(a) the foil's rotational motion Θ against the resulting effective angle of attack α is shown, and in Fig.4.18(b) the time history of the developed lift coefficient C_L is plotted together with the moment coefficient C_M (required for the enforced pitching motion) and the normalized heaving response X/c . In Fig.4.18(b) the non-linear character of the responses are clearly observed in the shape of the time signals, with the maximum values of heaving oscillation being comparable to the chord length $Z_{max}/c = 0.95$. The input power coefficient $C_{P\theta}$ and the output power coefficient C_{Pb} of the considered system, operating in the above conditions, are presented in Fig.4.18(c). We observe that the extracted energy, with mean value $\overline{C}_{Pb} = 0.281$ (denoted with continuous thick line), is significant, especially as compared to the power needed for controlling the pitching foil motion, with corresponding average pitching power coefficient $\overline{C}_{P\Theta} = 0.013$ (denoted with dashed thick line), resulting in the examined case to a net power extraction coefficient $\eta_P = 20\%$.

The corresponding time signals in the case of different pitching and wave frequency $\omega_\Theta/\omega = 2$ and $\psi = -90^\circ$, are presented in Fig.4.19. In this case, the foil performs two cycles of motion in one wave period, with larger power extraction during the second cycle, when the crest of the wave occurs over the foil. Although, the mean output power coefficient, compared to the previous case, is slightly smaller $\overline{C}_{Pb} = 0.237$, and the corresponding input power coefficient is larger $\overline{C}_{P\Theta} = 0.021$, the performance of the system is better $\eta_P = 33\%$ due to the smaller induced heaving motion $Z_{max}/c = 0.33$. In the sequel, we will demonstrate that even larger amounts of energy can be extracted from waves and sheared currents, with proper selection and control of the operational parameters, without reaching large angles of attack, avoiding thus excessive flow separation and unfavorable dynamic stall effects.

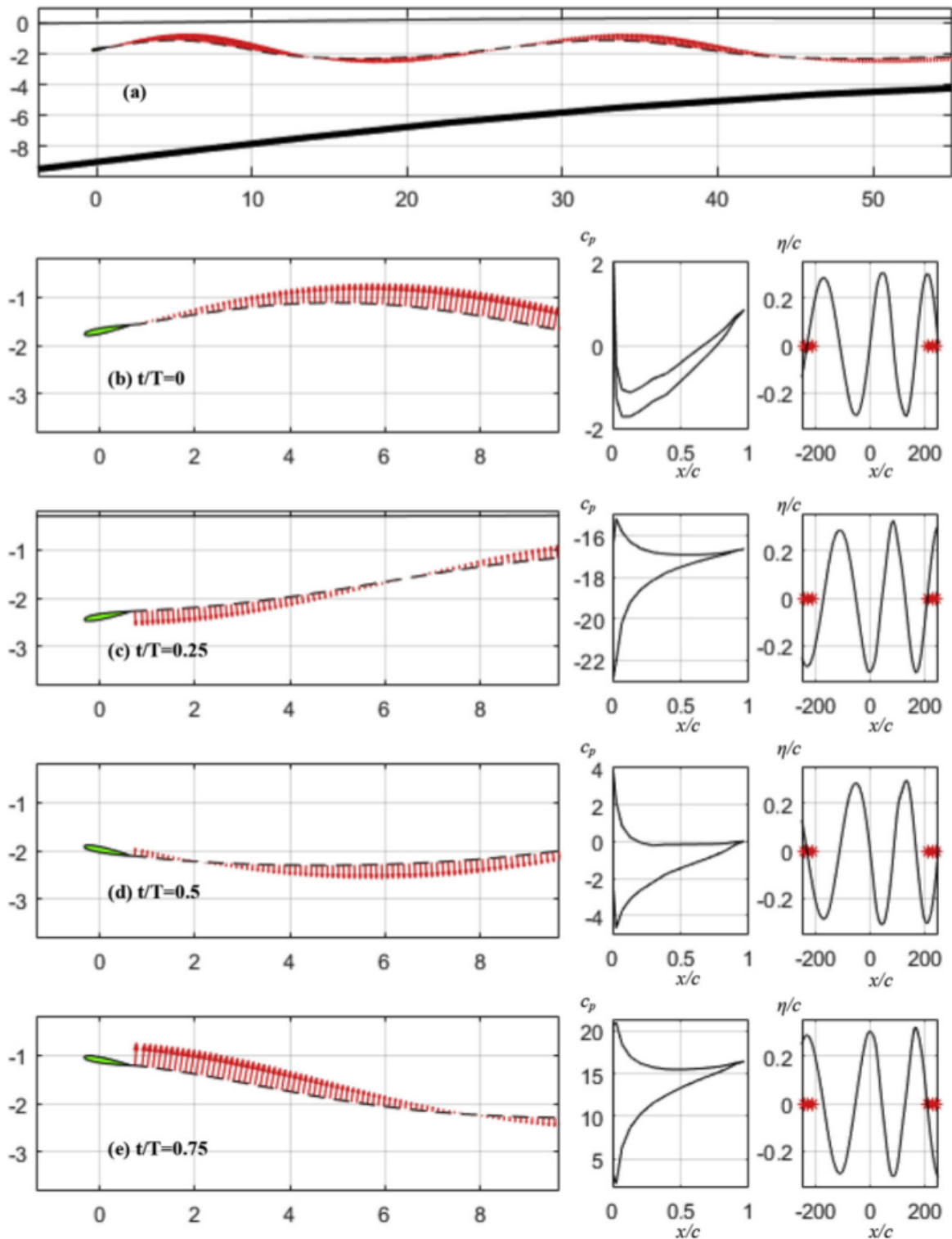
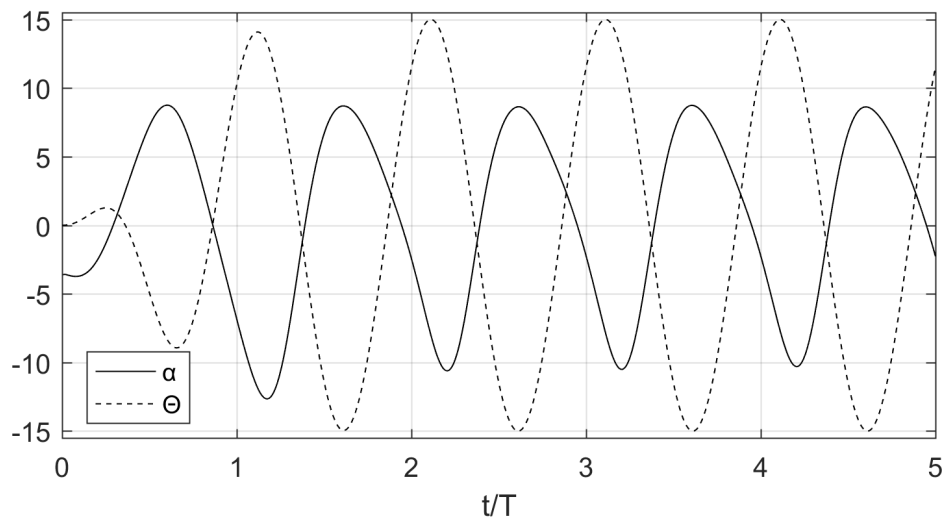
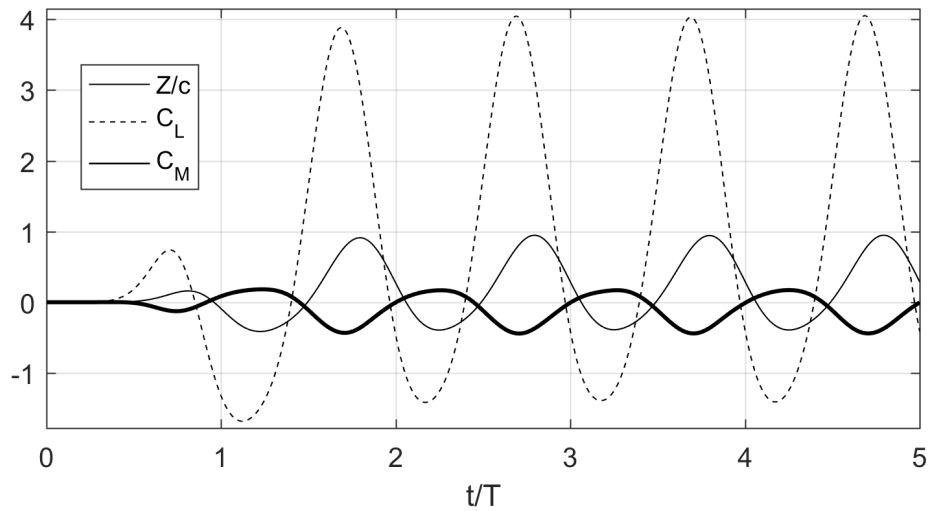


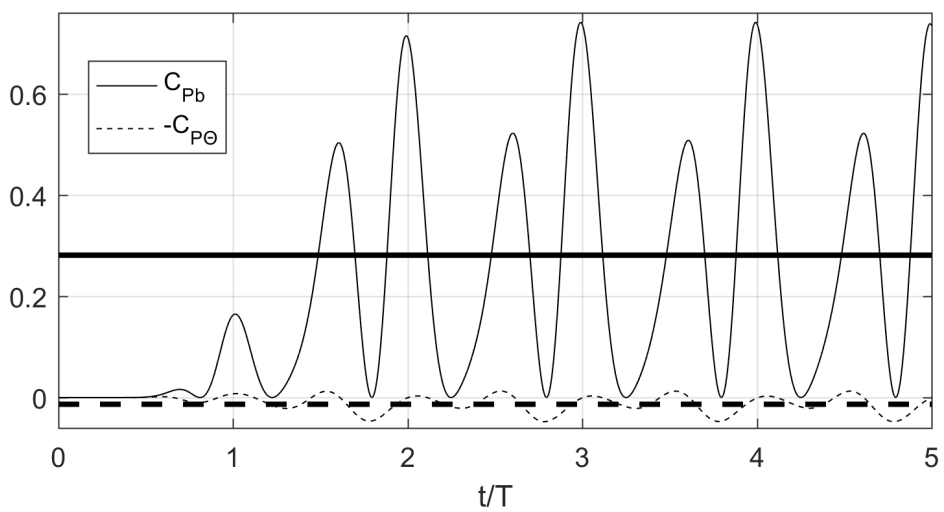
Figure 4.17: (a) Simulation of the system for $\omega_{\ominus}/\omega = 1$, $k_r = \omega_{\ominus}c/2U = 0.267$ and $\psi = -40^\circ$ during the fifth period. (b,c,d,e) Results at various instances: position of the foil and dipole intensities in the wake are shown in the left subplots, pressure coefficient on the flapping foil in the middle subplots, and calculated free-surface elevation over the shoaling environment in the right subplots.



(a)

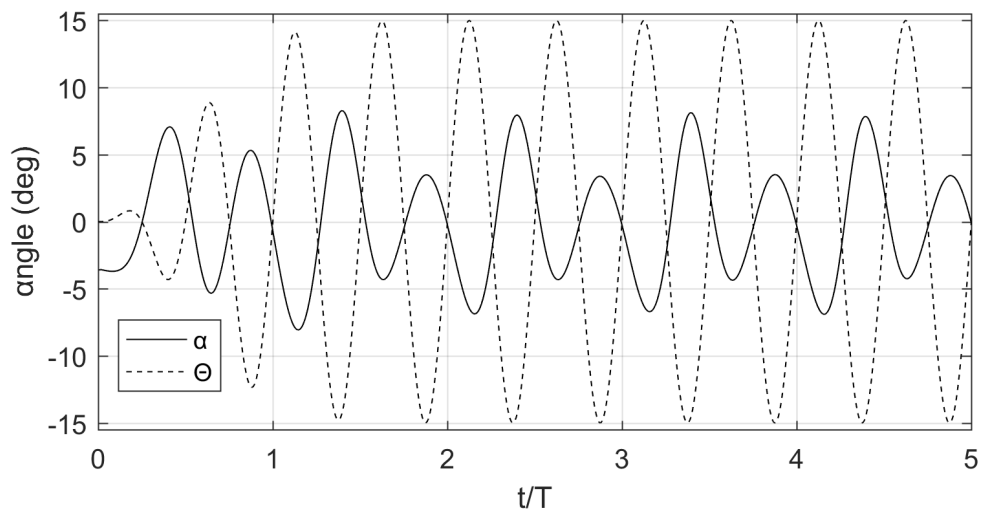


(b)

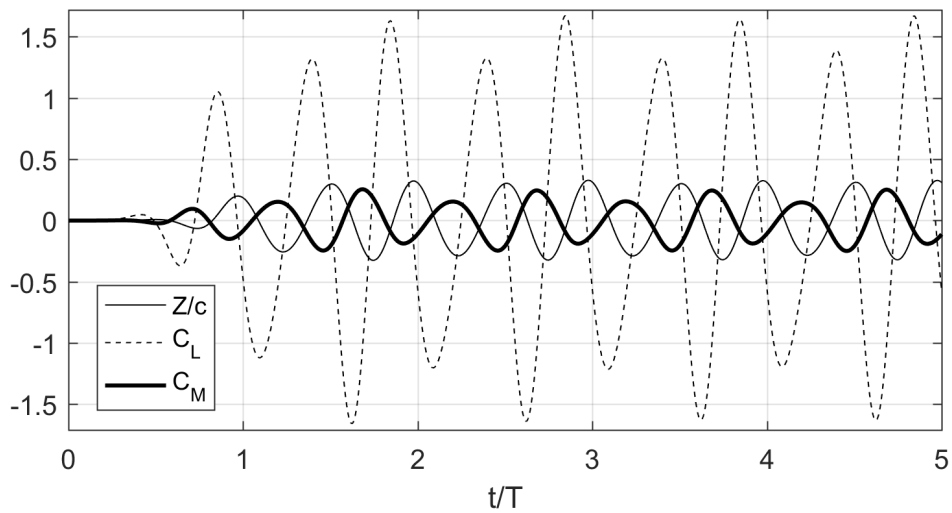


(c)

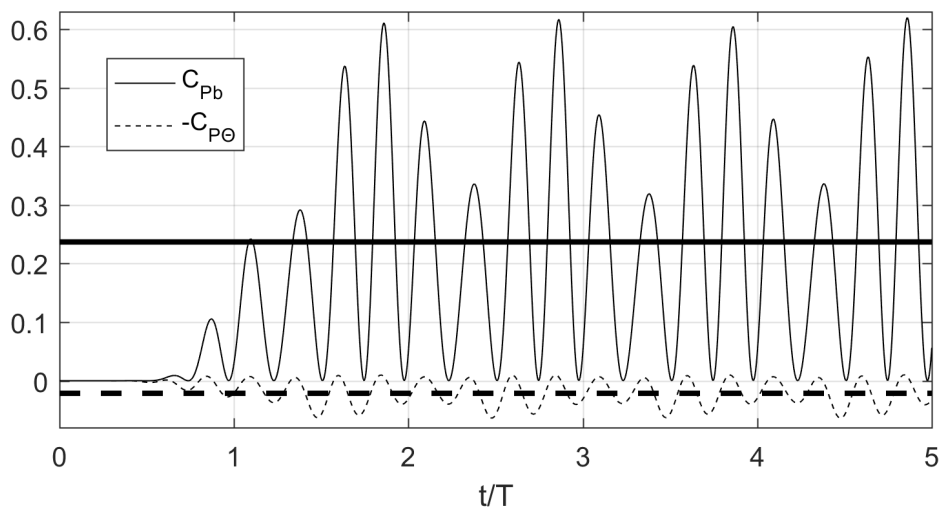
Figure 4.18: Time history of (a) enforced pitching angle and output angle of attack, (b) heaving motion, lift and moment coefficients of the hydrofoil, and (c) calculated input and output power coefficients, in the case of $\omega_{\Theta}/\omega = 1$ and $\psi = -40^\circ$.



(a)



(b)



(c)

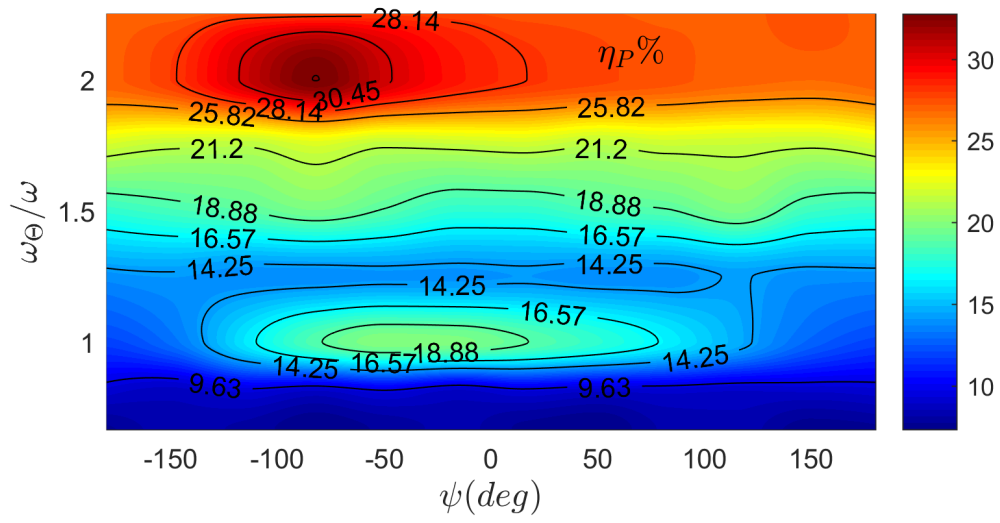
Figure 4.19: Time history of (a) enforced pitching angle and output angle of attack, (b) heaving motion, lift and moment coefficients of the hydrofoil, and (c) calculated input and output power coefficients, in the case of $\omega_{\Theta}/\omega = 2$ and $\psi = -90^\circ$.

4.5.4.2 Investigation of the operational parameters

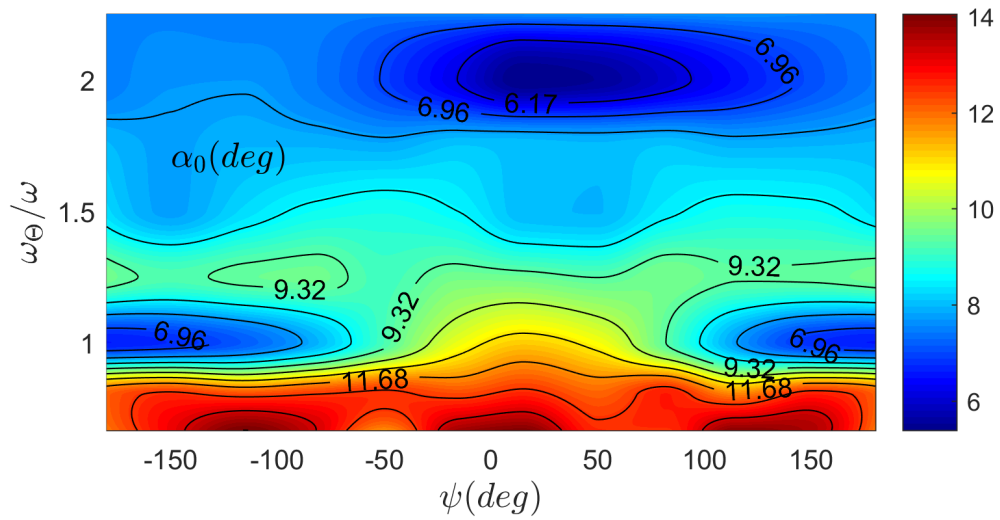
In this section we investigate the effects of the operational parameters of the present wave and hydrokinetic energy converter, using the same environmental parameters (sheared current and wave) as in Sec.4.5.4.1. For a specific value of incident wave frequency ω , the average net power coefficient η_P and the maximum amplitudes of the effective angle of attack α_0 and the heaving motion Z_0 are shown in Fig.4.20 using contour plots. In that figure, the effect of the frequency of pitching oscillation ω_Θ and the phase difference ψ between the free-surface elevation and the foil pitch are examined, for specific pitch amplitude $\theta_0 = 15^\circ$ and oscillator parameters $m^* = 4$, $\zeta = 0.5$, $\omega_0/\omega = 2$. Concerning the net power coefficient, Fig.4.20(a), in the examined range of parameters, it varies from $\eta_P = 7.5\%$ to $\eta_P = 33.3\%$ with greater values at larger frequencies of the foil's pitch, obtaining its maximum value at $\omega_\Theta/\omega = 2$. On the other hand, the angle of attack, Fig.4.20(b), and the heaving amplitude, Fig.4.20(c), follow, in general, the opposite trend. The reduction of heaving amplitude response at large frequencies is common, even in purely linear oscillators, and can be predicted also by linear theory in infinite domain, as shown by Zhu et al. (2009), Fig. 4 (a). The increase in the power extraction coefficient at large frequencies, is also reasonable and have been noticed by Zhu et al. (2009), Fig. 4 (c). This can be explained by the fact that when the pitching frequency raises the system operates in much smaller vertical regions (due to the smaller induced heave amplitude) while the absorbing power increases, and in the same time the pitching power cost is still not large enough; see e.g. Zhu et al. (2009), Fig. 5.

Moreover, in Fig.4.20, we observe that there are two maximum values of the efficiency located at regions where pitching frequency is integer multiple of the wave frequency as expected because the system is excited by two different frequencies. The global maximum of the power extraction coefficient $\eta_P = 33.3\%$, Fig.4.20(a), is obtained at the vicinity of $\omega_\Theta/\omega = 2$ and $\psi = -90^\circ$, where the maximum angle of attack equals $\alpha_0 = 7.5^\circ$ attaining reasonable values, Fig.4.20(b), and the heaving amplitude is rather small $Z_0/c = 0.32$, Fig.4.20(c). Another local peak is noticed for $\omega_\Theta/\omega = 1$ and $\psi = -40^\circ$, however the value of the net power extraction is less $\eta_P = 20\%$, corresponding to larger (still reasonable) angle of attack $\alpha_0 = 9.6^\circ$, and much larger heaving amplitude $Z_0/c = 0.67$. For both the above cases, $\omega_\Theta/\omega = 1, 2$, the phase difference ψ between pitching motion and the waves adjusts the angle of attack α_0 , Eq.(46) of Filippas et al. (2018), and larger power extraction is obtained when ψ maximizes the angle of attack α_0 , Fig.4.20(a, c). In the sequel we will focus on cases corresponding to the region of the global maximum of η_P , where larger amounts of energy can be extracted by the examined system, with reasonable values of the angle of attack.

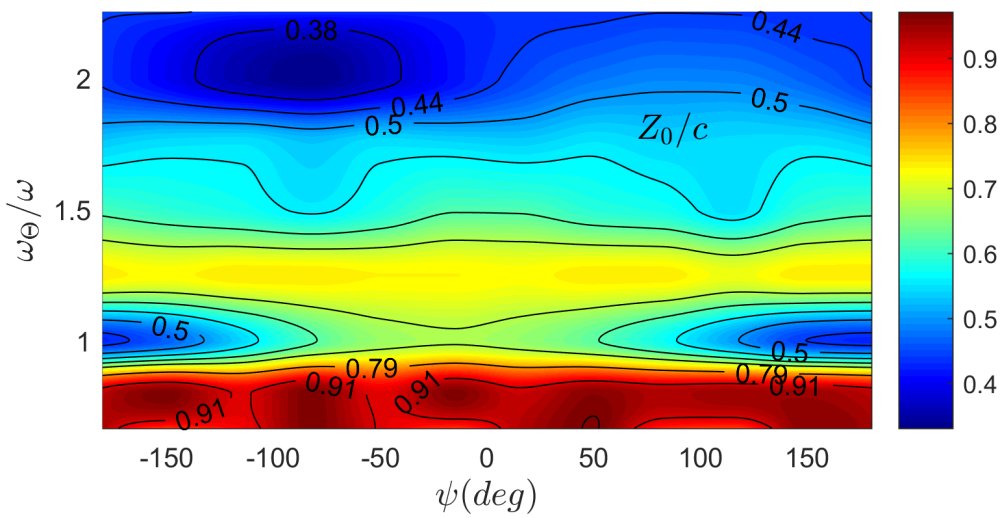
In Fig.4.21 we demonstrate the effect of the amplitude of pitching motion $\omega_\Theta/\omega = 2$ for $\omega_\Theta/\omega = 2$ and the phase difference between foil's pitch and the waves selected in the region where the global maximum appears $\psi \in [-90^\circ, 40^\circ]$. In the region of the parameters studied here, we observe a monotonic increase in η_P , α_0 , Z_0 (see Fig.4.21(a,b,c) respectively) as θ_0 increases, for the whole interval of ψ , with the maximum of the net power extraction reaching the level of $\eta_P = 53.5\%$, for $\theta_0 = 25^\circ$ and ψ around -100° . That monotonic behavior is expected and has been noticed by other researchers, using either linear theory or BEM, in infinite domain, see e.g. Zhu et al. (2009), Fig.6. In this case, the maximum angle of attack attains moderate value $\alpha_0 = 11.4^\circ$ and the heaving amplitude is $Z_0/c = 0.59$, indicating that the biomimetic wave-current energy device would lead to significant power output with proper selection of the control parameters. Although, in a realistic setup a pitching amplitude



(a)

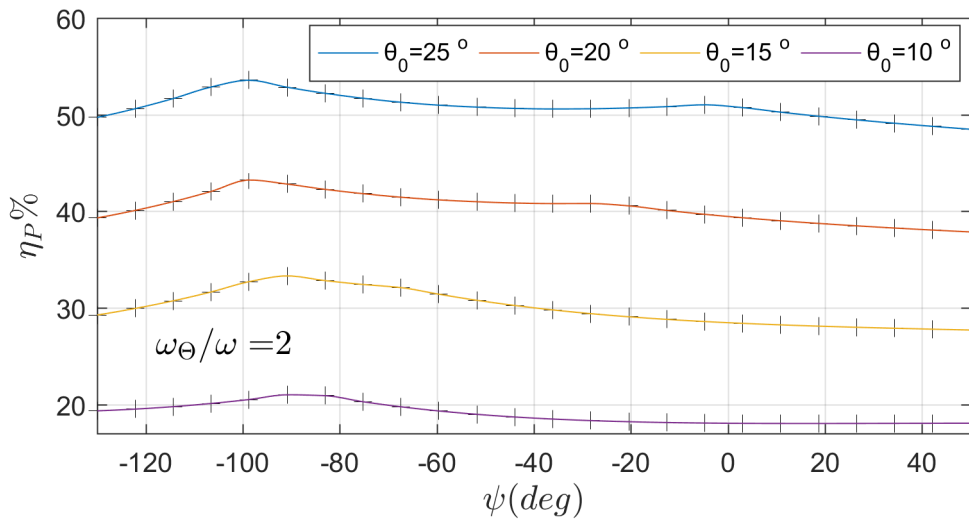


(b)

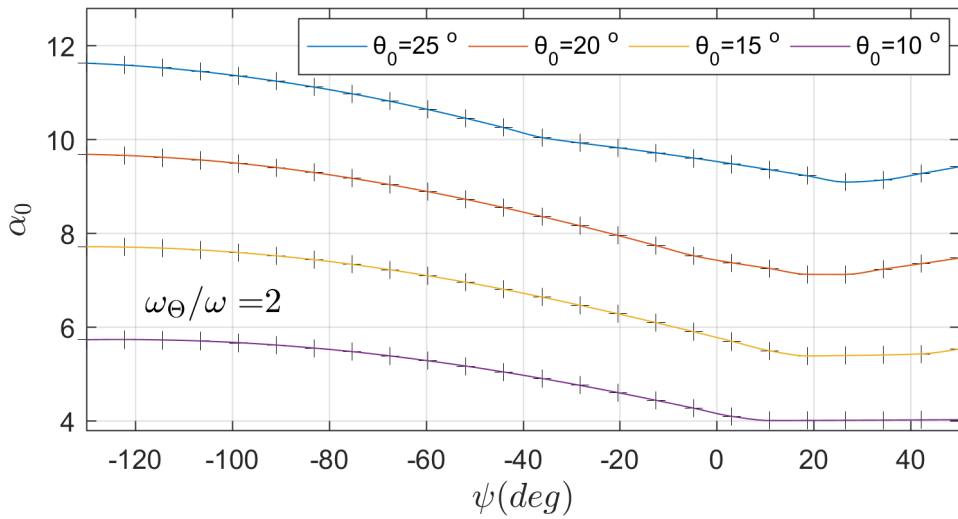


(c)

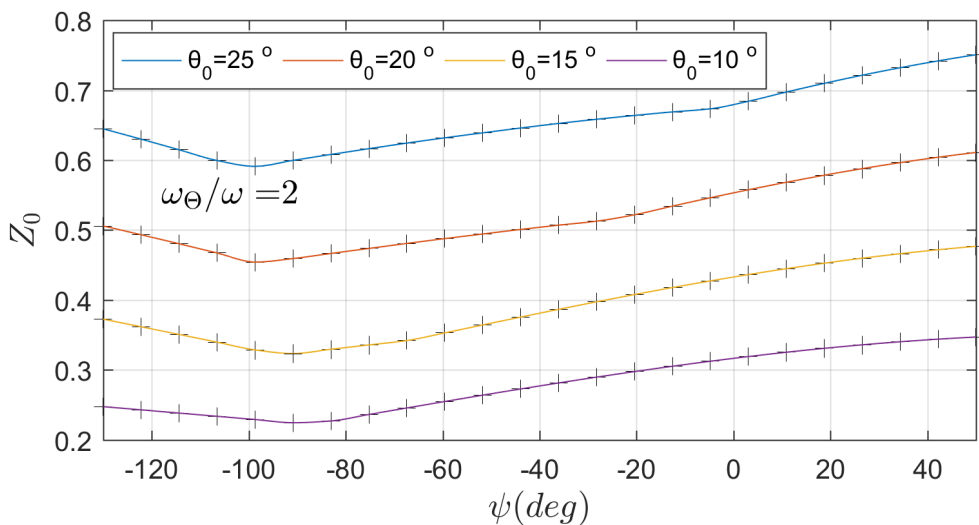
Figure 4.20: Contour plots of a) η_P , b) α_0 and c) Z_0 as functions of pitch frequency ω_Θ and pitch-wave phase difference ψ for specific Strouhal number $St = \omega \sqrt{h_1/g}$, pitch amplitude $\theta_0 = 15^\circ$, oscillator parameters $m^* = 4$, $\zeta = 0.5$, $\omega_0/\omega = 2$ and other parameters as in Fig.4.19.



(a)



(b)



(c)

Figure 4.21: (a) Average net power extraction η_P , (b) maximum amplitudes of the effective angle of attack α_0 , and (c) heaving amplitude Z_0 , as functions of ψ and θ_0 for $\omega_\Theta/\omega = 2$ and other parameters as in Fig.4.19.

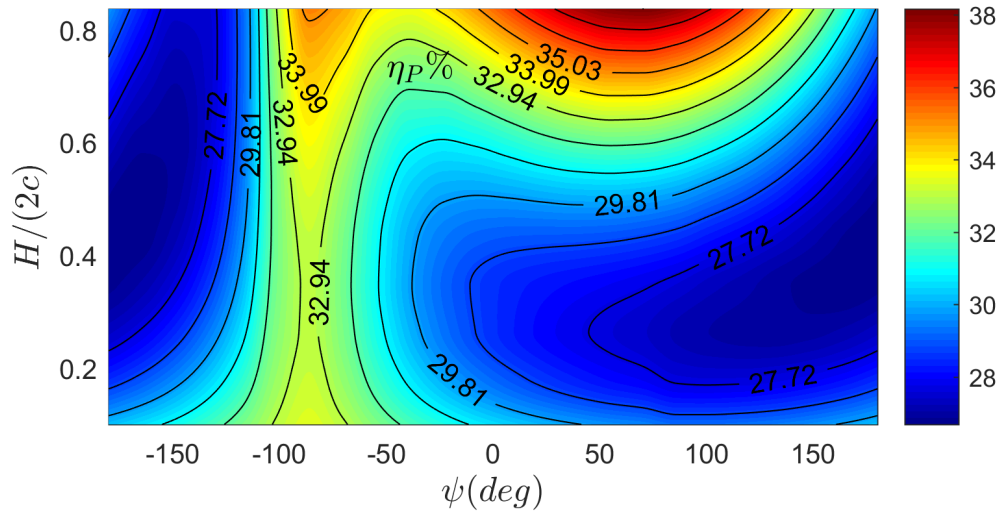
of $\theta_0 \geq 25^\circ$ corresponding to a moderate amplitude of the angle of attack ($\alpha_0 = 11.4^\circ$) seems a reasonable choice, in the present study a more conservative selection is used $\theta_0 \geq 25^\circ = 15^\circ$, resulting in lower maximum angle of attack ($\alpha_0 = 7.5^\circ$) and preventing flow separation and dynamic stall effects.

4.5.4.3 Investigation of the environmental parameters

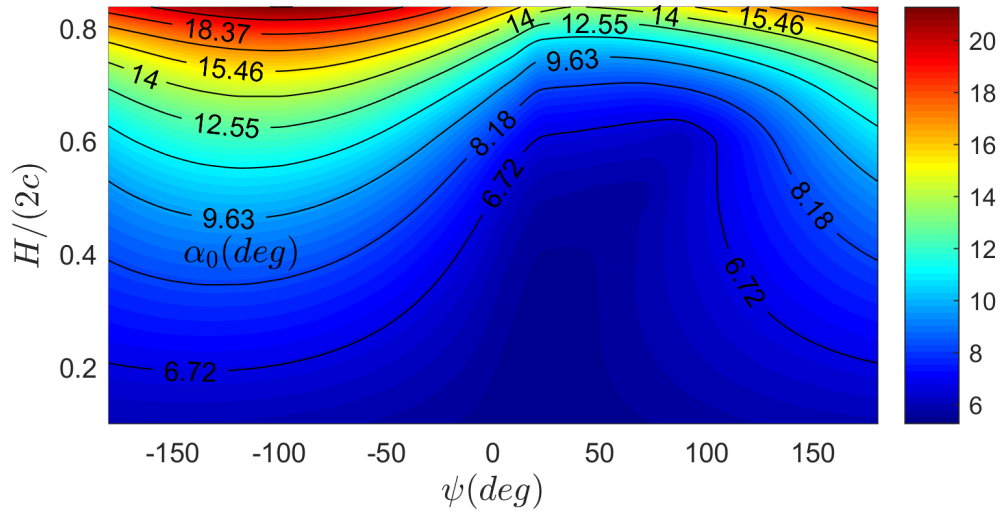
In the final section of the present chapter we examine the effects of the incident wave-current field and the mean vertical position of the foil on the performance of the system in the shoaling environment of Sec. 2.2 in Filippas et al. (2018). As before, the Strouhal number of the incident wave is $St = 0.4$, the foil's pitching motion parameters are $\omega_\Theta/\omega = 2$, $\theta_0 = 15^\circ$, and the sheared current characteristics are $F_d = U/\sqrt{gh_1} = 0.05$, $S_{max} = 0.05s^{-1}$. Also, the oscillator parameters are $m^* = 4$, $\zeta = 0.5$, $\omega_0/\omega = 2$. In Fig.4.22 the effect of the wave amplitude $H/(2c)$ on the operation of the system is shown, for a range of foil-wave phase difference ψ . In Fig.4.22(a) we observe that the net power coefficient varies from $\eta_P = 27\%$ to $\eta_P = 38\%$ with the global maximum at a region where the angle of attack becomes $\alpha_0 = 15^\circ$.

It is noticed that, with proper selection of the phase difference between the waves and foil's pitch, with optimum value around $\psi = -90^\circ$, the power extraction coefficient remains above $\eta_P = 33\%$ for any wave amplitude $H/(2c)$ in the studied interval. In the previous optimum region, smaller angle of attack and heaving response are obtained (see Fig.4.22(b,c) respectively) when wave amplitude decreases, without loss in power extraction efficiency. Concerning the induced heave amplitude Z_0 and the resulting angle of attack α_0 in general they increase along with the wave amplitude and this is reasonable because greater amounts of environmental energy is transformed to heaving motion, resulting also greater angles of attack in an amount that depends on the adjustment of the foil-wave phase difference ψ (see also the relevant discussion in the previous paragraph and the definition of the effective angle of attack in Filippas et al. (2018), Eq.(46)). Searching deeper, the effect of the phase difference ψ , in the region about $\psi = -90^\circ$, pitching excitation leads to a heaving response at a phase difference of 180° with the wave, i.e. foil's vertical velocity is in opposite direction to the corresponding wave velocity, resulting to greater angles of attack and smaller heaving amplitudes due the waves. Again in the aforementioned case ($\psi = -90^\circ$) the system operates in a smaller vertical region and with significant power extraction due to the adequate values of the angle of attack and concurrently the pitching power cost is still not large enough, explaining the maximum values of the net power coefficient in that region, see Fig. 4.22(a). A significant benefit of flapping-foil energy devices arises from their ability to operate in relatively small vertical region in comparison with conventional flow turbines. In this way they support the design of multicomponent systems with many horizontal foils in parallel arrangement increasing in this way the performance of such enhanced biomimetic systems; see e.g. Rozhdestvensky and Ryzhov (2003), Fig. 2 and Wu et al. (2015).

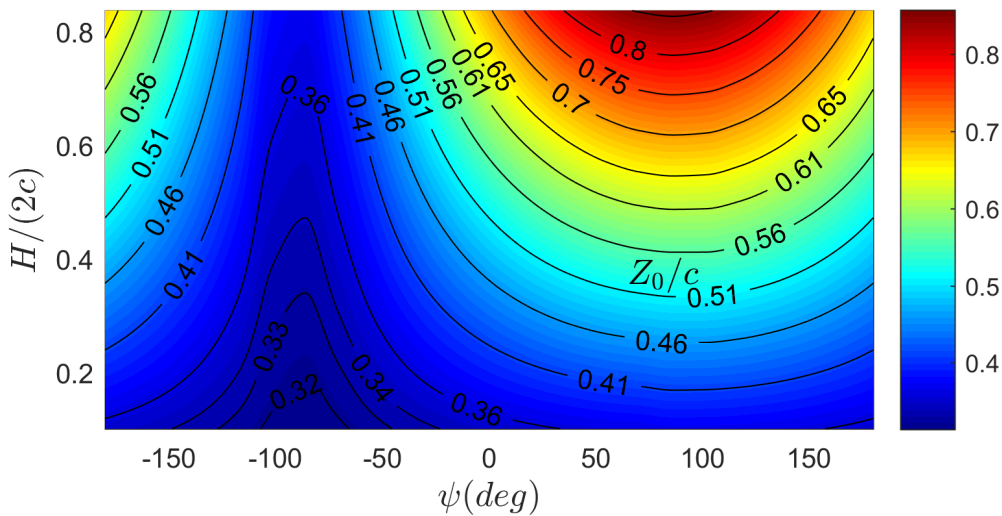
Next, in Fig.4.23 for the same set-up and $\psi = -90^\circ$, the effect of incident wave frequency ω and pitching frequency ω_Θ are examined. It is illustrated that for waves with frequencies less than $\omega/\omega_0 = 0.95$ the local maxima of the net power extraction are located around $\omega_\Theta/\omega = 2$ (indicated by the dashed line in Fig.4.23(a)). For comparison, the cases studied so far correspond to $\omega/\omega_0 = 0.5$ and $\omega_\Theta/\omega_0 = 1$.



(a)

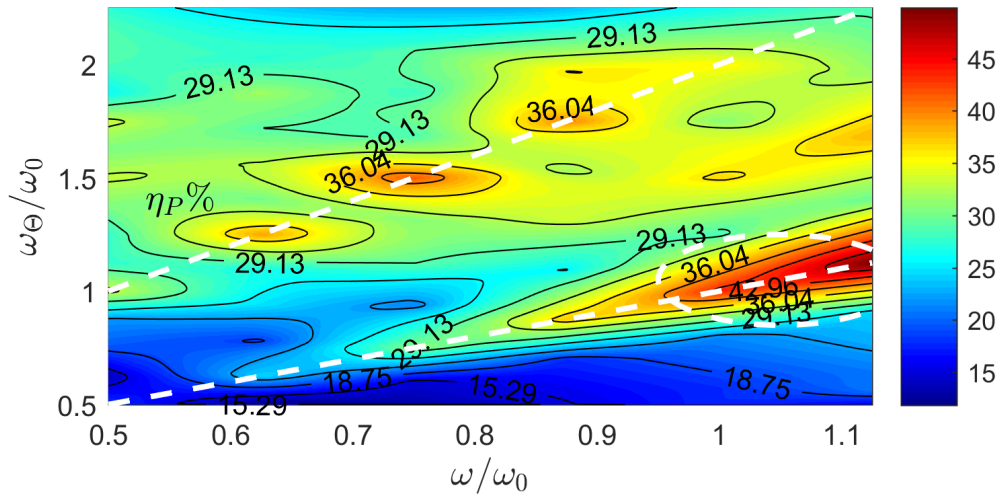


(b)

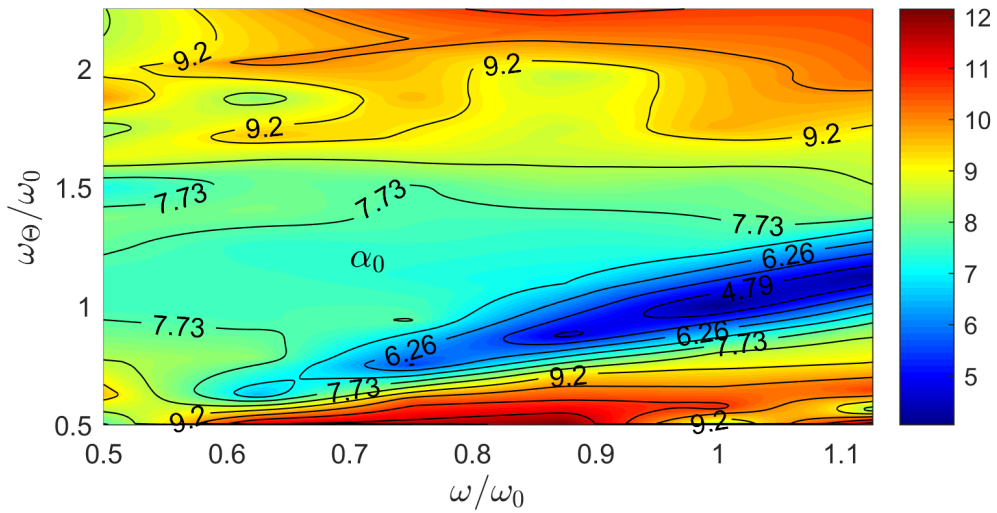


(c)

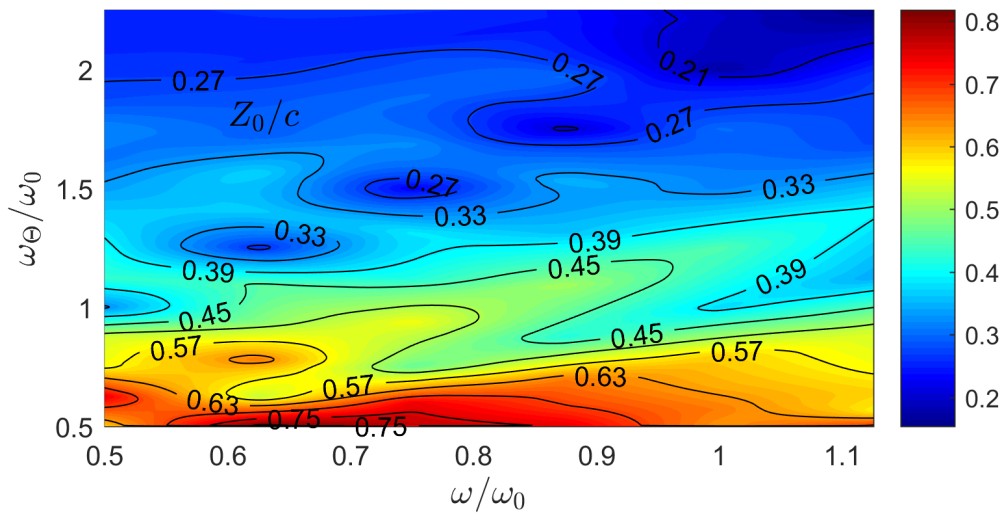
Figure 4.22: Contours of (a) η_p , (b) α_0 and (c) Z_0 for varying wave height H and foil-wave phase difference ψ for $\omega_\Theta/\omega = 2$ and other parameters as in Fig.4.19.



(a)



(b)



(c)

Figure 4.23: Contours of (a) η_P , (b) α_0 and (c) Z_0 for varying wave frequency ω and pitching frequency ω_Θ and other parameters as in Fig.4.19.

An interesting result is that there exists a region for $\omega/\omega_0 > 0.95$ close to $\omega_\Theta/\omega_0 = 1$ (shown by a dashed circle in Fig.4.23(a)) where high levels of power extraction $\eta_P > 40\%$ are achieved with very small angles of attack $\alpha_0 < 6.5^\circ$ and moderate heaving amplitude $Z_0/c < 0.45$ (see Fig.4.23(b,c) respectively). The peaks in the responses (heaving response Z_0 , resulting angle of attack α_0 , power extraction coefficient η_P) appearing at $\omega_\Theta/\omega = 1$ and $\omega_\Theta/\omega = 2$ can be physically interpreted using the basic principles of the theory of dynamic systems and linear hydrofoil theory. First of all, the lift actuating the heaving oscillator (right hand side of Eq. (46) in Filippas et al. (2018),) can be decomposed in the context of linear theory into (i) terms that oscillate with pitching frequency ω_Θ ; see e.g. Zhu et al. (2009), Eq. (5)), and (ii) other terms oscillating with the wave frequency ω . Therefore, the present system response peaks are expected for pitching frequency near an integer multiple of the wave frequency, which is reasonable for dynamical systems under bichromatic excitation. Moreover, the oscillatory behavior of the responses in the vicinity of $\omega_\Theta/\omega = l, l \in \mathbb{N}$, (as e.g. for the case of $\omega_\Theta/\omega = 2$ which is also clearly illustrated in Fig.4.24) is justified by the appearance of parametric resonance. In fact, analyzing again the developed lift force on the foil, by means of linear hydrofoil theory (see e.g. Zhu et al. (2009), Eq. (5)), terms proportional to heaving acceleration are observed, oscillating with pitching frequency ω_Θ , which are clearly added mass terms. The rest excitation forces contain the lift induced by the waves, which is therefore at frequency ω . Thus, the added mass of the system (and consequently, its natural frequency) oscillates at ω_Θ which is responsible for the manifestation of parametric resonance phenomena; see, e.g. Fossen and Nijmeijer (2011). A more detailed investigation of the above linear and non-linear aspects concerning the dynamic behavior of the present system will be subject of future work.

Finally, in Fig.4.24 the effects of shear on η_P , α_0 and Z_0 are presented, for three values of the hydrofoil mean submergence depth d . We observe in Fig.4.24(a,c), that the performance η_P and the amplitude of heaving motion Z_0 present a linear increase with maximum shear coefficient S_{max} , due to the increase of the local current velocity near the foil with S_{max} . As noted in Fig.4.24(a), for $d/c = 2$ when S_{max} increases from $0.05s^{-1}$ to $0.1s^{-1}$ the Froude number near the foil F_{foil} takes values from 0.12 to 0.134. With the present selection of the parameters, and especially the phase difference ψ , incident waves have positive effect on total power extraction. However, as also demonstrated in Fig.4.24, as the foil submergence depth increases, the power output of the present system decreases, due to the decay in depth of water waves.

To summarize, in the present feasibility study it is demonstrated that using biomimetic systems in the examined arrangement significant energy can be extracted from sea currents and the efficiency of the device can be further enhanced by exploiting wave energy. In particular, for moderate values of the wave-frequency parameter $St = 0.4$, significant efficiency can be achieved for both equal wave and pitching frequencies $\omega_\Theta/\omega = 1$ and in the case where the two input frequencies are different $\omega_\Theta/\omega \neq 1$, depending on the environmental conditions. An evidence is given that the local maxima of the efficiency are obtained when pitching frequency is an integer multiple of the wave frequency. Also, optimal values of the phase difference between pitching motion and waves, for the studied setup with $\omega_\Theta/\omega = 1, 2$ are identified near $\psi = -40^\circ, -90^\circ$, respectively. Moreover, in the region of the studied parameters, an increase in pitching amplitude θ_0 results in monotonic increase of efficiency, and the net power extraction may reach the level of $\eta_P = 53.5\%$, for $\theta_0 = 25^\circ$ and ψ around -100° . Even for smaller pitching amplitude $\theta_0 = 15^\circ$, preventing large angles of attack and avoiding flow separation and dynamic stall effects, it is demonstrated that the performance remains good of the order 35%. Furthermore, examining the effect of the wave amplitude together with the

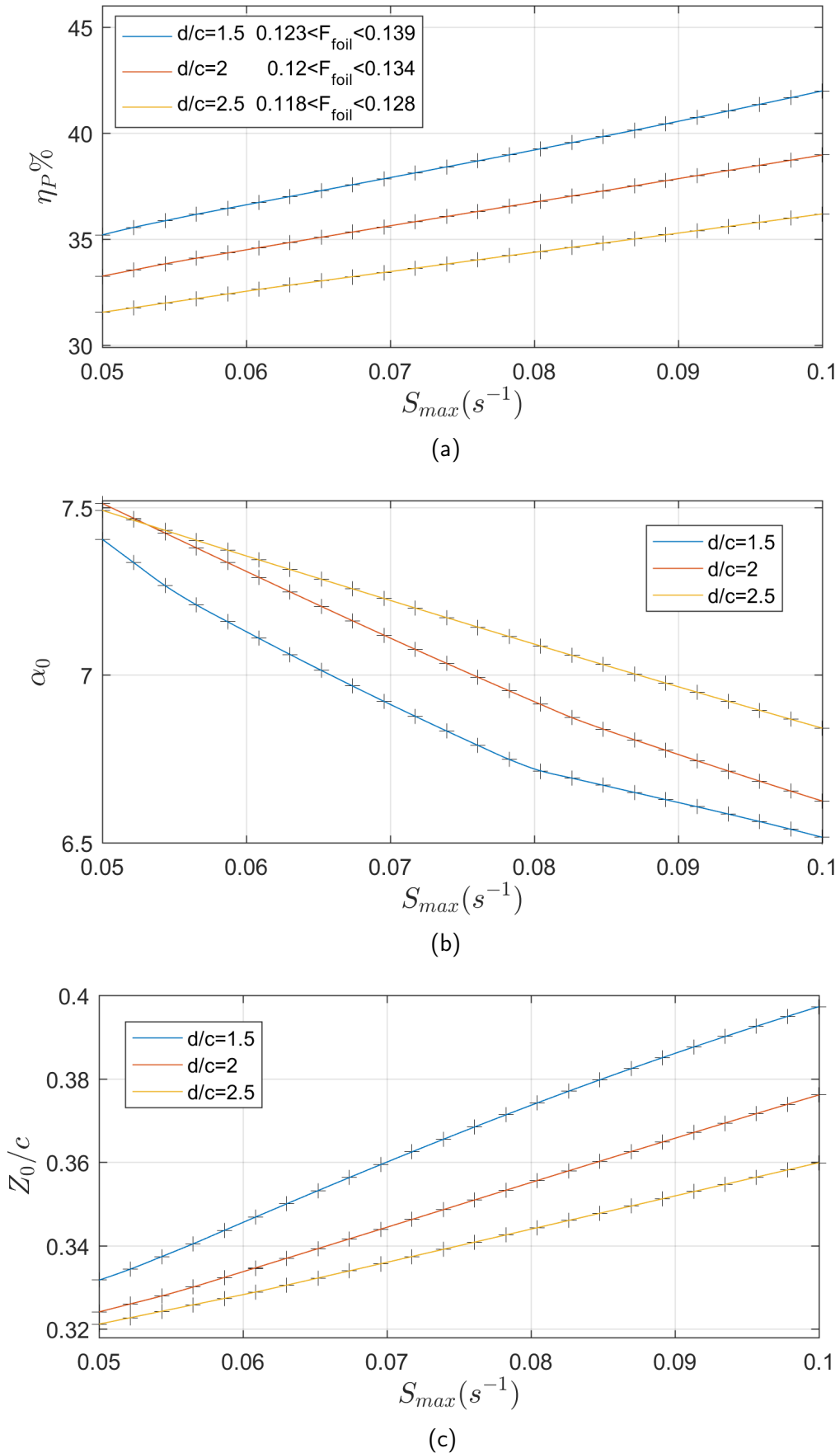


Figure 4.24: Effects of shear S_{max} and foil's mean submergence d on (a) η_P , (b) α_0 and (c) Z_0 for $St = 0.4$, $\omega_\Theta/\omega = 2$ and $\psi = -90^\circ$ and $\theta_0 = 15^\circ$ with other parameters as in Fig.4.19.

wave-foil phase difference, it is observed that with proper selection of ψ (e.g., $\psi = -100^\circ$, for $\omega_\Theta/\omega = 2$) the power extraction coefficient remains significant $\eta_P \approx 33\%$ for any wave amplitude, providing robust operation of the system. For higher values of the wave frequency $0.4 \leq St \leq 0.9$, a very important observation is that a region exists close to $\omega_\Theta/\omega = 1$ where high level of power extraction $\eta_P = 40\%$ is achieved with very small angles of attack $\alpha_0 < 6.5^\circ$ and moderate heaving amplitude $Z_0/c < 0.45$. The identification of such regions of optimum operation is important for the design of the studied biomimetic energy device.

4.6 Remarks and conclusions

In the last part of the present thesis the fully nonlinear time domain method for the general unsteady problem of flow around lifting bodies of general shape beneath the free surface is extended to treat problem in the presence of nonlinear oblique waves. Although, the problem of the system could be treated by the method presented in Chapter 3 using a classical numerical wave tank, a more efficient approach is selected for the following reasons. In the context of the present approach, the body operates in the fully developed wave-field from the beginning of the simulation and no time is necessary to pass for the wave to reach from the wavemaker to the region of operation of the system. Moreover, with the present approach an initial guess of the whole wavefield in space-time domain is exploited to accelerate the convergence of the iterative procedure that is used at a specific timestep to solve the fully nonlinear problem. By using the initial guess only the evolution of the corrector fields is necessary to be calculated by the time-integration of the dynamical system by exploiting the known initial guess and the total fields known from previous timesteps. The initial guess could be a simple, e.g. a Stokes wave in the absence of a body, or the solution of the problem including the body but with linearised free-surface boundary conditions. For these reasons, the present method and the GPU code could serve for efficient the assessment, preliminary design, optimisation and control of the studied systems.

The method is applied to the hydrodynamic analysis of foils in waves. Results are obtained, illustrating the superior numerical performance of the developed method and the GPU code and the accuracy of the method is tested through comparisons with other methods and experimental data. Numerical predictions for the thrust coefficient of the flapping hydrofoil operating beneath the free surface and in waves indicate that the present system, after experimental verification, could be exploited for efficient wave-devouring thrust production.

Moreover, the problem of augmentation of the ship's main propulsion in waves is studied and results are presented in Sec.4.5.3. The present method is applied to the hydrodynamic analysis of flapping hydrofoils operating beneath the free surface, in the presence of irregular incident waves, taking into account the coupling between the hull motion and the flapping foil dynamics. We consider operation of the hydrofoil in head waves characterized by a given frequency spectrum, corresponding to specific sea states. The transfer function from sea wave spectra to energy spectra of vertical foil motion is based on the Response Amplitude Operator of the coupled system at the exact longitudinal location of the flapping wing. Numerical results concerning the thrust coefficient are presented, indicating that significant thrust can be produced and that the free surface effects are important concerning the overall performance of the system. Thus, the present method can serve as a useful tool for the preliminary design, assessment

and optimum control of such biomimetic systems extracting energy from sea waves and augmenting marine propulsion.

Furthermore, the performance of biomimetic energy systems in the presence of waves and currents are studied for the exploitation of combined renewable marine energy sources in nearshore and coastal regions in Sec.4.5.4. The present method takes into account the effect of the wavy free surface and the variable bathymetry through the satisfaction of the corresponding boundary conditions, as well as the velocity component due to waves and sheared currents with linear vertical profile on the formation of the incident flow. An example of the system operating over a variable bathymetry region of the form of smooth shoal is considered and a wide range of parameters is studied including the velocity of the current and the shear, the frequency and the amplitude of the incident waves, the mean submergence of the foil, the pitching amplitude, phase difference with respect to the waves and corresponding frequency that can be different from wave frequency. Numerical results concerning the extracted power and the operability characteristics of the system are presented, indicating that significant output can be obtained and the improvement due to wave energy extraction is significant. The present method could be found useful for the design and control of such biomimetic systems operating in the nearshore/coastal region and extracting energy from waves and ambient sheared currents.

Future extensions include the systematic investigation of and optimisation of the foil geometry and motion and the study of multicomponent foil devices. Furthermore, full treatment of 3D effects is important for studying various additional parameters including the effects of directional seas and the interaction with the hull and other appendages. Another important direction for future work is the investigation of elasticity effects on foils performance in waves. Concerning the energy extraction from waves and currents, future work includes the examination of non-harmonic pitching motion and irregular waves. Very important for that system is also the investigation of the performance of enhanced biomimetic energy systems such as multicomponent flapping-foil arrangements and large arrays of devices in specific locations. Direct extension of the method could be a fully Lagrangian approach for the tracking of the surface in nearly breaking conditions. Breaking of waves and cavitation and detailed analysis of viscous effects could be treated by means of higher-fidelity CFD tools and efficient viscous-inviscid interaction approaches. Another direction deals with the implementation of high-order BEMs using B-Splines or NURBS for the representation of the geometry and the unknown distributions of singularities on the boundary, accelerating the convergence and leading to increased numerical efficiency. The above problems increase significantly the computational requirements and in some cases more resources than a single GPU may be required. That difficulty can be cost-efficiently tackled using shared memory multi-GPU systems or even large multi-GPU clusters on HPC platforms using MPI for inter GPU communication. Finally, a very interesting direction for future research includes the experimental demonstration and investigation of the present systems at model scale.

Conclusions and suggestions for future research

The main objective of this thesis is the development of a method and a high performance computational code to treat the fully nonlinear problem of lifting flows around bodies beneath the free surface in oblique waves and the exploitation of the method for the hydrodynamic analysis of ship and marine biomimetic systems in waves.

The motion and the geometry of the body are general, thus no linearisation has been applied. For simplicity in the description, in the present work the body motion is assumed to be prescribed, however the method has been extended to solve problems that include free motions of finite degrees of freedom (Filippas et al. 2018; Koutsogiannakis 2019). Also, research on elastic foils of infinite degrees of freedom is already in progress; see e.g. Priovolos et al. (2018) and Anevlavi (2019). The dynamics of the wake are also not linearised and the evolution of the wake is obtained in the context of a time-stepping method. Concerning the free-surface boundary conditions, no smallness assumptions are made and the present approach is a non-perturbative one. In specific cases, the additional effects of shear currents and general bathymetry are included in the modeling.

The coupling between the free-surface and the lifting body-wake dynamics is implemented in a strong explicit manner. The formulation of the problem is based on the potential theory while the boundary integral equations and the kinematics of the problem are exploited to set up a linear boundary integral constraint. Additionally, the dynamics of the free-surface and the pressure-type Kutta condition are used to set up the dynamical-system equations. The reformulation of the initial boundary value problem (IBVP) to a boundary integral formulation is performed and the extended Dirichlet-to-Neumann (DtN) operator is obtained in the form of a weakly singular boundary integral equation (BIE). The spatially discretised form of the dynamic system and the extended DtN is obtained by means of BEM, collocation, curvilinear finite difference method (CUFDM), deducing in this way a system of 1^{st} -order (spatially and temporarily) nonlocal differential equations, with explicit and implicit nonlinearities and linear algebraic constraints. A time-stepping method is then implemented, based on the time integration of the nonlinear constrained system of evolution equations. High-order multistep time-integration schemes, that belong to the family of Runge Kutta methods for 1^{st} -order systems, are exploited for the solution. Explicit high-order methods, with extended stability manifold, are used in general, while implicit schemes, that are theoretically A-stable, are selected when the system is stiff, implemented via a Newton-Raphson general iterative scheme, with the Jacobian calculated numerically with 2^{nd} -order central finite differences (Filippas et al. 2018; Priovolos et al. 2018). It is worthwhile to mention that the present formulation and the analysis that have been performed enabled the selection and storage of data in relatively small data structures that is important for efficient memory management in the programming.

For the numerical solution of the fully nonlinear, 3D and unsteady problem a computational code is developed, exploiting parallel programming techniques and general purpose programming on graphics processing units, using the CUDA C/C++ API. The combination of the aforementioned formulation (see also Sec.2.4) and the GPGPU programming supported the development of the efficient (in terms of both time and space complexity) high performance computational code.

Concerning the special treatment of flow around lifting bodies in waves presented in Chapter 4, although the problem of the system could be treated as discussed in Chapter 3 by means of a classical numerical wave tank, a more efficient approach is selected, as demonstrated by the calculations and the discussion in the concluding section of Chapter 4.

The importance of free-surface and 3D effects, nonlinearity as well as the superior performance of the developed GPU code in the case of 3D foils in oblique waves, are illustrated. The problem of augmentation of the ship's main propulsion in waves is studied. The present work can be exploited for the design and optimum control of biomimetic systems extracting energy from sea waves for augmenting marine propulsion in rough seas, with simultaneous reduction of ship responses offering also dynamic stabilization. Moreover, a semi-activated biomimetic energy device, with imposed pitching motion and induced heaving motion in harmonic incident waves and flow is proposed and a feasibility study is conducted. The present method can be applied to the design and optimum control of such biomimetic systems operating in the nearshore/coastal region and extracting energy from waves in the presence of ambient currents.

As already mentioned in the main part of this manuscript, our formulation opens several directions of research both in the enhancement of the method and in the application of marine biomimetic devices, some of which are already in progress. We shall summarize below some important points that deserve future attention.

The treatment of leading edge separation and dynamic stall effects would extend method's applicability to operation conditions corresponding to large angles of attack. Also, friction resistance could be taken into account using boundary layer theory (Papadakis, 2014; Riziotis and Voutsinas, 2007) and experimental and empirical coefficients. Direct extension of the method could be a fully Lagrangian approach for the tracking of the surface in nearly breaking conditions. Breaking of waves and cavitation and detailed analysis of viscous effects could be treated by means of higher-fidelity CFD tools and efficient viscous-inviscid interaction approaches.

All the above extensions would provide in the future even better comparison with experimental measurements, and support the derivation of systematic results for the detailed investigation of various arrangements of flapping hydrofoil systems operating in stationary fluid or in nonuniform background fields. Moreover, the experimental and numerical study of the self-propulsion problem of a ship with biomimetic flapping foil propulsors is of the utmost importance. That could be achieved using a viscous CFD method for the estimation of the wake where the foil operates. Then the wake could be approximated by a weakly rotational background field and the performance of the foil would be examined using the present method developing an iterative CFD-BEM coupling method. Another quite efficient and more accurate approach for the modeling of the biomimetic propulsor would require the combination of the present unsteady three-dimensional nonlinear BEM, a boundary layer solver and self-propelled equations of motion; see e.g. Moored (2018), where the problem of a self-propelled foil in uniform flow is studied. In that work the importance of high amplitude motions in

the propulsive efficiency of the system is underlined, rendering our fully nonlinear method appropriate for the study the problem of self-propulsion of marine vehicles.

Furthermore, future extensions include the systematic investigation and optimisation of the foil geometry and motion and the study of multicomponent foil devices. Furthermore, full treatment of 3D effects is important for studying various additional parameters including the effects of directional seas and the interaction with the hull and other appendages.

Also the effects of chordwise and spanwise elasticity could improve the performance of the studied biomimetic systems, as have been demonstrated in our work (Priovolos et al. 2018) and in the diploma thesis of Anevlavi (2019) and in references cited there.

Concerning the energy extraction from waves and currents, future work includes the examination of non-harmonic pitching motion and irregular waves. Very important is also the investigation of the performance of enhanced biomimetic energy systems, such as multicomponent flapping-foil arrangements and large arrays of devices in specific locations.

Moreover, biomimetic systems extracting wave energy operate in stochastic and nonuniform environment, therefore proper control of their motion is required. In the case of a wave-foil attached to ship hull a simple proportional control law is used and in the case of energy extraction from wave and currents a prescribed harmonic motion of the control pitching signal is examined. An important direction for future work would be the development of more sophisticated setups with feedback control, employing techniques of adaptive and nonlinear or even optimal control.

Another direction could be the implementation of high-order BEMs using B-Splines or NURBS for the representation of the geometry and the unknown distributions of singularities on the boundary, accelerating the convergence and leading to increased numerical efficiency; see e.g. Ning and Teng (2007), Ginnis et al. (2014), Abbasnia et al. (2017).

Furthermore, the problem of flapping foil in fully non-linear water waves can be treated in the context of the method described in Sec.4. Part of the lateral boundary could model a 3D wavemaker.

The above problems significantly increase the computational requirements and in some cases more resources than a single GPU may be required. That difficulty can be cost-efficiently tackled using shared memory multi-GPU systems or even large multi-GPU clusters on HPC platforms employing MPI for inter GPU communication.

Finally, a very interesting direction for future research includes the experimental demonstration and investigation of the present systems at model scale.

References

- Abbasnia, Arash, Mahmoud Ghiasi, and Amir Hossein Abbasnia (2017). "Irregular wave transmission on bottom bumps using fully nonlinear NURBS numerical wave tank". In: *Engineering Analysis with Boundary Elements* 82, pp. 130–140.
- Achieved Occupancy*. URL: <https://docs.nvidia.com/gameworks/content/developertools/desktop/analysis/report/cudaexperiments/kernellevel/achievedoccupancy.htm>.
- Anderson, JM, K Streitlien, DS Barrett, and MS Triantafyllou (1998). "Oscillating foils of high propulsive efficiency". In: *Journal of Fluid Mechanics* 360, pp. 41–72.
- Anevlavi, D. (2019). "Hydroelastic analysis of flapping foils by a coupled BEM-FEM with application to marine energy extraction devices". In: *Diploma Thesis NTUA*.
- Ausman, John Stanley (1954). "Pressure limitation on the upper surface of a hydrofoil". In: *Ph. D. Thesis in Mechanics Engineering at the University of California*.
- Bal, Sakir (1998). "A potential based panel method for 2-D hydrofoils". In: *Ocean Engineering* 26.4, pp. 343–361.
- Batchelor, George Keith (2000). *An introduction to fluid dynamics*. Cambridge university press.
- Batchelor, GK (1964). "Axial flow in trailing line vortices". In: *Journal of Fluid Mechanics* 20.4, pp. 645–658.
- Batista, Milan (2016). "An alternative proof of the Politis lemma". In: DOI: 10.13140/RG.2.2.19912.83201.
- Battjes, Jurjen A (2006). "Developments in coastal engineering research". In: *Coastal Engineering* 53.2-3, pp. 121–132.
- Belibasakis, KA and GK Politis (1995). "A boundary integral equation formulation of the Neumann problem for a vector field in R^3 with application to potential lifting flows". In: *Engineering analysis with Boundary elements* 16.1, pp. 5–17.
- (1998). "A nonlinear velocity based boundary element method for the analysis of marine propellers in unsteady flow". In:
- Belibassakis, K (2009). "Effects of wave-induced ship motion on propeller operation with application to fouling estimation and propulsion optimization". In: *13th Congress Int. Maritime Assoc. Mediterranean*.
- Belibassakis, KA and GA Athanassoulis (2011). "A coupled-mode system with application to nonlinear water waves propagating in finite water depth and in variable bathymetry regions". In: *Coastal Engineering* 58.4, pp. 337–350.
- Belibassakis, KA and ES Filippas (2015). "Ship propulsion in waves by actively controlled flapping foils". In: *Applied Ocean Research* 52, pp. 1–11.
- Belibassakis, KA, GA Athanassoulis, and Th P Gerostathis (2001). "A coupled-mode model for the refraction–diffraction of linear waves over steep three-dimensional bathymetry". In: *Applied Ocean Research* 23.6, pp. 319–336.
- Belibassakis, KA, Th P Gerostathis, and GA Athanassoulis (2011). "A coupled-mode model for water wave scattering by horizontal, non-homogeneous current in general bottom topography". In: *Applied Ocean Research* 33.4, pp. 384–397.

- Belibassakis, KA et al. (2013a). "A BEM-isogeometric method for the ship wave-resistance problem". In: *Ocean Engineering* 60, pp. 53–67.
- Belibassakis, KA, Th P Gerostathis, and GK Politis (2013b). "Calculation of ship hydrodynamic propulsion in rough seas by non-linear BEM with application to reduction of energy losses in waves". In: *ASME 2013 32nd International Conference on Ocean, Offshore and Arctic Engineering*. Vol. 5. American Society of Mechanical Engineers, pp. 9–14.
- Belibassakis, KA, GA Athanassoulis, and Th P Gerostathis (2014). "Directional wave spectrum transformation in the presence of strong depth and current inhomogeneities by means of coupled-mode model". In: *Ocean Engineering* 87, pp. 84–96.
- Belibassakis, KA, B Simon, J Touboul, and V Rey (2017). "A coupled-mode model for water wave scattering by vertically sheared currents in variable bathymetry regions". In: *Wave Motion* 74, pp. 73–92.
- Belibassakis, Kostas, Julien Touboul, Elodie Laffitte, and Vincent Rey (2019). "A Mild-Slope System for Bragg Scattering of Water Waves by Sinusoidal Bathymetry in the Presence of Vertically Sheared Currents". In: *Journal of Marine Science and Engineering* 7.1, p. 9.
- Belibassakis, Kostas A and Gerasimos K Politis (2013). "Hydrodynamic performance of flapping wings for augmenting ship propulsion in waves". In: *Ocean Engineering* 72, pp. 227–240.
- Berenger, Jean-Pierre (1994). "A perfectly matched layer for the absorption of electromagnetic waves". In: *Journal of computational physics* 114.2, pp. 185–200.
- Berg, A (1985). "Trials with passive foil propulsion on M/S Kystfangst". In: *Trondheim. Techn. Rep. Project 672.138*.
- Biot, Jean-Baptiste and Felix Savart (1820). "Note sur le magnetisme de la pile de Volta". In: *Ann. Chem. Phys* 15, p. 222.
- Bishop, Richard L and Samuel I Goldberg (2012). *Tensor analysis on manifolds*. Courier Corporation.
- Blevins, Robert D (1984). "Applied fluid dynamics handbook". In: *New York, Van Nostrand Reinhold Co., 1984, 568 p*.
- Bøckmann, Eirik (2015). "Wave Propulsion of Ships". In: *PhD NTNU*.
- Bøckmann, Eirik and Sverre Steen (2016). "Model test and simulation of a ship with wavefoils". In: *Applied Ocean Research* 57, pp. 8–18.
- Bøckmann, Eirik, Audun Yrke, and Sverre Steen (2018). "Fuel savings for a general cargo ship employing retractable bow foils". In: *Applied Ocean Research* 76, pp. 1–10.
- Booij, NRRC, RC Ris, and Leo H Holthuijsen (1999). "A third-generation wave model for coastal regions: 1. Model description and validation". In: *Journal of geophysical research: Oceans* 104.C4, pp. 7649–7666.
- Borisenko and Tarapov (1979). *Vector and tensor analysis with applications*. Courier Corporation.
- Bose, Neil (1992). "A time-domain panel method for analysis of foils in unsteady motion as oscillating propulsors". In: *Proceedings of the 11th Australian Fluid Mechanics Conference, 1992*. University of Tasmania, pp. 1201–1204.
- Bowker, James A (2018). "Coupled dynamics of a flapping foil wave powered vessel". PhD thesis. University of Southampton.
- Burgers, Johannes Martinus (1948). "A mathematical model illustrating the theory of turbulence". In: *Advances in applied mechanics*. Vol. 1. Elsevier, pp. 171–199.
- Burnett, RF (1979). *Wave energy for propelling craft-nothing new*.

- Cabezas, Javier, Marc Jordà, Isaac Gelado, Nacho Navarro, and Wen-mei Hwu (2015). "GPU-SM: shared memory multi-GPU programming". In: *Proceedings of the 8th Workshop on General Purpose Processing using GPUs*. ACM, pp. 13–24.
- Cavaleri, L et al. (2007). "Wave modelling—the state of the art". In: *Progress in oceanography* 75.4, pp. 603–674.
- Chatjigeorgiou, Ioannis K and Touvia Miloh (2015). "Radiation and oblique diffraction by submerged prolate spheroids in water of finite depth". In: *Journal of Ocean Engineering and Marine Energy* 1.1, pp. 3–18.
- Chen, Zhi-Min (2012). "A vortex based panel method for potential flow simulation around a hydrofoil". In: *Journal of Fluids and Structures* 28, pp. 378–391.
- Collino, Francis and Peter B Monk (1998). "Optimizing the perfectly matched layer". In: *Computer methods in applied mechanics and engineering* 164.1-2, pp. 157–171.
- Colville, RN, EJ Hutchinson, JS Mindell, and RF Warren (2001). "The transport sector as a source of air pollution". In: *Atmospheric environment* 35.9, pp. 1537–1565.
- Cottrell, J Austin, Thomas JR Hughes, and Yuri Bazilevs (2009). *Isogeometric analysis: toward integration of CAD and FEA*. John Wiley & Sons.
- Dabiri, John O (2007). "Renewable fluid dynamic energy derived from aquatic animal locomotion". In: *Bioinspiration & biomimetics* 2.3, p. L1.
- De Silva, Liyanarachchi Waruna Arampath and Hajime Yamaguchi (2012). "Numerical study on active wave devouring propulsion". In: *Journal of marine science and technology* 17.3, pp. 261–275.
- DeLaurier, JD and JM Harris (1982). "Experimental study of oscillating-wing propulsion". In: *Journal of Aircraft* 19.5, pp. 368–373.
- Fenton, John D (1985). "A fifth-order Stokes theory for steady waves". In: *Journal of waterway, port, coastal, and ocean engineering* 111.2, pp. 216–234.
- Filippas, E.S. (2013). "A boundary element method for the hydrodynamic analysis of flapping-foil thrusters operating beneath the free surface and in waves". In: *Diploma Thesis NTUA*.
- Filippas, ES and KA Belibassakis (2014). "Hydrodynamic analysis of flapping-foil thrusters operating beneath the free surface and in waves". In: *Engineering Analysis with Boundary Elements* 41, pp. 47–59.
- Filippas, ES, Th P Gerostathis, and KA Belibassakis (2018). "Semi-activated oscillating hydrofoil as a nearshore biomimetic energy system in waves and currents". In: *Ocean Engineering* 154, pp. 396–415.
- Filippas, Evangelos S (2015). "Augmenting ship propulsion in waves using flapping foils initially designed for roll stabilization". In: *Procedia Computer Science* 66, pp. 103–111.
- Flanders, Harley (1963). *Differential Forms with Applications to the Physical Sciences by Harley Flanders*. Vol. 11. Elsevier.
- Flannery, T (2005). "The Weather Makers: extract in". In: *The Sydney Morning Herald* 24, p. 19.
- Fochesato, Christophe, Stéphan Grilli, and Frédéric Dias (2007). "Numerical modeling of extreme rogue waves generated by directional energy focusing". In: *Wave motion* 44.5, pp. 395–416.
- Fossen, Thor and Henk Nijmeijer (2011). *Parametric resonance in dynamical systems*. Springer Science & Business Media.
- Garrett, Chris and Patrick Cummins (2007). "The efficiency of a turbine in a tidal channel". In: *Journal of fluid mechanics* 588, pp. 243–251.
- Geoghegan, JJ (2008). "Boat, moved only by waves, sails to a seafaring first". In: *The New York Times*.

- Giesing, Joseph P and AMO Smith (1967). "Potential flow about two-dimensional hydrofoils". In: *Journal of Fluid Mechanics* 28.1, pp. 113–129.
- Ginnis, AI et al. (2014). "Isogeometric boundary-element analysis for the wave-resistance problem using T-splines". In: *Computer Methods in Applied Mechanics and Engineering* 279, pp. 425–439.
- Grilli, Stephan T, Philippe Guyenne, and Frédéric Dias (2001). "A fully non-linear model for three-dimensional overturning waves over an arbitrary bottom". In: *International Journal for Numerical Methods in Fluids* 35.7, pp. 829–867.
- Grossmann, Christian, Hans-Görg Roos, and Martin Stynes (2007). *Numerical treatment of partial differential equations*. Vol. 154. Springer.
- Grue, John, Asbjörn Mo, and Enok Palm (1988). "Propulsion of a foil moving in water waves." In: *Journal of fluid mechanics* 186, pp. 393–417.
- Gunter, NM (1967). *Potential theory and its applications to basic problems of mathematical physics*. Ungar New York.
- Gurtin, Morton E, Eliot Fried, and Lallit Anand (2010). *The mechanics and thermodynamics of continua*. Cambridge University Press.
- Hague, CH and C Swan (2009). "A multiple flux boundary element method applied to the description of surface water waves". In: *Journal of Computational Physics* 228.14, pp. 5111–5128.
- Hess, John L (1972). *Calculation of potential flow about arbitrary three-dimensional lifting bodies*. Tech. rep. Douglas Aircraft Co Long Beach CA.
- Hocking, LM (1964). "The instability of a non-uniform vortex sheet". In: *Journal of Fluid Mechanics* 18.2, pp. 177–186.
- (1965). "Note on the instability of a non-uniform vortex sheet". In: *Journal of Fluid Mechanics* 21.2, pp. 333–336.
- Horton, Ivor (2007). *Beginning C: From Novice to Professional*. Apress.
- (2014). *Beginning C++*. Apress.
- Huang, Sheng-Wei et al. (2016). "Effective energy-saving device of Eco-Ship by using wave propulsion". In: *2016 Techno-Ocean (Techno-Ocean)*. IEEE, pp. 566–570.
- Huxham, GH, S Cochard, and J Patterson (2012). "Experimental parametric investigation of an oscillating hydrofoil tidal stream energy converter". In: *18th Australasian Fluid Mechanics Conference (AFMC), Launceston, Australia, Dec*, pp. 3–7.
- Isshiki, Hiroshi (1982). "A theory of wave devouring propulsion (1st report)". In: *Journal of the Society of Naval Architects of Japan* 1982.151, pp. 54–64.
- Isshiki, Hiroshi and Mitsunori Murakami (1984). "A theory of wave devouring propulsion (4th report)". In: *Journal of the society of naval architects of Japan* 1984.156, pp. 102–114.
- Jakobsen, E (1981). "The foil propeller, wave power for propulsion". In: *2nd International Symposium on Wave and Tidal Energy, 1981*. BHRA fluid Engineering, pp. 363–369.
- Johannessen, Thomas B and Chris Swan (1997). "Nonlinear transient water waves—part I. A numerical method of computation with comparisons to 2-D laboratory data". In: *Applied Ocean Research* 19.5-6, pp. 293–308.
- Jonsson, Ivar G (1990). "Wave-current interactions". In: *The Sea: Ocean Engineering Science* 9, pp. 65–119.
- Katz, Joseph and Allen Plotkin (2001). *Low-speed aerodynamics*. Vol. 13. Cambridge university press.
- Kinsey, Thomas and Guy Dumas (2008). "Parametric study of an oscillating airfoil in a power-extraction regime". In: *AIAA journal* 46.6, pp. 1318–1330.

- (2012). “Optimal tandem configuration for oscillating-foils hydrokinetic turbine”. In: *Journal of fluids engineering* 134.3, p. 031103.
- Kirby, James T (1984). “A note on linear surface wave-current interaction over slowly varying topography”. In: *Journal of Geophysical Research: Oceans* 89.C1, pp. 745–747.
- Kolmogorov, A N and S V Fomin (1957). *Elements of the theory of functions and functional analysis. Vol. 1, Metric and normed spaces.*
- Koutsogiannakis, P. (2019). “Acceleration of BEM using CUDA/GPU programming with application to marine renewable energy extraction”. In: *Diploma Thesis NTUA.*
- Krasny, Robert, Keith Lindsay, and Monika Nitsche (2002). “Simulation of vortex sheet roll-up: chaos, azimuthal waves, ring merger”. In: *Tubes, Sheets and Singularities in Fluid Dynamics.* Springer, pp. 3–12.
- Kress, Rainer, V Maz’ya, and V Kozlov (1989). *Linear integral equations.* Vol. 82. Springer.
- Kundu, Pijush K, IM Cohen, and HH Hu (2008). “Fluid mechanics. 2004”. In: *Elsevier Academic Press, San Diego).* *Two-and three-dimensional self-sustained flow oscillations* 307, pp. 471–476.
- La Mantia, Marco and Peter Dabnichki (2009). “Unsteady panel method for flapping foil”. In: *Engineering Analysis with Boundary Elements* 33.4, pp. 572–580.
- (2011). “Influence of the wake model on the thrust of oscillating foil”. In: *Engineering analysis with boundary elements* 35.3, pp. 404–414.
- (2012). “Added mass effect on flapping foil”. In: *Engineering Analysis with Boundary Elements* 36.4, pp. 579–590.
- (2013). “Structural response of oscillating foil in water”. In: *Engineering Analysis with Boundary Elements* 37.6, pp. 957–966.
- Lamb, Horace (1993). *Hydrodynamics.* Cambridge university press.
- Lanchester, Frederick William (1907). *Aerial Flight.* Constable.
- Lewis, Reginald Ivan (2005). *Vortex element methods for fluid dynamic analysis of engineering systems.* Vol. 1. Cambridge University Press.
- Liu, Peng, Yu-min Su, and Yu-lei Liao (2016). “Numerical and experimental studies on the propulsion performance of a wave glide propulsor”. In: *China Ocean Engineering* 30.3, pp. 393–406.
- Liu, Peng, Yebao Liu, Shuling Huang, Jianfeng Zhao, and Yumin Su (2018). “Effects of Regular Waves on Propulsion Performance of Flexible Flapping Foil”. In: *Applied Sciences* 8.6, p. 934.
- Longuet-Higgins, Michael Selwyn and ED Cokelet (1976). “The deformation of steep surface waves on water-I. A numerical method of computation”. In: *Proc. R. Soc. Lond. A* 350.1660, pp. 1–26.
- Macdonald, Alan (2017). “A survey of geometric algebra and geometric calculus”. In: *Advances in Applied Clifford Algebras* 27.1, pp. 853–891.
- Manolas, D (2015). “Hydro-Aero-Elastic analysis of offshore wind turbines”. In: *PhD NTUA.*
- Marchioro, Carlo and Mario Pulvirenti (2012). *Mathematical theory of incompressible nonviscous fluids.* Vol. 96. Springer Science & Business Media.
- MARINTEK, ECON, CM, and DNV (2000). “Study of greenhouse gas emission from ships”. In: *Final Report IMO.*
- Massel, Stanislaw R (1989). *Hydrodynamics of coastal zones.* Vol. 48. Elsevier.
- Maxwell, James Clerk (1861). “On physical lines of force”. In: *The London, Edinburgh, and Dublin Philosophical Magazine and Journal of Science* 21.139.
- McConnell, Albert Joseph (2014). *Applications of tensor analysis.* Courier Corporation.
- McKinney, William and James DeLaurier (1981). “Wingmill: an oscillating-wing windmill”. In: *Journal of energy* 5.2, pp. 109–115.

- Mikhlin, Solomon Grigorevich (2014). *Multidimensional singular integrals and integral equations*. Elsevier.
- Milne-Thomson, Louis Melville (1996). *Theoretical hydrodynamics*. Courier Corporation.
- Mohammadi-Amin, Meysam, Behzad Ghadiri, Mostafa M. Abdalla, Hassan Haddadpour, and Roeland De Breuker (2012). "Continuous-time state-space unsteady aerodynamic modeling based on boundary element method". In: *Engineering Analysis with Boundary Elements* 36.5, pp. 789–798.
- Moored, Keith W (2018). "Unsteady three-dimensional boundary element method for self-propelled bio-inspired locomotion". In: *Computers & Fluids* 167, pp. 324–340.
- Moran, Jack (2003). *An introduction to theoretical and computational aerodynamics*. Courier Corporation.
- Morino, L. and C.-C. Kuo (1974). "Subsonic potential aerodynamics for complex configurations : A general theory". In: *AIAA Journal* 12.2, pp. 191–197.
- Morino, Luigi and Massimo Gennaretti (1993). "Boundary integral equation methods for aerodynamics". In: *Progress in Astronautics and Aeronautics* 146, pp. 279–279.
- Muskhelishvili, NI (1953). "Singular integral equations, Naukah Moscow". In: *English transl, of Isted Noordhoff*.
- Naito, Shigeru and Hiroshi Isshiki (2005). "Effect of bow wings on ship propulsion and motions". In: *Applied Mechanics Reviews* 58.4, pp. 253–268.
- Newman, J.N. (1977). *Marine Hydrodynamics*. Wei Cheng Cultural Enterprise Company. ISBN: 9780262140263.
- Nikolaev, MN, AI Savitskiy, and YUF Senkin (1995). "Basics of Calculation of the Efficiency of a Ship with Propulsor of the Wing Type". In: *Sudostroenie* 4, pp. 7–10.
- Ning, DZ and Bin Teng (2007). "Numerical simulation of fully nonlinear irregular wave tank in three dimension". In: *International Journal for numerical methods in fluids* 53.12, pp. 1847–1862.
- Nishimura, Naoshi (2002). "Fast multipole accelerated boundary integral equation methods". In: *Applied mechanics reviews* 55.4, pp. 299–324.
- Nwogu, Okey G (2009). "Interaction of finite-amplitude waves with vertically sheared current fields". In: *Journal of Fluid Mechanics* 627, pp. 179–213.
- Oseen, CW (1912). "Hydromechanik". In: *Ark. F. Math. Astrom. Och.Fys.* 7, p. 82.
- Papadakis, G (2014). "Development of a hybrid compressible vortex particle method and application to external problems including helicopter flows". In: *PhD NTUA*.
- Papoutsellis, Ch E, AG Charalampopoulos, and GA Athanassoulis (2018). "Implementation of a fully nonlinear Hamiltonian Coupled-Mode Theory, and application to solitary wave problems over bathymetry". In: *European Journal of Mechanics-B/Fluids* 72, pp. 199–224.
- Peng, Zhangli and Qiang Zhu (2009). "Energy harvesting through flow-induced oscillations of a foil". In: *Physics of fluids* 21.12, p. 123602.
- Peregrine, DH (1976). "Interaction of water waves and currents". In: *Advances in applied mechanics*. Vol. 16. Elsevier, pp. 9–117.
- Politis, Gerasimos and Konstantinos Politis (2014). "Biomimetic propulsion under random heaving conditions, using active pitch control". In: *Journal of Fluids and Structures* 47, pp. 139–149.
- Politis, Gerasimos and Vasileios Tsarsitalidis (2013). "Biomimetic propulsion using twin oscillating wings". In: *Proceedings of Third International Symposium on Marine Propulsors (SMP'13), Launceston, Tasmania, Australia*.
- Politis, Gerasimos K (2004). "Simulation of unsteady motion of a propeller in a fluid including free wake modeling". In: *Engineering analysis with boundary elements* 28.6, pp. 633–653.

- (2011a). “Application of a BEM time stepping algorithm in understanding complex unsteady propulsion hydrodynamic phenomena”. In: *Ocean Engineering* 38.4, pp. 699–711.
 - (2011b). *The Boundary Element Method for 3-D Fluid Flow Problems*.
 - (2016). “Unsteady wake rollup modeling using a mollifier based filtering technique”. In: *Dev Appl Ocean Eng* 5, pp. 1–28.
- Politis, Gerasimos K and Vasileios T Tsarsitalidis (2014). “Flapping wing propulsor design: An approach based on systematic 3D-BEM simulations”. In: *Ocean Engineering* 84, pp. 98–123.
- Polyanin, AD and AV Manzhirov (2008). “Handbook of Integral Equations. Boca Raton”. In: Prandtl, Ludwig (1918). “Königliche Gesellschaft der Wissenschaften zu Göttingen”. In: *ed. Tragflügeltheorie*.
- Priovolos, AK, ES Filippas, and KA Belibassakis (2018). “A vortex-based method for improved flexible flapping-foil thruster performance”. In: *Engineering Analysis with Boundary Elements* 95, pp. 69–84.
- Read, Douglas A, FS Hover, and MS Triantafyllou (2003). “Forces on oscillating foils for propulsion and maneuvering”. In: *Journal of Fluids and Structures* 17.1, pp. 163–183.
- Riziotis, VA and SG Voutsinas (2007). “Dynamic stall modeling on hydrofoils based on strong viscous-inviscid interaction coupling”. In:
- Rozhdestvensky, Kirill V and Vladimir A Ryzhov (2003). “Aerohydrodynamics of flapping-wing propulsors”. In: *Progress in aerospace sciences* 39.8, pp. 585–633.
- Saffman, Philip G (1992). *Vortex dynamics*. Cambridge university press.
- Sanders, Jason and Edward Kandrot (2010). *CUDA by example: an introduction to general-purpose GPU programming*. Addison-Wesley Professional.
- Schouveiler, Lionel, FS Hover, and MS Triantafyllou (2005). “Performance of flapping foil propulsion”. In: *Journal of Fluids and Structures* 20.7, pp. 949–959.
- Shimizu, Eriko, Koji Isogai, and Shigeru Obayashi (2008). “Multiobjective design study of a flapping wing power generator”. In: *Journal of Fluids Engineering* 130.2, p. 021104.
- Soulsby, RL (1990). “Tidal-current boundary layers”. In: *The Sea* 9.part A, pp. 523–566.
- Spinneken, Johannes, Marios Christou, and Chris Swan (2014). “Force-controlled absorption in a fully-nonlinear numerical wave tank”. In: *Journal of Computational Physics* 272, pp. 127–148.
- Takahashi, Toru and Toshiro Matsumoto (2012). “An application of fast multipole method to isogeometric boundary element method for Laplace equation in two dimensions”. In: *Engineering Analysis with Boundary Elements* 36.12, pp. 1766–1775.
- Taylor, GK, MS Triantafyllou, and C Tropea (2010). “Animal locomotion”. In: *Animal Locomotion*, pp. 1–443.
- Terao, Y and H Isshiki (1991). “Wave devouring propulsion sea trial”. In:
- Terao, Yutaka (1982). “A FLOATING STRUCTURE WHICH MOVES TOWARD THE WAVES (POSSIBILITY OF WAVE DEVOURING PROPULSION)”. In:
- Terao, Yutaka and Norimitsu Sakagami (2013). “Application of wave devouring propulsion system for ocean engineering”. In: *Proceedings of the ASME 2013 32nd International Conference on Ocean, Offshore and Arctic Engineering (OMAE2013)*.
- Thomas, GP and G Klopman (1997). “Wave-current interactions in the near shore region”. In: *INTERNATIONAL SERIES ON ADVANCES IN FLUID MECHANICS* 10, pp. 255–319.
- Touboul, Julien and Christian Kharif (2010). “Two-dimensional direct numerical simulations of the dynamics of rogue waves under wind action”. In: *Advances in numerical simulation of nonlinear water waves*. World Scientific, pp. 43–74.

- Touboul, Julien, Jean-Paul Giovanangeli, Christian Kharif, and Efim Pelinovsky (2006). "Freak waves under the action of wind: experiments and simulations". In: *European Journal of Mechanics-B/Fluids* 25.5, pp. 662–676.
- Touboul, Julien, Jenna Charland, Vincent Rey, and K Belibassakis (2016). "Extended mild-slope equation for surface waves interacting with a vertically sheared current". In: *Coastal Engineering* 116, pp. 77–88.
- Triantafyllou, Michael S, GS Triantafyllou, and DKP Yue (2000). "Hydrodynamics of fishlike swimming". In: *Annual review of fluid mechanics* 32.1, pp. 33–53.
- Triantafyllou, Michael S, Alexandra H Tchet, and Franz S Hover (2004). "Review of experimental work in biomimetic foils". In: *IEEE Journal of Oceanic Engineering* 29.3, pp. 585–594.
- Trompoukis, X (2012). "Numerical solution of aerodynamic-aeroelastic problems on Graphics Processing Units". In: *PhD NTUA*.
- Tsarsitalidis, Vasileios (2015). "Hydrodynamic simulation of biological propulsion systems and application on the design of optimal marine propulsors". In: *PhD NTUA*.
- Turkel, Eli and A Yefet (1998). "Absorbing PML boundary layers for wave-like equations". In: *Applied Numerical Mathematics* 27.4, pp. 533–557.
- Vinje, Tor and Per Brevig (1981). *Breaking waves on finite water depths: a numerical study*. Ship Research Institute of Norway Marine Technology Center.
- Von Ellenrieder, KD, K Parker, and J Soria (2008). "Fluid mechanics of flapping wings". In: *Experimental Thermal and Fluid Science* 32.8, pp. 1578–1589.
- Winckelmans, GS and Anthony Leonard (1993). "Contributions to vortex particle methods for the computation of three-dimensional incompressible unsteady flows". In: *Journal of Computational Physics* 109.2, pp. 247–273.
- Wu, J, YL Chen, and N Zhao (2015). "Role of induced vortex interaction in a semi-active flapping foil based energy harvester". In: *Physics of Fluids* 27.9, p. 093601.
- Wu, Jie-Zhi, Hui-Yang Ma, and M-D Zhou (2007). *Vorticity and vortex dynamics*. Springer Science & Business Media.
- Wu, Sijue (1999). "Well-posedness in Sobolev spaces of the full water wave problem in 3-D". In: *Journal of the American Mathematical Society* 12.2, pp. 445–495.
- Wu, TYT (1971). *Extraction of flow energy by a wing oscillating in waves*. Tech. rep.
- Xiao, Qing and Qiang Zhu (2014). "A review on flow energy harvesters based on flapping foils". In: *Journal of fluids and structures* 46, pp. 174–191.
- Xu, GD, WY Duan, and BZ Zhou (2017). "Propulsion of an active flapping foil in heading waves of deep water". In: *Engineering Analysis with Boundary Elements* 84, pp. 63–76.
- Yeung, Ronald W and Yann C Bouger (1979). "A hybrid integral-equation method for steady two-dimensional ship waves". In: *International Journal for Numerical Methods in Engineering* 14.3, pp. 317–336.
- Young, John, Joseph CS Lai, and Max F Platzer (2014). "A review of progress and challenges in flapping foil power generation". In: *Progress in aerospace sciences* 67, pp. 2–28.
- Zhu, Qiang (2011). "Optimal frequency for flow energy harvesting of a flapping foil". In: *Journal of fluid mechanics* 675, pp. 495–517.
- Zhu, Qiang and Zhangli Peng (2009). "Mode coupling and flow energy harvesting by a flapping foil". In: *Physics of Fluids* 21.3, p. 033601.
- Zhu, Qiang, Yuming Liu, and Dick KP Yue (2006). "Dynamics of a three-dimensional oscillating foil near the free surface". In: *AIAA journal* 44.12, pp. 2997–3009.
- Zhu, Qiang, Max Haase, and Chin H Wu (2009). "Modeling the capacity of a novel flow-energy harvester". In: *Applied Mathematical Modelling* 33.5, pp. 2207–2217.

Curriculum Vitae



Mr Evangelos FILIPPAS (evfilip@central.ntua.gr, evanfilippas@gmail.com): Diploma in Naval Architecture and Marine Engineering (8.31/10.00, 3rd among the graduates of 2013, SNAME, NTUA). His diploma thesis is entitled: "A boundary element method for the hydrodynamic analysis of flapping-foil thrusters operating beneath the free surface and in waves", with supervisor Prof. Belibassakis. Heretofore, he has been working on his Ph.D, entitled "Hydrodynamic analysis of ship and marine biomimetic systems in waves using GPGPU programming", developing a 3D unsteady nonlinear BEM code in CUDA/C for the study of marine energy devices.

He was, until recently, supported by Alexander Onassis public benefit foundation. He participated in the EU and Greek funded research project BIO-PROPSHIP (2012-2015). He has co-authored 5 journal articles, 12 conference papers. Scopus Citations: 39, h-index 3. GoogleScholar 56 citations, h-index 3, i10-index 2. Researchgate: 27 citations, RGscore 8.38

Academic Degrees: Diploma in Naval Architecture and Marine Engineering from the School of Naval Architecture and Marine Engineering (S.N.A.M.E.), National Technical University of Athens (N.T.U.A.). Grade Point Average: 8.31/10.00, 3rd among the graduates of the year 2013.

Diploma thesis: "A boundary element method for the hydrodynamic analysis of flapping-foil thrusters operating beneath the free surface and in waves". Supervisor: Belibassakis K.A., Professor, S.N.A.M.E., N.T.U.A. In the above thesis the hydrodynamic analysis of a biomimetic flapping-foil propulsor is presented. The study is concentrated to the free-surface and incident-wave effects, with main purpose the wave-energy extraction for marine propulsion. Available at: http://dspace.lib.ntua.gr/bitstream/123456789/7806/3/filippase_waves.pdf

Current Position: PhD candidate at the S.N.A.M.E., N.T.U.A., under the supervision of Professor Kostas Belibassakis, Subject: "Hydrodynamic analysis of ship and marine biomimetic systems in waves using GPGPU programming".

Research interests: Mathematical modeling in fluid dynamics (focusing in potential theory and boundary integral equations solved numerically by time-domain nonlinear boundary element methods) and engineering, emphasizing to wave-current-flexible body-lifting flow-bottom interactions, using parallel programming (focusing in GPU-programming), for the design, assessment and control of biomimetic marine energy devices (e.g. flexible flapping-foil thruster, wave-foil energy device, flapping-foil wave-current energy device), offshore and nearshore.

Publications: Author and/or co-author of 5 international journal publications and 12 conference papers published in the corresponding proceedings.

Research Projects: Participation in the research project BIO-PROPSHIP: «Augmenting ship propulsion in rough sea by biomimetic-wing system» co-financed by the European Union (European Social Fund – ESF) and Greek national funds through the Operational Program "Education and Lifelong Learning" of the National Strategic Reference Framework (NSRF) 2007-2013: Program ARISTEIA: <http://arion.naval.ntua.gr/~biopropship>

Teaching assistance:

A) Assistant in the supervision of the following Diploma Thesis in SNAME NTUA, under the supervision of professor Belibassakis:

- i) Priovolos Andreas: "Effects of chordwise flexibility on flapping-foil thruster performance".
- ii) Koutsogiannakis Panagiotis: "Acceleration of BEM using CUDA/GPU programming with application to marine renewable energy extraction".
- iii) Anevlavi Dimitra: " Hydroelastic analysis of flapping foils by a coupled BEM-FEM with application to marine energy extraction devices".

B) Teaching Assistant in the following courses of SNAME NTUA

- i) Basic Ship and Marine Hydrodynamics, ii) Ship Resistance and Propulsion
- iii) Ship Design Project (Resistance and Propulsion), iv) Mathematical formulation of lifting flows
- v) Hydrodynamics of Modern Propulsion Systems

Reviewer for the following international scientific journals Ocean Engineering, Engineering Analysis with Boundary Elements and international conferences International Conference on Ocean, Offshore & Arctic Engineering (OMAE), International Congress of Intern. Maritime Association of the Mediterranean (IMAM).

Member of the Society of Naval Architects & Marine Engineers (SNAME).

Most significant publications categorised per main research direction are listed below:

Ship hydrodynamics. Propulsors and biomimetic systems.

FILIPPAS, E., Belibassakis K.A., 2014, Hydrodynamic analysis of flapping-foil thrusters operating beneath the free surface and in waves, **Engineering Analysis with Boundary Elements**, Vol.41, 47-59.

Belibassakis K.A., FILIPPAS, E., 2015, Ship propulsion in waves by actively controlled flapping foils, *Applied Ocean Research* Vol. 52, 1–11

FILIPPAS E.S., 2015, "Augmenting ship propulsion in waves using flapping foils initially designed for roll stabilization", **Proc. Computer Science**, vol. 66, 103–111.

Marine hydrodynamics. Wave - current energy extraction and biomimetic systems

FILIPPAS E.S., Gerostathis Th.P., Belibassakis K.A., 2018, "Semi-activated oscillating hydrofoil as a nearshore biomimetic energy system in waves and currents", **Ocean Engineering**, vol. 154, 396–415.

Fluid and Structure Interaction and biomimetic systems

Priovolos A.K., FILIPPAS E.S., Belibassakis K.A., 2018, "A vortex-based method for improved flexible flapping-foil thruster performance", **Engineering Analysis with Boundary Elements**, vol. 95, 69–84.

Awards:

2015 Awarded for the work Filippas E.S., 2015, "Augmenting ship propulsion in waves using flapping foils initially designed for roll stabilization" that was presented in the 4th International Young Scientists Conference and Summer School in Computer Modeling and Simulation (YSC 2015), 25 June - 5 July in Athens, Greece.

2013 Scholarship by Alexander S. Onassis Public Benefit Foundation for PhD studies at S.N.A.M.E., N.T.U.A.

2013 Award of academic excellence 2013. Awarded by Limmat Stiftung Foundation and by N.T.U.A. for graduating 3rd among the graduates of S.N.A.M.E. in the year 2013.

2011 American Bureau of Shipping Awards (2011 ABS Awards). Second award for excellent student work in undergraduate level: Boundary Element Methods and applications to simple problems of hydrodynamics and wave propagation in marine environment", (<http://arion.naval.ntua.gr/~banthy/panelm.pdf>).

Participation in conferences and presentation of the following works:

2013 " FILIPPAS, E., Belibassakis K.A., 2013, A boundary element method for the hydrodynamic analysis of flapping-foil thrusters operating beneath the free surface and in waves" at the "**15th International Congress of the Int. Mar Assoc of the Med (IMAM 2013)**" on 14-17 of October at La Coruna, Spain.

2014 "Belibassakis K.A., FILIPPAS, E.S., 2014, "A method for the analysis and design of flapping-foil thrusters for augmenting ship propulsion in waves", at the "**2nd International Conference on Maritime Technology and Engineering (MARTECH2014)**" on 15-17 of October in Lisbon, Portugal.

2014 Belibassakis K., FILIPPAS E., 2014, "Biomimetic flapping foil thrusters for augmenting ship propulsion in waves", at the "**Proc. Hellenic Institute of Marine Technology Annual Meeting**", 18-19 Nov.2014.

2015 "Belibassakis K.A., Gerostathis Th.P., FILIPPAS E., Touboul J., Rey V., 2015, Oscillating hydrofoils as energy devices operating in waves and currents" at the "**11th European Wave and Tidal Energy Conf (EWTEC 2015)**" on 6-11 of September in Nantes, France.

2015 "Belibassakis K.A., FILIPPAS E.S., Touboul J., Rey V., 2015, Hydrodynamic analysis of oscillating hydrofoils in waves and currents" at the "**16th International Congress of the Int. Maritime Assoc of the Mediterranean (IMAM 2015)**" on 21-24 of September in Pula, Croatia.

2015 " FILIPPAS, E.S., 2015, "Augmenting ship propulsion in waves using flapping foils initially designed for roll stabilization", at the "**4th International Young Scientists Conf and Summer School in Computer Modeling and Simulation (YSC 2015)**" on 25 June - 5 July in Athens, Greece.

2016 "Belibassakis K.A., FILIPPAS E.S., Gerostathis Th.P., 2016, Biomimetic systems operating as marine energy devices in waves and sheared currents" at the "**11th Int Congr on Mechanics (HSTAM 2016)**" on 27-30 of May in Athens

2018 FILIPPAS E., Belibassakis K., 2018, 3D flapping foil thrusters for augmenting ship propulsion in waves", "**Proc. 11th Panhellenic Conference FLOW 2018**", Kozani-Greece 23-24 Nov. 2018.